Universität Rostock

Traditio et Innovatio

Hydrogen Bond Lifetimes and Equilibria in Hydroxyl-functionalized Ionic Liquids

Cumulative Dissertation

to obtain the academic degree
doctor rerum naturalium (Dr. rer. nat.)
of the Faculty of Mathematics and Natural Sciences
at the University of Rostock

submitted by

Jan Neumann,
born on 30.10.1992 in Pritzwalk

June 14, 2021, Rostock

https://doi.org/10.18453/rosdok_id00003394

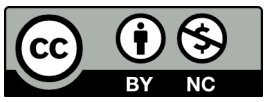

Year of submission: 2021
Year of oral defence: 2021

First Reviewer:
Prof. Dr. Ralf Ludwig
Physikalische und Theoretische Chemie
Institut für Chemie, Universität Rostock, Germany

Second Reviewer:
Prof. Dr. Imre Bakó
Research Centre for Natural Sciences
Budapest, Hungary

Contents

List of Abbreviations

ca	cation-anion
cc	cation-cation
DSC	differential scanning calorimetry
HB	hydrogen bond
IL	ionic liquid
IR	infrared
IUPAC	International Union of Pure and Applied Chemistry
KPL	Köddermann-Paschek-Ludwig force field for $[NTf_2]^-$[1]
MC	Monte Carlo
MD	molecular dynamics
MSD	mean square displacement
ND	neutron diffraction
NGOLP	Neumann-Golub-Odebrecht-Ludwig-Paschek force field for $[NTf_2]^-$[2]
NMR	nuclear magnetic resonance
PBC	periodic boundary condition
TST	transition state theory
VFT	Vogel-Fulcher-Tammann, temperature behavior according to equation 2.2

Substances

$\mathbf{[NTf_2]^-}$	bis(trifluoromethanesulfonyl)azanide
$\mathbf{[HOC_nPy]^+}$	1-(n-hydroxyalkyl)pyridinium
$\mathbf{[C_nPy]^+}$	1-alkylpyridinium
$\mathbf{[HOC_nMIm]^+}$	1-(n-hydroxyalkyl)-3-methylimidazolium
$\mathbf{[C_nMIm]^+}$	1-alkyl-3-methylimidazolium
$\mathbf{[HOC_nMPip]^+}$	1-(n-hydroxyalkyl)-methylpiperidinium

Acknowledgements

This work could not have been done without the help of many wonderful people. Firstly, I would like to thank Prof. Dr. Ralf Ludwig for providing the topic of my thesis, the means to independently research this interesting subject and the great atmosphere in his group with many science-reated and social activities, such as the group meeting in Bad Malente or the dinner parties at his home. In addition, I am very grateful for the opportunity to visit many national and international conferences to discuss my research with other fellow scientists.

Secondly, I would like to thank my supervisor Dr. Dietmar Paschek for the many scientific and non-scientific discussions over the years and the opportunity to impact the group beyond my research, be it the supervison of students or the extension of the simulation hardware.

I thank all current and former colleagues in the physical chemistry department, in particular Benjamin Golub, Johanna Busch, Sebastian Fritsch, Wigbert Polet, and Elias Reiter, for the fantastic working environment and all the lessons they taught me over the years. I also want to thank the technical staff of the physical chemistry department, namely Anika Wilhelms, Sabine Kindermann, Dagmar Klasen, and Nele Leopold, who were of great help organizing a plethora of things through the years. In addition, I would like to thank Andreas Appelhagen as well as the administrators of the HPC resources of the ITMZ for making sure that the hard- and software was always in working order for the many calculations done in this work.

Thanks to all the proofreaders, who caught many mistakes with their watchful eyes before this document was able to see the light of day: Susanne Fischer, Johanna Busch, Sebastian Fritsch, Benjamin Golub, Eduard Mock, and Jule Kristin Philipp.

Lastly, I would like to thank my family and friends, for accompanying and supporting me through my time as a student.

Abstract

In this work, we were able to study the structure and dynamics of the hydrogen bond (HB) network in pyridinium-based ILs. First, we developed classical force fields for the bis(trifluoromethanesulfonyl)azanide anion ($[NTf_2]^-$) and 1-(n-hydroxyalkyl)pyridinium cations ($[HOC_nPy]^+$), which were able to describe the bulk liquid phase of the respective ionic liquid (IL) $[HOC_nPy][NTf_2]$, when combined.[2,3] By comparing structural and dynamical data obtained from molecular dynamics (MD) simulations with data acquired from experiments, the accuracy of the used force fields was demonstrated.[4]

Employing MD simulations, it was shown that different HB species, cation-cation (cc) and cation-anion (ca) HBs, are present in the liquid as well as the gas phase.[5] The geometry of these HBs was compared to results acquired from neutron diffraction (ND) and quantum chemical calculations and the equilibrium between the different HB species was analyzed using a variety of methods.[6] Although the ca HBs are more common, the cc HBs were found to be on average stronger than the ca HBs in the respective IL. It was established that the population of cc HBs grows with increasing alkyl chain length and decreasing temperature. The equilibrium ca $\rightleftharpoons$ cc was described regarding its enthalpy and entropy of transition using a Van 't Hoff analysis.[4] For the pyridinium-based ILs investigated here, the cc HB is enthalpically stabilized but entropically destabilized compared to the respective ca HB.

The dynamics of the HB network were described using various HB lifetimes.[4] The intermittent HB lifetime is influenced by processes in two different time domains. The short-time behavior is dominated by the orientational correlation of the OH bond vector while the long-time behavior is governed by the interdiffusion of donor and acceptor moieties. The long-time behavior was shown to be the major component of the intermittent HB lifetimes, due to the high viscosity of the ILs. Using the reactive-flux mechanism, HB lifetimes, which are not influenced by diffusion, were obtained.[4] The various HB lifetimes show that the cc HB becomes kinetically more stable than the ca HB in the respective IL for longer alkyl chain lengths and at low temperatures.

1. Introduction

Despite being a crucial mode of intermolecular interaction in all phases of water and affiliated to many of its anomalies, the hydrogen bond (HB) was only discovered at the beginning of the 20th century. Stillinger credits Latimer and Rodebush with the first systematic study of HBs,[7,8] however, they refer to unpublished results of M. L. Huggins, stating a theory of hydrogen bonding in organic compounds. Even earlier, a number of German and British researchers reported effects hinting at the existence of HB in different systems.[9,10] Since then, many scientists have been engaged in researching and modelling HBs in a plethora of systems, improving our understanding.[9–13]

Despite the strong Coulomb interaction between the ions, hydrogen bonding can play an important role in structural and dynamical properties of ionic liquids (ILs).[14–23] Generally, these substances are defined as salts with a melting point below 100 °C, although this boundary was chosen rather arbitrarily.[24] To obtain such a low melting point, the lattice energy has to be lowered, most often by introducing large organic or inorganic ions with a diffuse charge distribution. Compared to molecular liquids, ILs generally have distinctive properties, such as a wide liquid range and electrochemical window, a high viscosity, and a low vapor pressure, making them appealing for applications as electrolytes and solvents.[25–28]

The properties of ILs can be "designed" due to the many possible combinations of anions and cations. This makes them especially interesting as research subjects, as it reveals the interplay between interactions on the molecular level and macroscopic properties. In 2015, Knorr et al. were the first to report spectroscopic evidence of so-called "like-charged" HBs.[29] Despite the repulsive Coulomb interaction between the cations, these intermolecular HBs form between hydroxyl functions located on the cholinium cation. They are, of course, in equilibrium with the expected HBs to the bis(trifluoromethanesulfonyl)azanide ($[NTf_2]^-$) anion. The cation-anion (ca) HBs heavily outnumber the cation-cation (cc) HBs in this particular IL, partly due to the favorable Coulomb interaction between anion and cation. Subsequently, an effort

was made to influence this equilibrium in favor of the cc HBs and investigate its effect on macroscopic properties of the respective ILs, by fine-tuning the composition of the cation and anion.[30–38] For pure ILs, three main influences on the ability to form cc HBs were found: the polarizability of the cation, the distance of the functional group from the charge center, and the interaction strength of the anion.[38]

The family of 1-(n-hydroxyalkyl)pyridinium cations ($[HOC_nPy]^+$) combines the first two factors: due to the aromatic pyridinium-ring the positive charge is delocalized over a large volume and by varying the length of the alkyl chain one can tune the distance between the hydroxyl group and the charge center. Combining this with the weakly interacting $[NTf_2]^-$ anion results in a class of ILs which is ideally suited to study the HB equilibrium and its influences on the structure and dynamics in the IL. In this work, the different HBs in this IL family are studied using molecular dynamics (MD) simulation. The access to direct structural and dynamical information from the same experiment makes MD simulation a useful tool to study HBs in various systems, from liquid water to, more recently, ILs.[39–50] The first part of this work is concerned with the development and testing of force fields appropriate to describe the bulk liquid phase of $[HOC_nPy][NTf_2]$ ILs. In the second part, we will use these simulations to investigate the different HB species regarding their geometry, population, and dynamics and draw comparisons to experimental data, where available.

2. Development and Validation of Force Fields

Force fields govern the intra- and intermolecular interactions between the particles and therefore every physico-chemical property in MD simulations. Thus, it is of utmost importance to deliberately select the employed force fields in order to attain the most trustworthy data possible. The following chapter will discuss the design of the force fields of the $[NTf_2]^-$ anion and the pyridinium-based $[HOC_nPy]^+$ cations. Furthermore, dynamical data obtained by using these force fields is presented and compared to experimental data, where available.

2.1. Anion Force Field

In 2007 Köddermann, Paschek, and Ludwig reported the KPL force field, named after the authors initials, for imidazolium-based ILs with the $[NTf_2]^-$ anion (Fig. 2.1), which was subsequently improved in 2013 and was able to reliably describe the structural and dynamical properties of the system.[1,51] In publication I, we were able to improve the force field of the $[NTf_2]^-$ anion by investigating the conformation space explored by the anion and suggested an enhanced version, which will be referenced as the NGOLP force field.[2]

The conformation of the $[NTf_2]^-$ anion is mainly dependent on the two dihedral angles S1-N-S2-C2 (ϕ_1) and S2-N-S1-C1 (ϕ_2). The only other independent type of dihedral angle, the F-C-S-N dihedral, describes the rotation of the trifluoromethyl group and plays only a minor role in describing the overall anion conformation. Fig. 2.2 shows the relative energy of the $[NTf_2]^-$ anion as a function of the conformation described by the two dihedral angles ϕ_1 and ϕ_2 according to ab initio calculations.[2] Due to the symmetry of the anion, the global minima at $\phi_1 = \phi_2 = 90°$ and $\phi_1 = \phi_2 = 270°$ both describe the *trans* conformation, which is shown in Fig. 2.1 a). The *gauche* conformation, which is depicted in Fig. 2.1 b), is found at the four local

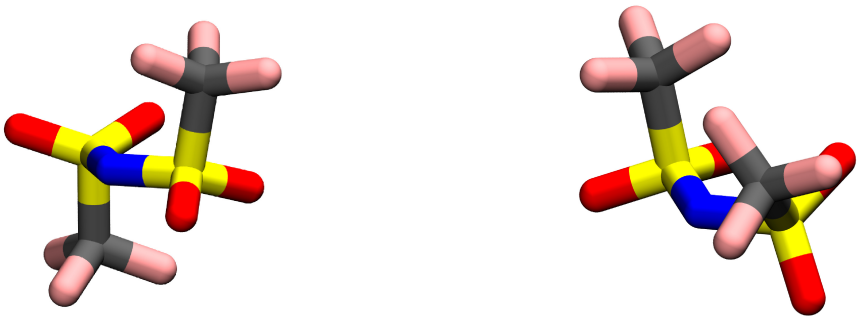

a) *trans* conformation

b) *gauche* conformation

Fig. 2.1.: Global and local minima of the conformational energy surface of the $[NTf_2]^-$ anion obtained by ab initio calculations. The *trans* conformation is energetically favored by about $3\,kJ\,mol^{-1}$ compared to the *gauche* conformation.[2] The following color code is used for the atoms: nitrogen: blue, sulfur: yellow, oxygen: red, carbon: black, fluorine: pink.

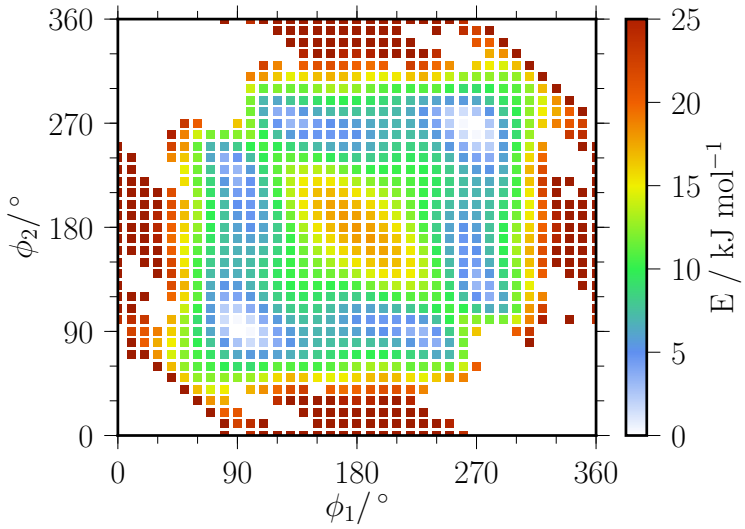

Fig. 2.2.: Conformational energy surface as a function of the S1-N-S2-C2 (ϕ_1) and S2-N-S1-C1 (ϕ_2) dihedral angle obtained from ab initio calculations. The white areas on the edge of the diagram represent high energy conformations where the geometry optimization was aborted.[2]

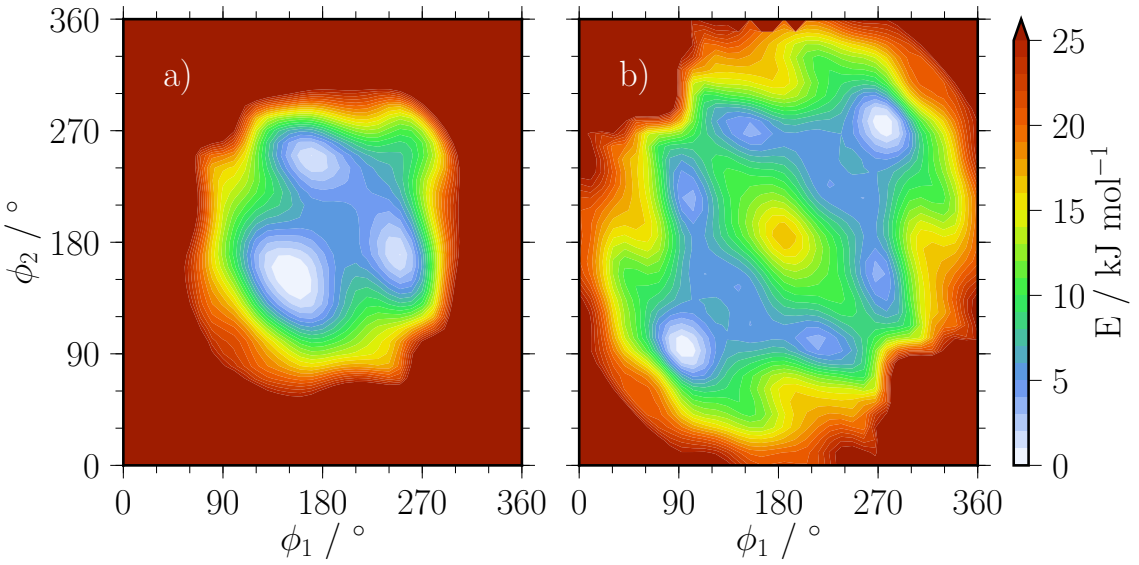

Fig. 2.3.: Conformational energy surface as a function of the S1-N-S2-C2 (ϕ_1) and S2-N-S1-C1 (ϕ_2) dihedral angle obtained from the KPL (a) and the NGOLP force field (b), respectively.[2]

minima, for instance at $\phi_1 = 90°$ and $\phi_2 = 230°$. These local minima are, again, indistinguishable from one another due to the symmetry of the $[NTf_2]^-$ anion. Both the *trans* as well as the *gauche* conformer were also shown to be present in the liquid phase by Fujii et al. using Raman spectroscopy.[52]

As seen in Fig. 2.3 a) the KPL force field is unable to reproduce this energy landscape or its symmetry. By reparameterizing the charges and the two independent dihedrals S-N-S-C and F-C-S-N we were able to improve the description of the energy surface, as seen in Fig. 2.3 b). While there are still some noticable differences comparing Fig. 2.3 b) and Fig. 2.2, the global and local minima as well as the transitions between those minima are well represented in relative energy and location. At ambient temperature, the anion mostly explores the low energy conformations around and transitions between these minima, so differences pertaining to higher energy conformations are negligible for simulations at those conditions.

We were able to show that these changes in the anion force field lead to an improved agreement between MD simulation and experiment for ILs with 1-alkyl-3-methylimidazolium cations $[C_nMIm]^+$ for a variety of properties, such as densities, self-diffusion coefficients, vaporization enthalpies, and viscosities.[2] The changes were also shown to increase the amount of HBs between the C(2)-hydrogen of the

imidazolium cation and the oxygen atoms of the anion compared to the KPL force field. Presumably, the changes regarding the minimum conformation should also affect the HB statistics for the hydroxyl-functionalized ILs investigated in this work.

The NGOLP force field is capable of accurately describing structural and dynamical data without including polarizability or scaled charges. It was since used by multiple groups to investigate a variety of IL related topics, such as structural investigations,[53] gas diffusivities,[54] and HB dynamics.[50] The anion force field can also be combined with non-imidazolium-based cations to describe a variety of ILs.[6,55–57]

2.2. Cation Force Fields

At the beginning of this work, only few reliable force fields for hydroxyl-functionalized cations were available. Those available were limited to the often used imidazolium- or phosphonium-based cations and not the "more exotic" pyridinium-based cations. For the investigation of the HB equilibrium, functionalized pyridinium-based ILs are desirable, as they are highly polarizable by delocalizing the positive charge in the aromatic pyridinium-ring and thereby increasing the amount of cc HBs.[38,58] In principle, the same applies to the imidazolium-based cations, but the acidic protons in the imidazolium-ring also affect the HB equilibrium and are therefore unnecessarily complicating the system.[59–61]

The force fields of the functionalized pyridinium-based cations $[\mathrm{HOC}_n\mathrm{Py}]^+$ are derived using a combination of the OPLS-AA force fields for pyridine and the respective alcohols from Jorgensen et al.[62,63] They were published in part over a series of publications[5,6,56] but were finally gathered and published in their entirety for all alkyl chain lengths $n = 2$–5 in publication V.[3] The point-charges on the atom positions as well as the dihedral potentials of the hydroxyl-alkyl chain were recalculated using the same approach employed for the $[\mathrm{NTf}_2]^-$ anion described above, with emphasis on the reproduction of conformational changes.

It is to be expected that the hydroxyl group is influenced more by the charge distribution in the aromatic ring for short alkyl chains than for long ones. For that reason, we decided to fit the charges of every cation separately, sacrificing transferability of the force field for a better emulation of the charge density of the

respective cation. Unfortunately, this means that the dihedral potentials are also not transferrable, because the charges affect the non-bonded interactions.

2.3. Influence of Conformational Changes on the Enthalpy of Vaporization

That an accurate representation of conformational changes is crucial for correctly describing physico-chemical properties could be shown in publication IV.[5] Previously, it was determined that functionalized ILs typically exhibit a lower enthalpy of vaporization $\Delta_l^g H_m^\circ$ than their unfunctionalized counterparts because the HB is transferred to the gas phase and stabilizes the ion pair.[64] Comparing $\Delta_l^g H_m^\circ$ of $[C_3MIm][NTf_2]$ and $[HOC_2MIm][NTf_2]$, however, showed that the difference in the enthalpies of vaporization $\Delta(\Delta_l^g H_m^\circ)$, between the unfunctionalized and functionalized IL, is almost zero.[5] In the case of the pyridinium-based cations $[HOC_2Py]^+$ and $[HOC_3Py]^+$, when comparing them to their unfunctionalized counterparts $[C_3Py]^+$ and $[C_4Py]^+$ in their respective $[NTf_2]^-$ based IL, the values of $\Delta(\Delta_l^g H_m^\circ)$ are even negative. This means that the unfunctionalized IL possesses the lower enthalpy of vaporization in both cases. Infrared (IR) spectra of the functionalized ILs revealed that HBs between cation and anion through the hydroxyl group are present in the liquid phase. For the imidazolium-based ILs HBs involving the C(2)-, C(4)-, and C(5)-hydrogen were detected as well. As these HBs are also present in the unfunctionalized IL, one could argue that the HB involving the hydroxyl group might not be present in the gas-phase ion pair, which could explain the differences in $\Delta_l^g H_m^\circ$.

Using MD simulation, we were able to elucidate the effects leading to the uncommon behavior of $\Delta(\Delta_l^g H_m^\circ)$.[5] For the functionalized ILs $[HOC_2Py][NTf_2]$ and $[HOC_2MIm][NTf_2]$ and their respective unfunctionalized counterparts $[C_3Py][NTf_2]$ and $[C_3MIm][NTf_2]$, we performed simulations representing the liquid phase with 512 ion pairs and employing periodic boundary conditions (PBCs) as well as gas-phase simulations constituted of a single ion pair without PBCs. The differences in enthalpy of vaporization $\Delta(\Delta_l^g H_m^\circ)$ can be calculated as the change in potential energy differences $\Delta(\Delta_l^g E_{pot})$ due to the contributions of $p \cdot V$ canceling each other out. We demonstrated that the behavior of $\Delta(\Delta_l^g H_m^\circ)$ in the experiment can be reproduced by our MD simulation approach and is dominated by the change in intermolecular interaction energy.

We found that the $[NTf_2]^-$ anion adopts energetically less favorable conformations in the gas-phase ion pair than the global minimum conformation (*trans*) discussed above.[5] Gauche-like conformations allow for a better contact between the negative charge, mainly located on the oxygen atoms of the anion, and the positive charge, which is delocalized in the aromatic ring of the imidazolium- and pyridinium-based cations. However, this intramolecular energy penalty is present in all of the investigated ILs and is therefore not able to justify the behavior of $\Delta(\Delta_l^g H_m^\circ)$. The simulations show that the intermolecular HB through the hydroxyl group is present in the majority of configurations in the gas-phase ion pair of the functionalized ILs. We were able to demonstrate that the formation of this ca HB disturbs the matching of the charge centers for both imidazolium- and pyridinium-based ILs. This increases the intermolecular interaction energy difference between gas and liquid phase and thereby decreases $\Delta_l^g H_m^\circ$ of the functionalized IL.[5] The difference between both types of ILs is that the imidazolium-based IL is less affected by this disturbance, possibly due to the formation of HBs involving the ring-hydrogens, further stabilizing the gas-phase ion pair. Therefore, compared to other ILs, the perturbances in the conformation of the gas-phase ion pair can negate and, in the case of the pyridinium-based cation, even overcompensate the energy benefit of the HB.

2.4. Viscosity

To calculate the viscosities of the $[HOC_nPy][NTf_2]$ ILs, we employed a procedure suggested by Zhang et al.[65] The pressure tensor $\boldsymbol{P}$ is linked to the viscosity η via a Green-Kubo relation

$$\eta = \frac{V}{k_B T} \int_0^\infty \langle P_{\alpha\beta}(0) \cdot P_{\alpha\beta}(t) \rangle \, \mathrm{d}t, \tag{2.1}$$

with the volume of the system V, the Boltzman constant k_B, the temperature T, and the $\alpha\beta$ element of the pressure tensor $\boldsymbol{P}$, $\alpha \neq \beta$.[4] Due to the noise of the autocorrelation function, the integral does not converge at long times, leading to a non-constant running integral $\langle \eta(t) \rangle$. Zhang et al. suggest an approach to extract η from the running integral by fitting it to a sum of two exponential functions.

To obtain the correlation function $\langle P_{\alpha\beta}(0) \cdot P_{\alpha\beta}(t) \rangle$ with good statistics, multiple independent NVT simulations are needed. The more viscous the investigated fluid, the longer these simulations have to be to reach the time region, where the

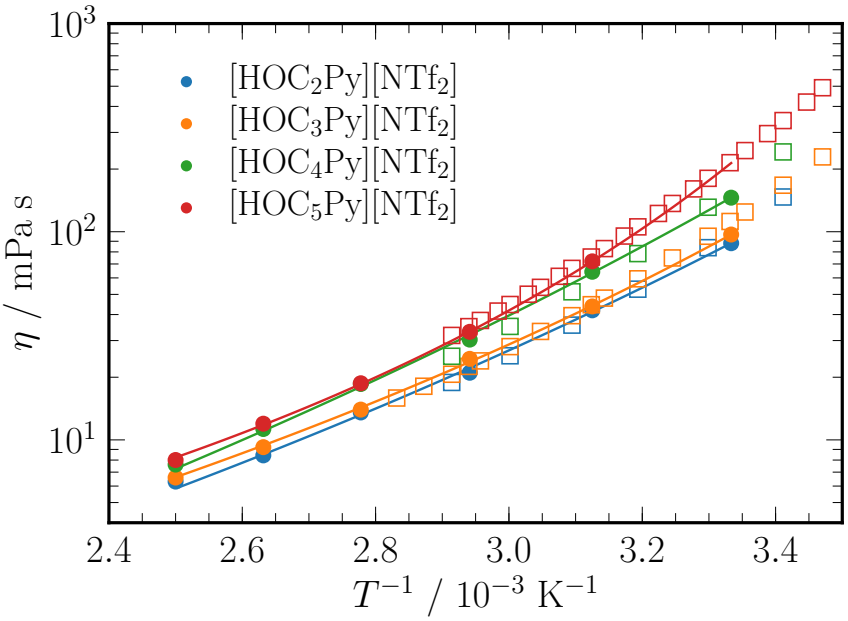

Fig. 2.4.: Simulated (circles) and experimental (squares) viscosities η of various [HOC$_n$Py][NTf$_2$] ILs as a function of the inverse temperature T^{-1}. The lines represent a VFT-fit of the simulated viscosities.[4]

integral is approximately constant. Thus, 100 independent NVT simulations were performed to obtain the viscosity of one IL per temperature, each 16 to 40 ns in length depending on the temperature of interest. While these long simulations are needed to improve the statistics for highly viscous fluids such as ILs, they yield additional problems. To describe the function $\langle\eta(t)\rangle$ as suggested in reference [65], the integral in equation 2.1 is needed with a high time resolution of $P_{\alpha\beta}(t)$. Regarding the amount of independent simulations necessary here, this results in considerable data storage requirements. Furthermore, the time required to compute the autocorrelation function of n values with a "brute force" algorithm is of the order $\mathcal{O}(n^2)$, leading to high computational costs. By implementing an algorithm based on the convolution theorem, we were able to lower the time complexity to $\mathcal{O}(n \log n)$.

The reported viscosities η are in good agreement with experimental data obtained in our laboratory (Fig. 2.4).[4] As expected, η decreases with increasing temperature

T, which can be described by a Vogel-Fulcher-Tammann (VFT) equation

$$\eta = \eta_0 \cdot \exp\left(\frac{B}{T - T_0}\right), \tag{2.2}$$

where η_0, B, and T_0 are fitting parameters. The VFT-like behavior is common in ILs as opposed to Arrhenius-like behavior.[66,67] The growth of η with the increase of the alkyl chain length n occurs likely due to the additional dispersion interaction with each CH_2 element. Other effects, such as the shift in equilibrium between ca HBs and the sligthly stronger cc HBs, may also play a subtle role. In classical MD simulations of ILs, reproduction of dynamical data is often difficult without the use of polarizable force fields or scaled charges, as thoroughly discussed in the literature.[68–82] These problems seem not to apply here, in part due to the scaled Lennard-Jones interactions of the original $[NTf_2]^-$ force field from Köddermann, which were adopted in the NGOLP force field.[1,2,51] The good agreement between experimental and simulated viscosities encouraged us to further investigate dynamic properties using the force fields at hand.

2.5. Self-Diffusion

The movement of particles in absence of a chemical gradient is called self-diffusion and its measure is the self-diffusion coefficient D.[83] Experimentally it can be obtained using pulsed-field-gradient nuclear magnetic resonance (NMR) spectroscopy or by investigating the self-diffusion of a tracer particle sufficiently similar to the fluid of interest. Due to the ability to discriminate between different particles of the same type in MD simulations, D can be obtained by using the Einstein relation

$$D = \frac{1}{6} \lim_{t\to\infty} \frac{\partial}{\partial t} \left\langle |\boldsymbol{r}_i(t) - \boldsymbol{r}_i(0)|^2 \right\rangle, \tag{2.3}$$

where $\boldsymbol{r}_i(t)$ denotes the position of the particle i at time t and $\langle |\boldsymbol{r}_i(t) - \boldsymbol{r}_i(0)|^2 \rangle$ denotes the mean square displacement (MSD). The MSD is a measure for the distance travelled by the particle i during a time period t. The self-diffusion coefficient is obtained by averaging over many times $t = 0$ and particles of the same species, e. g. cations or anions, and fitting the slope of the MSD at long times $t \to \infty$.[3]

Particle positions in MD simulations are commonly subjected to PBCs, to the effect that particles leaving the simulation box on one site are wrapped back into

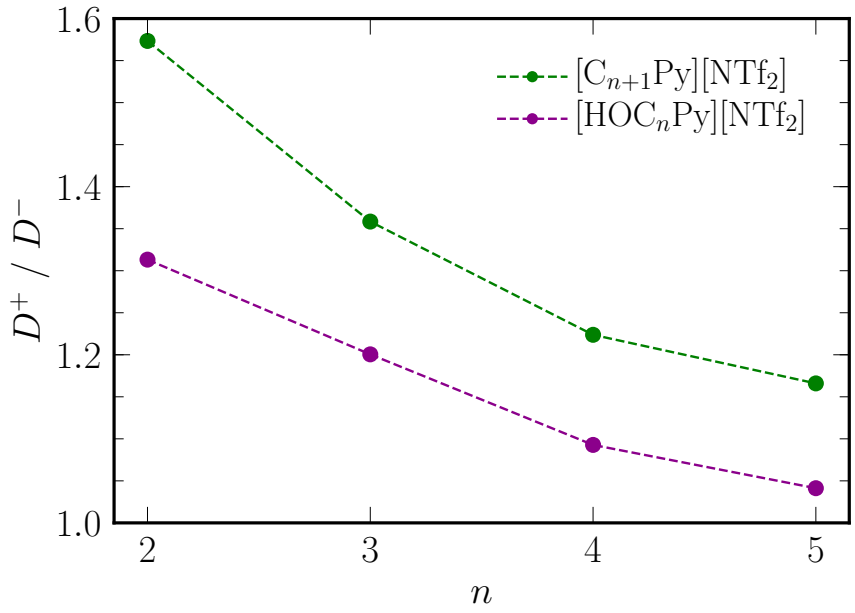

Fig. 2.5.: Ratio of the self-diffusion coefficients of the cation D^+ and the anion D^- in the respective functionalized and non-functionalized IL at 300 K as a function of the alkyl chain length n.[3]

the box on the opposite site under preservation of their velocity vector. As a consequence, the displacement from a reference position $|\boldsymbol{r}_i(t) - \boldsymbol{r}_i(0)|$ can at most be half a box-length, assuming a cubic simulation box. To obtain an accurate MSD and diffusion coefficient from those simulations the particle trajectories have to be processed to undo this wrapping. It was recently pointed out by Bülow et al. that some common analysis tools are not suitable to "unwrap" trajectories of NpT simulations, as they fail to account for the changing box-lengths under those conditions.[84] In our analysis we employed a similar scheme as described by Bülow et al. to avoid those problems. The position of the particle i at the time step t_k in the unwrapped trajectory $\boldsymbol{r}_i^{\mathrm{u}}(t_k)$ is updated using the displacement vector calculated from the wrapped trajectory $\boldsymbol{r}_i^{\mathrm{w}}(t_{k+1}) - \boldsymbol{r}_i^{\mathrm{w}}(t_k)$. PBCs are applied directly to the displacement vector before calculating the particle position $\boldsymbol{r}_i^{\mathrm{u}}(t_{k+1})$ using the current box-lengths. As long as the time step $t_{k+1} - t_k$ is moderate in size, this method is suitable to describe particle motion in the NpT ensemble.

In publication V, we were able to show that due to the formation of HBs the ions of the hydroxyl-functionalized IL $[HOC_nPy][NTf_2]$ ($n = 2$–5) move significantly slower than their counterparts in the non-functionalized IL $[C_{n+1}Py][NTf_2]$.[3] The self-diffusion coefficient of the hydroxyl-functionalized cation D^+_{func} is on average 66 % lower than that of the unfunctionalized cation D^+_{unfunc}, but the reduction is temperature as well as chain-length dependent. Due to the reduced influence of the HBs at high temperatures, the ratio $D^+_{\text{func}}/D^+_{\text{unfunc}}$ approaches unity with increasing temperature, implying that at higher temperatures the mobility of the functionalized cation approaches that of the unfunctionalized cation.

The ratio $D^+_{\text{func}}/D^+_{\text{unfunc}}$ decreases with increasing chain length n, which was attributed to the shift in equilibrium between ca and cc HBs. For all ILs described here we found that the cation is more mobile than the anion, hence $D^+/D^- > 1$ as seen in Fig. 2.5. Due to the correlation of anion and cation via the ca HB, D^+/D^- is closer to one for the functionalized ILs. With increasing chain length the cation grows in size, leading to a reduction of mobility and lowering the ratio D^+/D^- for both types of ILs. The factor between both ratios decreases with increasing chain length and is about constant going from $n = 4$ to $n = 5$.[3] As will be explained in chapter 3, this coincides with the behavior seen in the HB equilibrium (Fig. 3.4) where the amount of cc HBs increases in a similar fashion. The surge in cc HBs slows the cation mobility leading to a rise in $D^+_{\text{func}}/D^+_{\text{unfunc}}$ for longer chain lengths, but partly decouples the anion and cation movement inducing a relative increase in D^+/D^- compared to the respective non-functionalized IL.

2.6. Reorientational Dynamics

The reorientational correlation time τ_c is used to describe the reorientational motion of a certain vector in a fluid. This quantity is connected to the spin-lattice relaxation time T_1 and can therefore be probed experimentally by NMR spectroscopy.[85] In MD simulation we can compute τ_c using an orientational autocorrelation function $R_2(t)$

$$R_2(t) = \langle P_2\{\cos[\theta(t_0)]\} \cdot P_2\{\cos[\theta(t)]\}\rangle\,, \tag{2.4}$$

where the brackets $\langle \ldots \rangle$ imply averaging over all times t_0 and $P_2\{\cos[\theta(t)]\}$ denotes the second Legendre polynomial

$$P_2\{\cos[\theta(t)]\} = \frac{3}{2} \cdot \cos^2[\theta(t)] - \frac{1}{2}. \tag{2.5}$$

The angle θ denotes the angle between the vector of interest and an arbitrary external axis of the laboratory frame of reference.

The vector of interest $\boldsymbol{r}$ can be a bond vector, such as the O–H bond vector of the hydroxyl group, or any other intra- or intermolecular vector in the system and even vectors that are not directly defined by atom positions, for instance the vector connecting the center of mass to the center of charge. Since the orientation of the external reference vector does not influence $R_2(t)$ in an isotropic medium, we are free to choose the reference vector at will. By selecting $\boldsymbol{r}(t_0)$ as our reference vector we can simplify equation 2.4 to

$$R_2(t) = \langle P_2\{\cos[\theta(t_0, t)]\}\rangle\,, \tag{2.6}$$

as $P_2\{\cos[\theta(t_0, t_0)]\} = 1$ in that case. The angle $\theta(t_0, t)$ references the angle between the vector $\boldsymbol{r}$ at time t_0 and at time t

$$\cos[\theta(t_0, t)] = \frac{\boldsymbol{r}(t_0) \cdot \boldsymbol{r}(t)}{|\boldsymbol{r}(t_0)| \cdot |\boldsymbol{r}(t)|}. \tag{2.7}$$

The reorientational correlation time τ_c can be computed by integrating the orientational autocorrelation function $R_2(t)$

$$\tau_\mathrm{c} = \int_0^\infty R_2(t)\mathrm{d}t. \tag{2.8}$$

It quantifies the time needed for the vector $\boldsymbol{r}$ to lose its orientational correlation and is therefore sensitive to directional interactions, such as hydrogen bonding. Due to the energetic barrier needed to break the HB, the reorientation of the O–H bond vector is hampered while the HB is intact. The reorientational correlation times of the O–H bond vector for the ILs $[\mathrm{HOC}_n\mathrm{Py}][\mathrm{NTf}_2]$ and their relation to HB lifetimes are discussed in section 3.3 and publication VI.[4]

3. Hydrogen Bonds

3.1. Hydrogen Bond Geometry and Criteria

Developments in recent decades caused the International Union of Pure and Applied Chemistry (IUPAC) to set up a task force to revise the definition of the HB in 2005, only a few years after publishing theirs.[83,86–88] The new suggested definition was reported in 2011 and gives a non-exclusive list of common HB criteria and characteristics, including energetic, geometric, and spectroscopic criteria.[88] The new IUPAC definition states:

"*The hydrogen bond is an attractive interaction between a hydrogen atom from a molecule or a molecular fragment X–H in which X is more electronegative than H, and an atom or a group of atoms in the same or a different molecule, in which there is evidence of bond formation. A typical HB may be depicted as X–H* $\cdots$ *Y–Z, where the three dots denote the bond. X–H represents the HB donor. The acceptor may be an atom or an anion Y, or a fragment or a molecule Y–Z, where Y is bonded to Z.*"[88]

It continues with mentioning special cases of X, Y, and Z, such as X=Y. For almost all systems examined here, HB donor X–H is the hydroxyl group O–H of a cation in the IL. The acceptor Y can be one of the oxygen atoms of the $[NTf_2]^-$ anion in case of the ca HB, or the hydroxyl group of another cation in case of the cc HB.

Due to the diversity and complexity of hydrogen-bonded systems, the definition of IUPAC does not rely on numerical cutoffs for the criteria characterizing the interaction. All quantities which are used to describe a HB are continuously distributed, thus every cutoff is somewhat arbitrary. Nevertheless, the introduction of criteria separating hydrogen-bonded species from those which are not is necessary to study HBs. Geometric criteria are especially convenient to characterize HBs in MD simulations. For strong HBs, a distance criterion can suffice,[47] whereas for moderate to weak HBs, a second criterion based on an angle is common. Kumar et al. investigated various distance-angle pairs and their suitability to reflect the electronic

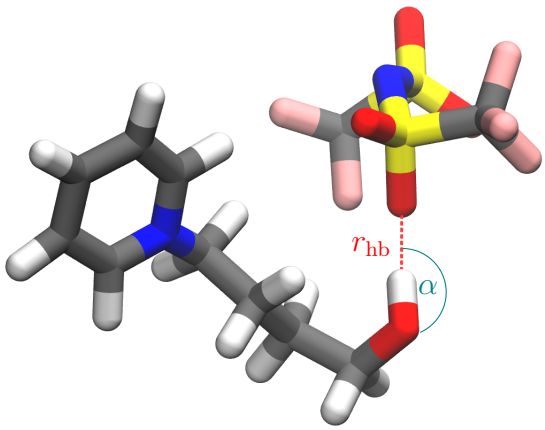

Fig. 3.1.: Example of a ca HB in $[HOC_4Py][NTf_2]$ and the geometric criteria r_{hb} and α used to define it.

structure of liquid water.[89] Although one particular distance-angle pair describes the electronic structure especially well, they conclude that the different cutoff pairs result in similar HB statistics and dynamics.

We employed the distance r_{hb} between the acceptor atom (Y) and the hydrogen atom and the cosine of the angle $\alpha\angle$O–H$\cdots$Y (Fig. 3.1) as HB defining geometric criteria for our MD simulations. To determine the numeric values of these criteria, we first examined the pair correlation functions $g_{\mathrm{HO}}(r)$ of the hydrogen atoms and the corresponding acceptor atoms. As shown in Fig. 3.2, the density of HB acceptors near the hydrogen atom is large compared to the bulk density of the respective acceptor, regardless of the HB species. The first maximum, at around 2 Å, denotes intermolecular H-O-pairs close to each other, likely forming a HB. These pairs are separated from non-hydrogen-bonded pairs by the first minimum in the pair correlation functions at around 2.7 Å. There is, however, a slight overlap of H-O-distances between hydrogen-bonded and non-hydrogen-bonded H-O-pairs as is shown by the pair correlation function not reaching $g_{\mathrm{HO}}(r) = 0$ at the respective minimum distances. This demonstrates the need for another HB criterion apart from the donor-acceptor distance r_{hb} for the systems investigated here.

By binning r_{hb} and the corresponding cosine of the HB angle $\cos(\alpha)$ of a sufficient amount of H-O-pairs one can obtain the probability density function $P(r_{\mathrm{hb}}, \cos(\alpha))$. The natural logarithm of the weighted probability density function

$$W(r_{\mathrm{hb}}, \cos(\alpha)) = r^{-2} \cdot P(r_{\mathrm{hb}}, \cos(\alpha)) \tag{3.1}$$

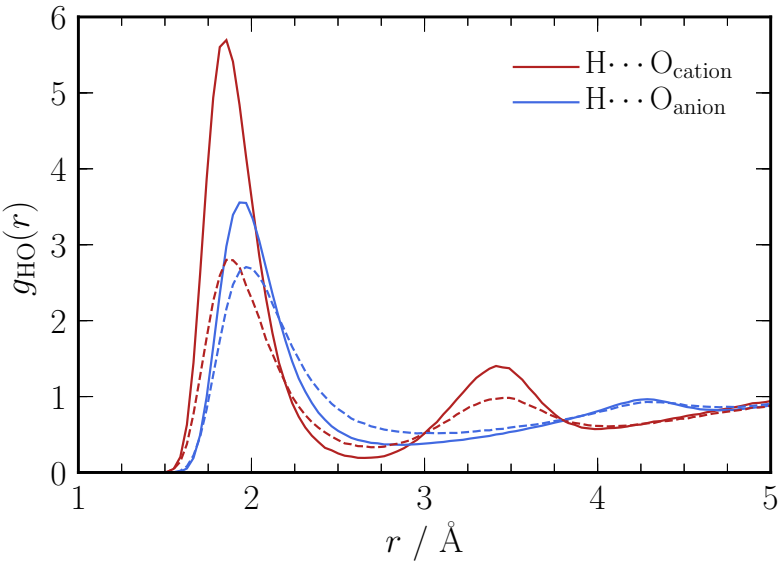

Fig. 3.2.: Pair correlation functions of the hydroxyl hydrogen atom of the cations and the oxygen atom of the cations (red) or the oxygen atoms of the anions (blue) in $[HOC_4Py][NTf_2]$ at 300 K (solid line) and 400 K (dashed line), respectively.

is connected to the free energy surface F with the Boltzmann constant k_B, the temperature T and an unknown constant c via

$$F = -k_B T \cdot \ln\left[W(r_{hb}, \cos(\alpha))\right] + c. \tag{3.2}$$

Fig. 3.3 shows the weighted probability density function $W(r_{hb}, \cos(\alpha))$ of finding an intermolecular H-O-pair with a specific r_{hb} and $\cos(\alpha)$.[3,4] In these two dimensional free energy profiles the maximum, which corresponds to a hydrogen-bonded H-O-pair, can be separated from other configurations using a distance cutoff r_c and an angle cutoff $\cos(\alpha_c)$, which are shown as red lines. For the pyridinium-based ILs $[HOC_nPy][NTf_2]$ the cc HB was defined by a distance cutoff r_c of 2.7 Å and an angle cutoff of $\cos(\alpha_c) = -0.5$ so that every donor-acceptor pair with $r_{hb} < 2.7$ Å and $\cos(\alpha) < -0.5$ is defined as hydrogen-bonded. For the ca HB the same angle cutoff was chosen but a higher distance cutoff of $r_c < 2.8$ Å must be employed. While the choice of the specific values of the geometric criteria is somewhat arbitrary, due to the low probability density at the crossover from hydrogen-bonded to non-hydrogen-bonded states, a small shift of the value will barely affect the statistic.[4]

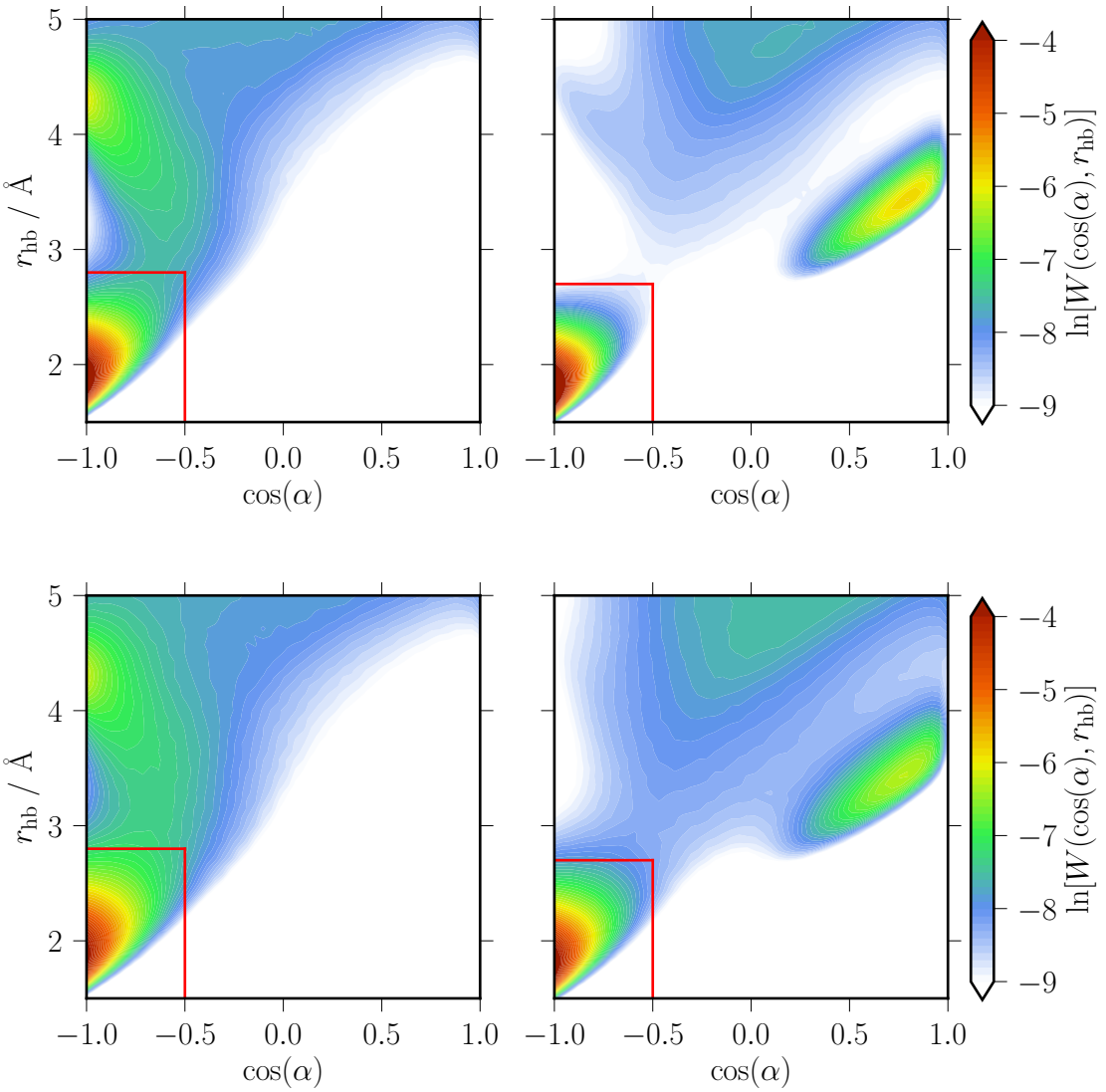

Fig. 3.3.: Weighted logarithmic probability density functions $W(r_{\mathrm{hb}}, \cos(\alpha))$ of finding a H-O-pair with a HB distance r_{hb} and a corresponding HB angle $\cos(\alpha)$ for $[HOC_4Py][NTf_2]$ at 300 K (top) and 400 K (bottom). The functions describe the free energy profile of the interaction between the hydroxyl hydrogen atom of the cation and the oxygen atoms of the anion (left) or the oxygen atom of the cation (right), respectively. The red line represents the chosen cutoff criteria r_{c} and $\cos(\alpha_{\mathrm{c}})$ for the respective HB with the distance cutoff $r_{\mathrm{c}} = 2.8$ Å for the ca HB and $r_{\mathrm{c}} = 2.7$ Å for the cc HB, and the angle cutoff $\cos(\alpha_{\mathrm{c}}) = -0.5$ ($\alpha_{\mathrm{c}} = 120°$) for both types of HB.[3,4]

It is not unexpected to find individual criteria for the different HB species ca and cc. Simply looking at the charge distribution in the force fields of the respective ions, which were derived from ab initio calculations on the individual ions in the gas phase,[2,3] one can ascertain the difference in HB acceptor strength. Due to the symmetry of the $[NTf_2]^-$ anion, all oxygen atoms bear the same point charge, namely $-0.579 \cdot e$.[2] The charge of the hydroxyl oxygen of the $[HOC_nPy]^+$ cation varies between $-0.6649 \cdot e$ and $-0.6988 \cdot e$, while that of the hydroxyl hydrogen varies between $0.4268 \cdot e$ and $0.4394 \cdot e$.[3] Thus, the Coulomb interaction between the hydroxyl hydrogen and the hydroxyl oxygen is more attractive than the interaction to an oxygen of the anion. Although oxygen and hydrogen charges vary regarding the different chain lengths of the $[HOC_nPy]^+$ cation, the effect on $W(r_{hb}, \cos(\alpha))$ is too minute to justify separate cutoff criteria depending on n.[3,4]

In publication II the geometry and population of the different HB species in $[HOC_4Py][NTf_2]$ were examined using neutron diffraction (ND), quantum chemical calculations, and MD simulations.[6] In the study, structural information of the liquid phase was derived from ND data using a process called Empirical Potential Structure Refinement.[90,91] Thereby, a Monte Carlo (MC) simulation of the substance, employing an empirical potential on top of a regular force field, is used to calculate theoretical structure factors. By changing the empirical potential in the MC simulation, the theoretical structure factors can be refined to fit the experimental structure factors yielding configurational information about the substance from the MC simulation. This data can be analyzed in a similar way to MD trajectories but is, of course, lacking dynamical information.

The geometry of the different HB species were examined by the respective hydrogen-oxygen and oxygen-oxygen pair correlation functions $g_{HO}(r)$ and $g_{OO}(r)$. These correlation functions from ND data show that the cc HBs are on average about 8 to 10 pm shorter than the ca HBs, as seen in the shift of the first maximum in the respective $g(r)$. For instance, the maximum of $g_{OO}(r)$ is at 2.88 Å for the ca HB and at 2.78 Å for the cc HB. Additionally, the cc HB is also "more linear" than the ca HB, when comparing the distribution of the HB angle $\alpha\angle$O–H$\cdots$O population. Both results indicate that the cc HB is stronger than the ca HB, contrary to the notion that the ca HB benefits from the attractive Coulomb interaction between the ions.

This is in good agreement with previous IR studies in the liquid as well as the gas phase of various functionalized imidazolium- and pyridinium-based ILs, showing a

red-shifted vibrational band of the OH bond assigned to cc hydrogen-bonded cations when compared to their ca hydrogen-bonded brethren.[32,34,35,58] This behavior is also reproduced by the MD simulation (compare Fig. 3.2 and 3.3). The distance at the first maximum of $g_{\mathrm{HO}}(r)$ and $g_{\mathrm{OO}}(r)$ differs at most by 0.02 Å between MD and ND for both types of HBs.

In publication II, these geometries were then compared to geometries obtained from quantum chemical calculations using density functional theory and Grimme's dispersion correction.[92,93] Therefore, clusters of different sizes n, here referencing the number of ion pairs included in the calculation, were prepared. It was shown that the average oxygen-oxygen distance for the cc HB decreases with increasing n due to cooperative effects strengthening the HBs. On the other hand, the average distance of the ca HB is independent of the considered cluster size at about 2.90 Å, as there is no chance for cooperativity in those configurations. The oxygen-oxygen distances for the cc HB obtained by MD and ND are between the values of the dimer ($n = 2$) and trimer ($n = 3$) from the quantum chemical calculation, indicating an average cluster size between two and three in the bulk liquid phase at 300 K. These distances were also compared to those found experimentally in molecular liquids, showing that the oxygen-oxygen distances of the cc HB are similar to those found in liquid and solid water and methanol.[94–96]

3.2. Hydrogen Bond Equilibrium

The definition of geometric criteria for the MD simulation enables us to assess the average number of cations forming a cc and ca HB, respectively. For this purpose, we evaluated whether a specific donor satisfies the HB criteria to any acceptors at a certain time step. Regarding the two types of HB considered here, there are four possibilities for every cation: forming a ca HB, a cc HB, both at the same time, or no HB according to our criteria ("free"). Averaging these for a sufficient amount of independent donors and time steps enables us to compute HB statistics from the point of view of the donor group and examine the effect of the alkyl chain length of the cation.

The average percentage of cations forming a specific HB $N_{\mathrm{hb}}/N_{\mathrm{total}}$ as a function of the alkyl chain length n is presented in Fig. 3.4.[3,4,56] Although the cc HB seems to be stronger than the ca HB, as discussed in section 3.1, the ca HB is energetically

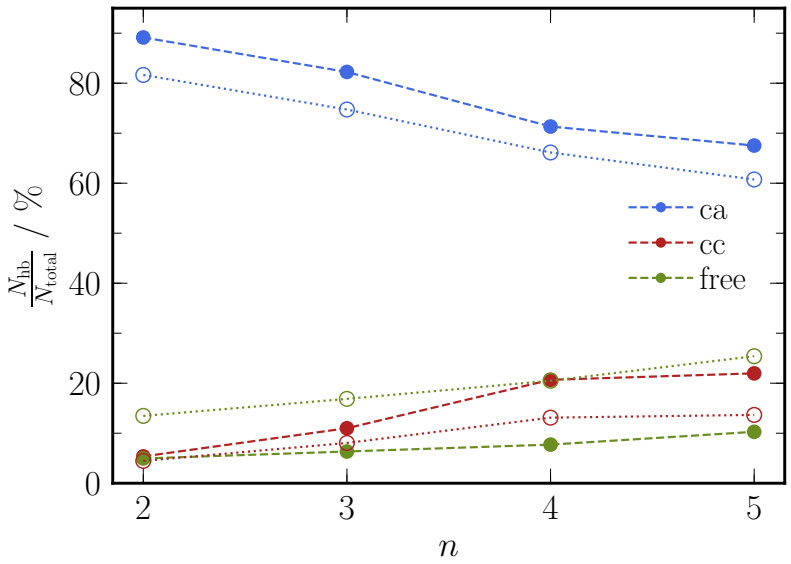

Fig. 3.4.: Percentage of cations donating a ca HB blue, cc HB (red), or no HB at all (green, "free") as a function of alkyl chain length n at 300 K (closed symbols) and 400 K (open symbols), respectively.[4]

favored for small alkyl chain lengths due to the attractive Coulomb interaction between anion and cation. Furthermore, the number of oxygen atoms and thus HB acceptors in the $[NTf_2]^-$ anion is four times higher than the number of oxygen atoms in the cation, hence an increased number of ca HBs is to be expected in these systems. While there are always more cations forming ca HBs, the number of cations forming cc HBs grows with increasing chain length und decreasing temperature. A longer alkyl chain increases the average distance of the interacting hydroxyl groups to the respective charge centers of the cations, resulting in decreased Coulomb repulsion and thus stabilizing cc-bonded cation pairs. This shifts the HB equilibrium towards more cc HBs. Such an effect was also suggested earlier following IR experiments on the same ILs.[38]

The third species, the "free" cations, do not form a cc or ca HB at the observed time step. They interact with other parts of the ions, such as the aromatic ring of the cation or the trifluoromethyl groups of the anion, or are in transition between different hydrogen-bonded states. Formation of HBs to the trifluoromethyl groups (O–H $\cdots$ F–C) is rare.[4] The amount of "free" cations increases with the alkyl chain

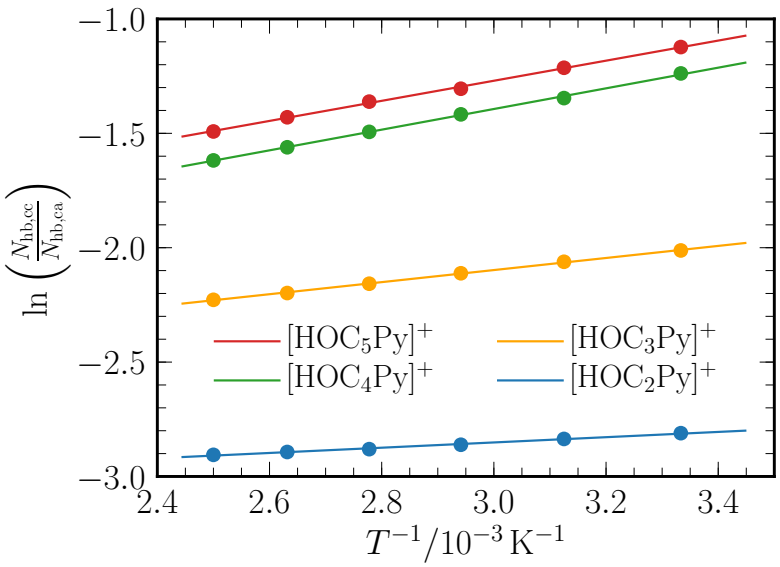

Fig. 3.5.: Van 't Hoff plot of $\ln(N_{\mathrm{hb,cc}}/N_{\mathrm{hb,ca}})$ for $[\mathrm{HOC}_n\mathrm{Py}][\mathrm{NTf_2}]$ with $n = 2$–5 as a function of the inverse temperature. The solid lines represent linear fits according to $\ln(K) = -\Delta H^\circ/(RT) + \Delta S^\circ/R$. Fitted thermodynamic parameters are given in Tab. 3.1.[4]

length, presumably due to the decreasing relative HB acceptor density. It is possible for one cation to form a HB to both an anion and another cation at the same time, however this is rarely the case with under 0.6 % for every chain length and temperature.

It was also possible to extract HB populations from the ND data in publication II, showing that on average 87 % of cations are involved in a ca HB, whereas the remaining 13 % are forming cc HBs.[6] This is in good agreement with the populations obtained by MD simulations, which showed 75 % ca HBs and 20 % cc HBs for this IL. While the MD simulation shows the existence of "free" (unbound) cations, the ND data does not reproduce this behavior, possibly due to a low lifetime of the corresponding state.

By using the temperature dependent populations obtained by MD simulation, we were able to calculate standard enthalpies and entropies connected to the transition ca $\rightleftharpoons$ cc via the Van 't Hoff plot shown in Fig. 3.5..[3,4] The transition enthalpies ΔH° and the transition entropies ΔS° are gathered in Tab. 3.1 for the respective ILs.

Tab. 3.1.: Thermodynamic parameters describing the temperature dependence of the equilibrium ca ⇌ cc for $[HOC_nPy][NTf_2]$ according to the Van 't Hoff plot shown in Fig. 3.5.[4]

n	ΔH° / kJ mol^{-1}	ΔS° / J K^{-1} mol^{-1}
2	-0.96	-26.6
3	-2.19	-24.0
4	-3.76	-22.9
5	-3.65	-21.5

The data suggests that the cc HB is enthalpically stabilized, but entropically destabilized for all investigated pyridinium-based ILs. The most stable cc HB is found in $[HOC_4][NTf_2]$ with $\Delta H^\circ = -3.76\,\mathrm{kJ\,mol^{-1}}$. For the shorter alkyl chains the enthalpic stabilization is gradually reduced to $\Delta H^\circ = -0.96\,\mathrm{kJ\,mol^{-1}}$ for $[HOC_2][NTf_2]$ and no further stabilization is detected for $n = 5$. The differences ΔS° show an entropy penalty for the formation of cc HBs which gradually decreases with increasing alkyl chain length from $\Delta S^\circ = -26.6\,\mathrm{J\,K^{-1}\,mol^{-1}}$ for $n = 2$ to $-21.5\,\mathrm{J\,K^{-1}\,mol^{-1}}$ for $n = 5$. A reason for this behavior might be that more cc HB acceptors are "in reach" for cations with longer alkyl chains.[4]

In publication III functionalized piperidinium- ($[HOC_nMPip]^+$) and pyridinium-based ILs were investigated in their hydrogen bonding and phase behavior by employing solid-state NMR spectroscopy, MD simulation, and differential scanning calorimetry (DSC) measurements.[56] The ^{2}H NMR spectra of $[HOC_nMPip][NTf_2]$ and $[HOC_nPy][NTf_2]$ (n = 2–3) at 183 K were reported and analyzed. By modelling the Pake-powder patterns seen in the ^{2}H NMR spectra one is able to extract deuteron quadrupol coupling constants χ_D, which describe the interaction of the electric-field gradient with the nuclear quadrupol moment, as well the asymmetry parameter η, which characterizes the shape of the electric-field gradient. Both quantities can be used as sensitive probes for hydrogen bonding: a smaller χ_D indicates a stronger HB, whereas a smaller asymmetry parameter implies a "more linear" HB.

It was found that the spectrum of $[HOC_2MPip][NTf_2]$ can be described by a single Pake-powder spectrum whereas the spectra of the other substances, $[HOC_3MPip]$-$[NTf_2]$, $[HOC_2Py][NTf_2]$, and $[HOC_3Py][NTf_2]$, can each be deconvoluted into two individual patterns, which were attributed to the equilibrium between cc and ca HBs respectively. In accordance with the findings of publication II, the component

with the lower χ_D and smaller η for each IL was ascribed to contributions from the cc HB. $[HOC_2MPip][NTf_2]$ does not exhibit two components in the spectrum as the positive charge of the cation is relatively localized at the nitrogen atom, increasing the Coulomb repulsion of two interacting cations and, therefore, seemingly not allowing cc HBs. As discussed before, in pyridinium-based ILs the charge of the cation is delocalized in the aromatic ring reducing this repulsion. The longer alkyl chain length in $[HOC_3MPip][NTf_2]$ also reduces the energy penalty by keeping the charge center of the interacting cations further apart, as described above for $[HOC_nPy][NTf_2]$, which seems to be enough to allow for the formation of cc HBs. For the same reasons χ_D for the cc HB decreases with increasing chain length (from 205 kHz to 165 kHz), when comparing the spectra of $[HOC_2Py][NTf_2]$ and $[HOC_3Py][NTf_2]$. The parameter of the components attributed to the ca HB show no chain-length dependence for the piperidinium-based ILs but χ_D also decreases for the ca HB in the pyridinium-based ILs, albeit to a lesser degree than for the cc HB.

Using natural bond orbital analysis, these differences in χ_D can be linked to the second order stabilization energy $\Delta E^{(2)}_{n\to\sigma^*}$ and the charge transfer of the HB. We were able to show that HB configurations with smaller χ_D are linked to higher stabilization energies and more charge transfer.[56] The higher charge transfer for cc HBs could possibly be due to the higher charge density on the acceptor sites, as discussed in section 3.1. In the $[NTf_2]^-$ anion four oxygen atoms compete with the trifluoromethyl groups for the charge density, reducing the supply of electron density at each individual HB acceptor site. Comparing this to the hydroxyl group of the cation, where the alkyl chain supplies the electron density to the oxygen atom and on top of that "shields" it from the charge deficiency of the pyridinium ring, the differences in charge distribution can in part explain the different strength of ca and cc HBs.

The ^2H NMR spectra can also be used to quantify the populations of the different HB states. About 65 % of hydroxyl groups in $[HOC_3Py][NTf_2]$ (15 % in $[HOC_2Py][NTf_2]$) are forming cc HBs, while the remaining ones are forming ca HBs, respectively. These measurements were performed at 183 K in the glassy state of the ILs. With our MD simulations we were not able to reach such low temperatures for various reasons. At the lowest temperature for our MD simulations of 300 K we find that about 11 % of cations in $[HOC_3Py][NTf_2]$ (5 % in $[HOC_2Py][NTf_2]$) form cc HBs. This percentage decreases with increasing temperature due to the entropic

penalty for cc HBs discussed above. Combining the results from solid state NMR, MD, and ND it was shown that the length of the alkyl chain influences the HB equilibrium with longer chains enabling more cc HBs. The longer alkyl chain even compensates for the lower polarizability of the piperidinium cation, permitting cc HBs in $[HOC_3MPip][NTf_2]$ when none occure in $[HOC_2MPip][NTf_2]$. The results also show that the equilibrium is dependent on the temperature, as cc HBs are enthalpically favored to ca HBs but entropically destabilized.

Using DSC, we were also able to show that the formation of cc HBs leads to a change in phase behavior.[56] While $[HOC_2MPip][NTf_2]$, which seemingly exhibits no cc HBs at 183 K, crystallizes at about 277 K and undergoes two solid/solid phase transitions, the DSC traces of $[HOC_3MPip][NTf_2]$, $[HOC_2Py][NTf_2]$, and $[HOC_3Py][NTf_2]$ only show a liquid-glass transition at about 200 K. This results in a wide temperature range in which these substances are only forming a liquid phase, which could be desirable for some applications.

In a later study, we were able to bridge the temperature gap between solid state NMR (183 K) on one side and MD simulation and ND (300 K) on the other side, using IR spectroscopy.[57] The varying transition dipole moments and resulting broad vibrational bands of the HB species encumber the efforts of quantitatively analyzing the IR spectra. Diluting the functionalized IL $[HOC_4Py][NTf_2]$ with the unfunctionalized counterpart $[C_5Py][NTf_2]$ inhibits the formation of cc HBs, as the hydroxyl concentration depletes. The percentage of ca HBs in the functionalized IL can be estimated by comparing spectra of the diluted IL, where no cc HBs are present, with the pure functionalized IL. Since no "free" hydroxyl groups are detected in the IR spectra the remaining percentage was allocated to the cc HBs. Assuming a transition enthalpy of about $40\,\mathrm{J\,K^{-1}\,mol^{-1}}$ and a heat capacity difference between the two states of $\Delta C_\mathrm{p} = 80\,\mathrm{J\,K^{-1}\,mol^{-1}}$ the populations obtained from the IR spectra fit nicely with both the population from solid NMR spectroscopy at 183 K and MD simulation at above 300 K.

3.3. Hydrogen Bond Dynamics

F. Stillinger introduced the concept of the HB lifetime as a means to examine kinetic properties of HBs.[39] He suggested a "continuous" HB lifetime, reflecting the average time a donor-acceptor pair is hydrogen-bonded without interruptions, as well as

an "intermittent" HB lifetime, disregarding those interruptions. These definitions were subsequently used by Rapaport and others to investigate the HB dynamics, especially in liquid water.[40–43]

3.3.1. Intermittent Hydrogen Bond Lifetime

First, we focus on the "intermittent" HB lifetime using a method described by Bennett and Chandler.[44,97] Therefore, we define the HB population function $h(t)$ for a specific donor-acceptor pair:

$$h(t) = \begin{cases} 1, \text{if HB exists} \\ 0, \text{if no HB exists} \end{cases} . \tag{3.3}$$

We can group $h(t)$ of different donor-acceptor pairs depending on what type of HB it is associated with. For the ca HB a donor-acceptor pair consists of the hydroxyl hydrogen atom of the cation (donor) and one oxygen atom of the anion (acceptor), while for the cc HB the acceptor is the oxygen atom of a different hydroxyl group. Switching to a different oxygen atom on the same anion is counted as a different donor-acceptor pair as is "flipping" a cc HB, so that the previously donating cation becomes the acceptor of the HB.

In a system of infinite size, $\langle h \rangle = 0$ as the probability of two randomly picked molecules being hydrogen-bonded is zero.[43] In systems of finite size, such as in MD simulations, $\langle h \rangle \neq 0$. To describe the fluctuations of $h(t)$ and eliminate finite size effects, we can define the HB population correlation function $C(t)$ as

$$C(t) = \frac{\langle h(0)h(t) \rangle - \langle h \rangle^2}{\langle h^2 \rangle - \langle h \rangle^2}, \tag{3.4}$$

where the brackets $\langle \ldots \rangle$ denote averaging over all donor-acceptor pairs of the same HB type, cc or ca, as well as over all times "0". It should be pointed out that $\langle h \rangle = \langle h^2 \rangle$, due to $h(t) = h^2(t)$, which leads to the denominator of equation 3.4 being equal to $\langle h \rangle - \langle h \rangle^2$ and $\langle h \rangle [1 - \langle h \rangle]$. The often used approximation of $\langle h^2 \rangle = 0$ leads to a misrepresentation of the long-time behavior and is therefore omitted here.[4,43] It was recently shown that equation 3.4 also leads to inaccuracies of the long time behavior, when applying PBCs to the system.[98,99] The size of this effect is dependent on the interdiffusion coefficient between the donor- and acceptor-particles as well as the size of the simulation box. The long-time behavior of $C(t)$ calculated by equation

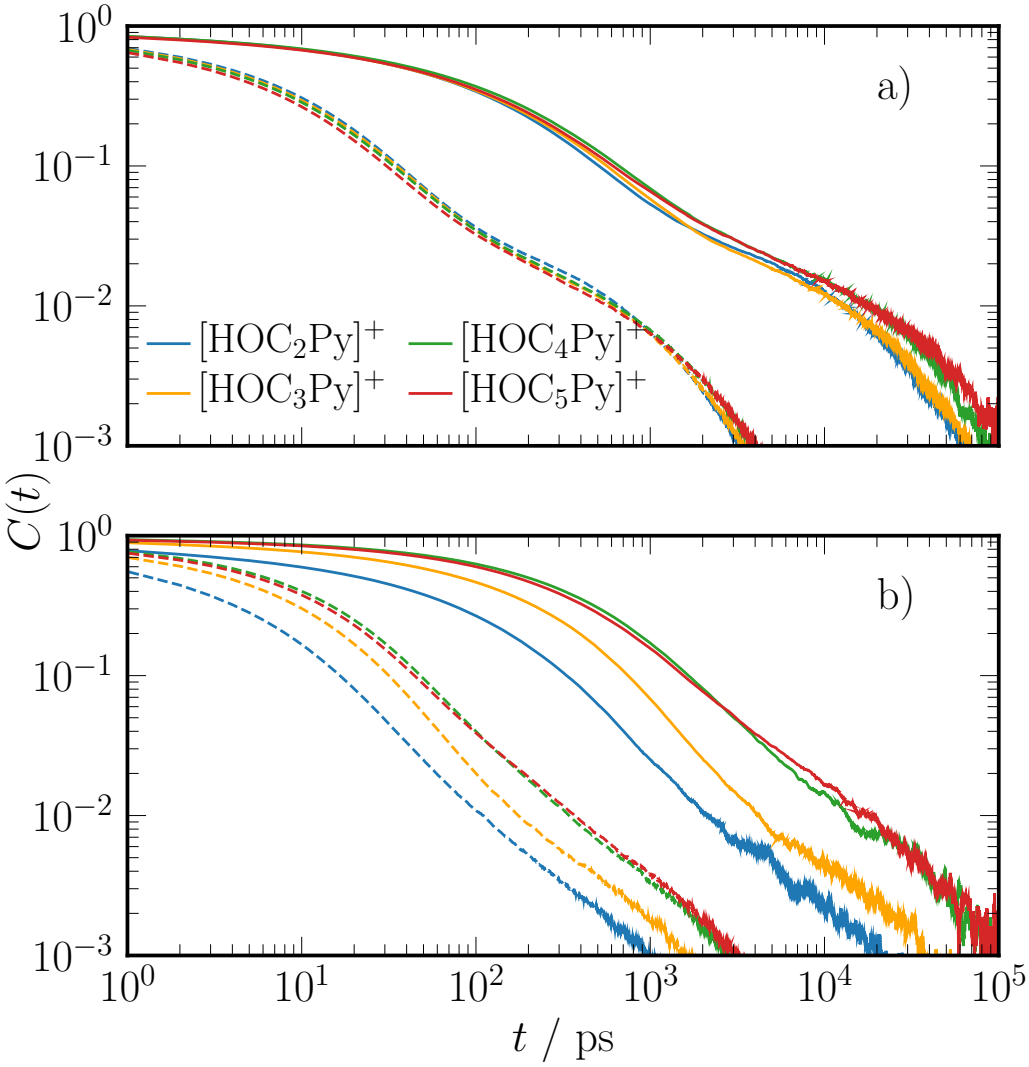

Fig. 3.6.: HB population correlation functions for the ca HB (a) and the cc HB (b) of the respective $[HOC_nPy][NTf_2]$ IL. The solid lines represent data for $T = 300\,K$, whereas dashed lines indicate $T = 400\,K$.[4]

3.4 when employing PBCs can be corrected to the "true" correlation function using an analytical correction term. This correction was not yet applied to the systems discussed here, but considering the slow diffusion and relative large box sizes, it was estimated that the error in the overall lifetime τ_{hb} would be under 1 %.[4]

In contrast to a "continuous" HB population correlation function, the "intermittent" $C(t)$ defined here represents the probability of a HB between a given donor-acceptor pair still being intact at time t if it was intact at time $t_0 = 0$, regardless of what occurs in the time intervall $t - t_0$.

We reported the HB population correlation functions $C(t)$ for $[\mathrm{HOC}_n\mathrm{Py}][\mathrm{NTf}_2]$ ($n = 2$–5) in publications V and VI and found two distinct time domains, as seen in Fig. 3.6: an initial fast decay to only a few percent of its original value followed by a much slower decay to zero.[3,4] This behavior is especially apparent in the correlation functions of the ca HB. The time interval t at which the transition between short- and long-time behavior occurs, is temperature as well as IL dependent. The correlation functions for the ca HB show only a small dependence on the alkyl chain length n in contrast to those for the cc HB, where the functions decay slower for longer chains. The overall increased dynamics at higher temperatures lead to a much faster decay of $C(t)$ for both HB types. To understand the mechanisms of HB breaking in these two time domains we fitted the calculated $C(t)$ with a combination of two stretched exponential functions

$$C(t) = C_{\mathrm{short}}(t) + C_{\mathrm{long}}(t) \tag{3.5}$$

and

$$C(t) = A_1 \exp\left[-\left(\frac{t}{\tau_1}\right)^{\beta_1}\right] + A_2 \exp\left[-\left(\frac{t}{\tau_2}\right)^{\beta_2}\right], \tag{3.6}$$

where $C_{\mathrm{short}}(t)$ and $C_{\mathrm{long}}(t)$ describe the short- and long-time behavior, respectively, and A, τ, and β are parameters of the fit. The separation of $C(t)$ into its two components is exemplarily shown in Fig. 3.7.

The HB lifetime τ_{hb} is a measure for the kinetic stability of the HB and can be obtained by integrating the HB population correlation function $C(t)$:

$$\tau_{\mathrm{hb}} = \int_0^\infty C(t)\mathrm{d}t. \tag{3.7}$$

For fluid systems and long simulation times it can be sufficient to perform this integration numerically. To counteract the noise in the correlation functions at small

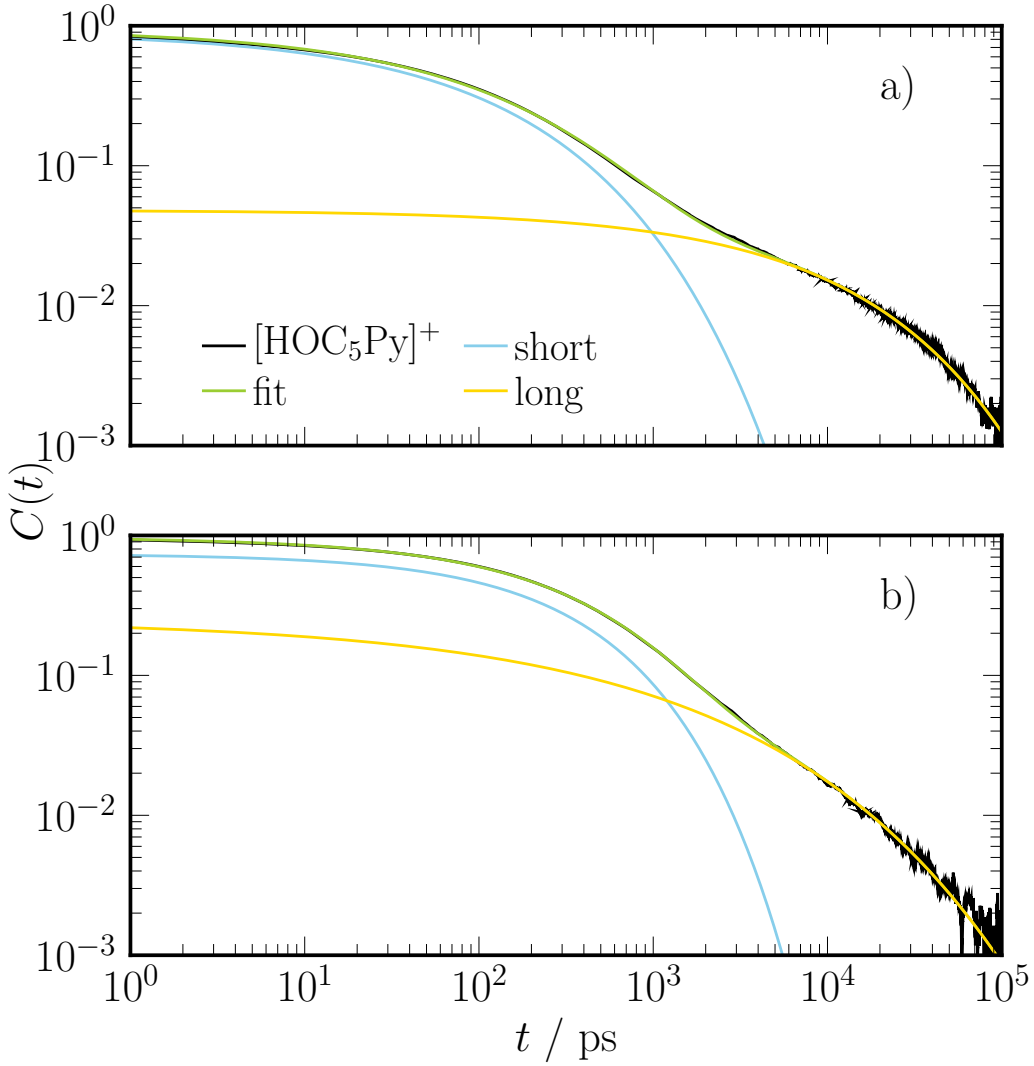

Fig. 3.7.: HB population correlation functions according to equation 3.4 for the ca HBs (a) and the cc HBs (b) for $[HOC_5Py][NTf_2]$ at 300 K (black line). The correlation functions of the respective HB types can be represented by the sum of two stretched exponential functions (equation 3.6, green line), being composed of the short-time behavior (blue line) and the long-time behavior (yellow line).[4]

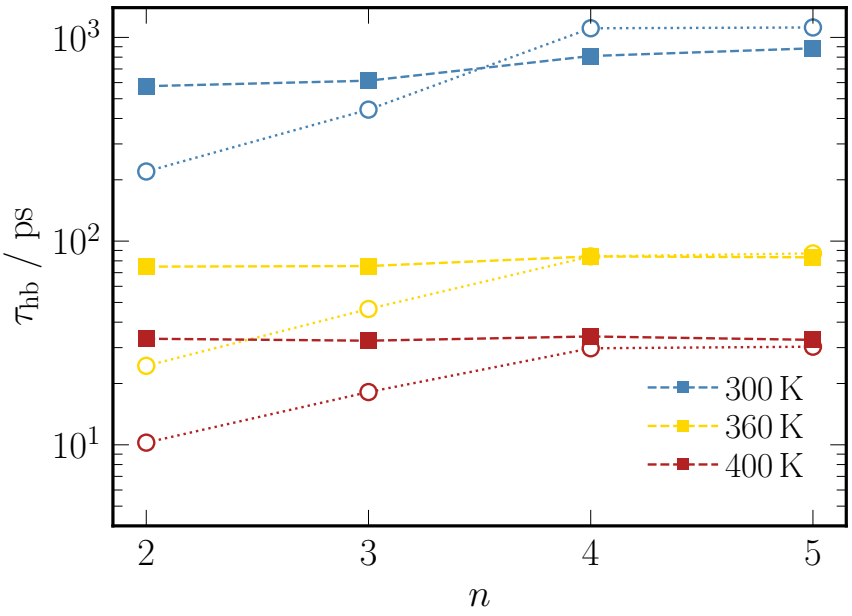

Fig. 3.8.: Average HB lifetime τ_{hb} as a function of the alkyl chain length n in $[HOC_nPy][NTf_2]$ at $T = 300\,K$, $360\,K$, and $400\,K$. Lifetimes for the cc HB are indicated as circles, whereas lifetimes for ca HBs are given as squares.[4]

values of $C(t)$ (Fig. 3.6), which can lead to inaccuracies of the numerical integration, and to better represent the decay of $C(t)$ at long times, τ_{hb} was determined by integrating the fitted $C(t)$ (equation 3.6) analytically with

$$\tau_{hb} = A_1 \frac{\tau_1}{\beta_1} \Gamma\left(\frac{1}{\beta_1}\right) + A_2 \frac{\tau_2}{\beta_2} \Gamma\left(\frac{1}{\beta_2}\right), \tag{3.8}$$

where $\Gamma(a)$ denotes the gamma function. This approach has also the advantage that the resulting lifetime can easily be separated into two terms

$$\tau_{hb} = \tau_{short} + \tau_{long}, \tag{3.9}$$

where τ_{short} and τ_{short} represent the part of the HB lifetime due to the short- and long-time behavior, respectively.

The overall HB lifetimes τ_{hb} presented in Fig. 3.8 show quantitatively, what was already qualitatively visible by comparing $C(t)$ of the respective species in Fig. 3.6: The ca HB lifetime τ_{ca} is mostly independent of the chain length n, while the cc HB

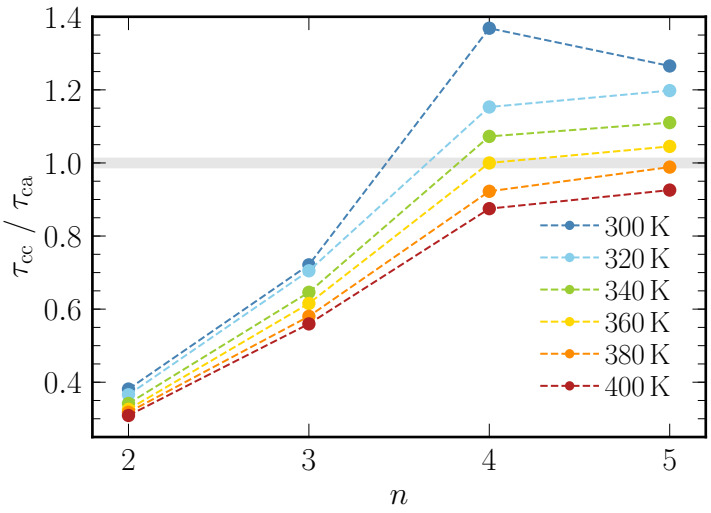

Fig. 3.9.: Ratio of the cc and ca HB lifetime τ_{hb} as a function of the alkyl chain length n in [HOC$_n$Py][NTf$_2$] at various temperatures. A ratio below unity indicates that the ca HB is more stable than the cc HB and vice versa for $\tau_{cc}/\tau_{ca} > 1$.[4]

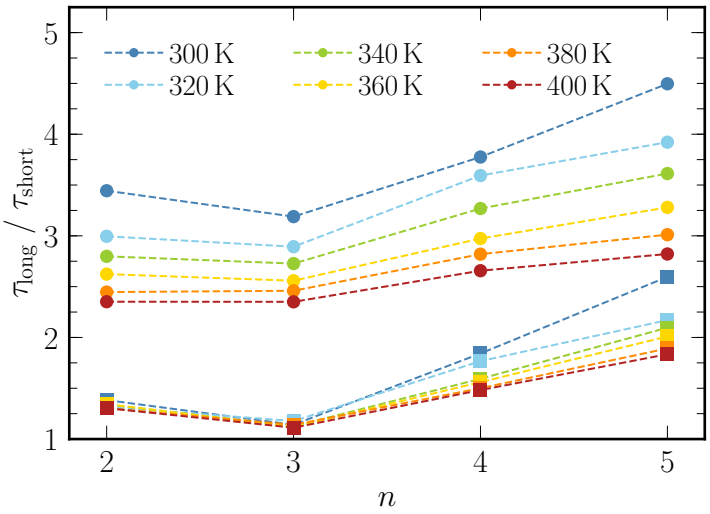

Fig. 3.10.: Ratio of two parts of the HB lifetme τ_{long} and τ_{short} for the ca HBs (circles) and the cc HBs (squares) as a function of the alkyl chain length n in [HOC$_n$Py][NTf$_2$] at various temperatures. For both types of HBs τ_{long} is greater than τ_{short} but especially for the ca HBs the ratio indicates a considerable difference between the two time domains.[4]

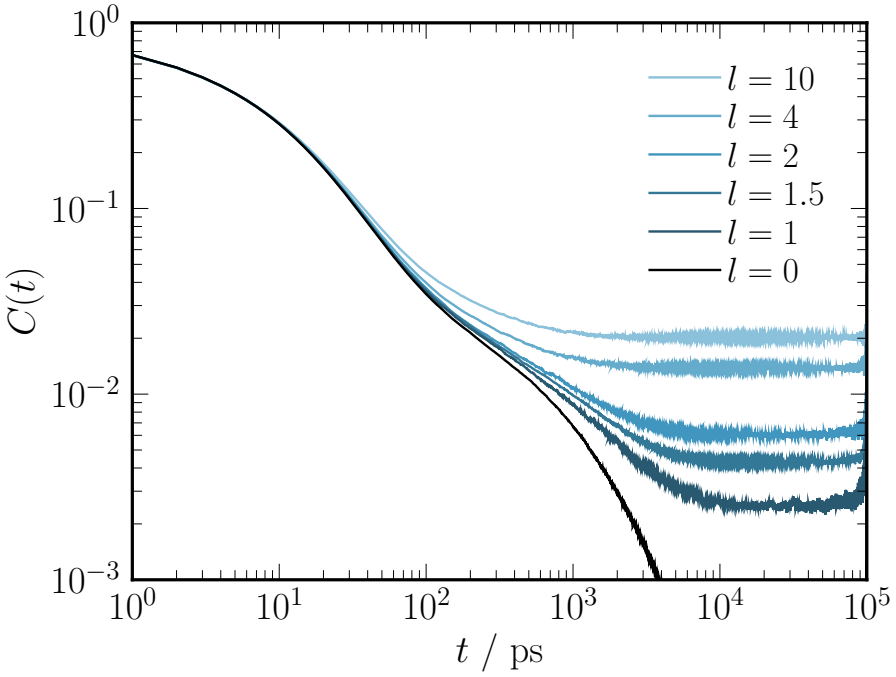

Fig. 3.11.: HB population correlation function $C(t)$ for the ca HB in the undisturbed $[HOC_4Py][NTf_2]$ at 400 K shown in black and with position restraints with different force constants $k' = l \cdot k$ shown in different shades of blue.[4]

lifetime τ_{cc} increases with n but levels off for $n \geq 4$.[3,4] One should keep in mind that the viscosity also grows with increasing n (compare section 2.4 and Fig. 2.4), slowing the overall dynamic of the systems and thereby increasing τ_{hb} for longer chains. To illuminate and compare the relative changes of the HB lifetimes the ratio τ_{cc}/τ_{ca} is shown as a function of the alkyl chain length n and the temperature in Fig. 3.9. Effects due to a change in viscosity are minimized by this treatment, as both lifetimes are subjected to the same fluidity changes. Generally, τ_{cc}/τ_{ca} grows with increasing n but decreasing temperature. Only for $n \geq 4$ and $T \leq 360$ K the ratio is above 1, meaning that under those conditions the cc HB is kinetically more stable than the ca HB. This is consistent with our previous findings regarding the HB populations, where we established that the cc HB formation is enhanced at low temperatures and for longer alkyl chains.[56,57]

Calculating the two terms of equation 3.8 seperately yields the respective short- and long-time part of the HB lifetime τ_{short} and τ_{long}. In Fig. 3.10 the ratio τ_{long}/τ_{short} is presented as a function of n. For all ILs and temperatures and for both HB types

we see that the long-time behavior exceeds the short-time behavior ($\tau_{\mathrm{long}}/\tau_{\mathrm{short}} > 1$), despite the small amplitude of the long-time behavior seen in the correlation functions (Fig. 3.7). Again we see that generally the difference between the two time domains grows with increasing n but decreasing temperature. The change of $\tau_{\mathrm{long}}/\tau_{\mathrm{short}}$ with the temperature shows us that the mechanisms behind HB breaking in these two time domains are affected differently by a change of the viscosity. In publication VI, we were able to show that both τ_{short} and τ_{long} scale approximately linearly with the viscosity of the respective IL for both HB types, but the slope of this dependence differs by a factor of about 3.3 between the short- and long-time behavior.[4] So how can the separation into two time domains be explained and what mechanisms are involved in HB making and breaking in those domains?

In publication VI, we were able to show that the short-time behavior matches the reorientational correlation time τ_{c} of the OH bond vector (τ_{OH}) (section 2.6 and equation 2.8).[4] The reorientational correlation time is sensitive to a loss in orientational correlation of a certain vector and it is established for water and small alcohols that the breaking of a HB is often coupled to "jumps" in the angular orientation of the OH bond vector.[100–102] This motion is fast compared to the reorientational and translational diffusion of the whole molecule, especially in the case of our large cations.

The HB population correlation function would not decay to zero through reorientation of the OH bond vector alone, as HBs could easily be reformed at a later point in time by another "jump" back to the original position, leading to a plateau in $C(t)$ for $t \to \infty$. To break a HB indefinitely, the donor-acceptor pair has to be separated by translational diffusion. By employing position restraints on all ions in our simulation and thereby limiting translational diffusion to a small volume, we were able to illuminate this effect on $C(t)$.[4] Position restraints apply a harmonic potential with the force constant k' to the positions of certain atoms, in our case the nitrogen atom in the cation and anion respectively, thereby restricting their movement. Fig. 3.11 shows the influence of these restraints with different force constants $k' = l \cdot k$ on the ca HB population correlation function $C(t)$ of $[\mathrm{HOC_4Py}][\mathrm{NTf_2}]$ at 400 K. While the short-time behavior is barely influenced for moderate restraints, the long-time behavior vanishes in favor of a plateau. The inverse of the plateau value C_∞ of these functions was found to be proportional to the average number of HB acceptors accessible to a HB donor and therefore the volume explored by an ion. Higher force constants restrict this volume leading to higher values of C_∞.

In publication VI, we were able to show the connection between the long-time behavior of $C(t)$ and diffusion.[4] The dependence of the long-time behavior on temperature as well as alkyl chain length can accurately be described by analytical expressions when we account for the interdiffusion coefficient between donor and acceptor, the topology of the HB network, and the volume accessible to the functional group. However, these models of course fail to reproduce the correct short-time behavior of $C(t)$. To propose a model which can emulate both the short- and long-time behavior at the same time, the combination of both motions, reorientation and translation, is essential. Therefore, we suggested a minimalist random-walker model, where the movement is divided into two domains (Fig. 3.12).[4] Reflecting the increased mobility of the OH group in its environment, the random walker has an enhanced diffusivity in its "local domain". After a certain residence time inside this domain the random walker is able to leave it and subsequently move with a lower diffusivity based on the interdiffusion coefficient between anion and cation. More detailed information about the model, such as the exact parameters used, as well as a Fortran implementation of the algorithm can be found in publication VI.

Fig. 3.13 shows the HB population functions of the ca HB of $[HOC_4Py][NTf_2]$ as well as the predictions obtained from the minimalist random-walker model. The model is able to adequately predict the temperature dependence of $C(t)$ by only changing the diffusivity outside the local domain in accordance to the change in the interdiffusion coefficient between anion and cation at those temperatures. The prediction of the correlation functions of the cc HB are also possible by sensibly changing other parameters, for example increasing the size of the local domain, as now the acceptor is able to explore larger volumes than in the case of the ca HB.

To summarize, the "intermittent" HB lifetime τ_{hb} comprises dynamics of different time domains. The viscous nature of the ILs leads to an increased separation between the short-time behavior, which mostly describes the breaking of HBs through reorientation of the intramolecular OH bond vector, and the long-time behavior, which is characterized by the interdiffusion of donor and acceptor. For the ILs described here, both the ca and cc HB lifetimes are dominated by the long-time behavior. The slow decay more than compensates for its low amplitude in comparison to the short-time behavior. Comparing ca and cc HBs, we see that the cc HB can be kinetically more stable for long alkyl chain length and low temperatures.

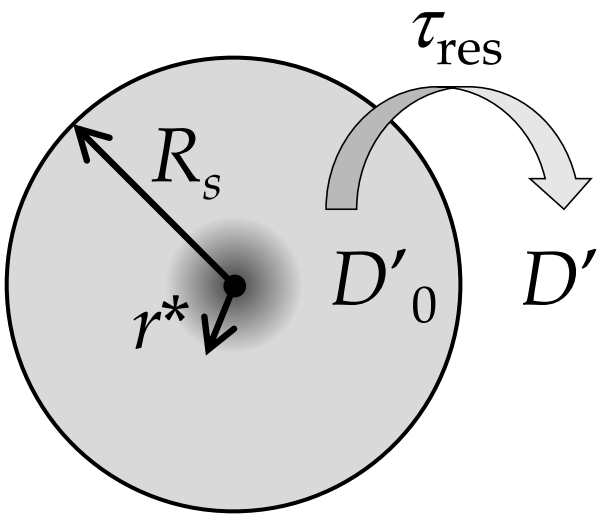

Fig. 3.12.: Schematic representation of the minimalist model used to describe the time evolution of the HB population correlation functions.[4]

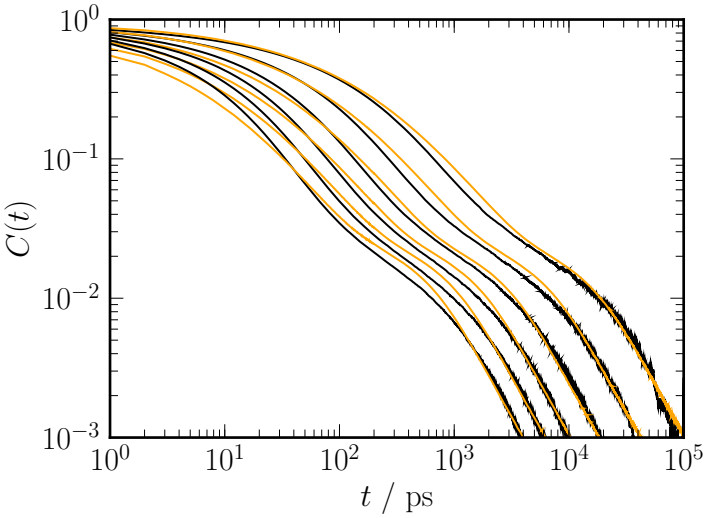

Fig. 3.13.: HB population correlation function $C(t)$ for the ca HB in $[HOC_4Py][NTf_2]$ at 300 K, 320 K, 340 K, 360 K, 380 K, and 400 K, respectively, shown as black lines. The orange lines indicate the prediction of the minimalist random-walker model. For the parameters used in the model see publication VI.[4]

3.3.2. Reactive Flux Approach

The "intermittent" HB lifetime τ_{hb} encompasses all dynamics present in the system: from short-time libration to reorientation and diffusion. It may not be desirable to include all of those kinetics in the definition of a HB lifetime, depending on the question at hand. The reactive flux method is an approach to define a HB lifetime without pertubations caused by diffusion.[50,103–105] The making and breaking of HBs can be viewed as an reaction equilibrium

$$A \underset{k_{\mathrm{f}}}{\overset{k_{\mathrm{d}}}{\rightleftharpoons}} B, \tag{3.10}$$

where A represents the state of a HB between donor and acceptor ($\langle h \rangle$), B implies no HB ($[1 - \langle h \rangle]$), and k_{f} and k_{d} signify the rate constants of formation and decay of the HB.

In equilibrium the probability that a specific donor-acceptor pair is hydrogen-bonded is minuscule. If a HB is present at $t_0 = 0$, the system relaxes back to equilibrium with a time dependent rate constant $k(t)$, the reactive flux:

$$k(t) = -\frac{\mathrm{d}C(t)}{\mathrm{d}t} = \frac{\left\langle \dot{h}(0)[1 - h(t)] \right\rangle - \langle h \rangle^2}{\langle h^2 \rangle - \langle h \rangle^2}. \tag{3.11}$$

Considering $\langle h(0)\dot{h}(t) \rangle = -\langle \dot{h}(0)h(t) \rangle$ and $\langle \dot{h}(0) \rangle = 0$, equation 3.11 directly results from equation 3.4, due to the time symmetry of $C(t)$. According to transition state theory (TST), trajectories crossing the transition point of the decay reaction can never reform the HB.[105] The corresponding reaction rate k_{TST} can be acquired from $\lim_{t \to 0^+} k(t) = k_{\mathrm{TST}}$ and represents an upper limit of the reaction rate as, contrary to the assumptions of TST, recrossings are allowed in our systems. The complementary lifetime $\tau_{\mathrm{TST}} = k_{\mathrm{TST}}^{-1}$ represents a "continuous" HB lifetime.

It was shown for water that $k(t)$ does not relax exponentially as one would expect from first order kinetics.[105] Thus, we have to revisit the definitions of the states A and B in the scheme 3.10. By introducing a vicinity operator $H(t)$, being unity if the donor and acceptor are "near" each other and zero otherwise, we can redefine state B as a non-bonded donor-acceptor pair, which is still positionally close to each other. This leads us to the restrictive reactive flux correlation function

$$k_{\mathrm{in}}(t) = -\frac{\left\langle \dot{h}(0)[1 - h(t)]H(t) \right\rangle - \langle h \rangle^2}{\langle h^2 \rangle - \langle h \rangle^2}, \tag{3.12}$$

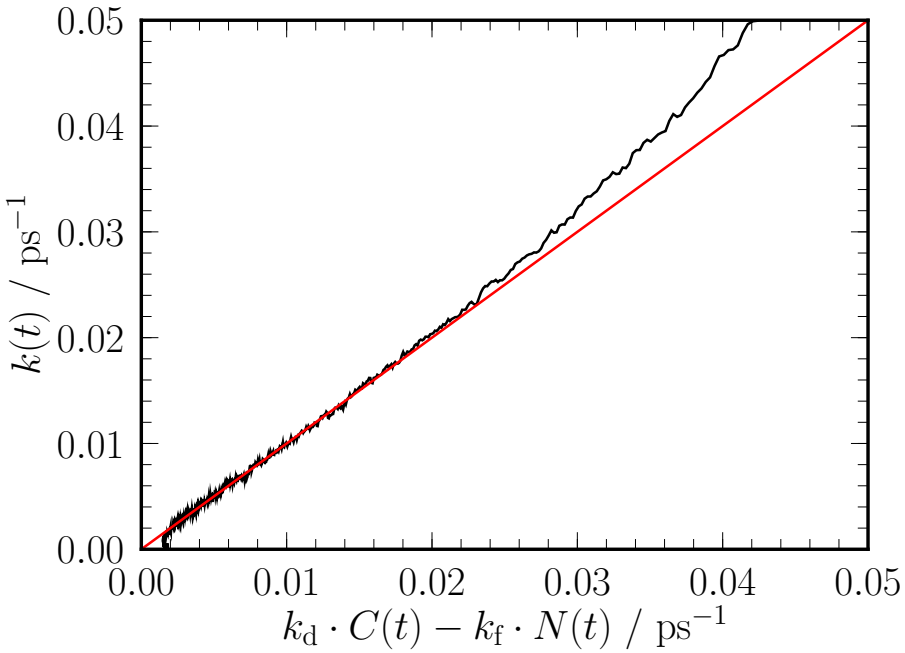

Fig. 3.14.: Correlation plot according to equation 3.14 with $k_\mathrm{d}^{-1} = 13.0\,\mathrm{ps}$ and $k_\mathrm{f}^{-1} = 15.1\,\mathrm{ps}$ for $[\mathrm{HOC_4Py}][\mathrm{NTf_2}]$ at 400 K. The red solid line indicates the unity slope.[4]

which measures the time dependent rate constant of bond reformation. The integral

$$N(t) = \int_0^t k_\mathrm{in}(t')\mathrm{d}t' \tag{3.13}$$

represents the probability of finding the previously defined state B at time t if the donor-acceptor pair was hydrogen-bonded at $t = 0$. This enables us to find the rate constant of decay k_d from the kinetic equation

$$k(t) = k_\mathrm{d}C(t) - k_\mathrm{f}N(t) \tag{3.14}$$

by fitting equation 3.14 to data of $C(t)$, $N(t)$, and $k(t)$ obtained by MD simulation (Fig. 3.14). It should be pointed out that, while $C(t)$ and $N(t)$ are local populations which interconvert through a first order kinetic reaction, the total population $C(t) + N(t)$ is not constant, as $N(t)$ (state B) also depletes via translational diffusion.[4] The inverse of k_d represents another HB lifetime, which hereafter is referenced as $\tau_\mathrm{hb,d}$.

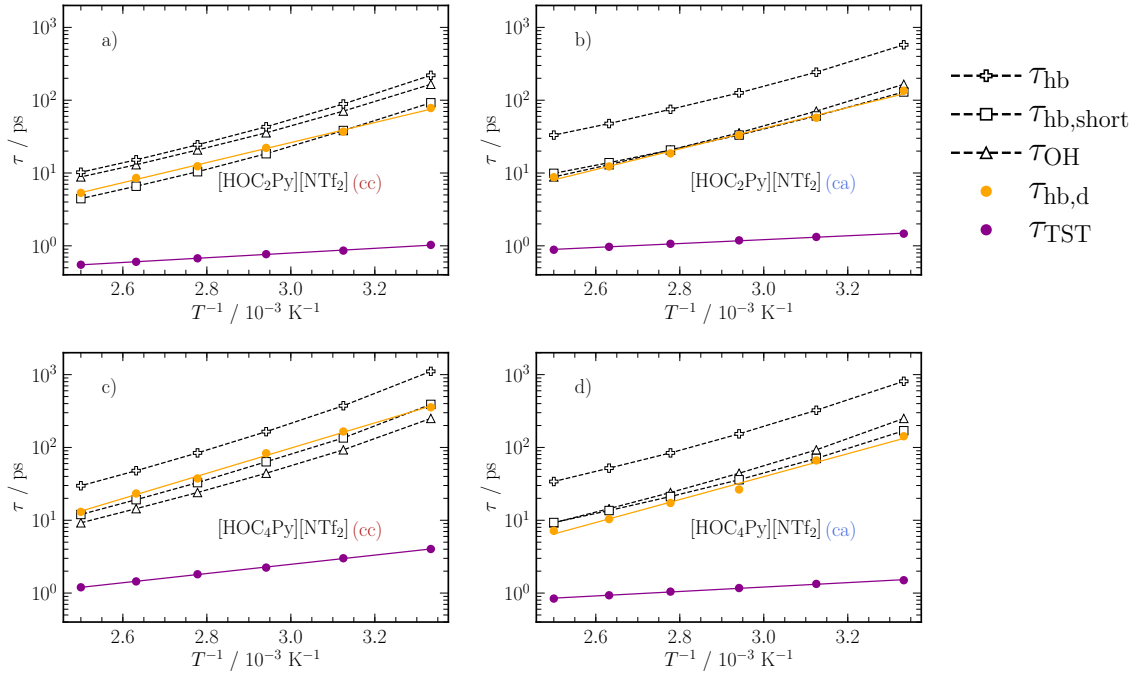

Fig. 3.15.: HB lifetimes $\tau_{\mathrm{hb,d}}$ and τ_{TST} determined via the reactive flux approach compared to the lifetimes τ_{hb} and τ_{short} obtained via integrating C(t) and $C_{\mathrm{short}}(t)$, respectively, and the the reorientational correlation time of the OH bond vector τ_{OH}. Top panels: $[HOC_2Py][NTf_2]$. Bottom panels: $[HOC_4Py][NTf_2]$. Left panels: cc HB. Right panels: ca HB. Dashed lines are linearly connecting adjacent data points. Solid lines represent Arrhenius fits.[4]

All lifetimes discussed to this point are presented in Fig. 3.15 for the ca and cc HBs in $[HOC_2Py][NTf_2]$ and $[HOC_4Py][NTf_2]$ as representatives for the respective ILs with short and long alkyl chains.[4] Their values are distributed over a large range of time, from the sub-picosecond regime to a few nanoseconds. As discussed before, τ_{TST} is found to be the smallest lifetime in all cases, due to the corresponding reaction rate being somewhat of a "speed limit" for HB breaking.[4] It is shorter than $\tau_{\mathrm{hb,d}}$ and τ_{short} by about one order of magnitude. This is in accordance with earlier work from Gehrke et al. on non-hydroxyl-functionalized imidazolium-based ILs.[48,50] In comparison to the other HB lifetimes it shows a weaker dependence on the temperature, but exhibits Arrhenius behavior together with $\tau_{\mathrm{hb,d}}$. For both lifetimes extracted by the reactive flux approach, the dynamics seem to be unaffected by the collective molecular motions, which is leading to VFT behavior of the other

lifetimes. An Arrhenius temperature dependence for τ_{TST} and $\tau_{\mathrm{hb,d}}$ has also been shown for imidazolium-based ILs and water.[50,105]

The lifetimes $\tau_{\mathrm{hb,d}}$ and τ_{short} are found in the same time range for both HB types and ILs. Whether this is coincidental or by design is unclear and more research could be done here. Although mostly dominated by reorientational dynamics, the non-monoexponential behavior of $C_{\mathrm{short}}(t)$ indicates influences from diffusion which are eliminated for $\tau_{\mathrm{hb,d}}$ by the reactive flux approach. Unsurprisingly, τ_{OH} lies also in the same time range. It measures the orientational correlation of the OH bond vector but is, in contrast to the various HB lifetimes, not able to discriminate between different bonded, ca or cc, or even non-bonded states, as it is an average over all those states. As stated before, the strength of a HB also affects τ_{OH}, so cc hydrogen-bonded hydroxyl groups should reorientate slower than ca hydrogen-bonded ones, but dividing τ_{OH} in such a way is not possible with the methodology discussed in section 2.6. So it is not unexpected for τ_{OH} to fit the lifetimes of the ca HBs in both $[\mathrm{HOC_2Py}][\mathrm{NTf_2}]$ and $[\mathrm{HOC_4Py}][\mathrm{NTf_2}]$ rather than the respective cc HBs, as the HB population is dominated by the ca HBs in all ILs as discussed in section 3.2. Finally, the by far largest HB lifetime is the full "intermittent" HB lifetime τ_{hb} which is dominated by the interdiffusion of donor and acceptor reflected in its long-time behavior.

4. Perspective

While light was shed on the structure of functionalized pyridinium-based ILs and the dynamics of their HB network, some questions remain unanswered. In the MD trajectories we are able to see hydroxyl groups which are not forming a HB during the respective time step (called "free" in section 3.2). These species can not be found with experimental methods. This may be due to a short lifetime of this species or various unspecific interactions of these hydroxyl groups causing for instance a broad distribution in the IR spectra. To elucidate this effect, small clusters taken from the MD trajectory could be analyzed by quantum chemical calculations regarding the frequency of the OH bond vibration in an effort to reproduce the experimental IR spectrum or show where the vibrations of those "free" hydroxyl groups could be found, if they exist outside of the MD simulation.

Until now, the HB statistic was analyzed from the point of view of the HB donor. A more diverse analysis of the HB network, including the perspective of the HB acceptor, could further illuminate the structure of the bulk liquid phase. Are cc chains always ending in a ca HB? Is a cation accepting a cc HB more likely to form a ca HB than other cations? The balance between those interactions governs the formation of multi-dimensional structures like chains, ring, and lassos.

By mixing the two ILs $[HOC_4Py][NTf_2]$ and $[C_5Py][NTf_2]$ we are effectively creating hydroxyl defects in the IL. Due to the lower acceptor density, the amount of cc HB diminishes but the bulk liquid structure remains largely the same. We are currently analyzing those mixtures with different methods to shed a light on the impact of cc HBs on the overall structure and dynamics in the IL. An understanding of the HB network and its effect on the dynamics helps to create substances or mixtures with specifically designed macroscopic properties.

5. Publications

Tab. 5.1.: Declaration about my approximate contribution to the publications discussed in this work.

Publication	contribution
I. Revisiting imidazolim based ionic liquids: Effect of the conformation bias of the [NTf_2] anion studied by molecular dynamics simulation	40 %
II. The Double-Faced Nature of Hydrogen Bonding in Hydroxy-Functionalized Ionic Liquids Shown by Neutron Diffraction and Molecular Dynamics Simulations	20 %
III. Hydrogen Bonding Between Ions of Like Charge in Ionic Liquids Characterized by NMR Deuteron Quadropole Coupling Constants – Comparison with Salt Bridges and Molecular Systems	15 %
IV. Isolating the role of hydrogen bonding in hydroxyl-functionalized ionic liquids by means of vaporization enthalpies, infrared spectroscopy and molecular dynamics simulations	20 %
V. Kinetics of Hydrogen Bonding between Ions of Opposite and Ions of Like Charge in Hydroxyl-Functionalized Ionic Liquids	60 %
VI. Hydrogen Bonds between Ions of Opposite and Like Charge in Hydroxyl-functionalized Ionic Liquids: an Exhaustive Examination of the Interlay Between Global and Local Motions and Intermolecular Hydrogen Bond Lifetimes and Kinetics	60 %

I. Revisiting imidazolim based ionic liquids: Effect of the conformation bias of the [NTf_2] anion studied by molecular dynamics simulation

J. Neumann, B. Golub, L.-M. Odebrecht, R. Ludwig, D. Paschek, *J. Chem. Phys.* **2018**, *148*, 193828.
DOI: 10.1063/1.5013096

Contribution:
I performed the quantum chemical calculations of the $[NTf_2]^-$ anion necessary for the potential energy surfaces, new dihedral potentials and point charges. B. Golub and I fitted the potentials of the S-N-S-C as well as the F-C-S-N dihedrals for the MD simulation. Together we wrote the draft and revised the manuscript. I supervised the work of L.-M. Odebrecht, who simulated and analyzed the $[C_n MIm][NTf_2]$ ILs with the new $[NTf_2]^-$ force field as part of her bachelor thesis. My contribution to the publication sums up to approximately 40 %.

Revisiting imidazolium based ionic liquids: Effect of the conformation bias of the [NTf_2] anion studied by molecular dynamics simulations

Cite as: J. Chem. Phys. **148**, 193828 (2018); https://doi.org/10.1063/1.5013096
Submitted: 10 November 2017 . Accepted: 31 January 2018 . Published Online: 20 February 2018

Jan Neumann, Benjamin Golub, Lisa-Marie Odebrecht, Ralf Ludwig, and Dietmar Paschek

THE JOURNAL OF CHEMICAL PHYSICS **148**, 193828 (2018)

Revisiting imidazolium based ionic liquids: Effect of the conformation bias of the [NTf_2] anion studied by molecular dynamics simulations

Jan Neumann,[1,a)] Benjamin Golub,[1,b)] Lisa-Marie Odebrecht,[1,c)] Ralf Ludwig,[2,3,d)] and Dietmar Paschek[1,e)]

[1]*Institut für Chemie, Abteilung Physikalische und Theoretische Chemie, Universität Rostock, Albert-Einstein-Straße 21, D-18059 Rostock, Germany*

[2]*Institut für Chemie, Abteilung Physikalische und Theoretische Chemie, Universität Rostock, Dr.-Lorenz-Weg 2, D-18059 Rostock, Germany*

[3]*Leibniz Institut für Katalyse an der Universität Rostock, Albert-Einstein-Straße 29a, D-18059 Rostock, Germany*

(Received 10 November 2017; accepted 31 January 2018; published online 20 February 2018)

We study ionic liquids composed of 1-alkyl-3-methylimidazolium cations and bis(trifluoromethyl-sulfonyl)imide anions ([C_nMIm][NTf_2]) with varying chain-length n = 2, 4, 6, 8 by using molecular dynamics simulations. We show that a reparametrization of the dihedral potentials as well as charges of the [NTf_2] anion leads to an improvement of the force field model introduced by Köddermann, Paschek, and Ludwig [ChemPhysChem **8**, 2464 (2007)] (KPL-force field). A crucial advantage of the new parameter set is that the minimum energy conformations of the anion (*trans* and *gauche*), as deduced from *ab initio* calculations and Raman experiments, are now both well represented by our model. In addition, the results for [C_nMIm][NTf_2] show that this modification leads to an even better agreement between experiment and molecular dynamics simulation as demonstrated for densities, diffusion coefficients, vaporization enthalpies, reorientational correlation times, and viscosities. Even though we focused on a better representation of the anion conformation, also the alkyl chain-length dependence of the cation behaves closer to the experiment. We strongly encourage to use the new NGOLP (Neumann, Golub, Odebrecht, Ludwig, Paschek) force field for the [NTf_2] anion instead of the earlier KPL parameter set for computer simulations aiming to describe the thermodynamics, dynamics, and also structure of imidazolium-based ionic liquids. *Published by AIP Publishing.*
https://doi.org/10.1063/1.5013096

INTRODUCTION

Having a reliable force field available is one of the most important prerequisites for setting up a molecular dynamics (MD) simulation. Hence, a lot of effort has been put into the development of new as well as the improvement of existing force field models. There are essentially two different approaches on how to improve or optimize force fields:

One approach is trying to develop a "universal" force field parameter set which can be applied to a broad range of different molecules or ions, such as the force field parameters for ionic liquids introduced by Pádua *et al.*[1–10] These force fields are very popular in the ionic liquid molecular simulation community and yield in general good results in comparison with experimental data.

An alternative, less universal approach is to focus on a specific subset of molecules and ions and to enhance the quality of the model by fitting the parameters of a system to a set of selected thermodynamical, dynamical, and structural properties, which then can be accurately emulated by the force field. The most well-known example for the application of such a strategy is perhaps the water molecule. In 2002, Bertrand Guillot gave a comprehensive overview over (at the time) more than 40 different water models,[11] and the number has been increasing since then.[12–15] Obviously, water is of great scientific interest. As a consequence, there exist a variety of force field models consisting mostly of three (SPC, TIP3P) to five (TIP5P, ST2) interaction sites, including (POL5) or without (SPC/E) polarizability and even force fields optimized to best represent the solid phases of water (TIP4P/ICE) and their phase transitions.

The second strategy was employed by Köddermann *et al.* in 2007 to arrive at the KPL (Köddermann, Paschek, Ludwig) force field for a selected class of imidazolium-based ionic liquids composed of 1-alkyl-3-methylimidazolium cations and bis(trifluoromethyl-sulfonyl)imide anions ([C_nMIm][NTf_2]).[16] The aim of this work was to further optimize the force field of Pádua *et al.* to better represent dynamical properties like self-diffusion coefficients, reorientational correlation times, and viscosities. As shown in their original work from 2007 as well as in further studies published by different groups, the KPL force field has been proven to yield reliable results for dynamical properties, but also for thermodynamical properties, such as the free energies of solvation for light gases in ionic liquids,[17,18] and is still used frequently to date.[19–21]

Here we want to present our take on further improving the KPL force field by revisiting the conformation-space explored by the [NTf_2] anion. Extensive studies of the conformation of

[a)]jan.neumann@uni-rostock.de
[b)]benjamin.golub@uni-rostock.de
[c)]lisa-marie.odebrecht@uni-rostock.de
[d)]ralf.ludwig@uni-rostock.de
[e)]dietmar.paschek@uni-rostock.de

the [NTf_2] anion using the KPL force field in comparison to experimental as well as quantum chemical calculations have revealed a significant mismatch of the energetically favored conformations. Therefore we feel the need for presenting a modified version of the force field, removing this conformation bias. We will discuss the implications of this modification for a wealth of thermodynamical, dynamical, and structural quantities.

CONFORMATION-SPACE OF THE ANION

During MD simulations of ionic liquids of the type [C_nMIm][NTf_2] with the force field of Köddermann *et al.*, it became apparent that the favored [NTf_2] anion conformations observed in the simulation differ from what has been shown earlier from quantum chemical (QC) calculations[6] as well as from Raman experiments[22] (see Figs. 1 and 2).

For locating the minimum energy conformations, we performed extensive quantum chemical calculations with the Gaussian 09 program[23] following the approach of Lopes and Pádua.[2] We started by calculating the potential energy surface as a function of the two dihedral angles S1–N–S2–C2 (ϕ_1) and S2–N–S1–C1 (ϕ_2) on the Hartree-Fock (HF) level with a small basis set (6-31G*). Subsequent to these optimizations, we performed single point calculations on the 2nd order Møller-Plesset Many Body Perturbation Theory (MP2) level using the cc-pvtz basis set for all HF optimized conformations. In agreement with earlier calculations by Pádua *et al.*[6] and Raman measurements of Fujii *et al.*,[22] we observe essentially two structurally distinct minimum energy conformations that can be identified as energy minima on the energy landscape depicted in Fig. 3. The *trans* conformations of the [NTf_2] anion are energetically preferred, followed by the gauche-conformations, which are elevated by about 3 kJ mol^{-1} (see Fig. 2). Due to the symmetry of the [NTf_2] anion, the in essence two structurally distinct conformations appear in the form of the six minima of the energy landscape shown in Fig. 3. The two global minima describe *trans* conformations located at $\phi_1 = 90°$, $\phi_2 = 90°$ and $\phi_1 = 270°$, $\phi_2 = 270°$, respectively. The four additional local minima are all representing structurally identical *gauche* conformations, based on the symmetry of the ion. This is in agreement with Pádua *et al.* and discussed in more detail in their publication from 2008.[6]

To compare these *ab initio* calculations with the KPL force field model, we employed the molecular dynamics package Moscito 4.180 and computed the same potential energy

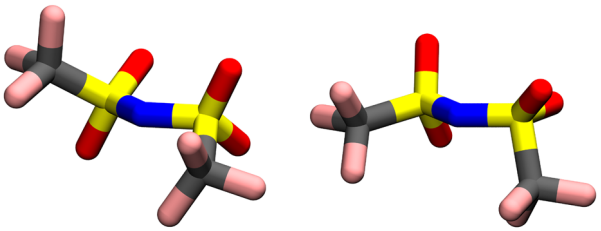

(a) (b)

FIG. 1. Minimum energy conformations of the [NTf_2] anion taken from a MD simulation employing the KPL force field.

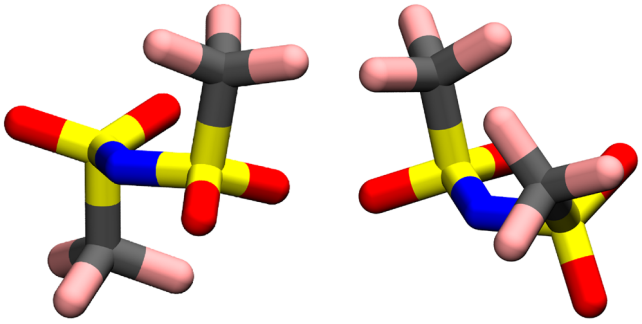

(a) (b)

FIG. 2. Minimum energy conformations of the [NTf_2] anion obtained from *ab initio* calculations. The *trans* conformation (left) represents the global energy minimum, while the energy of the *gauche* conformation (right) is elevated by about 3 kJ mol^{-1}.

surface as a function of the two dihedral angles ϕ_1 and ϕ_2 (see Fig. 4, top panel) by fixing the two dihedral angles and optimizing all other degrees of freedom. We would like to add that in the force field-optimizations all bond lengths were kept fixed. It is quite obvious that the KPL force field does not adequately reproduce the potential energy surface obtained from the quantum chemical calculations (compare the top panel in Fig. 4 with Fig. 3). The minimum energy conformations of the KPL model reveal essentially two structurally distinct conformations illustrated in Fig. 1. However, both are somewhat similar, being positioned between the *trans* and *gauche* conformations favoured in the *ab initio* calculations. The fact that the energy landscape does not reflect all the symmetry-features of the molecule, however, might be a lesser problem since energy barriers are rather large and the anion could explore similar conformations simply by rotation.

However, for arriving at a better representation of the *ab initio* energy surface, we reparameterized the charges as well as the two distinct independent dihedral potentials (S–N–S–C and F–C–S–N), while keeping the other parameters unchanged. From our quantum chemical calculations, we yield the global minimum conformations at $\phi_1 = \phi_2 = 90°$ and $\phi_1 = \phi_2 = 270°$. Due to the symmetry of the [NTf_2] anion, these two minima are conformationally identical. To calculate the parameters for the S–N–S–C dihedral angle, we fixed ϕ_1 at 90° and calculated the energy as a function of the dihedral

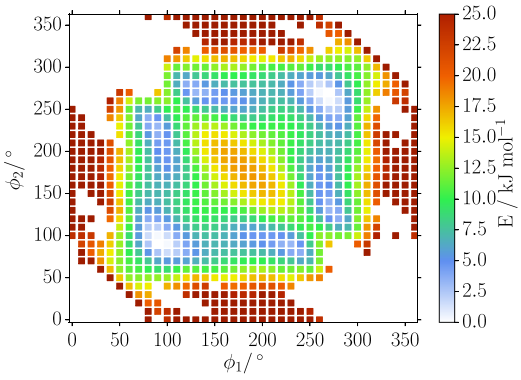

FIG. 3. *Ab initio* computation of the energy surface of the [NTf_2] anion as a function of the S1–N–S2–C2 and S2–N–S1–C1 dihedral angles ϕ_1 and ϕ_2.

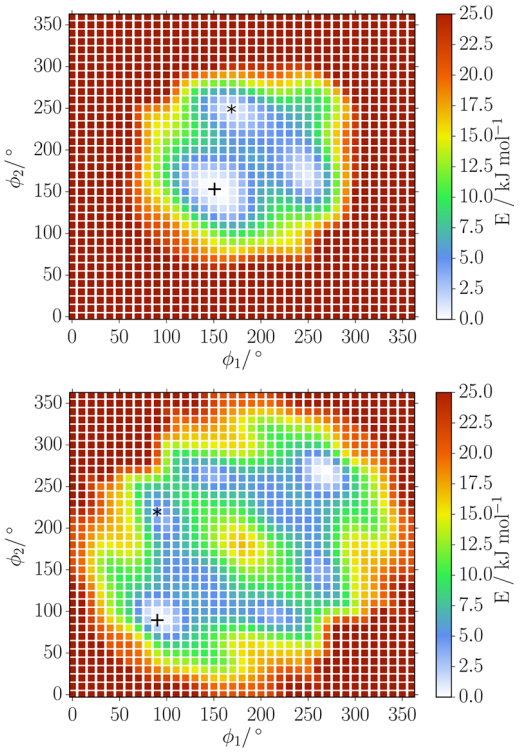

FIG. 4. Potential energy surface of the [NTf_2] anion computed for the two force field models. The new force field (bottom panel) provides a much better representation of the *ab initio* calculations shown in Fig. 3 than the original KPL force field (top panel). The plus-sign and asterisk indicate the location of the global and local minima of the energy landscape as depicted in Figs. 1 and 2, respectively.

angle ϕ_2 on the MP2 level using a cc-pvtz basis set (as shown in Fig. 5). The same procedure was applied using the KPL

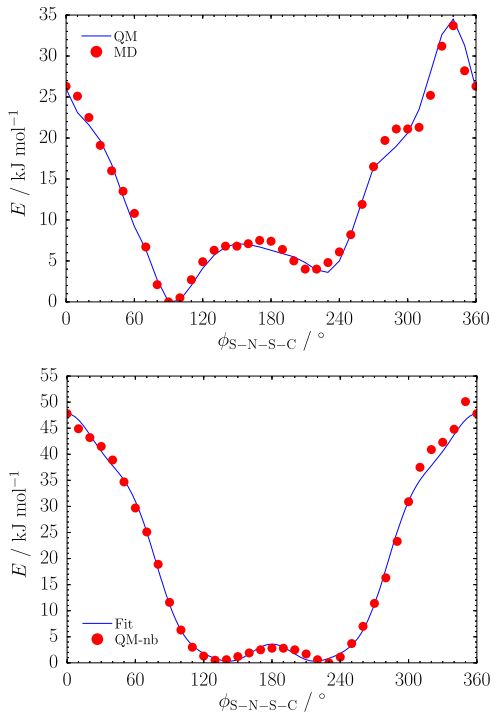

FIG. 5. (Top panel) Potential energy of the entire [NTf_2] anion as a function of the of S2–N–S1–C1 dihedral angle ϕ_2 with ϕ_1 being fixed at $\phi_1 = 90°$. (Bottom panel) Torsion potential fitted to the difference between the QC and force field model (with switched off torsion potential).

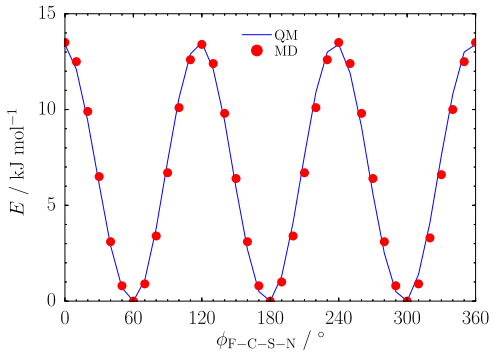

FIG. 6. Potential energy of the [NTf_2] anion as a function of the F–C–S–N dihedral angle.

force field while switching of the dihedral potential, such that only the nonbonding (nb) interactions matter. We then subtracted the latter energy function from the energies obtained via the QC calculations and arrived at the dihedral potential for the dihedral angle S–N–S–C, which should be reproduced by the torsion potential in our force field (see Fig. 5, bottom panel). The value of ϕ_1 at 90° was chosen deliberately since it represents a path very close to the minimum energy transition path between adjacent *trans* and *gauche* conformations, thus providing an optimized representation of the states with the lowest energies and their interconversion.

In contrast to the work of Köddermann *et al.*, we chose to fit a dihedral potential function obeying the conformational symmetry-features of the anion using

$$V^{\mathrm{dp}}_{\kappa\lambda\omega\tau} = \sum_n k^{\mathrm{dp}}_m [1 + \cos(m_n \psi_m - \psi^0_m)] \qquad (1)$$

(with $n = 6$ and $\psi^0_m = 0$) to the computed *ab initio* potential, leading to the proper minimum energy conformations of the [NTf_2] anion.[2] Similarly obtained were parameters for the F–C–S–N dihedral potential of the terminal CF_3-groups (see Fig. 6). The complete set of new parameters for the NGOLP (Neumann, Golub, Odebrecht, Ludwig, Paschek) force field is given in Table III. Similar to the procedure used in the OPLS (Optimized Potential for Liquid Simulations) force field, Coulomb and Lennard-Jones non-bonded 1-4 interactions are scaled by a factor of 0.5. We would like to point out that the representation of the *ab initio* conformational energy landscape by our model requires an intricate interplay of electrostatic and Lennard-Jones nonbonding interactions and dihedral potentials. We have made the observation that by using a newly derived set of partial charges, although the overall changes seem to be small, a significantly better

TABLE I. Lennard-Jones parameters σ, ϵ (all taken from Ref. 16) and charges q (all newly calculated in this work) for all interaction sites of the [NTf_2] anion.

Site	σ (Å)	ϵ (K)	q (e)
F	2.6550	8.00	−0.189
C	3.1500	9.96	0.494
S	4.0825	37.73	1.076
O	3.4632	31.70	−0.579
N	3.2500	25.66	−0.690

TABLE II. Bond length $r^0_{\kappa\lambda}$, angle $\phi^0_{\kappa\lambda\omega}$, and $k^a_{\kappa\lambda\omega}$ (all taken from Ref. 16) for the angle potential $V^a_{\kappa\lambda\omega} = \frac{1}{2}k^a_{\kappa\lambda\omega}(\phi_{\kappa\lambda\omega} - \phi^0_{\kappa\lambda\omega})^2$ in the force field of the [NTf_2] anions.

Bond	$r^0_{\kappa\lambda}$ (Å)	Angle	$\phi^0_{\kappa\lambda\omega}$ (deg)	$k^a_{\kappa\lambda\omega}$/kJ mol^{-1}rad^{-2}
C–F	1.323	F–C–F	107.1	781.0
C–S	1.818	S–C–F	111.8	694.0
S–O	1.442	C–S–O	102.6	870.0
N–S	1.570	O–S–O	118.5	969.0
		O–S–N	113.6	789.0
		C–S–N	100.2	816.0
		S–N–S	125.6	671.0

TABLE III. Parameters k^{dp}_m and ψ^0_m for the torsion potential $V^{dp}_{\kappa\lambda\omega\tau} = \sum_n k^{dp}_m[1 + \cos(m_n\psi_m - \psi^0_m)]$ in the force field of the [NTf_2] anion.

	$n(\kappa\lambda\omega\tau)$	m_n	k^{dp}_m (kJ mol^{-1})	ψ^0_m (deg)
F–C–S–N	1	3	2.0401	0.0
S–N–S–C	1	1	23.7647	0.0
	2	2	6.2081	0.0
	3	3	−2.3684	0.0
	4	4	−0.0298	0.0
	5	5	0.6905	0.0
	6	6	1.0165	0.0

representation of the energy landscape was feasible as compared to the previously employed charge model. Therefore we re-computed partial charges from the MP2-wavefunction using the method of Singh and Kollman as implemented in the Gaussian 09 program.[24] The refined charges are listed in Table I.

Finally, employing new refined parameters for the dihedral potentials and partial charges, we re-calculated the energy surface as a function of the two dihedral angles ϕ_1 and ϕ_2 (see Fig. 4, bottom panel). The result is in much better agreement with the *ab initio* calculations and resolves the conformational mismatch issue for the force field of the [NTf_2] anion. In addition, we would like to emphasize that this procedure also leads to a proper description of the barrier height between the two adjacent *gauche* conformations, which is critical for properly describing the conformational interconversion of the molecule between the two global energy minimum states on the energy landscape located at $\phi_1 = 90°$, $\phi_2 = 90°$ and $\phi_1 = 270°$, $\phi_2 = 270°$, respectively.

All parameters for the new [NTf_2] anion force field are listed in Tables I–III. The original parameters as well as the parameters for the cations can be found in the publication of Köddermann *et al.*[16]

MOLECULAR DYNAMICS SIMULATIONS

We performed MD simulations for the two force fields KPL and NGOLP with Gromacs 5.0.6[25–29] over a temperature range from $T = 273$–483 K to calculate thermodynamical and dynamical properties and compare them with the original KPL force field. All simulations were carried out in the *NpT* ensemble. However, to compute viscosities, we performed additional *NVT* simulations using starting configurations sampled along the *NpT*-trajectory. Periodic boundary conditions were applied using cubic simulation boxes containing 512 ion-pairs. We applied smooth particle mesh Ewald summation[30] for the electrostatic interactions with a real space cutoff of 0.9 nm, a mesh spacing of 0.12 nm, and 4th order interpolation. The Ewald convergence factor α was set to 3.38 nm^{-1} (corresponding to a relative accuracy of the Ewald sum of 10^{-5}). All simulations were carried out with a time step of 2.0 fs, while keeping bond lengths fixed using the LINCS algorithm.[31]

An initial equilibration was done for 2 ns at $T = 500$ K using the Berendsen thermostat as well as the Berendsen barostat with coupling times $\tau_T = \tau_p = 0.5$ ps.[32] After this another equilibration was done for 2 ns at each of the desired temperatures. For each of the six temperatures 273 K, 303 K, 343 K, 383 K, 423 K, and 483 K, we performed production runs of 30 ns, keeping the pressure fixed at 1 bar applying Nosé-Hoover thermostats[33,34] with $\tau_T = 1$ ps and Rahman-Parrinello barostats[35,36] with $\tau_p = 2$ ps.

RESULTS AND DISCUSSION

Analogous to the publication of Köddermann *et al.* from 2007,[16] we will compare densities, self-diffusion coefficients, and vaporization enthalpies for [C_nMIm][NTf_2] as a function of temperature and alkyl chain-length as well as viscosities and reorientational correlation times for [C_2MIm][NTf_2] as a function of temperature. It is important to keep in mind that the original force field was optimized to reproduce these properties and yields a good agreement between the experiment and simulation. By resolving the mismatch of the favored conformations of the [NTf_2] anion, we are able to describe these properties as good as the KPL force field or even better.

Structural features

Here we take a look at structural features of the liquid phase and how they are influenced by changes in the conformation-population of the [NTf_2] anion.

Before discussing the inter-ionic structural features of the ionic liquids, we would like to briefly elaborate on the conformational states adopted by the anion and their transitions in the condensed ionic liquid phase. From the energy landscape depicted in Fig. 4, it is evident that the anion possesses two dominant low energy states, both labeled *trans* located at $\phi_1 = 90°$, $\phi_2 = 90°$ and $\phi_1 = 270°$, $\phi_2 = 270°$, respectively. In Fig. 7, we illustrate the time evolution of the conformation adapted by a single anion in the ionic liquid at $T = 273$ K over a time period of 16 ns. As expected it is evident that the anion resides mostly in either of the two *trans* states with rather frequent changes between them due to rapid conformational interconversions. It is rarely observed being resting in a *gauche* state as indicated in Fig. 7. It is mostly passing through the *gauche* states as a transitional state. By counting the number of transitions, we estimate the average residence time in either of the distinct *trans* states to be in the range of about 1 ns. As pointed out by Pádua *et al.*,[6] the observed rapid conformational interconversions illustrate the importance of a proper description of the conformational energy landscape.

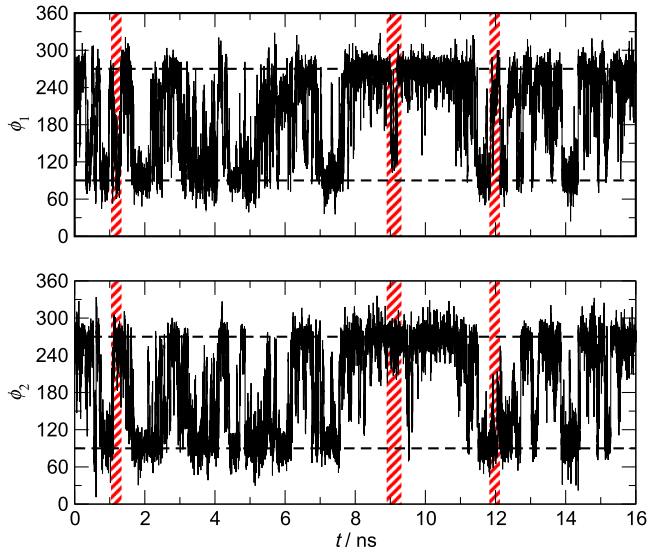

FIG. 7. Time evolution of the conformation-state of a single $[NTf_2]$-anion over a time interval of 16 ns at $T = 273$ K indicated by the two dihedral angles $\phi_1(t)$ and $\phi_1(t)$. The red shaded regions indicate time intervals where one of the dihedral angles is resting in a *gauche* state.

First we inspect the three distinct center of mass pair distribution functions between the different ions computed for $[C_nMIm][NTf_2]$ with $n = 2$ at $T = 303$ K (shown in Fig. 8). It is quite apparent that these distribution functions are only slightly affected by the alterations in the force field. Most notable are the differences observed in the anion-anion pair distribution function depicted in Fig. 8(c) with the first peak being significantly broadened. It is quite obvious to assume that this behavior is related to the more distinct conformational states (*trans* and *gauche*) that the reparameterized $[NTf_2]$ anion is adopting as shown in Fig. 2. In the *trans* state, the molecule is more elongated along the molecular axis and more compact perpendicular to it. In addition, the gauche-state is generally more compact than the minimum energy conformations adopted by the original KPL force field model shown in Fig. 1. This leads to an enhanced population of both short and long anion-anion distances. This effect manifests itself also in the slight shift of the maximum of the first peak of the anion-cation pair distribution function towards smaller distances [see Fig. 8(a)]. Another interesting distribution function is the pair distribution function of the anion-oxygens surrounding the C(2)-hydrogen site on the cation. The C(2)-position is deemed to act as a hydrogen-bond donor.[37,38] With changing conformations, we expect an effect on the hydrogen bonding situation between the anion and cation. Here we observe

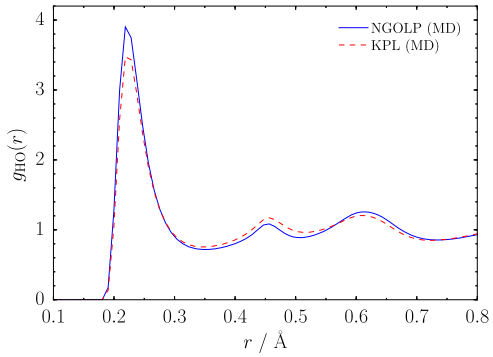

FIG. 9. Radial pair distribution function of the anion-oxygens around the C(2) hydrogen site on the cation for $[C_2MIm][NTf_2]$ at $T = 303$ K. The NGOLP force field is shown as the blue line, and the KPL force field as the red dashed line.

that the NGOLP force field promotes hydrogen bonds between anions and cations as indicated by an increased first peak of the O–H pair distribution function shown in Fig. 9. The computed number of hydrogen bonds increases throughout by about 4%, mostly unaffected by the alkyl chain-length and temperature (not shown). Taking into account the importance of more elongated *trans* configurations of the anion, it is also not surprising that the second peak is somewhat depleted, while the third peak is again enhanced (see Fig. 9). We further investigate the hydrogen-bond situation by not just looking at the distance between the oxygen and hydrogen but also at the angular distribution. Therefore we compute the probability density map of the anion-oxygens surrounding the C(2) hydrogen site on the cation. Again we focus on the C(2) hydrogen because its hydrogen-bond interaction with the anion is deemed the strongest and most important. To calculate this map, we compute both the O–H distance and the angle between the C–H bond-vector on the cation and the intermolecular C–O vector, where C is the C(2)-position of the cation and O represents the oxygen-sites on the anions. In addition, the computed probabilities are weighted by r_{OH}^{-2}. It is revealed that the maximum of this probability density map does not quite represent a linear hydrogen bond at a distance of 2.3 Å but is tilted by about 25° and is characterized by a rather broad angular distribution (Fig. 10).

Densities and self-diffusion coefficients

To get an idea on how the changing conformation-populations influence the properties of the imidazolium-based ionic liquids, we first take a look at the mass density of $[C_2MIm][NTf_2]$. In molecular simulations, the density has

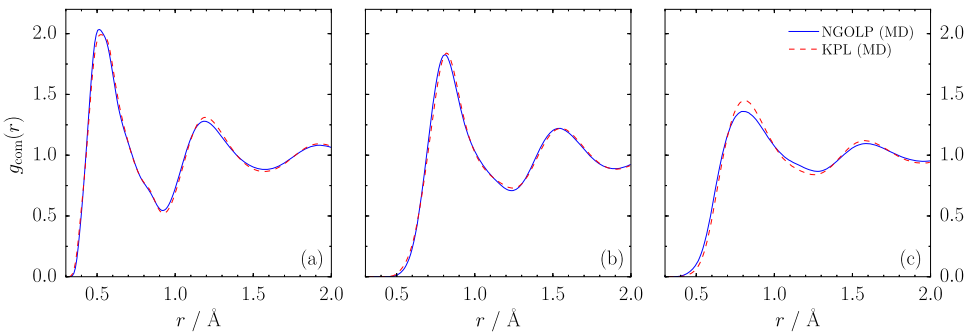

FIG. 8. Center of mass radial pair distribution functions for cation-anion (a), anion-anion (b), and cation-cation (c) for $[C_2MIm][NTf_2]$ at $T = 303$ K. The NGOLP-data are shown as blue lines, and the KPL-data force is shown as red dashed lines.

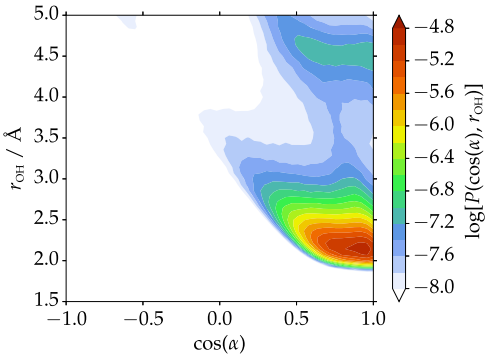

FIG. 10. Probability density of the anion-oxygens around the C(2) hydrogen sites as a function of the intermolecular distance r_{OH} and the angle between the C(2)–H bond-vector and the intermolecular C(cation)–O(anion) vector shown for the NGOLP force field at T = 303 K.

always been an important property for evaluating the force field. The enhanced conformational diversity of the [NTf_2] anion leads to a slight increase in the density over the whole temperature range (see Fig. 11 and Table IV). This overall increase is in better agreement with the experimental data from the work of Tokuda *et al.*[39] For lower temperatures, the NGOLP force field even matches the experimental values. The thermal expansivity, however, is significantly overestimated, although at the highest temperatures the difference between the experiment and simulation is still within about 5%. Despite the overall density increase from KPL to NGOLP, the thermal expansivities of both models are practically identical.

With this increasing density, also slightly reduced self-diffusion coefficients for the [NTf_2] anion are observed (see Fig. 12). We calculated the self-diffusion coefficient using the Einstein relation

$$D = \frac{1}{6} \lim_{t\to\infty} \frac{d}{dt} \left\langle |\vec{r}_i(t) - \vec{r}_i(0)|^2 \right\rangle \qquad (2)$$

as a function of the temperature for [C_2MIm][NTf_2] (Fig. 12) as well as a function of the alkyl chain-length of [C_nMIm][NTf_2] at T = 303 K (Fig. 13 and Table V). As shown in 2007, the KPL force field is able to yield self-diffusion coefficients in good agreement with the experimental data. Nevertheless, using the new NGOLP parameters, we are able

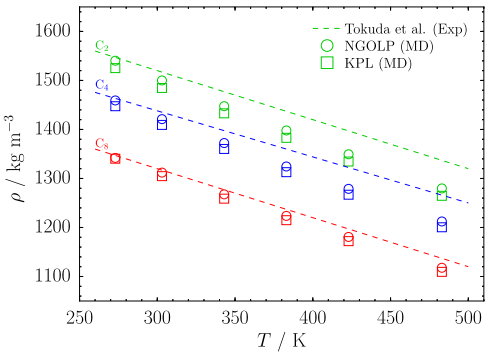

FIG. 11. Mass densities of [C_nMIm][NTf_2] with n = 2, 4, 8 as a function of temperature. The experimental data of Tokuda *et al.* are given according to their fitted temperature dependence (dashed lines).[39] The results from our molecular dynamics simulation are shown as open symbols: NGOLP (open circles) and KPL (open squares). See also Table IV.

TABLE IV. Temperature dependence of the density ρ and the self-diffusion coefficients of the [NTf_2] anion D_- in [C_2MIm][NTf_2] according to the KPL and NGOLP force fields. See also Figs. 11 and 12.

	ρ (kg m^{-3})		$D_-/10^{-11}$ (m^2 s^{-1})	
T (K)	KPL	NGOLP	KPL	NGOLP
273	1525	1540	1.4	1.1
303	1485	1500	4.8	3.6
343	1433	1448	13.0	10.9
383	1383	1398	26.4	23.0
423	1335	1349	49.4	43.6
483	1265	1280	92.7	90.0

to describe the temperature dependence of the self-diffusion coefficient of the [NTf_2] anion in [C_2MIm][NTf_2] even better (Fig. 12 and Table IV). Taking a look at the alkyl chain-length dependence, we can support the findings for the n = 2 imidazolium ionic liquid. The NGOLP force field is able to reproduce the dependence better, especially for $n \leq 4$; for longer chains, the KPL force field is closer to the experiment (see Fig. 13). As observed for the temperature dependence, the general trend of the self-diffusion coefficient as a function of the alkyl chain-length is identical for the KPL and NGOLP force fields.

Vaporization enthalpies

The magnitude of the vaporization enthalpy of ionic liquids was studied extensively over the last few years and has been sometimes discussed quite emotionally.[40–48] For the purpose of this study, we will compare our results with the more recent quartz-crystal microbalance (QCM) data of imidazolium-based ionic liquids of type [C_nMIm][NTf_2] from the work of Verevkin *et al.* of 2013[47] as shown in Fig. 14. We would like to point out that an exhaustive overview of the huge amount of vaporization enthalpy data from different experiments as well as molecular simulation studies is provided in the supporting information in the work of Verevkin *et al.*[47] and in the COSMO-RS (conductor like screening model for real solvents) study by Schröder and Coutinho.[48] The vaporization enthalpies per mole of [C_nMIm][NTf_2] were here calculated by assuming ideal gas behavior with

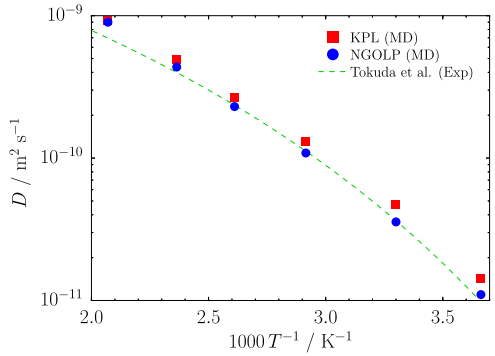

FIG. 12. Self-diffusion coefficients as a function of the temperature for [C_2MIm][NTf_2]. The experimental data of Tokuda *et al.* are represented according to their fitted temperature dependence (green dashed line).[39] The red squares (KPL) and blue dots (NGOLP) represent the results from our molecular dynamics simulations. See also Table IV.

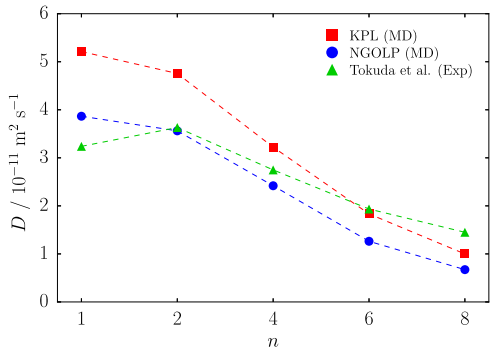

FIG. 13. Self-diffusion coefficients as a function of the alkyl chain-length for $[C_nMIm][NTf_2]$ at T = 303 K. The experimental data are shown as green triangles, the KPL force field is shown as red squares, and the NGOLP force field is shown as blue dots. The dashed lines are only guide to the eye. See also Table V.

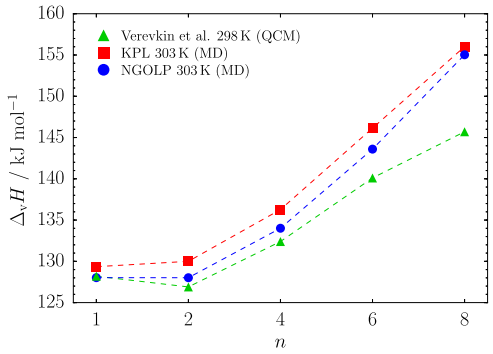

FIG. 14. Vaporization enthalpies as a function of the alkyl chain-length for NGOLP (blue dots) and KPL (red squares) at T = 303 K. For comparison, we also show the QCM data of Verevkin *et al.* for T = 298 K (green triangles).[47] See also Table VI.

$$\Delta_vH \approx \Delta_vU + RT\ , \tag{3}$$

which is a well-justified approximation, given the low vapor pressures of ionic liquids at low temperatures. The energy difference between the liquid and gas phases was computed via

$$\Delta_vU = U'_g - U'_l, \tag{4}$$

where U'_l and U'_g are the internal energies per mole ion-pairs of the liquid and gas phases, respectively. To determine U'_g, we performed gas phase simulations of individual ion-pairs without periodic boundary conditions. It has been shown in the literature that the gas phase of ionic liquids consists mostly of ion-pairs[47,49–55] tied together by strong long-range electrostatic forces. Hence, simulating an isolated ion-pair instead of separated ions is the most realistic approximation of the gas phase. As it is standard practice, during the simulation of both the liquid phase and the isolated ion-pair, the total linear momentum was set to zero, thus eliminating the systems' center of mass translational motion. In addition, in the simulations of the isolated ion-pairs, also the total angular momentum was set to zero. However, when comparing the internal energy of the gas phase and the liquid phase, we have to correct for differences in the kinetic energy stored in the translational/rotation motion of either system by adding

$$U'_g = U_g + \frac{6}{2}RT, \tag{5}$$

$$U'_l = U_l + \frac{3}{2}RT \times \frac{1}{N_{IP}} \tag{6}$$

per mole of ion-pairs, where N_{IP} = 512 is the number of ion-pairs used in the liquid simulation, and U_g and U_g are the total energies per ion-pair as computed directly from the MD simulations. With these corrected molar internal energies U'_g and U'_l, we compute the heat of vaporization Δ_vH using Eq. (3) for a temperature of T = 303 K shown in Fig. 14 and given in Table VI.

Both the data computed from the KPL and from the NGOLP force field as a function of alkyl chain-length are rather close to the experimental data of Verevkin *et al.*[47] However, we would like to point out that the optimized NGOLP force field is in even better agreement with the QCM experiments, particularly for chain-lengths up to n = 4. Not only are the data for n = 2 now in quantitative agreement with the experimental data but also the step from n = 1 to n = 2 is better captured by the new model, suggesting a significant influence of the enhanced conformational diversity of the $[NTf_2]$ anion.[56] Since the exact slope of Δ_vH as a function of the alkyl chain-length has been shown to be controlled by the counterbalance of electrostatic and van der Waals forces,[57] the increasing deviation for longer chain-length might indicate a slight misrepresentation of the size of the dispersion interaction introduced by increasing the alkyl chain-length.

Viscosities and reorientational correlation times

To further compare dynamical properties of the simulated ionic liquids with experimental data, the temperature dependence of the reorientational correlation times for the C(2)–H vector and viscosities for $[C_2MIm][NTf_2]$ were

TABLE V. MD simulated self-diffusion coefficients of the $[NTf_2]$ anion D_- as a function of the alkyl chain-length n in $[C_nMIm][NTf_2]$ for the KPL and the new NGOLP force field as well as the experimental values by Tokuda *et al.*[39] at T = 303 K. See also Fig. 13.

	$D_-/10^{-11}$ (m^{2}s^{-1})		
n	KPL	NGOLP	Expt.
1	5.21	3.87	3.24
2	4.76	3.56	3.63
4	3.22	2.42	2.75
6	1.83	1.26	1.93
8	1.00	0.67	1.45

TABLE VI. MD simulated vaporization enthalpies of the $[NTf_2]$ anion Δ_vH as a function of the alkyl chain-length n in $[C_nMIm][NTf_2]$ for the KPL and the new NGOLP force field as well as the experimental values by Verevkin *et al.*[47] at T = 303 K. See also Fig. 14.

	Δ_vH (kJ mol^{-1})		
n	KPL	NGOLP	Expt.
1	129.2	127.5	128.2
2	130.2	127.0	126.9
4	136.1	133.6	132.4
6	145.1	143.1	140.1
8	156.1	154.5	145.7

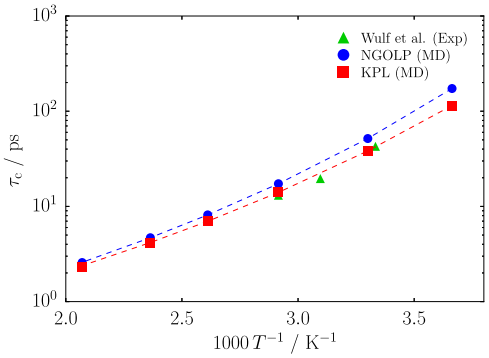

FIG. 15. Reorientational correlation time of the C(2)–H vector in $[C_2MIm][NTf_2]$ as a function of temperature. The experimental data of Wulf *et al.*[58] are shown as green triangles, the KPL-data are shown as red squares, and the NGOLP-data are shown as blue dots. The data are summarized in Table VII.

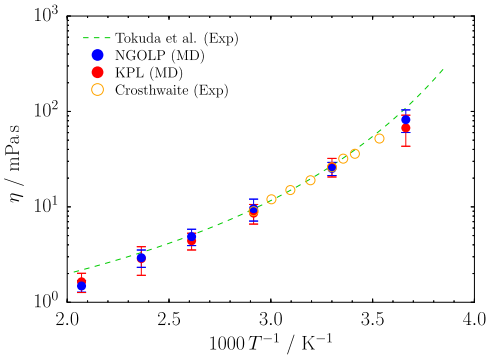

FIG. 16. Viscosities as a function of temperature for $[C_2MIm][NTf_2]$ for NGOLP (blue dots) and KPL (red squares). The experimental data were taken from the work of Tokuda *et al.* (green dashed line).[39] See also Table VII.

calculated. To compare with the quadrupolar relaxation experiments of Wulf *et al.*,[58] we computed reorientational correlation functions $R(t)$ of the C(2)–H bond-vector according to

$$R(t) = \langle P_2\{\cos[\theta_{CH}(t)]\}\rangle\,, \tag{7}$$

where P_2 is the second Legendre polynomial and

$$\cos[\theta_{CH}(t)] = \frac{\vec{r}_{CH}(0)\cdot\vec{r}_{CH}(t)}{|\vec{r}_{CH}|^2} \tag{8}$$

represents the angle-cosine between the CH-bond vector at times "0" and t and $|\vec{r}_{CH}|$ is the CH-bond length, which is kept fixed during the simulation. The reorientational correlation times τ_c are obtained as integral over the correlation function

$$\tau_c = \int_0^\infty R(t)\,dt\,. \tag{9}$$

Here, the long-time behavior is fitted to a stretched exponential function and the total correlation time is determined by numerical integration. Again we find that both force fields are in good agreement with the experimental values, albeit with the original KPL model being slightly closer to the experimental data (see Fig. 15 and Table VII).

To determine the viscosities, we used the approach of Zhang *et al.*[59] to compute viscosities from equilibrium-fluctuations of the off-diagonal elements of the pressure tensor via the Green-Kubo relation

TABLE VII. Viscosities η and reorientational correlation times of the C(2)–H vector τ_c as a function of temperature calculated from MD simulations of $[C_2MIm][NTf_2]$ employing the KPL and the NGOLP force fields. See also Figs. 15 and 16.

	η (mPa s)		τ_c (ps)	
T/K	KPL	NGOLP	KPL	NGOLP
273	67 ± 24	82 ± 22	173.1	114.7
303	26 ± 6	25 ± 4	51.6	38.2
343	8.6 ± 2.0	9.6 ± 2.4	17.3	14.1
383	4.4 ± 0.9	4.9 ± 0.9	8.1	7.0
423	2.9 ± 1.0	2.9 ± 0.6	4.7	4.1
483	1.6 ± 0.3	1.48 ± 0.21	2.6	2.3

$$\eta = \frac{V}{k_B T}\int_0^\infty \left\langle P_{\alpha\beta}(0)\cdot P_{\alpha\beta}(t)\right\rangle dt. \tag{10}$$

For each temperature, we performed 15 independent *NVT* simulations, where the starting configurations were sampled from the earlier *NpT* simulations with a constant time interval of 2 ns. After a 1 ns equilibration, we computed 8 ns long production runs for each of the sampled configurations storing the pressure tensor data for each time step. Finally, the correlation function was calculated and integrated over a time-window of 1 ns for each of the 15 simulations. The average of the running integrals was calculated as well as standard deviation. The average over the running integrals as well as the standard deviation were handled as suggested by Zhang *et al.*[59] with a fitting cutoff t_{cut} at the point where $\sigma(t)$ is 40% of the calculated average viscosity.

We find that the differences between the KPL and NGOLP models to be rather small. Both are basically lying within the statistical errors of this method. However, both force field models yield viscosities very close to the experiment (Fig. 16 and Table VII).

CONCLUSIONS

We showed that the reparametrization of the dihedral potentials as well as charges of the $[NTf_2]$ anion leads to an improvement of the force field model of Köddermann *et al.* for imidazolium-based ionic liquids from 2007. The most prominent advantage of the new parameter set is that the minimum energy conformations (*trans* and *gauche*) of the anion, as demonstrated from *ab initio* calculations and Raman experiments, are now well reproduced.

The results obtained for $[C_nMIm][NTf_2]$ show that this correction leads to a slightly better agreement between experiment and molecular dynamics simulation for a variety of properties, such as densities, diffusion coefficients, vaporization enthalpies, reorientational correlation times, and viscosities. Even though we focused on optimizing the anion parameters, the alkyl chain-length dependence is found to be generally also closer to the experiment.

With this work, we want to point out that it is important to re-examine the established force field and, if necessary, to improve them. We highly recommend to use the new NGOLP force field for the $[NTf_2]$ anion instead of the original KPL force field. Especially for simulation aiming to

describe the thermodynamics, dynamics, and also structure of imidazolium-based ionic liquids.

ACKNOWLEDGMENTS

B.G. is thankful for financial support provided by COST Action CM 1206 (EXIL—Exchange on Ionic Liquids).

[1]J. N. C. Lopes, J. Deschamps, and A. A. H. Pádua, J. Phys. Chem. B **108**, 2038 (2004).
[2]J. N. C. Lopes and A. A. H. Pádua, J. Phys. Chem. B **108**, 16893 (2004).
[3]J. N. A. C. Lopes and A. A. H. Pádua, J. Phys. Chem. B **110**, 7485 (2006).
[4]J. N. A. C. Lopes and A. A. H. Pádua, J. Phys. Chem. B **110**, 19586 (2006).
[5]J. N. A. C. Lopes, A. A. H. Pádua, and K. Shimizu, J. Phys. Chem. B **112**, 5039 (2008).
[6]J. N. A. C. Lopes, K. Shimizu, A. A. H. Pádua, Y. Umebayashi, S. Fukuda, K. Fujii, and S. I. Ishiguro, J. Phys. Chem. B **112**, 1465 (2008).
[7]J. N. A. C. Lopes, K. Shimizu, A. A. H. Pádua, Y. Umebayashi, S. Fukuda, K. Fujii, and S. i. Ishiguro, J. Phys. Chem. B **112**, 9449 (2008).
[8]T. Köddermann, K. Fumino, R. Ludwig, J. N. A. C. Lopes, and A. A. H. Pádua, ChemPhysChem **10**, 1181 (2009).
[9]K. Shimizu, D. Almantariotis, M. F. C. Gomes, A. A. H. Pádua, and J. N. A. C. Lopes, J. Phys. Chem. B **114**, 3592 (2010).
[10]J. N. A. C. Lopes and A. A. H. Pádua, Theor. Chem. Acc. **131**, 1129 (2012).
[11]B. Guillot, J. Mol. Liq. **101**, 219 (2002).
[12]P. T. Kiss and A. Baranyai, J. Chem. Phys. **137**, 084506 (2012).
[13]J. F. Ouyang and R. P. Bettens, CHIMIA Int. J. Chem. **69**, 104 (2015).
[14]I. Shvab and R. J. Sadus, Fluid Phase Equilib. **407**, 7 (2015).
[15]G. A. Cisneros, K. T. Wikfeldt, L. Ojamäe, J. Lu, X. Xu, H. Torabifard, A. P. Bartok, G. Csanyi, V. Molinero, and F. Paesani, Chem. Rev. **116**, 7501 (2016).
[16]T. Köddermann, D. Paschek, and R. Ludwig, ChemPhysChem **8**, 2464 (2007).
[17]D. Kerlé, R. Ludwig, A. Geiger, and D. Paschek, J. Phys. Chem. B **113**, 12727 (2009).
[18]D. Kerlé, M. N. Jorabchi, R. Ludwig, S. Wohlrab, and D. Paschek, Phys. Chem. Chem. Phys. **19**, 1770 (2017).
[19]R. P. Daly, J. C. Araque, and C. J. Margulis, J. Chem. Phys. **147**, 061102 (2017).
[20]R. Lynden-Bell and A. J. Stone, J. Chem. Sci. **129**, 883 (2017).
[21]M. M. Kazemi, M. Namboodiri, P. Donfack, A. Materny, D. Kerle, B. Rathke, and J. Kiefer, Phys. Chem. Chem. Phys. **19**, 15988 (2017).
[22]K. Fujii, T. Fujimori, T. Takamuku, R. Kanzaki, Y. Umebayashi, and S. i. Ishiguro, J. Phys. Chem. B **110**, 8179 (2006).
[23]M. J. Frisch, G. W. Trucks, H. B. Schlegel, G. E. Scuseria, M. A. Robb, J. R. Cheeseman, G. Scalmani, V. Barone, B. Mennucci, G. A. Petersson *et al.*, GAUSSIAN 09, Revision D.01, Gaussian, Inc., 2013.
[24]U. C. Singh and P. A. Kollman, J. Comput. Chem. **5**, 129 (1984).
[25]E. Lindahl, B. Hess, and D. van der Spoel, J. Mol. Model. **7**, 306 (2001).
[26]H. J. C. Berendsen, D. van der Spoel, and R. van Drunen, Comput. Phys. Commun. **91**, 43 (1995).
[27]B. Hess, C. Kutzer, D. van der Spoel, and E. Lindahl, J. Chem. Theory Comput. **4**, 435 (2008).
[28]S. Pronk, S. Pall, R. Schulz, P. Larsson, P. Bjelkmar, R. Apostolov, M. R. Shirts, J. C. Smith, P. M. Kasson, D. van der Spoel *et al.*, Bioinformatics **29**, 845 (2013).
[29]M. Abraham, B. Hess, D. van der Spoel, E. Lindahl, E. Apol, R. Apostolov, H. J. C. Berendsen, A. van Buuren, P. Bjelkmar, R. van Drunen *et al.*, GROMACS 5.0.6, 2015.
[30]U. Essmann, L. Perera, M. L. Berkowitz, T. A. Darden, H. Lee, and L. G. Pedersen, J. Chem. Phys. **103**, 8577 (1995).
[31]B. Hess, H. Bekker, H. J. C. Berendsen, and J. G. E. M. Fraaije, J. Comput. Chem. **18**, 1463 (1997).
[32]H. J. C. Berendsen, J. P. M. Postma, W. F. van Gunsteren, A. DiNola, and J. R. Haak, J. Chem. Phys. **81**, 3684 (1984).
[33]S. Nosé, Mol. Phys. **52**, 255 (1984).
[34]W. G. Hoover, Phys. Rev. A **31**, 1695 (1985).
[35]M. Parrinello and A. Rahman, J. Appl. Phys. **52**, 7182 (1981).
[36]S. Nosé and M. L. Klein, Mol. Phys. **50**, 1055 (1983).
[37]K. Fumino, A. Wulf, and R. Ludwig, Angew. Chem., Int. Ed. **47**, 8731 (2008).
[38]A. Wulf, K. Fumino, and R. Ludwig, Angew. Chem., Int. Ed. **49**, 449 (2010).
[39]H. Tokuda, K. Hayamizu, K. Ishii, M. A. B. H. Susan, and M. Watanabe, J. Phys. Chem. B **109**, 6103 (2005).
[40]D. H. Zaitsau, G. J. Kabo, A. A. Strechan, Y. U. Paulechka, A. Tschersich, S. P. Verevkin, and A. Heintz, J. Phys. Chem. A **110**, 7303 (2006).
[41]J. P. Armstrong, C. Hurst, R. G. Jones, P. Licence, K. R. J. Lovelock, C. J. Satterley, and I. J. Villar-Garcia, Phys. Chem. Chem. Phys. **9**, 982 (2007).
[42]V. N. Emel'yanenko, S. P. Verevkin, and A. Heintz, J. Am. Chem. Soc. **129**, 3930 (2007).
[43]L. M. N. B. F. Santos, J. N. C. Lopes, J. A. P. Coutinho, J. M. S. S. Esperanca, L. R. Gomes, I. M. Marrucho, and L. P. N. Rebelo, J. Am. Chem. Soc. **129**, 284 (2007).
[44]H. Luo, G. A. Baker, and S. Dai, J. Phys. Chem. B **112**, 10077 (2008).
[45]F. Heym, B. J. M. Etzold, C. Kern, and A. Jess, Green Chem. **13**, 1453 (2011).
[46]M. A. A. Rocha, C. F. R. A. Lima, L. R. Gomes, B. Schröder, J. A. P. Coutinho, I. M. Marrucho, J. M. S. S. Esperanca, L. P. N. Rebelo, K. Shimizu, J. N. C. Lopes *et al.*, J. Phys. Chem. B **115**, 10919 (2011).
[47]S. P. Verevkin, D. H. Zaitsau, V. N. Emel'yanenko, A. V. Yermalayeu, C. Schick, H. Liu, E. J. Maginn, S. Bulut, I. Krossing, and R. Kalb, J. Phys. Chem. B **117**, 6473 (2013).
[48]B. Schröder and J. A. P. Coutinho, Fluid Phase Equilib. **370**, 24 (2014).
[49]D. H. Zaitsau, V. Emel'yanenko, P. Stange, C. Schick, S. P. Verevkin, and R. Luwdig, Angew. Chem., Int. Ed. **55**, 11682 (2016).
[50]S. P. Verevkin, D. H. Zaitsau, V. N. Emel'yanenko, and A. Heintz, J. Phys. Chem. B **115**, 12889 (2011).
[51]D. H. Zaitsau, K. Fumino, V. N. Emel'yanenko, A. V. Yermalayeu, R. Ludwig, and S. P. Verevkin, ChemPhysChem **13**, 1868 (2012).
[52]S. P. Verevkin, R. V. Ralys, D. H. Zaitsau, V. N. Emel'yanenko, and C. Schick, Thermochim. Acta **538**, 55 (2012).
[53]M. Ahrenberg, M. Brinckmann, J. W. P. Schmelzer, M. Beck, C. Schmidt, O. Keßler, U. Kragl, S. P. Verevkin, and C. Schick, Phys. Chem. Chem. Phys. **16**, 2971 (2014).
[54]S. P. Verevkin, D. H. Zaitsau, V. N. Emel'yanenko, C. Schick, S. Jayaraman, and E. J. Maginn, Chem. Commun. **48**, 6915 (2012).
[55]V. N. Emel'yanenko, G. Boeck, S. P. Verevkin, and R. Ludwig, Chem. - Eur. J. **20**, 11640 (2014).
[56]K. Fumino, A. Wulf, S. Verevkin, A. Heintz, and R. Ludwig, ChemPhysChem **11**, 1623 (2010).
[57]T. Köddermann, D. Paschek, and R. Ludwig, ChemPhysChem **9**, 549 (2008).
[58]A. Wulf, R. Ludwig, P. Sasisanker, and H. Weingärtner, Chem. Phys. Lett. **439**, 323 (2007).
[59]Y. Zhang, A. Otani, and E. J. Maginn, J. Chem. Theory Comput. **11**, 3537 (2015).

II. The Double-Faced Nature of Hydrogen Bonding in Hydroxy-Functionalized Ionic Liquids Shown by Neutron Diffraction and Molecular Dynamics Simulations

T. Niemann, J. Neumann, P. Stange, S. Gärtner, T. G. A. Youngs, D. Paschek, G. G. Warr, R. Atkin, R. Ludwig, *Angew. Chem. Int. Ed.* **2019**, *58*, 12887.
DOI: 10.1002/anie.201904712

Contribution:
For this work, all MD simulations were performed and analyzed by me. I developed the force field used in the MD simulations and aided T. Niemann in evaluating the EPSR data to characterize the HBs from the ND experiments. I helped to finalize the text of the manuscript and took part in its revision. My contribution to the work amounts to approximately 20 %.

Ionic Liquids

International Edition: DOI: 10.1002/anie.201904712
German Edition: DOI: 10.1002/ange.201904712

The Double-Faced Nature of Hydrogen Bonding in Hydroxy-Functionalized Ionic Liquids Shown by Neutron Diffraction and Molecular Dynamics Simulations

*Thomas Niemann, Jan Neumann, Peter Stange, Sabrina Gärtner, Tristan G. A. Youngs, Dietmar Paschek, Gregory G. Warr, Rob Atkin, and Ralf Ludwig**

Abstract: *We characterize the double-faced nature of hydrogen bonding in hydroxy-functionalized ionic liquids by means of neutron diffraction with isotopic substitution (NDIS), molecular dynamics (MD) simulations, and quantum chemical calculations. NDIS data are fit using the empirical potential structure refinement technique (EPSR) to elucidate the nearest neighbor H···O and O···O pair distribution functions for hydrogen bonds between ions of opposite charge and the same charge. Despite the presence of repulsive Coulomb forces, the cation–cation interaction is stronger than the cation–anion interaction. We compare the hydrogen-bond geometries of both "doubly charged hydrogen bonds" with those reported for molecular liquids, such as water and alcohols. In combination, the NDIS measurements and MD simulations reveal the subtle balance between the two types of hydrogen bonds: The small transition enthalpy suggests that the elusive like-charge attraction is almost competitive with conventional ion-pair formation.*

Since the early days of Huggins, Latimer, and Rodebush, understanding hydrogen bonding in liquids and solutions has attracted much interest.[1–9] Hydrogen bonds are local and directional with interaction strengths ranging from weak to strong. They compete with other intermolecular forces, such as Coulomb and dispersion interactions. Hydrogen bonds are key to many aspects of liquid chemistry, including dynamics, solvation, and macroscopic properties.[6–9] In contrast to molecular liquids, ionic liquids (ILs) are composed entirely of ions, and it is expected that the cation–anion interactions dominate the structural, dynamic, and macroscopic properties of this particular class of liquids.[10–12] However, hydrogen bonding and dispersion forces have to be taken into account to understand how the delicate balance between the different types of interactions influence the IL properties.[13–22] In hydroxy-functionalized ILs, as investigated here, the situation may become even more complex. In this type of IL, hydrogen bonding has a double-faced nature. Two distinct types of hydrogen bonding coexist: The conventional hydrogen bonds between the cations and anions (c–a) are enhanced by attractive Coulomb interactions, whereas the elusive hydrogen bonds between like-charged ions (c–c) are presumed to be much weaker as a result of the repulsive Coulomb force.[23–28] Despite this expectation, however, structural motifs involving hydrogen-bonded cationic clusters were recently observed in the bulk liquid and the gas phase.[29–35] Vibrational spectroscopy clearly identified two distinct vibrational bands that were assigned to (c–a) and (c–c) hydrogen-bonded species (see Scheme 1). The magnitudes of the observed red shifts indicated that the (c–c) hydrogen bonds are evidently stronger than the (c–a) hydrogen bonds.[33–35] However, bulk infrared (IR) spectroscopy has some shortcomings. As a consequence of the different transition dipole moments for every single hydrogen bond, the vibrational bands are broad and unspecific, and the observed red-shifts cannot be simply related to the cluster sizes and the cluster distributions. Neutron diffraction can be used to determine liquid structure at very high resolution, and H/D isotopic substitution renders it particularly sensitive to the positions of hydrogen atoms, thereby allowing the location of hydrogen atoms participating in hydrogen bonds to be unambiguously determined.

[*] M. Sc. T. Niemann, P. Stange, Prof. Dr. R. Ludwig
Universität Rostock, Institut für Chemie
Abteilung für Physikalische Chemie
Dr.-Lorenz-Weg 2, 18059, Rostock (Germany)
E-mail: ralf.ludwig@uni-rostock.de

M. Sc. J. Neumann, Dr. D. Paschek
Universität Rostock, Institut für Chemie
Abteilung für Physikalische Chemie
Albert-Einstein-Strasse 21, 18059, Rostock (Germany)

Dr. S. Gärtner, Dr. T. G. A. Youngs
ISIS Faculty, STFC, Rutherford Appleton Laboratory
Didcot OX11 0QX (UK)

Prof. G. G. Warr
School of Chemistry and Sydney Nano
The University of Sydney
NSW 2006 (Australia)

Prof. R. Atkin
School of Molecular Sciences
The University of Western Australia, Perth
Western Australia 6009 (Australia)

Prof. Dr. R. Ludwig
Department LL&M, University of Rostock
Albert-Einstein-Strasse 25, 18059, Rostock (Germany),
and
Leibniz-Institut für Katalyse an der Universität Rostock e.V.
Albert-Einstein-Strasse 29a, 18059 Rostock (Germany)

Supporting information and the ORCID identification numbers for some of the authors of this article can be found under: https://doi.org/10.1002/anie.201904712.

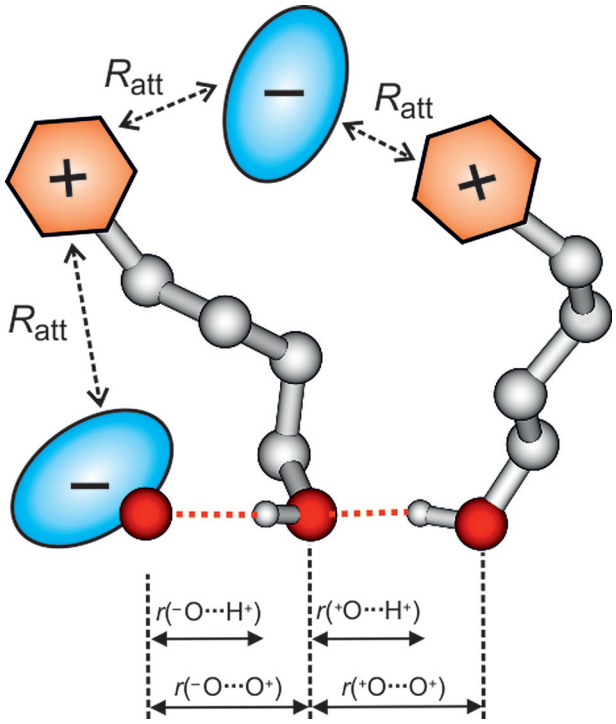

Scheme 1. Hydrogen-bonded dimer of the hydroxy-functionalized ionic liquid [OHC_4Py][NTf_2] showing both types of possible hydrogen bonding: (c–a) between cation and anion, and (c–c) between two cations. We obtained both hydrogen-bond geometries from ND experiments and MD simulations. The aliphatic and aromatic H atoms of OHC_4Py^+ are omitted for clarity.

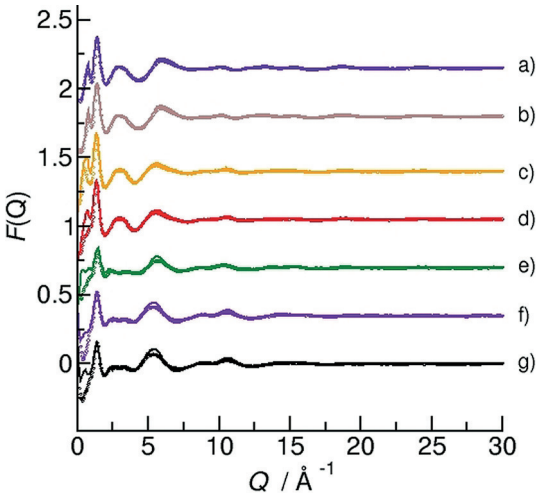

Figure 1. Measured neutron diffraction $F(Q)$ (colored circles) and fitted EPSR $F(Q)$ (solid lines) for seven deuteration schemes: a) [OHC_4Py]NTf_2], b) [OHC_4Py-d_1]NTf_2], c) [OHC_4Py d_6]NTf_2], d) [OHC_4Py-d_8]NTf_2], e) [OHC_4Py-d_9]NTf_2], f) [OHC_4Py-d_{13}]NTf_2], and g) [OHC_4Py-d_{14}]NTf_2]. The data are offset for clarity (see also the Supporting Information).

To that end we have examined the bulk structure of 1-(4-hydroxybutyl)pyridinium bis(trifluoromethylsulfonyl)imide [HOC_4Py][NTf_2] using neutron diffraction with isotopic substitution (NDIS), a well-established technique for probing inter- and intramolecular interactions in ionic and molecular liquids.[36–40] Neutron diffraction spectra were refined using the empirical potential structure refinement (EPSR) to extract atomic and molecular-level structure information.[36–40] The IL [HOC_4Py][NTf_2] was chosen to maximize the opportunity for like-charge hydrogen bonding: $[NTf_2]^-$ is a weakly interacting anion, whereas $[OHC_4Py]^+$ is a highly polarizable cation. In addition, the hydroxybutyl group of the cation allows for ample separation between the positively charged pyridinium ring and the hydroxy group. Strong spectroscopic evidence for hydrogen bonding between the cations (c–c) has been found with this cation/anion combination.[29–35]

It is the aim of this study to characterize the (c–a) (^+O–H···O^-) and the (c–c) (^+O–H···O^+) hydrogen bonds in this hydroxy-functionalized ionic liquid (IL) by means of neutron diffraction, molecular dynamics (MD) simulations, and quantum chemical calculations. A similar approach combining X-ray scattering and MD simulations has been successfully applied to analyze the structure of ILs and organic phases.[41,42] The measured hydrogen-bond lengths for the two types of ionic interactions, which describe the attraction between ions of opposite and repulsion between ions of like charge, are compared to those of molecular liquids, such as water and alcohols.[23–28] In addition, we carefully address the different types of (c–a) and (c–c) clusters and their distributions in the bulk liquid. The accompanying MD simulations support the concept of the double-faced nature of hydrogen bonding in this particular class of liquids.

Figure 1 shows the neutron diffraction (NDIS) data along with the EPSR-derived differential scattering cross sections $F(Q)$ (solid black lines) for momentum transfers (Q) from 0.1 to 50 $Å^{-1}$. Seven chemically identical, but isotopically different IL samples were synthesized: the fully hydrogenous [HOC_4Py][NTf_2] and the fully deuterated [HOC_4Py-d_{14}]-[NTf_2] along with the compounds partially deuterated at the hydroxy group [HOC_4Py-d_1][NTf_2], at the pyridinium ring and the hydroxy group [HOC_4Py-d_6][NTf_2], at the butyl chain [HOC_4Py-d_8][NTf_2], at the butyl chain and the hydroxy group [HOC_4Py-d_9][NTf_2], and at the pyridinium ring and the butyl chain [HOC_4Py-d_{13}][NTf_2]. Details regarding the synthesis of the different compounds for the neutron diffraction experiments are provided in the Supporting Information. Since hydrogen and deuterium have different neutron scattering lengths, isotopic substitution enables contrast between different molecular regions of interest in a neutron diffraction experiment.

The EPSR analysis of the total structure factors $F(Q)$ yields the partial structure factors $S(Q)$, which are the Fourier transforms of the partial pair distribution functions $g(r)$ for atom–atom pairs as a function of their radial separation, normalized to the bulk density (see the Supporting Information). Here, we solely focus on the intermolecular hydrogen–oxygen (H···O) and associated oxygen–oxygen (O···O) pair distribution functions $g_{HO}(r)$ and $g_{OO}(r)$, which describe the nature of the hydrogen bonding in the IL. As a result of the large number of isotopically labeled compounds used, both pair distribution functions could be derived confidently for the (c–a)- and the (c–c)-bound species. The first peak in the $g(r)$ functions corresponds to the first coordination shell of

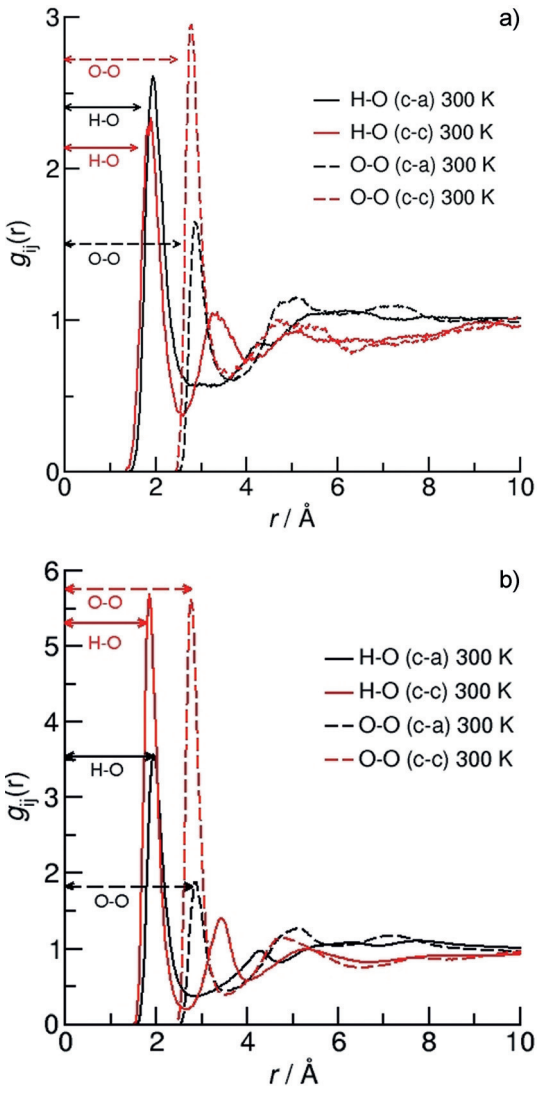

Figure 2. Pair distribution functions $g_{HO}(r)$ and $g_{OO}(r)$ for the (c–a) and (c–c) hydrogen bonds in the IL $[OHC_4Py]NTf_2$ from a) neutron diffraction with H/D substitution and b) molecular dynamics simulations. The nearest neighbor distances are indicated by the arrows.

the nearest neighbors. Figure 2a shows the $g_{HO}(r)$ and $g_{OO}(r)$ functions for the (c–a)- and (c–c)-bound species. The maxima of the first nearest neighbor peaks in the two functions give the average hydrogen-bond lengths $r(^{+}H\cdots O^{-})$ and $r(^{+}O\cdots O^{-})$ for the (c–a) as well as $r(^{+}H\cdots O+)$ and $r(^{+}O\cdots O+)$ for the (c–c) binding motifs, respectively. The (c–c) hydrogen bonds are noticeably shorter (1.87 Å and 2.78 Å) than the (c–a) hydrogen bonds (1.95 Å and 2.88 Å), which indicates stronger attraction between ions of like charge (c–c) than between ions of opposite charge (c–a). Both (c–a) and (c–c) hydrogen bonds prefer a linear configuration, as demonstrated in 2D distance/angle probability density plots derived from EPSR data, as shown in Figures S2 and S3 in the Supporting Information. Moreover, in addition to being shorter, the (c–c) hydrogen bonds are also "more linear" than the (c–a) hydrogen bonds, as revealed by a narrower distribution of the O–H···O hydrogen-bond angles (see Figure S5). This observation is quite remarkable because the total interaction in the (c–a)-bound species results from hydrogen bonding plus attractive Coulomb forces between the oppositely charged ions. It is evident that the (c–a) interaction is only weakly strengthened by Coulomb attraction, whereas the (c–c) interaction is strongly enhanced by potentially cooperative hydrogen bonding. Despite the Coulomb repulsion, the hydrogen bond is shorter for the (c–c) than for the (c–a) species.[40] The shortening of the H···O and O···O distances by about 8 pm and 10 pm, respectively, is substantial and comparable to the differences in the hydrogen-bond lengths in water and ice (see Table 1). This result is in accord with

Table 1: Hydrogen-bond distances r(O···O) and r(H···O) for the (c–a)- and (c–c)-bound species in the IL $[HOC_4Py][NTf_2]$. For comparison, the values known for water, methanol, and ethanol in the liquid (l) and solid (s) phases are given.[50–56]

	r(O···O)/Å	r(H···O)/Å
$[HOC_4Py]NTf_2$, NDIS	2.88 (c–a), 2.78 (c–c)	1.95 (c–a), 1.87 (c–c)
$[HOC_4Py][NTf_2]$, MD	2.87 (c–a), 2.77 (c–c)	1.94 (c–a), 1.85 (c–c)
water	2.80 [l][50] 2.759 [s][51] 2.76 [s][52] 2.825(2) [s][53]	1.880(2) [s][53]
methanol	2.798(6) [l][54] 2.792(3) [s][53]	1.804(4) [s][53]
ethanol	2.808(8) [l] 2.716(3) [s][55] 2.730(2) [s][56]	1.93(4) [s][55]

recent IR studies in the bulk and the gas phases, which show strongly red-shifted OH vibrational bands as a result of cooperative hydrogen bonding in the (c–c) cluster species.[29–35] However, the IR intensities of the (c–a) and (c–c) vibrational bands result from different transition dipole moments for each single hydrogen bond and does not allow determination of cluster sizes or distributions.

We complemented the NDIS measurements by MD simulations using independently derived molecular force fields (see the Supporting Information).[43–45] In Figure 2b we show that the $r(^{+}H\cdots O^{-})$, $r(^{+}O\cdots O^{-})$, $r(^{+}H\cdots O^{+})$, and $r(^{+}O\cdots O^{+})$ distances again show shorter hydrogen bonds for (c–c) than (c–a) and agree almost quantitatively with the geometries derived from the ND measurements. In addition, the O–H···O hydrogen bond angles obtained from the MD simulations behave similarly to the ND data (Figures S6–S9). Here the (c–c) hydrogen bonds are also found to be more linearly aligned than the (c–a) hydrogen bonds. Both simulated intermolecular O···O distances differ by only ±0.02 Å from the experimental geometries, thereby demonstrating the quality of the force field used in the MD simulations. The NDIS experiments and MD simulation agree in the pair distribution functions and allow (c–a)- and (c–c)-bound species to be clearly distinguished. The average $r(^{+}O\cdots O^{-})$ and $r(^{+}O\cdots O^{+})$ hydrogen-bond lengths of the (c–a) and (c–c) species in the liquid phase have also been compared to

geometries of (c–a) and (c–c) clusters calculated by density functional theory (DFT) including Grimme's D3 correction (see the Supporting Information).[46–49] These calculations show that, whereas the (c–a) bond distances remain almost constant at 2.90 Å as a function of cluster size, the distances of the (c–c) clusters decrease monotonically from 2.78 Å for the dimer to 2.75 Å for the cyclic tetramer as a result of cooperative effects. The average dimer and trimer values include the oxygen–oxygen distances derived for the liquid phase from ND experiments and MD simulations, which indicates that the present (c–c) cluster sizes range between two and three (see Figure 3a).

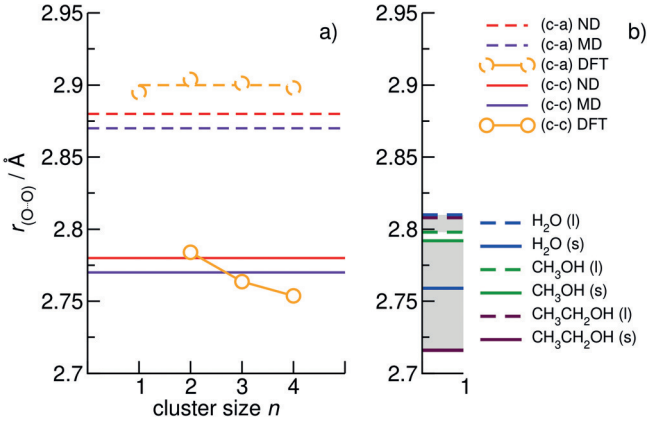

Figure 3. a) The oxygen–oxygen nearest neighbor distances $r_{(O\cdots O)}$ for the (c–a) (dotted lines) and (c–c) hydrogen bonds (straight lines) of $[OHC_4Py][NTf_2]$ from NDIS (red lines) and MD simulations (violet lines). Yellow circles: the B3LYP-D3/6-31+G* calculated geometries of the (c–a) and (c–c) clusters for $[OHC_4Py][NTf_2]$ versus cluster sizes *n*. b) The literature values for water, methanol, and ethanol for the liquid and solid phases.[50–56] The two gray shaded areas indicate the liquid (top) and the solid-state (bottom) values.

Finally, we compare the $r(^+O\cdots O^-)$ and $r(^+O\cdots O^+)$ distances of this ionic liquid with those of molecular liquids. The given reference values for the O···O distances of water, methanol, and ethanol in their liquid and solid phases were measured by a variety of X-ray and neutron scattering experiments.[50–56] As shown in Figure 3b, the (c–a) hydrogen-bond length of the IL is longer than the liquid-phase hydrogen-bond lengths of the molecular liquids, thus indicating weaker hydrogen bonds despite the attractive Coulomb interaction. In contrast, the (c–c) hydrogen-bond length of the IL lies between the liquid and solid-phase values of the hydrogen-bonded molecular liquids. Apparently, the polarizable counterion fully compensates for the positive charge of the pyridinium ring, and the hydroxy groups of the cations can form cooperative hydrogen bonds with each other nearly as well as in molecular liquids. This finding is consistent with recent reports of long-range electrostatic forces in ionic liquids, similar to those found for weak electrolytes, which occur because the vast majority of cations and anions neutralize one another.[57]

The NDIS experiments and MD simulations allow quantification of the populations of these local arrangements. In Figure 4, we show that at 300 K between 87% (NDIS) and

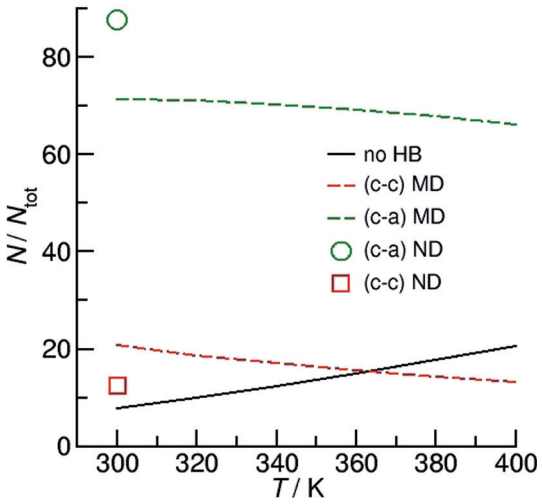

Figure 4. Analysis of (c–a) and (c–c) cluster populations in $[OHC_4Py][NTf_2]$ from MD simulations as a function of temperature. The symbols show the cluster distribution obtained from NDIS experiments at 303 K.

75% (MD) of the cations form (c–a) hydrogen bonds with the counterions, whereas between 13% (NDIS) and 20% (MD) of the cations are involved in (c–c) structural motifs. This agreement is excellent, given the possible uncertainties of the experiments and simulations (±0.02 Å). MD simulations were performed for temperatures between 300 and 400 K to reveal the temperature-dependence of the cluster populations. We observe that the (c–a) and (c–c) species decrease to the benefit of quasi-free OH groups as the temperature is increased. The decrease with temperature is more pronounced for the (c–c)- than for the (c–a)-bound species, probably for entropic reasons (formation of larger aggregates). From a van't Hoff plot of the ratio for the (c–c) and the (c–a) hydrogen-bonded species versus the inverse temperature obtained from MD simulations data we determine the transition enthalpy from (c–c) to (c–a) to be about 3.75 kJ mol^{-1}. Such a small transition enthalpy suggests that the (c–c)-bound species exist in equilibrium and that kinetic trapping is not a requirement for finding cationic clusters at room temperature.

In conclusion, pair distribution functions $g_{HO}(r)$ and $g_{OO}(r)$ for both (c–a) and (c–c) hydrogen bonding in a hydroxy-functionalized ionic liquid have been revealed by ND experiments, MD simulations, and quantum chemical calculations. Each individual approach clearly distinguished hydrogen bonding between ions of opposite (c–a) and ions of like charge (c–c). The average r_{HO} and r_{OO} hydrogen-bond lengths for the (c–c)-bound species are 8 pm and 10 pm shorter than those obtained for the (c–a)-bound species. Apparently, the (c–c) hydrogen bonds are significantly stronger, despite the presence of repulsive Coulomb forces between the cations. The agreement between the NDIS and the MD results are almost quantitative. We show by means of quantum chemical calculations that cooperative effects enhance the favorable (c–c) hydrogen bonds, as has been reported earlier for clusters of water and alcohol. Our study provides strong evidence for the presence of (c–c) hydrogen

bonding at room temperature. Kinetic trapping in the supercooled state is thus not a prerequisite for like-charge attraction through hydrogen bonding. This observation is supported by the small transition enthalpies derived from MD simulations.

Acknowledgements

R.L. thanks the Deutsche Forschungsgemeinschaft (DFG) under grant LU 506/14-1 for support of this work. T.N. thanks the "Deutscher Akademischer Austauschdienst" for supporting his research at the University of Western Australia, Perth. R.A. thanks the University of Western Australia for funding support. We gratefully acknowledge the Science and Technology Facilities Council (STFC) for access to neutron beamtime at the SANDALS instrument at the ISIS neutron and muon source, and also for the provision of sample preparation by the D-Lab. The data are available at the ISIS Neutron and Muon Source Data Journal under doi.org/10.5286/ISIS.E.RB1800066.

Conflict of interest

The authors declare no conflict of interest.

Keywords: hydrogen bonding · ionic liquids · like-charge attraction · molecular dynamics simulations · neutron diffraction

How to cite: *Angew. Chem. Int. Ed.* **2019**, *58*, 12887 – 12892
Angew. Chem. **2019**, *131*, 13019 – 13024

[1] M. L. Huggins, *Science* **1922**, *55*, 459 – 460.
[2] W. M. Latimer, W. H. Rodebush, *J. Am. Chem. Soc.* **1920**, *42*, 1419.
[3] M. L. Huggins, *Angew. Chem. Int. Ed. Engl.* **1971**, *10*, 147 – 152; *Angew. Chem.* **1971**, *83*, 163 – 168.
[4] L. Pauling, *The Nature of the Chemical Bond*, Cornell University Press, Ithaca, **1960**; G. A. Jeffrey, *An Introduction to Hydrogen Bonding*, Oxford University Press, New York, **1997**.
[5] G. Gilli, P. Gilli, *The Nature of the Hydrogen Bond: Outline of a Comprehensive Hydrogen Bond Theory*, Oxford University Press, Oxford, **2009**.
[6] G. R. Desiraju, T. Steiner, *The Weak Hydrogen Bond: In Structural Chemistry and Biology*, Oxford University Press, Oxford, **2001**.
[7] Y. Marechal, *The Hydrogen Bond and the Water Molecule*, Elsevier, Amsterdam, **2007**.
[8] G. A. Jeffrey, *An Introduction to Hydrogen Bonding*, Oxford University Press, New York, **1997**.
[9] A. C. Legon, *Chem. Soc. Rev.* **1993**, *22*, 153.
[10] K. Fumino, S. Reimann, R. Ludwig, *Phys. Chem. Chem. Phys.* **2014**, *16*, 21903 – 21929.
[11] P. A. Hunt, C. R. Ashworth, R. P. Matthews, *Chem. Soc. Rev.* **2015**, *44*, 1257 – 1288.
[12] C. R. Ashworth, R. P. Matthews, T. Welton, P. A. Hunt, *Phys. Chem. Chem. Phys.* **2016**, *18*, 18145 – 18160.
[13] T. L. Greaves, C. J. Drummond, *Chem. Rev.* **2008**, *108*, 206.
[14] R. Hayes, G. G. Warr, R. Atkin, *Phys. Chem. Chem. Phys.* **2010**, *12*, 1709.
[15] M. Yoshizawa, W. Xu, C. A. Angell, *J. Am. Chem. Soc.* **2003**, *125*, 15411.
[16] K. Fumino, A. Wulf, R. Ludwig, *Angew. Chem. Int. Ed.* **2009**, *48*, 3184; *Angew. Chem.* **2009**, *121*, 3230.
[17] K. Fumino, A. Wulf, R. Ludwig, *Phys. Chem. Chem. Phys.* **2009**, *11*, 8790.
[18] C. Roth, T. Peppel, K. Fumino, M. Köckerling, R. Ludwig, *Angew. Chem. Int. Ed.* **2010**, *49*, 10221; *Angew. Chem.* **2010**, *122*, 10419.
[19] K. Fumino, E. Reichert, K. Wittler, R. Hempelmann, R. Ludwig, *Angew. Chem. Int. Ed.* **2012**, *51*, 6236; *Angew. Chem.* **2012**, *124*, 6340.
[20] R. Hayes, N. Borisenko, B. Corr, G. B. Webber, F. Endres, R. Atkin, *Chem. Commun.* **2012**, *48*, 10246.
[21] R. Hayes, S. Imberti, G. G. Warr, R. Atkin, *Angew. Chem. Int. Ed.* **2013**, *52*, 4623 – 4627; *Angew. Chem.* **2013**, *125*, 4721 – 4725.
[22] R. Hayes, G. G. Warr, R. Atkin, *Chem. Rev.* **2015**, *115*, 6357 – 6426.
[23] K. M. Murdoch, T. D. Ferris, J. C. Wright, T. C. Farrar, *J. Chem. Phys.* **2002**, *116*, 5717.
[24] F. Huisken, A. Kulcke, C. Laush, J. Lisy, *J. Chem. Phys.* **1991**, *95*, 3924 – 3929.
[25] M. Huelsekopf, R. Ludwig, *J. Mol. Liq.* **2002**, *98 – 99*, 163 – 171.
[26] R. Ludwig, F. Weinhold, T. C. Farrar, *Mol. Phys.* **1999**, *97*, 465 – 477.
[27] R. Ludwig, *ChemPhysChem* **2000**, *1*, 53 – 56.
[28] R. Ludwig, *Phys. Chem. Chem. Phys.* **2002**, *4*, 5481 – 5487.
[29] A. Knorr, K. Fumino, A.-M. Bonsa, R. Ludwig, *Phys. Chem. Chem. Phys.* **2015**, *17*, 30978 – 30982.
[30] A. Knorr, R. Ludwig, *Sci. Rep.* **2015**, *5*, 17505.
[31] A. Knorr, P. Stange, K. Fumino, F. Weinhold, R. Ludwig, *ChemPhysChem* **2016**, *17*, 458 – 462.
[32] A. Strate, T. Niemann, P. Stange, D. Michalik, R. Ludwig, *Angew. Chem. Int. Ed.* **2017**, *56*, 496 – 500; *Angew. Chem.* **2017**, *129*, 510 – 514.
[33] T. Niemann, D. Zaitsau, A. Strate, A. Villinger, R. Ludwig, *Sci. Rep.* **2018**, *8*, 14753.
[34] F. S. Menges, H. J. Zeng, P. J. Kelleher, O. Gorlova, M. A. Johnson, T. Niemann, A. Strate, R. Ludwig, *J. Phys. Chem. Lett.* **2018**, *9*, 2979 – 2984.
[35] T. Niemann, A. Strate, R. Ludwig, F. Menges, H. Zeng, P. Kelleher, O. Gorlova, M. Johnson, *Angew. Chem. Int. Ed.* **2018**, *57*, 15364 – 15368; *Angew. Chem.* **2018**, *130*, 15590 – 15594.
[36] A. K. Soper, Empirical Potential Structure Refinement—A User's Guide, ISIS, Rutherford Appleton Labortory, Didcot, U.K., **2006**.
[37] A. K. Soper, *Phys. Rev. B* **2005**, *72*, 104204 – 104212.
[38] C. J. Benmore, A. K. Soper, *The SANDALS Manual: A Guide to Performing Experiments on the Small Angle Neutron Diffractometer for Amorphous and Liquid Samples at ISIS.*, Version 1.0, RAL Technical Reports, RAL-TR-1998-1006, 1998.
[39] A. K. Soper, W. S. Howells, A. C. Hannon, *ATLAS-Analysis of Time-of-Flight Diffraction Data from Liquid and Amorphous Samples*, RAL-89-046 1989.
[40] S. E. Norman, A. H. Turner, T. G. A. Youngs, *RSC Adv.* **2015**, *5*, 67220 – 67226.
[41] R. Kanzaki, T. Mitsugi, S. Fukuda, K. Fujii, M. Takeuchi, Y. Soejima, T. Takamuku, T. Yamaguchi, Y. Umebayashi, S. Ishiguro, *J. Mol. Liq.* **2009**, *147*, 77 – 82.
[42] G. Ferru, D. Gomes Rodrigues, L. Berthon, O. Diat, P. Baudin, P. Guilbaud, *Angew. Chem. Int. Ed.* **2014**, *53*, 5346 – 5350; *Angew. Chem.* **2014**, *126*, 5450 – 5454.
[43] J. Neumann, B. Golub, L.-M. Odebrecht, R. Ludwig, D. Paschek, *J. Chem. Phys.* **2018**, *148*, 193828.
[44] W. L. Jorgensen, D. S. Maxwell, J. Tirado-Rives, *J. Am. Chem. Soc.* **1996**, *118*, 11225 – 11236.

[45] W. L. Jorgensen, N. A. McDonald, *J. Mol. Struct. THEOCHEM* **1998**, *424*, 145 – 155.
[46] Gaussian 09, Revision A.02, M. J. Frisch, G. W. Trucks, H. B. Schlegel, G. E. Scuseria, M. A. Robb, J. R. Cheeseman, G. Scalmani, V. Barone, G. A. Petersson, H. Nakatsuji, X. Li, M. Caricato, A. Marenich, J. Bloino, B. G. Janesko, R. Gomperts, B. Mennucci, H. P. Hratchian, J. V. Ortiz, A. F. Izmaylov, J. L. Sonnenberg, D. Williams-Young, F. Ding, F. Lipparini, F. Egidi, J. Goings, B. Peng, A. Petrone, T. Henderson, D. Ranasinghe, V. G. Zakrzewski, J. Gao, N. Rega, G. Zheng, W. Liang, M. Hada, M. Ehara, K. Toyota, R. Fukuda, J. Hasegawa, M. Ishida, T. Nakajima, Y. Honda, O. Kitao, H. Nakai, T. Vreven, K. Throssell, J. A. Montgomery, Jr., J. E. Peralta, F. Ogliaro, M. Bearpark, J. J. Heyd, E. Brothers, K. N. Kudin, V. N. Staroverov, T. Keith, R. Kobayashi, J. Normand, K. Raghavachari, A. Rendell, J. C. Burant, S. S. Iyengar, J. Tomasi, M. Cossi, J. M. Millam, M. Klene, C. Adamo, R. Cammi, J. W. Ochterski, R. L. Martin, K. Morokuma, O. Farkas, J. B. Foresman, and D. J. Fox, Gaussian, Inc., Wallingford CT, 2016.
[47] S. Grimme, J. Antony, S. Ehrlich, H. Krieg, *J. Chem. Phys.* **2010**, *132*, 154104.
[48] S. Ehrlich, J. Moellmann, W. Reckien, T. Bredow, S. Grimme, *ChemPhysChem* **2011**, *12*, 3414 – 3420.
[49] S. Grimme, A. Jansen, *Chem. Rev.* **2016**, *116*, 5105 – 5154.
[50] L. B. Skinner, C. Huang, D. Schlesinger, L. G. M. Pettersson, A. Nilsson, C. J. Benmore, *J. Chem. Phys.* **2013**, *138*, 074506.
[51] F. Huisken, M. Kaloudis, A. Kulcke, D. Voelkel, *Infrared Phys. Technol.* **1995**, *36*, 171.
[52] U. Bergmann, A. Di Cicco, P. Wernet, E. Principi, P. Glatzel, A. Nilsson, *J. Chem. Phys.* **2007**, *127*, 174504.
[53] T. Steiner, *Angew. Chem. Int. Ed.* **2002**, *41*, 48 – 76; *Angew. Chem.* **2002**, *114*, 50 – 80.
[54] A. H. Narten, A. Habenschuss, *J. Chem. Phys.* **1984**, *80*, 3387 – 3391.
[55] S. Saker, R. N. Joarder, *J. Chem. Phys.* **1994**, *100*, 5118 – 5122.
[56] P.-G. Jönsson, *Acta Crystallogr. Sect. B* **1976**, *32*, 232 – 235.
[57] M. A. Gebbie, A. M. Smith, H. A. Dobbs, A. A. Lee, G. G. Warr, X. Banquy, M. Valtiner, M. W. Rutland, J. N. Israelachvili, S. Perkin, R. Atkin, *Chem. Commun.* **2017**, *53*, 1214 – 1224.

Manuscript received: April 16, 2019
Revised manuscript received: May 25, 2019
Accepted manuscript online: June 8, 2019
Version of record online: July 9, 2019

Angewandte Chemie
Eine Zeitschrift der Gesellschaft Deutscher Chemiker

Supporting Information

The Double-Faced Nature of Hydrogen Bonding in Hydroxy-Functionalized Ionic Liquids Shown by Neutron Diffraction and Molecular Dynamics Simulations

*Thomas Niemann, Jan Neumann, Peter Stange, Sabrina Gärtner, Tristan G. A. Young, Dietmar Paschek, Gregory G. Warr, Rob Atkin, and Ralf Ludwig**

anie_201904712_sm_miscellaneous_information.pdf

Author Contributions

S.G. Data curation: Equal; Formal analysis: Equal.

Contents

1. Synthesis of isotopically labelled ionic liquids [HOC$_4$Py][NTf$_2$]

Apart from the reactions in aqueous solutions all reactions were performed in a moisture guarded assembly and reflux condenser was used while heating. The used solvents were dried with molecular sieves to a water content less than 50 ppm and distilled freshly. Except for THF-d$_8$ and Pyrridin-d$_5$, which were purchased from DEUTERO, all starting materials used in the synthesis were purchased from SIGMA ALDRICH. All starting materials were dried by conventional methods for the use in moisture-free reactions.

4-Bromo-1-trimethylsiloxybutane-d$_x$ *

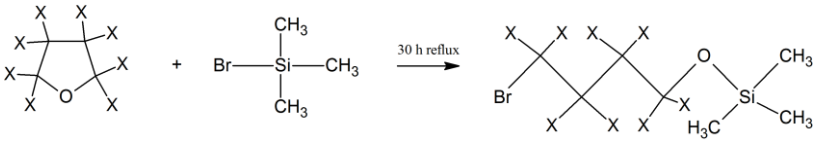

A mixture of equimolar amounts of dry tetrahydrofuran-d$_x$ and bromotrimethylsilane was refluxed for 30 h and the crude product was then isolated by distillation in vacuum (78 °C; 17 mbar). The product was obtained as a colorless liquid. Yield 80 %.
4-Bromo-1-trimethylsiloxybutane-d$_0$: ^{1}**H-NMR**(298.2 K, DMSO-d$_6$, 300.13 MHz, [ppm]): δ = 0.05 (s, 9H, −Si(C*H*$_3$)); 1.52 (tt, 2H, C*H*$_2$−CH$_2$−O−); 1.84 (tt, 2H, Br−CH$_2$−C*H*$_2$−); 3.41 (t, 2H, CH$_2$−C*H*$_2$−O−); 3.53 (t, 2H, Br−C*H*$_2$−CH$_2$−). ^{13}**C-NMR**(298 K, DMSO-d$_6$, 75.46 MHz, [ppm]): δ = 2.05 (s, −Si(*C*H$_3$); 29.24 (s, *C*H$_2$−CH$_2$−O−); 31.01 (s, Br−CH$_2$−*C*H$_2$−); 35.28 (s, Br−*C*H$_2$−CH$_2$−); 59.82 (s, CH$_2$−*C*H$_2$−O−).
4-Bromo-1-trimethylsiloxybutane-d$_8$: ^{1}**H-NMR**(298.2 K, DMSO-d$_6$, 300.13 MHz, [ppm]): δ = 0.05 (s, 9H, −Si(C*H*$_3$)). ^{13}**C-NMR**(298 K, DMSO-d$_6$, 75.46 MHz, [ppm]): δ = 2.05 (s, −Si(*C*H$_3$); 24.28 (quint, *C*D$_2$−CD$_2$−O−); 29.90 (quint, Br−CD$_2$−*C*D$_2$−); 33.34 (quint, Br−*C*D$_2$−CD$_2$−); 66.39 (quint, CD$_2$−*C*D$_2$−O−).

* H. R. Kricheldorf, G. Mörber, W. Regel, *Synthesis* **1981**, 5, 383

1-(4-Trimethylsiloxybutyl)-pyridinium-bromide-d$_{x+y}$

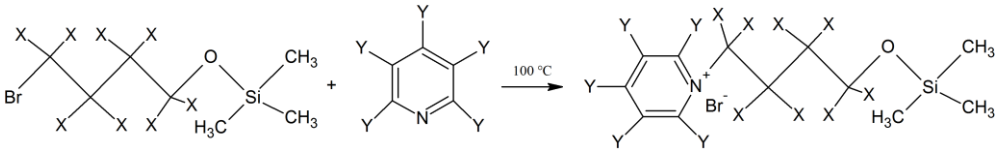

Equimolar amounts of pyridine-d$_y$ and 4-Bromo-1-trimethylsiloxybutane-d$_x$ were mixed at room temperature and heated slowly up to round about 100 °C - 110 °C. When the reaction begins, the solution starts to cloud. After a few minutes two phases are formed, the lower one is yellow and the upper one is colorless. After about 5 h only one yellow phase is obtained. All volatiles were removed in vacuum. The crude product was cooled to room temperature whereby it starts to crystallize. Yield 75 %.
1-(4-Trimethylsiloxybutyl)-pyridinium-bromide-d$_0$: ^{1}**H-NMR**(298.2 K, DMSO-d$_6$, 300.13 MHz, [ppm]): δ = 0.05 (s, 9H, −Si(C*H*$_3$)); 1.41 (tt, 2H, C*H*$_2$−CH$_2$−O−); 1.96 (tt, 2H, N−CH$_2$−C*H*$_2$−); 3.41 (t, 2H, CH$_2$−C*H*$_2$−O−); 4.68 (t, 2H, N−C*H*$_2$−CH$_2$−); 8.14-8.21 (m, 2H, *m*-C*H*); 8.60-8.67 (m, 1H, *p*-C*H*); 9.03-9.09 (m, 2H, *o*-C*H*). ^{13}**C-NMR**(298 K, DMSO-d$_6$, 75.46 MHz, [ppm]): δ = 2.05 (s, −Si(*C*H$_3$); 26.36 (s, *C*H$_2$−CH$_2$−O−); 27.34 (s,

N−CH_2−CH_2−); 58.96 (s, N−CH_2−CH_2−); 60.19 (s, CH_2−CH_2−O−); 127.67 (s, *m*-CH); 144.65 (s, *p*-CH); 145.46 (s, *o*-CH).
1-(4-Trimethylsiloxybutyl)-pyridinium-bromide-d_5: ^{1}**H-NMR**(298.2 K, DMSO-d_6, 300.13 MHz, [ppm]): δ = 0.05 (s, 9H, −Si(CH_3)); 1.41 (tt, 2H, CH_2−CH_2−O−); 1.96 (tt, 2H, N−CH_2−CH_2−); 3.41 (t, 2H, CH_2−CH_2−O−); 4.68 (t, 2H, N−CH_2−CH_2−). ^{13}**C-NMR**(298 K, DMSO-d_6, 75.46 MHz, [ppm]): δ = 2.05 (s, −Si(*C*H_3); 26.36 (s, *C*H_2−CH_2−O−); 27.34 (s, N−CH_2−*C*H_2−); 58.96 (s, N−*C*H_2−CH_2−); 60.19 (s, CH_2−*C*H_2−O−); 126.76-128.00 (m, *m*-*C*D); 143.53-145.57 (m, *p*-*C*D + *o*-*C*D).
1-(4-Trimethylsiloxybutyl)-pyridinium-bromide -d_8: ^{1}**H-NMR**(298.2 K, DMSO-d_6, 300.13 MHz, [ppm]): δ = 0.05 (s, 9H, −Si(CH_3)); 8.14-8.21 (m, 2H, *m*-C*H*); 8.60-8.67 (m, 1H, *p*-C*H*); 9.03-9.09 (m, 2H, *o*-C*H*). ^{13}**C-NMR**(298 K, DMSO-d_6, 75.46 MHz, [ppm]): δ = 2.05 (s, −Si(*C*H_3); 26.18-28.21 (m, *C*D_2−CD_2−O− + N−CD_2−*C*D_2−); 58.86-61.27 (m, CD_2−*C*D_2−O− + N−*C*D_2−CD_2−); 127.67 (s, *m*-*C*H); 144.65 (s, *p*-*C*H); 145.46 (s, *o*-*C*H).
1-(4-Trimethylsiloxybutyl)-pyridinium-bromide -d_{13}: ^{1}**H-NMR**(298.2 K, DMSO-d_6, 300.13 MHz, [ppm]): δ = 0.05 (s, 9H, −Si(CH_3)). ^{13}**C-NMR**(298 K, DMSO-d_6, 75.46 MHz, [ppm]): δ = 2.05 (s, −Si(*C*H_3); 26.18-28.21 (m, *C*D_2−CD_2−O− + N−CD_2−*C*D_2−); 58.86-61.27 (m, CD_2−*C*D_2−O− + N−*C*D_2−CD_2−); 126.76-128.00 (m, *m*-*C*D); 143.53-145.57 (m, *p*-*C*D + *o*-*C*D).

1-(4-Hydroxybutyl)-pyridinium-bromide-d_{x+y}

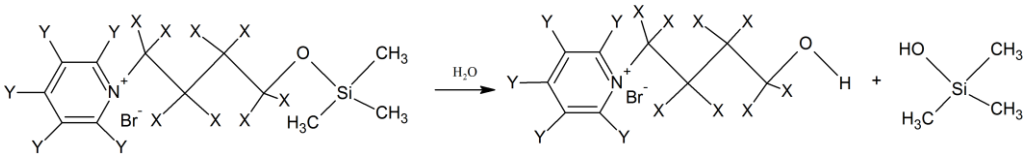

1-(4-Trimethylsiloxybutyl)-pyridinium-bromide-d_{x+y} was dissolved in a tenfold excess of H_2O. The solution was stirred for 4 h at 80 °C. Two phases were formed. All volatiles were removed in vacuum. The procedure was repeated to remove all trimethylsilyl residuals. The crude product was cooled to room temperature whereby it starts to crystallize. The almost colorless cristalline crude product was recristallized from a small amount of acetonitrile. Yield 80 %.
1-(4-Hydroxybutyl)-pyridinium-bromide-d_0: ^{1}**H-NMR**(298.2 K, DMSO-d_6, 300.13 MHz, [ppm]): δ = 1.41 (tt, 2H, CH_2−CH_2−O−); 1.96 (tt, 2H, N−CH_2−CH_2−); 3.41 (t, 2H, CH_2−CH_2−O−); 4.13 (s, 1H, −O*H*); 4.68 (t, 2H, N−CH_2−CH_2−); 8.14-8.21 (m, 2H, *m*-C*H*); 8.60-8.67 (m, 1H, *p*-C*H*); 9.03-9.09 (m, 2H, *o*-C*H*). ^{13}**C-NMR**(298 K, DMSO-d_6, 75.46 MHz, [ppm]): δ = 26.36 (s, *C*H_2−CH_2−O−); 27.34 (s, N−CH_2−*C*H_2−); 58.96 (s, N−*C*H_2−CH_2−); 60.19 (s, CH_2−*C*H_2−O−); 127.67 (s, *m*-*C*H); 144.65 (s, *p*-*C*H); 145.46 (s, *o*-*C*H).
1-(4-Hydroxybutyl)-pyridinium-bromide-d_5: ^{1}**H-NMR**(298.2 K, DMSO-d_6, 300.13 MHz, [ppm]): δ = 1.41 (tt, 2H, CH_2−CH_2−O−); 1.96 (tt, 2H, N−CH_2−CH_2−); 3.41 (t, 2H, CH_2−CH_2−O−); 4.13 (s, 1H, −O*H*); 4.68 (t, 2H, N−CH_2−CH_2−). ^{13}**C-NMR**(298 K, DMSO-d_6, 75.46 MHz, [ppm]): δ = 26.36 (s, *C*H_2−CH_2−O−); 27.34 (s, N−CH_2−*C*H_2−); 58.96 (s, N−*C*H_2−CH_2−); 60.19 (s, CH_2−*C*H_2−O−); 126.76-128.00 (m, *m*-*C*D); 143.53-145.57 (m, *p*-*C*D + *o*-*C*D).
1-(4-Hydroxybutyl)-pyridinium-bromide-d_8: ^{1}**H-NMR**(298.2 K, DMSO-d_6, 300.13 MHz, [ppm]): δ = 4.13 (s, 1H, −O*H*); 8.14-8.21 (m, 2H, *m*-C*H*); 8.60-8.67 (m, 1H, *p*-C*H*); 9.03-9.09 (m, 2H, *o*-C*H*). ^{13}**C-NMR**(298 K, DMSO-d_6, 75.46 MHz, [ppm]): δ = 26.18-28.21 (m, *C*D_2−CD_2−O− + N−CD_2−*C*D_2−); 58.86-61.27 (m, CD_2−*C*D_2−O− + N−*C*D_2−CD_2−); 127.67

(s, *m*-*C*H); 144.65 (s, *p*-*C*H); 145.46 (s, *o*-*C*H).
1-(4-Hydroxybutyl)-pyridinium-bromide-d$_{13}$: ^{1}**H-NMR**(298.2 K, DMSO-d$_6$, 300.13 MHz, [ppm]): δ = 4.13 (s, 1H, −O*H*); 8.14-8.21 (m, 2H, *m*-C*H*); 8.60-8.67 (m, 1H, *p*-C*H*); 9.03-9.09 (m, 2H, *o*-C*H*). ^{13}**C-NMR**(298 K, DMSO-d$_6$, 75.46 MHz, [ppm]): δ = 26.18-28.21 (m, *C*D$_2$−CD$_2$−O− + N−CD$_2$−*C*D$_2$−); 58.86-61.27 (m, CD$_2$−*C*D$_2$−O− + N−*C*D$_2$−CD$_2$−); 126.76-128.00 (m, *m*-*C*D); 143.53-145.57 (m, *p*-*C*D + *o*-*C*D).

1-(4-Hydroxybutyl)-pyridinium-bis(trifluoromethanesulfonyl)imide-d$_{x+y}$

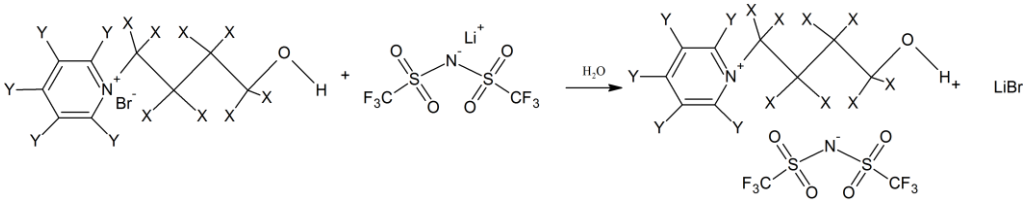

1-(4-Hydroxybutyl)-pyridinium-bromide-d$_{x+y}$ was solved in a few milliliters H_2O. This solution was added to an equimolar aqueous solution of $LiNTf_2$. The mixture was stirred for 1h. During this time two phases were formed. The lower phase was washed several times with water until no residual bromine could be detected with silver nitrate solution. The thus obtained colorless liquid was dried for 6 h at 60 °C in vacuum (< $1 \cdot 10^{-6}$ mbar). Yield: 90 %.
1-(4-Hydroxybutyl)-pyridinium-bis(trifluoromethanesulfonyl)imide-d$_0$: ^{1}**H-NMR**(298.2 K, DMSO-d$_6$, 300.13 MHz, [ppm]): δ = 1.41 (tt, 2H, C*H*$_2$−CH$_2$−O−); 1.96 (tt, 2H, N−CH$_2$−C*H*$_2$−); 3.41 (t, 2H, CH$_2$−C*H*$_2$−O−); 4.13 (s, 1H, −O*H*); 4.68 (t, 2H, N−C*H*$_2$−CH$_2$−); 8.14-8.21 (m, 2H, *m*-C*H*); 8.60-8.67 (m, 1H, *p*-C*H*); 9.03-9.09 (m, 2H, *o*-C*H*). ^{13}**C-NMR**(298 K, DMSO-d$_6$, 75.46 MHz, [ppm]): δ = 26.36 (s, *C*H$_2$−CH$_2$−O−); 27.34 (s, N−CH$_2$−*C*H$_2$−); 58.96 (s, N−*C*H$_2$−CH$_2$−); 60.19 (s, CH$_2$−*C*H$_2$−O−); 119.43 (q, *C*F$_3$); 127.67 (s, *m*-*C*H); 144.65 (s, *p*-*C*H); 145.46 (s, *o*-*C*H).
1-(4-Hydroxybutyl)-pyridinium-bis(trifluoromethanesulfonyl)imide-d$_5$: ^{1}**H-NMR**(298.2 K, DMSO-d$_6$, 300.13 MHz, [ppm]): δ = 1.41 (tt, 2H, C*H*$_2$−CH$_2$−O−); 1.96 (tt, 2H, N−CH$_2$−C*H*$_2$−); 3.41 (t, 2H, CH$_2$−C*H*$_2$−O−); 4.13 (s, 1H, −O*H*); 4.68 (t, 2H, N−C*H*$_2$−CH$_2$−). ^{13}**C-NMR**(298 K, DMSO-d$_6$, 75.46 MHz, [ppm]): δ = 26.36 (s, *C*H$_2$−CH$_2$−O−); 27.34 (s, N−CH$_2$−*C*H$_2$−); 58.96 (s, N−*C*H$_2$−CH$_2$−); 60.19 (s, CH$_2$−*C*H$_2$−O−); 119.43 (q, *C*F$_3$); 126.76-128.00 (m, *m*-*C*D); 143.53-145.57 (m, *p*-*C*D + *o*-*C*D).
1-(4-Hydroxybutyl)-pyridinium-bis(trifluoromethanesulfonyl)imide-d$_8$: ^{1}**H-NMR**(298.2 K, DMSO-d$_6$, 300.13 MHz, [ppm]): δ = 4.13 (s, 1H, −O*H*); 8.14-8.21 (m, 2H, *m*-C*H*); 8.60-8.67 (m, 1H, *p*-C*H*); 9.03-9.09 (m, 2H, *o*-C*H*). ^{13}**C-NMR**(298 K, DMSO-d$_6$, 75.46 MHz, [ppm]): δ = 26.18-28.21 (m, *C*D$_2$−CD$_2$−O− + N−CD$_2$−*C*D$_2$−); 58.86-61.27 (m, CD$_2$−*C*D$_2$−O− + N−*C*D$_2$−CD$_2$−); 119.43 (q, *C*F$_3$); 127.67 (s, *m*-*C*H); 144.65 (s, *p*-*C*H); 145.46 (s, *o*-*C*H).
1-(4-Hydroxybutyl)-pyridinium-bis(trifluoromethanesulfonyl)imide-d$_{13}$: ^{1}**H-NMR**(298.2 K, DMSO-d$_6$, 300.13 MHz, [ppm]): δ = 4.13 (s, 1H, −O*H*); 8.14-8.21 (m, 2H, *m*-C*H*); 8.60-8.67 (m, 1H, *p*-C*H*); 9.03-9.09 (m, 2H, *o*-C*H*). ^{13}**C-NMR**(298 K, DMSO-d$_6$, 75.46 MHz, [ppm]): δ = 26.18-28.21 (m, *C*D$_2$−CD$_2$−O− + N−CD$_2$−*C*D$_2$−); 58.86-61.27 (m, CD$_2$−*C*D$_2$−O− + N−*C*D$_2$−CD$_2$−); 126.76-128.00 (m, *m*-*C*D); 143.53-145.57 (m, *p*-*C*D + *o*-*C*D).

1-(4-Hydroxybutyl)-pyridinium-bis(trifluoromethanesulfonyl)imide-d_{x+y+1}

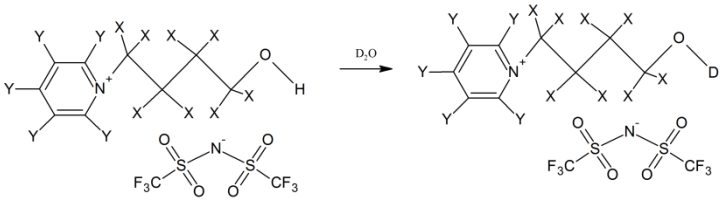

Equal volumes of the ionic liquid 1-(4-Hydroxybutyl)-pyridinium bis(trifluoromethanesulfonyl)imide-d_{x+y} and D_2O were mixed. The water was evaporated in vacuum. This procedure was repeated several times (3-5) until the OH stretching band in the IR spectra disappeared completely to the benefit of the OD contributions. The thus obtained colorless liquid was dried for 6 h at 60 °C in vacuum (< $1 \cdot 10^{-6}$ mbar). Yield: > 99 %.

1-(4-Hydroxybutyl)-pyridinium-bis(trifluoromethanesulfonyl)imide-d_1: ^{1}**H-NMR**(298.2 K, DMSO-d_6, 300.13 MHz, [ppm]): δ = 1.41 (tt, 2H, C*H*$_2$−CH$_2$−O−); 1.96 (tt, 2H, N−CH$_2$−C*H*$_2$−); 3.41 (t, 2H, CH$_2$−C*H*$_2$−O−); 4.68 (t, 2H, N−C*H*$_2$−CH$_2$−); 8.14-8.21 (m, 2H, *m*-C*H*); 8.60-8.67 (m, 1H, *p*-C*H*); 9.03-9.09 (m, 2H, *o*-C*H*). ^{13}**C-NMR**(298 K, DMSO-d_6, 75.46 MHz, [ppm]): δ = 26.36 (s, *C*H$_2$−CH$_2$−O−); 27.34 (s, N−CH$_2$−*C*H$_2$−); 58.96 (s, N−*C*H$_2$−CH$_2$−); 60.19 (s, CH$_2$−*C*H$_2$−O−); 119.43 (q, *C*F$_3$); 127.67 (s, *m*-*C*H); 144.65 (s, *p*-*C*H); 145.46 (s, *o*-*C*H).

1-(4-Hydroxybutyl)-pyridinium-bis(trifluoromethanesulfonyl)imide-d_6: ^{1}**H-NMR**(298.2 K, DMSO-d_6, 300.13 MHz, [ppm]): δ = 1.41 (tt, 2H, C*H*$_2$−CH$_2$−O−); 1.96 (tt, 2H, N−CH$_2$−C*H*$_2$−); 3.41 (t, 2H, CH$_2$−C*H*$_2$−O−); 4.68 (t, 2H, N−C*H*$_2$−CH$_2$−). ^{13}**C-NMR**(298 K, DMSO-d_6, 75.46 MHz, [ppm]): δ = 26.36 (s, *C*H$_2$−CH$_2$−O−); 27.34 (s, N−CH$_2$−*C*H$_2$−); 58.96 (s, N−*C*H$_2$−CH$_2$−); 60.19 (s, CH$_2$−*C*H$_2$−O−); 119.43 (q, *C*F$_3$); 126.76-128.00 (m, *m*-*C*D); 143.53-145.57 (m, *p*-*C*D + *o*-*C*D).

1-(4-Hydroxybutyl)-pyridinium-bis(trifluoromethanesulfonyl)imide-d_9: ^{1}**H-NMR**(298.2 K, DMSO-d_6, 300.13 MHz, [ppm]): δ = 8.14-8.21 (m, 2H, *m*-C*H*); 8.60-8.67 (m, 1H, *p*-C*H*); 9.03-9.09 (m, 2H, *o*-C*H*). ^{13}**C-NMR**(298 K, DMSO-d_6, 75.46 MHz, [ppm]): δ = 26.18-28.21 (m, *C*D$_2$−CD$_2$−O− + N−CD$_2$−*C*D$_2$−); 58.86-61.27 (m, CD$_2$−*C*D$_2$−O− + N−*C*D$_2$−CD$_2$−); 119.43 (q, *C*F$_3$); 127.67 (s, *m*-*C*H); 144.65 (s, *p*-*C*H); 145.46 (s, *o*-*C*H).

1-(4-Hydroxybutyl)-pyridinium-bis(trifluoromethanesulfonyl)imide-d_{14}: ^{13}**C-NMR**(298 K, DMSO-d_6, 75.46 MHz, [ppm]): δ = 26.18-28.21 (m, *C*D$_2$−CD$_2$−O− + N−CD$_2$−*C*D$_2$−); 58.86-61.27 (m, CD$_2$−*C*D$_2$−O− + N−*C*D$_2$−CD$_2$−); 119.43 (q, *C*F$_3$); 126.76-128.00 (m, *m*-*C*D); 143.53-145.57 (m, *p*-*C*D + *o*-*C*D).

2. Neutron diffraction and EPSR-Analysis

Sample preparation

All samples were dried for 6 h at 60 °C in vacuum (< $1 \cdot 10^{-6}$ mbar). The final water contend of the IL was determined by Karl-Fischer titration and for all samples below 10 ppm (H_2O). The dry samples were sealed in glass vials under vacuum for shipping.

Neutron diffraction

The Neutron scattering experiments were performed at the SANDALS (Small Angle Neutron Diffractometer for Amorphous and Liquid Samples) time of flight diffractometer at at the ISIS pulsed neutron and muon source at the Rutherford Appelton Laboratory in Didcot, UK. The instrument makes use of neutrons with wavelengths ranging from 0.05 – 4.95 Å, and covers a Q range of 0.1 – 50 $Å^{-1}$. The Samples were contained in chemically inert, null scattering $Ti_{0.68}Zr_{0.32}$ flat plate cans of known atomic density (0.0541 atoms per $Å^3$) which were sealed with PTFE O-rings. The dimensions of the cans were 35 x 35 mm^2 with a path length of 1 mm and 1 mm wall thicknesses. Prior filling the cans with the ILs in a moister free glove box, diffraction measurements were performed on the empty cans (4 x 250 μA), the empty instrument (4 x 125 μA) and a vanadium standard sample (4 x 250 μA) for data correction and normalization. The diffraction experiments were conducted at 25 ± 0.1 °C under vacuum. The sample chamber was left to equilibrate for at least 10 min prior each measurement. At least 5 scans, each to an accumulated Intensity of 250 μA per sample were performed and accumulated. After the measurements the cans were emptied and cleaned. Again diffraction measurements were performed on the empty cans (1 x 250 μA), the empty instrument (1 x 125 μA) and a vanadium standard sample (1 x 250 μA) to ensure that no changes of conditions were taken place during the time of the experiment.

Data reduction

The data reduction was carried out using GUDRUN software, as described in the GudrunN and GudrunX manual. [1] This corrects the raw data by normalization to the incedent neutron flux, for absorption and multiple scattering, Ti-Zr can subtraction and normalization to absolute units by dividing the measured differential cross section by the scattering of a vanadium standard of known thickness. Corrections for single atom scattering and hydrogen inelasticity were also applied.

Data fitting

The fitting and the analysis of the data was made using the EPSR (Empirical Potential Structure Refinement) technique as described in the user's guide and the EPSRgui Manual. [2, 3] The Lennard-Jones parameters σ and ε as well as the charges *q* for the [NTf_2] forcefield were taken from the NGOLP forcefield [16]. The Lennard-Jones parameters for the [HOC_4Py] cation where taken from Jorgensens OPLS forcefield [17,18], whereas the charges were derived from MP2 calculations as described in Table 2. The final input parameters are displayed in Table 1-2. An EPSR model was developed consisting of 1000 anions and 1000 cations in a simulation box with a box axis 77.9566 Å and a resulting atomic number density of 0.084431 atoms/$Å^3$ consistent to density measurements of the bulk liquid. Atomic and molecular translations and rotations were governed by the standard rules for a Monte Carlo simulation with respect to a reference potential of Lenard-Jones and Coulombic interactions.

The potential has been corrected following an iterative algorithm until agreement between the simulated and experimental structure factors was reached. The seven contrasts for the IL were modeled simultaneously with the same box by normalizing for isotope populations. All presented ND results were taken from this simulated box.

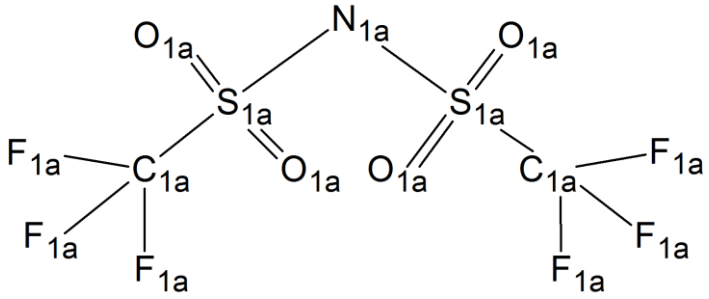

Table 1- Lennard-Jones and Coulombic charge parameters for EPSR modelling of the NTf_2 anion.

Atom Type	ε / kJ mol^{-1}	σ / Å	AW / amu	q / e	Element
N_{1a}	0.2133	3.2500	14.007	-0.690	N
S_{1a}	0.3137	4.0825	32.066	1.076	S
O_{1a}	0.2636	3.4632	15.999	-0.579	O
C_{1a}	0.0828	3.1500	12.011	0.494	C
F_{1a}	0.0655	2.6550	18.998	-0.189	F

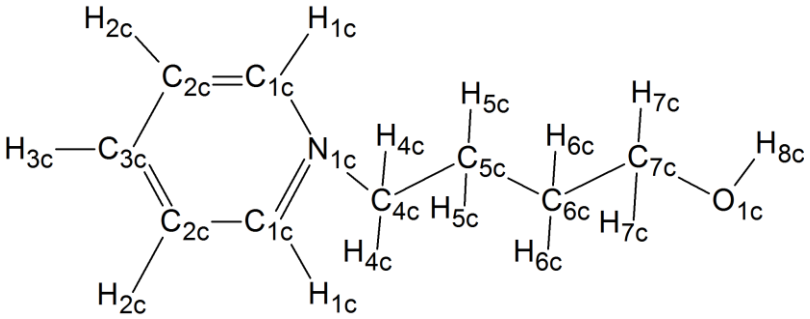

Table 2- Lennard-Jones and Coulombic charge parameters for EPSR modelling of the [HOC4Py] cation. Atom point charges were determined from ab initio calculations at the MP2 level of theory with a cc-pvtz basis set using the chelpg method in Gaussian 09.

Atom Type	ε / kJ mol^{-1}	σ / Å	AW / amu	q / e	Element
N_{1c}	0.71130	3.25	14.007	0.10140	N
C_{1c}	0.29290	3.55	12.011	0.05680	C
C_{2c}	0.29290	3.55	12.011	-0.22140	C
C_{3c}	0.29290	3.55	12.011	0.17470	C
H_{1c}	0.12555	2.42	2.000	0.18020	H
H_{2c}	0.12555	2.42	2.000	0.17590	H
H_{3c}	0.12555	2.42	2.000	0.12750	H
C_{4c}	0.27600	3.50	12.011	-0.15090	C
C_{5c}	0.27600	3.50	12.011	0.01600	C
C_{6c}	0.27600	3.50	12.011	0.07800	C
C_{7c}	0.27600	3.50	12.011	0.29110	C
H_{4c}	0.12555	2.50	2.000	0.10150	H

H_{5c}	0.12555	2.50	2.000	0.00430	H
H_{6c}	0.12555	2.50	2.000	0.03160	H
H_{7c}	0.12555	2.50	2.000	-0.02050	H
O_{1c}	0.71170	3.12	15.999	-0.69106	O
H_{8c}	0.00000	0.00	2.000	0.43700	H

Quality of the data fitting

Using the procedure of the EPSR model we obtain good fits to the SANDALS data over the entire Q range examined by us. Some discrepancies appear between the fits and data in the Q range < 1.5 $Å^{-1}$ where the data shows a decline in intensity. This is principally due to inelastic scattering by light hydrogen atoms, which is slightly overcompensated by the correction methods. As such, it is more pronounced for hydrogen-rich samples. [1,2]

[1] A. K. Soper, Mol. Phys. 2009, 107, 1667–84.

[2] R Hayes, S Imberti, GG Warr, R Atkin, Phys. Chem. Chem. Phys. 2010, 13, 3237-3247

3. Density functional theory (DFT) calculations on [HOC_4Py][NTf_2] clusters

*** pyridinium_C4_NTf2_b3lyp_6-31+Gp_monomer_D3.g09

6	0	-3.009856	-2.119282	-0.235794
7	0	-2.654843	-0.912146	0.262238
6	0	-2.097035	-0.813662	1.491622
6	0	-1.906744	-1.942456	2.273423
6	0	-2.279781	-3.190354	1.780898
6	0	-2.841067	-3.275281	0.505099
6	0	-2.759239	0.303834	-0.608141
6	0	-3.446978	1.482083	0.082168
6	0	-3.581984	2.703064	-0.847103
6	0	-2.249793	3.307253	-1.301165
8	0	-1.644949	2.466518	-2.284752
8	0	0.817138	1.703947	-0.966775
16	0	0.723969	1.246525	0.431756
6	0	2.319725	1.827559	1.248073
9	0	3.376090	1.269521	0.645671
8	0	-0.350048	1.823201	1.265575
7	0	0.824421	-0.341575	0.700855
16	0	0.716907	-1.489707	-0.437518
8	0	0.523998	-2.765494	0.260071
6	0	2.440764	-1.614941	-1.198436
9	0	2.450282	-2.605289	-2.103024
8	0	-0.176058	-1.156301	-1.558713
9	0	2.772870	-0.468232	-1.801255
9	0	3.345427	-1.885934	-0.247665
9	0	2.404394	3.160806	1.134207
9	0	2.331006	1.500307	2.546409
1	0	-1.426005	-1.831049	3.238342
1	0	-0.715337	2.303352	-2.042979
1	0	-4.150932	3.473098	-0.308738
1	0	-4.166456	2.441462	-1.740014
1	0	-2.433993	4.298489	-1.740314
1	0	-1.584231	3.436441	-0.437449
1	0	-3.121423	-4.227489	0.069295
1	0	-2.109885	-4.087429	2.367613
1	0	-1.767849	0.170752	1.796769
1	0	-3.404686	-2.122110	-1.243801
1	0	-2.871741	1.785882	0.962745
1	0	-4.442061	1.166375	0.425505
1	0	-3.307858	0.001075	-1.501769
1	0	-1.747945	0.535650	-0.930882

*** pyridinium_C4_NTf2_b3lyp_6-31+Gp_dimer_D3.g09

6	0	-1.258894	3.147046	-0.032101
7	0	-2.229421	3.312341	-0.965042
6	0	-2.326976	2.464102	-2.012685
6	0	-1.432120	1.416258	-2.155434
6	0	-0.424367	1.241216	-1.209207
6	0	-0.334231	2.125123	-0.129254

6	0	-3.183907	4.447444	-0.821669
6	0	-4.140305	4.329813	0.391765
6	0	-5.616081	4.080345	0.023637
6	0	-5.933564	2.650495	-0.401121
8	0	-3.407595	1.143282	0.700696
16	0	-3.050203	-0.162245	1.271995
7	0	-2.717498	-1.310468	0.188410
16	0	-3.326115	-1.414906	-1.307970
8	0	-4.366615	-0.441377	-1.679631
8	0	-2.009807	-0.232589	2.302670
6	0	-4.622634	-0.724470	2.151122
9	0	-4.883499	0.120543	3.160659
9	0	-4.476500	-1.960450	2.641174
9	0	-5.659249	-0.709479	1.298874
8	0	-2.221074	-1.671068	-2.243002
6	0	-4.219497	-3.072077	-1.203135
9	0	-5.171832	-3.038462	-0.264011
9	0	-4.780660	-3.346895	-2.387232
9	0	-3.343266	-4.043908	-0.901024
6	0	0.277975	-2.408630	-0.187230
7	0	1.270112	-2.032547	0.650631
6	0	2.461054	-2.674922	0.655887
6	0	2.682445	-3.742703	-0.198436
6	0	1.673858	-4.141055	-1.077813
6	0	0.454383	-3.463114	-1.067241
6	0	1.088029	-0.808825	1.485041
6	0	1.242223	-1.048963	2.985879
6	0	1.011805	0.246860	3.788656
6	0	2.049349	1.346560	3.558305
8	0	1.859014	1.944379	2.265700
8	0	4.626261	1.659619	1.355050
16	0	4.826298	0.223502	1.100636
6	0	6.668606	0.027369	0.754414
9	0	7.023222	0.753021	-0.312849
8	0	4.560090	-0.720989	2.200027
7	0	4.181448	-0.386139	-0.250156
16	0	3.237782	0.403861	-1.292788
8	0	2.346266	-0.590406	-1.911328
6	0	4.401543	0.923323	-2.681899
9	0	3.682009	1.437079	-3.691480
8	0	2.643710	1.653964	-0.800366
9	0	5.259138	1.852476	-2.241983
9	0	5.093701	-0.131062	-3.134099
9	0	7.362702	0.447396	1.820264
9	0	6.961201	-1.260171	0.523286
1	0	3.651375	-4.229128	-0.184582
1	0	2.729445	2.126611	1.865113
1	0	1.026662	-0.011603	4.855953
1	0	0.011361	0.640813	3.572988
1	0	1.936652	2.121531	4.330335
1	0	3.063422	0.935096	3.634203
1	0	-3.143983	2.642661	-2.696851
1	0	0.289508	0.433858	-1.324469
1	0	0.440804	2.035695	0.626054
1	0	-0.361546	-3.716983	-1.734496
1	0	1.840754	-4.962808	-1.767987
1	0	3.215406	-2.292040	1.330752
1	0	-0.652001	-1.857268	-0.120210
1	0	-1.542553	0.733598	-2.989176

1	0	-1.253860	3.860624	0.783336
1	0	2.244324	-1.434483	3.206080
1	0	0.508045	-1.802397	3.297589
1	0	0.088210	-0.433600	1.276611
1	0	1.808236	-0.077295	1.128529
8	0	-5.175902	2.320299	-1.566231
1	0	-5.685846	1.960729	0.413092
1	0	-7.009392	2.559732	-0.615278
1	0	-4.958083	1.370232	-1.541030
1	0	-2.562280	5.344808	-0.746417
1	0	-3.743039	4.501969	-1.755211
1	0	-3.791777	3.534503	1.058976
1	0	-4.076286	5.268353	0.954952
1	0	-6.238060	4.316311	0.897649
1	0	-5.921816	4.775916	-0.771150

*** pyridinium_C3_NTf2_b3lyp_6-31+Gp_trimer_D3.g09

6	0	0.369450	-1.187663	0.704449
7	0	-0.669639	-1.663548	-0.013889
6	0	-1.211372	-2.871600	0.258583
6	0	-0.748766	-3.626596	1.321594
6	0	0.310908	-3.143329	2.091166
6	0	0.882090	-1.913613	1.767047
6	0	-1.224138	-0.859334	-1.140429
6	0	-0.710527	-1.374572	-2.485472
6	0	-1.149348	-0.499642	-3.670908
6	0	-2.650216	-0.520086	-3.968243
8	0	-3.360884	0.208925	-2.963484
8	0	-5.311450	-1.417606	-1.609135
16	0	-4.757821	-2.750575	-1.288486
6	0	-6.101169	-3.976266	-1.776369
9	0	-7.228299	-3.719956	-1.102663
8	0	-3.558013	-3.164177	-2.041727
7	0	-4.636676	-3.140231	0.274696
16	0	-4.368176	-2.054787	1.433461
8	0	-3.770625	-2.726427	2.588496
6	0	-6.098103	-1.584653	2.026425
9	0	-5.994533	-0.683432	3.026440
8	0	-3.773405	-0.793925	0.957829
9	0	-6.813684	-1.035201	1.033659
9	0	-6.747270	-2.658720	2.484939
9	0	-6.336691	-3.840252	-3.090116
9	0	-5.713804	-5.231742	-1.530733
1	0	-1.233100	-4.570955	1.540992
1	0	-4.103029	-0.325870	-2.624537
1	0	-0.621468	-0.851117	-4.569586
1	0	-0.838926	0.541955	-3.506764
1	0	-2.836111	-0.049475	-4.944259
1	0	-3.010045	-1.556016	-4.012456
1	0	1.730162	-1.514744	2.306609
1	0	0.694727	-3.721172	2.926436
1	0	-2.018945	-3.192115	-0.386997
1	0	0.761714	-0.223472	0.413483
1	0	-1.057291	-2.404212	-2.635931
1	0	0.382725	-1.412526	-2.433025

1	0	-0.916590	0.172530	-0.974653
1	0	-2.306262	-0.904920	-1.060144
6	0	-4.773441	2.072448	2.079547
7	0	-3.477006	2.086434	1.704781
6	0	-3.139653	2.036674	0.398064
6	0	-4.106895	2.001820	-0.590561
6	0	-5.449641	1.988529	-0.220450
6	0	-5.783800	2.022179	1.134855
6	0	-2.386744	2.129345	2.722439
6	0	-1.729961	0.755856	2.886359
6	0	-0.571218	0.755335	3.896219
6	0	0.662710	1.550684	3.468678
8	0	0.372943	2.947153	3.517997
8	0	1.190111	4.020938	0.907247
16	0	0.519123	3.279869	-0.174031
6	0	1.811065	3.113801	-1.532715
9	0	2.085382	4.291889	-2.101508
8	0	0.136457	1.881579	0.131920
7	0	-0.593178	4.034488	-1.043777
16	0	-1.701245	5.034194	-0.402302
8	0	-2.843447	5.090182	-1.313113
6	0	-0.887426	6.731540	-0.543452
9	0	-1.734359	7.668481	-0.092129
8	0	-1.925745	4.826681	1.037293
9	0	0.238985	6.776582	0.177370
9	0	-0.592467	6.994631	-1.825070
9	0	2.938719	2.618324	-1.006006
9	0	1.390129	2.260059	-2.496118
1	0	-3.794215	1.959678	-1.626715
1	0	0.797385	3.398074	2.766056
1	0	-0.268530	-0.288230	4.058397
1	0	-0.913237	1.135500	4.868982
1	0	1.496201	1.321228	4.149296
1	0	0.967608	1.257488	2.455732
1	0	-6.815319	1.997482	1.467137
1	0	-6.225873	1.938560	-0.977331
1	0	-2.080901	2.018885	0.181335
1	0	-4.965610	2.093408	3.145072
1	0	-1.361265	0.429367	1.909556
1	0	-2.487944	0.024514	3.187690
1	0	-2.832532	2.472828	3.659130
1	0	-1.678860	2.889726	2.401020
6	0	4.401082	0.912908	-3.105631
7	0	4.627345	-0.371373	-2.744841
6	0	5.869272	-0.780628	-2.391226
6	0	6.934163	0.104887	-2.411192
6	0	6.719222	1.430433	-2.784841
6	0	5.430924	1.836325	-3.136210
6	0	3.479741	-1.326690	-2.645373
6	0	3.682295	-2.589820	-3.485584
6	0	2.486956	-3.556823	-3.395900
6	0	2.278264	-4.196257	-2.021058
8	0	1.788267	-3.225234	-1.090564
8	0	3.615958	-3.010266	1.135367
16	0	4.977862	-2.756651	0.619905
6	0	6.132160	-3.459758	1.932207
9	0	5.921757	-2.841635	3.100633
8	0	5.356769	-3.437476	-0.633456
7	0	5.485810	-1.229253	0.582819

16	0	4.552081	0.083715	0.724749
8	0	5.289910	1.205406	0.142352
6	0	4.493386	0.446820	2.573412
9	0	3.860554	1.606334	2.775109
8	0	3.147567	-0.126561	0.340100
9	0	3.822437	-0.533676	3.208230
9	0	5.728300	0.520621	3.078476
9	0	5.880235	-4.767697	2.075970
9	0	7.409149	-3.296625	1.570102
1	0	7.909738	-0.247472	-2.096524
1	0	2.303207	-3.273500	-0.264241
1	0	2.651344	-4.362540	-4.123733
1	0	1.560820	-3.049246	-3.696269
1	0	1.542531	-5.008507	-2.108386
1	0	3.221731	-4.626528	-1.660958
1	0	5.209483	2.862041	-3.408823
1	0	7.537853	2.143251	-2.781395
1	0	5.964652	-1.806884	-2.061484
1	0	3.377144	1.171613	-3.340172
1	0	4.581150	-3.118466	-3.149697
1	0	3.841895	-2.298651	-4.532648
1	0	2.593215	-0.778246	-2.969257
1	0	3.341176	-1.550040	-1.591014

*** pyridinium_C4_NTf2_b3lyp_6-31+Gp_tetramer_D3.g09

6	0	-2.191810	-0.809122	4.006213
7	0	-2.235561	0.288671	3.215921
6	0	-3.391976	0.672598	2.616546
6	0	-4.549026	-0.066556	2.786530
6	0	-4.522810	-1.208632	3.595451
6	0	-3.330091	-1.568176	4.227565
6	0	-0.973556	1.014253	2.892287
6	0	-0.518701	2.016700	3.954808
6	0	0.708532	2.785392	3.410432
6	0	0.270996	3.916046	2.472052
8	0	-2.746973	3.158224	0.652471
16	0	-3.320632	4.015724	-0.399681
7	0	-2.428903	4.109367	-1.753210
16	0	-0.851550	3.731223	-1.770608
8	0	0.019369	4.477402	-0.837178
8	0	-4.712599	3.804631	-0.791224
6	0	-3.307216	5.766644	0.319228
9	0	-4.171617	5.817605	1.341157
9	0	-3.675380	6.651613	-0.609938
9	0	-2.087462	6.085340	0.769456
8	0	-0.557806	2.293962	-1.925591
6	0	-0.478645	4.478558	-3.464464
9	0	-0.609433	5.804178	-3.438887
9	0	0.792742	4.170939	-3.773280
9	0	-1.283840	3.966146	-4.399700
6	0	-4.416639	1.097072	-2.080635
7	0	-5.609339	0.536495	-1.766925
6	0	-5.737579	-0.805529	-1.632614
6	0	-4.644282	-1.634072	-1.847383
6	0	-3.406457	-1.074647	-2.165272

6	0	-3.287584	0.315942	-2.262530
6	0	-6.810114	1.410613	-1.567855
6	0	-7.684130	1.432067	-2.830796
6	0	-8.824325	2.468891	-2.761247
6	0	-10.006734	2.055913	-1.880407
8	0	-9.588362	1.866568	-0.533810
8	0	-10.526942	-0.743418	-0.299736
16	0	-9.595253	-1.886509	-0.317619
6	0	-10.673227	-3.401694	-0.644216
9	0	-11.649236	-3.491387	0.260396
8	0	-8.584513	-1.874798	-1.391617
7	0	-9.053449	-2.378465	1.136199
16	0	-8.080669	-1.458744	2.022603
8	0	-7.347796	-2.309729	2.965476
6	0	-9.223400	-0.460045	3.151091
9	0	-8.462583	0.275542	3.982033
8	0	-7.320961	-0.437459	1.271990
9	0	-10.004334	0.359008	2.443183
9	0	-9.988123	-1.278488	3.879788
9	0	-11.217872	-3.257740	-1.861853
9	0	-9.943856	-4.520756	-0.627091
1	0	-4.771515	-2.705757	-1.737372
1	0	-9.916820	1.005707	-0.207488
1	0	-9.204044	2.623788	-3.780424
1	0	-8.433615	3.436743	-2.417904
1	0	-10.772930	2.844692	-1.910996
1	0	-10.457292	1.135134	-2.274986
1	0	-3.332837	1.558322	1.991480
1	0	-5.436757	-1.796185	3.666423
1	0	-3.260977	-2.450797	4.854255
1	0	-2.322198	0.788063	-2.419150
1	0	-2.537696	-1.710217	-2.309606
1	0	-6.716606	-1.185773	-1.345892
1	0	-4.400895	2.177950	-2.148637
1	0	-5.465194	0.189952	2.259623
1	0	-1.217614	-1.074457	4.398883
1	0	-8.110962	0.433236	-2.987331
1	0	-7.044305	1.657632	-3.695027
1	0	-6.436833	2.406845	-1.322837
1	0	-7.352011	1.023755	-0.707212
8	0	1.338830	4.315953	1.603570
1	0	-0.581143	3.595278	1.868581
1	0	-0.053625	4.784611	3.063403
1	0	0.924629	4.574699	0.753848
1	0	-0.208891	0.255703	2.707817
1	0	-1.168599	1.537200	1.957232
1	0	-1.334658	2.719871	4.169314
1	0	-0.270888	1.507762	4.893889
1	0	1.302190	3.175008	4.244967
1	0	1.360207	2.100118	2.852975
6	0	2.959049	2.527009	-0.514592
7	0	4.202290	2.592935	0.016542
6	0	5.208143	1.849935	-0.508756
6	0	4.972007	0.956411	-1.540323
6	0	3.683952	0.837655	-2.074945
6	0	2.687246	1.683224	-1.584800
6	0	4.438959	3.410201	1.249474
6	0	5.567898	4.460289	1.109897
6	0	6.596205	4.361302	2.254711

6	0	7.485266	3.132946	2.086647
8	0	8.518685	1.230950	-0.558059
16	0	8.724822	-0.177413	-0.906856
7	0	9.327339	-1.154356	0.242667
16	0	9.461455	-0.738958	1.818326
8	0	8.432853	0.193841	2.301382
8	0	7.618304	-0.868849	-1.607962
6	0	10.106937	-0.223425	-2.198842
9	0	9.748287	0.563863	-3.223476
9	0	10.273512	-1.472629	-2.649058
9	0	11.261786	0.217935	-1.696938
8	0	9.674212	-1.988442	2.554080
6	0	11.111534	0.196628	2.002422
9	0	11.314028	1.018344	0.967587
9	0	11.069675	0.919717	3.129000
9	0	12.121102	-0.672056	2.077885
6	0	6.728881	-3.295017	0.326651
7	0	5.529690	-3.683431	-0.163010
6	0	4.769822	-4.583552	0.505390
6	0	5.222250	-5.132974	1.696152
6	0	6.463436	-4.745674	2.215097
6	0	7.224836	-3.810398	1.514786
6	0	5.033154	-3.075276	-1.436291
6	0	4.930847	-4.101018	-2.571929
6	0	4.636097	-3.423927	-3.925574
6	0	3.188432	-2.979676	-4.113119
8	0	2.819798	-1.999657	-3.134422
8	0	0.610211	-3.428296	-2.164307
16	0	0.599091	-4.224485	-0.919015
6	0	-0.900791	-5.375584	-1.086015
9	0	-1.883128	-4.756276	-1.756548
8	0	1.751641	-5.100978	-0.681322
7	0	0.060386	-3.393963	0.383017
16	0	0.944020	-2.154381	0.919014
8	0	0.534896	-1.841873	2.293355
6	0	0.300044	-0.667040	-0.051786
9	0	0.857307	0.448066	0.452399
8	0	2.372267	-2.205181	0.582176
9	0	0.597792	-0.739272	-1.350670
9	0	-1.037230	-0.570605	0.073022
9	0	-0.513667	-6.450588	-1.781850
9	0	-1.362274	-5.767547	0.101166
1	0	4.589736	-5.847527	2.211900
1	0	2.004526	-2.314779	-2.694679
1	0	4.870095	-4.136982	-4.727791
1	0	5.308970	-2.566960	-4.068693
1	0	3.064053	-2.548183	-5.116321
1	0	2.520440	-3.846304	-4.034269
1	0	6.189830	1.950855	-0.062802
1	0	3.449892	0.046580	-2.792436
1	0	1.673510	1.693079	-1.968817
1	0	8.182047	-3.404550	1.833971
1	0	6.822546	-5.160623	3.152330
1	0	3.802033	-4.817049	0.074053
1	0	7.284432	-2.540145	-0.219740
1	0	5.817015	0.350694	-1.856509
1	0	2.189455	3.102404	-0.001779
1	0	4.150273	-4.839244	-2.348212
1	0	5.884847	-4.638527	-2.649647

1	0	5.759175	-2.305500	-1.695112
1	0	4.073879	-2.603682	-1.220350
8	0	8.302268	2.946364	3.229484
1	0	6.867258	2.235632	1.937249
1	0	8.101437	3.251151	1.181490
1	0	8.641137	2.033523	3.178958
1	0	3.480677	3.876877	1.487930
1	0	4.675704	2.690312	2.039202
1	0	6.083391	4.340364	0.148087
1	0	5.116347	5.457914	1.090832
1	0	7.219462	5.263229	2.266379
1	0	6.084603	4.316674	3.225606

*** pyridinium_C4_NTf2_cation_cation_b3lyp_6-31+Gp_dimer_D3.g09

6	0	5.273715	1.776668	-0.534768
7	0	4.732330	2.231537	-1.687230
6	0	4.522690	3.555828	-1.883496
6	0	4.875807	4.479836	-0.916437
6	0	5.452743	4.030320	0.276765
6	0	5.648969	2.664300	0.465400
6	0	2.845697	0.776614	-2.468059
6	0	1.769308	1.858726	-2.586413
6	0	0.372689	1.251508	-2.468931
8	0	0.213853	0.325580	-3.535684
8	0	-2.034983	-1.046086	-2.764252
6	0	-2.363765	-2.426021	-2.963466
6	0	-1.296796	-3.308589	-2.313404
6	0	-1.333264	-3.339015	-0.773983
7	0	-1.037802	-2.033960	1.337883
6	0	0.049898	-2.123942	2.134752
6	0	-0.081806	-2.100243	3.515167
6	0	-1.352605	-1.974616	4.076771
6	0	-2.463887	-1.887175	3.236038
6	0	-2.281023	-1.925536	1.864802
8	0	-1.825233	0.951052	0.053800
16	0	-2.888589	1.387870	0.974833
8	0	-2.604763	1.463048	2.409049
7	0	-4.303673	0.632577	0.768844
16	0	-4.675461	-0.184566	-0.568702
8	0	-4.277986	0.411615	-1.862185
6	0	-6.544670	0.017509	-0.479069
9	0	-7.024653	-0.498074	0.658744
9	0	-6.879252	1.309273	-0.555724
9	0	-7.087796	-0.637666	-1.516359
8	0	-4.433921	-1.637634	-0.423559
6	0	-3.256597	3.166159	0.464654
9	0	-4.234793	3.679228	1.222013
9	0	-2.147553	3.910151	0.627631
9	0	-3.627106	3.221458	-0.820694
9	0	2.469626	1.859659	0.568652
6	0	2.067321	1.188004	1.670407
9	0	2.085096	2.037623	2.705589
16	0	3.242970	-0.242528	2.037626
7	0	2.912784	-1.126627	0.721510
16	0	4.069410	-2.047953	0.048973

6	0	2.901423	-3.110176	-0.983303
9	0	2.053111	-3.788530	-0.188157
8	0	2.718810	-0.827763	3.276473
8	0	4.592245	0.351739	2.046986
9	0	0.821819	0.754529	1.472875
8	0	4.880430	-1.319499	-0.949495
8	0	4.754368	-2.962558	0.964582
9	0	2.180237	-2.359754	-1.830792
9	0	3.625797	-3.985385	-1.687537
1	0	-3.468392	-1.760101	3.623110
1	0	-2.839923	-0.510971	-2.611468
1	0	-1.441660	-4.334473	-2.677572
1	0	-0.307083	-2.986734	-2.663909
1	0	-2.409238	-2.635949	-4.041690
1	0	-3.347976	-2.634777	-2.526777
1	0	-0.607924	-0.186367	-3.372581
1	0	0.260145	0.757891	-1.492477
1	0	-0.387189	2.046436	-2.515060
1	0	1.848375	2.365070	-3.560411
1	0	1.883600	2.619372	-1.802613
1	0	5.366376	0.700201	-0.438021
1	0	5.732235	4.738241	1.051184
1	0	4.694018	5.533217	-1.099178
1	0	0.817860	-2.140220	4.116630
1	0	-1.473995	-1.928867	5.154877
1	0	-3.099557	-1.857929	1.157385
1	0	1.011247	-2.181657	1.640268
1	0	6.053684	2.259038	1.384448
1	0	4.065816	3.832297	-2.825662
1	0	-2.355247	-3.568890	-0.446381
1	0	-0.681790	-4.142732	-0.406823
1	0	2.796730	0.298147	-1.485998
1	0	2.641290	-0.006164	-3.206202
6	0	-0.889745	-2.014389	-0.148117
1	0	0.158093	-1.799332	-0.360288
1	0	-1.478109	-1.176516	-0.511384
6	0	4.275991	1.247353	-2.721139
1	0	4.970850	0.408157	-2.681380
1	0	4.373113	1.746461	-3.689661

*** pyridinium_C3_NTf2_cation_cation_b3lyp_6-31+Gp_trimer_D3.g09,

6	0	5.867164	0.329330	0.918053
7	0	4.929174	-0.486382	1.457716
6	0	5.171343	-1.804977	1.633810
6	0	6.385135	-2.355486	1.250320
6	0	7.361210	-1.537613	0.680487
6	0	7.094845	-0.176005	0.520583
6	0	2.945495	-0.440274	3.056703
6	0	1.675481	0.371854	3.342176
6	0	0.877163	-0.167924	4.529915
8	0	0.355340	-1.465348	4.286224
8	0	-2.011657	-1.175786	2.804506
6	0	-2.938217	-1.341576	3.886487
6	0	-3.403857	0.036313	4.347687
6	0	-4.265088	0.780857	3.299352

7	0	-2.388860	1.846929	1.943172
6	0	-2.338606	0.913790	0.969992
6	0	-1.206416	0.781299	0.181702
6	0	-0.122695	1.629754	0.375546
6	0	-0.188348	2.589754	1.392267
6	0	-1.330413	2.669401	2.162829
8	0	-1.759813	-3.443687	1.359284
6	0	-2.168405	-3.878074	0.054140
6	0	-2.214214	-2.727118	-0.952156
6	0	-2.299619	-3.272299	-2.384915
7	0	-2.166742	-0.912020	-3.314245
6	0	-0.816942	-0.779610	-3.359820
6	0	-0.227156	0.470122	-3.282307
6	0	-1.038636	1.603226	-3.162167
6	0	-2.423498	1.446178	-3.104792
6	0	-2.967290	0.172483	-3.178404
8	0	0.812828	-4.448405	1.022196
16	0	2.234993	-4.076714	1.015975
6	0	3.067571	-5.466383	0.044686
9	0	2.967063	-6.611166	0.727898
8	0	2.985768	-4.030419	2.275219
7	0	2.591276	-2.713808	0.226831
16	0	1.874893	-2.176823	-1.112777
6	0	3.330180	-2.193631	-2.314941
9	0	2.986970	-1.498851	-3.413720
8	0	0.874666	-3.051708	-1.744202
8	0	1.549612	-0.751543	-0.953891
9	0	2.500337	-5.617780	-1.156360
9	0	4.371164	-5.173100	-0.124233
9	0	4.422624	-1.638149	-1.771317
9	0	3.622597	-3.450238	-2.671225
9	0	3.976422	1.008563	-1.297461
6	0	4.149202	2.058548	-2.125252
9	0	4.017412	1.625642	-3.388536
16	0	2.829460	3.380544	-1.776344
7	0	2.559042	3.334881	-0.178777
16	0	3.591086	3.825499	0.959112
6	0	3.672815	5.720706	0.900716
9	0	4.467352	6.142600	-0.081010
8	0	1.626884	2.803163	-2.395560
8	0	3.397421	4.626057	-2.292276
9	0	5.389948	2.528972	-1.961087
8	0	2.940945	3.535255	2.247321
8	0	4.985315	3.381794	0.763962
9	0	2.440078	6.220159	0.725260
9	0	4.155509	6.159293	2.073700
8	0	-4.244706	2.623219	-0.375898
16	0	-5.369584	1.838377	-0.910198
8	0	-5.530599	1.738142	-2.369912
7	0	-5.404341	0.434268	-0.121579
16	0	-6.156217	-0.871324	-0.755403
8	0	-7.581927	-0.715890	-1.041187
6	0	-6.045573	-1.926803	0.803156
9	0	-6.723585	-1.372149	1.814967
9	0	-4.761910	-2.087655	1.183332
9	0	-6.563162	-3.131366	0.536064
8	0	-5.309443	-1.581924	-1.734104
6	0	-6.887745	2.779444	-0.297391
9	0	-6.830277	2.889676	1.045167

9	0	-6.889015	4.010587	-0.827430
9	0	-8.013465	2.152514	-0.633155
1	0	0.852053	0.558514	-3.278686
1	0	-1.183894	0.011832	-0.576857
1	0	-2.010492	-1.985074	2.234948
1	0	-3.974947	-0.094076	5.275246
1	0	-2.516314	0.626603	4.616571
1	0	-2.448704	-1.871544	4.715379
1	0	-3.795465	-1.941145	3.554592
1	0	-0.397622	-1.371677	3.663476
1	0	1.517028	-0.249178	5.417495
1	0	0.067556	0.540762	4.774585
1	0	1.026362	0.342033	2.458769
1	0	1.933171	1.426043	3.509189
1	0	-0.820736	-3.689293	1.469390
1	0	-3.161518	-4.330490	0.156761
1	0	-1.471819	-4.650553	-0.292144
1	0	-1.293357	-2.147755	-0.841061
1	0	-3.064145	-2.073763	-0.732876
1	0	5.600130	1.376386	0.815683
1	0	8.314761	-1.952894	0.367739
1	0	6.540460	-3.418919	1.395167
1	0	-0.245351	-1.697110	-3.420738
1	0	-0.577593	2.581485	-3.084023
1	0	-4.032270	-0.009072	-3.110074
1	0	0.649589	3.246171	1.591506
1	0	0.763527	1.554272	-0.241898
1	0	-3.224614	0.316005	0.823666
1	0	-3.097831	2.284650	-2.979643
1	0	-1.443153	3.388973	2.964822
1	0	7.821927	0.502598	0.088139
1	0	4.381947	-2.401079	2.069000
1	0	3.651163	-0.339347	3.893118
1	0	2.677358	-1.496969	2.968462
1	0	-4.552700	0.108238	2.488098
1	0	-5.212271	1.107975	3.745473
1	0	-1.324726	-3.685908	-2.663095
1	0	-3.016452	-4.103543	-2.430126
6	0	-2.788883	-2.267419	-3.434537
1	0	-2.574767	-2.621205	-4.448218
1	0	-3.860985	-2.112213	-3.336223
6	0	3.580878	0.086412	1.773617
1	0	2.948790	-0.124010	0.908154
1	0	3.723898	1.163268	1.842976
6	0	-3.651932	2.052206	2.712427
1	0	-4.347852	2.530174	2.019627
1	0	-3.410431	2.760562	3.508966

*** pyridinium_C4_NTf2_cation_cation_b3lyp_6-31+Gp_tetramer_D3.g09

6	0	-7.434792	-1.093044	1.443750
7	0	-6.974536	-0.050817	0.715847
6	0	-7.576017	1.158686	0.768129
6	0	-8.678110	1.365120	1.584983
6	0	-9.167638	0.306497	2.352550
6	0	-8.537697	-0.937170	2.270185
6	0	-4.477374	-0.110465	0.710106

6	0	-3.244927	-0.510000	-0.112984
6	0	-1.981390	-0.481326	0.743429
8	0	-0.831271	-0.958278	0.035356
8	0	1.549698	-1.593947	1.184052
6	0	1.622801	-3.016044	1.433438
6	0	0.242971	-3.659236	1.579953
6	0	0.260462	-5.183970	1.410522
7	0	0.034985	-4.884203	-1.058793
6	0	-1.302383	-5.021903	-1.200533
6	0	-2.009207	-4.220899	-2.078758
6	0	-1.332705	-3.240333	-2.806034
6	0	0.048019	-3.114557	-2.649571
6	0	0.716075	-3.961558	-1.777696
8	0	2.460406	-1.308589	-1.397322
6	0	3.860776	-1.006985	-1.519291
6	0	4.191716	0.411625	-1.064197
6	0	3.837344	0.731826	0.393496
7	0	6.056445	-0.032263	1.266193
6	0	6.671836	1.169087	1.378119
6	0	8.035204	1.292752	1.160984
6	0	8.774485	0.158968	0.814605
6	0	8.121285	-1.069368	0.704690
6	0	6.754429	-1.141785	0.936076
8	0	0.365207	0.291487	-2.073507
6	0	0.814568	1.618309	-2.380102
6	0	-0.386223	2.504319	-2.685478
6	0	-1.263173	2.819880	-1.463850
7	0	-0.386685	5.132019	-1.028688
6	0	-1.449418	5.926758	-1.294953
6	0	-1.255203	7.196771	-1.815089
6	0	0.044745	7.654703	-2.052899
6	0	1.124615	6.814336	-1.775862
6	0	0.876270	5.547794	-1.269311
9	0	4.664492	4.408747	3.250286
6	0	5.057464	5.512792	2.588248
9	0	3.968851	6.129584	2.106227
16	0	6.234776	5.041408	1.188406
7	0	5.297363	4.051769	0.288770
16	0	4.385173	4.564010	-0.931864
8	0	3.981364	5.977270	-0.947498
8	0	7.219609	4.170721	1.846577
8	0	6.648899	6.298294	0.570069
6	0	5.500632	4.360998	-2.440711
9	0	6.588153	5.128855	-2.331246
8	0	3.321658	3.558027	-1.147136
9	0	5.884876	3.079197	-2.570853
9	0	4.815271	4.717942	-3.539955
9	0	5.684566	6.330242	3.442250
9	0	6.636100	-3.265833	-1.245072
6	0	6.278370	-4.261944	-2.088665
9	0	7.308568	-5.101482	-2.214051
9	0	6.007244	-3.716018	-3.283530
16	0	4.747756	-5.138480	-1.427912
8	0	3.767506	-4.035590	-1.337645
8	0	4.518462	-6.236368	-2.363631
7	0	5.259571	-5.677534	-0.005727
16	0	4.773691	-4.991758	1.370962
8	0	4.891269	-3.515688	1.436590
8	0	3.541646	-5.582101	1.918045

6	0	6.189268	-5.607960	2.448499
9	0	5.967034	-5.189791	3.704774
9	0	7.349612	-5.080662	2.019977
9	0	6.279858	-6.937352	2.436949
9	0	-5.205769	-4.593934	-3.561387
6	0	-5.897559	-3.702277	-2.835895
9	0	-5.072171	-2.664693	-2.557724
16	0	-6.558942	-4.478587	-1.244136
8	0	-7.279725	-3.380247	-0.573715
7	0	-5.145863	-4.919091	-0.562997
16	0	-4.608140	-4.400076	0.863704
8	0	-4.967586	-3.027515	1.260899
8	0	-3.200818	-4.805386	0.974293
6	0	-5.508312	-5.489689	2.113125
9	0	-6.835179	-5.307709	1.998738
9	0	-5.224472	-6.778233	1.905687
9	0	-5.131080	-5.150368	3.355610
8	0	-7.300116	-5.648329	-1.704626
9	0	-6.917668	-3.241769	-3.567285
8	0	-2.851660	2.997729	1.727343
16	0	-3.784733	4.083832	1.394468
7	0	-5.042716	3.523846	0.536174
16	0	-5.329565	3.945563	-0.982189
8	0	-4.145747	4.385996	-1.740422
8	0	-3.219878	5.366649	0.945115
6	0	-4.695080	4.446151	3.003274
9	0	-5.641003	5.374128	2.804590
9	0	-5.273124	3.329639	3.474097
9	0	-3.818368	4.898297	3.906990
8	0	-6.220260	2.921613	-1.551752
6	0	-6.427502	5.478019	-0.884536
9	0	-7.538663	5.189205	-0.185007
9	0	-5.783382	6.484115	-0.282231
9	0	-6.775712	5.856926	-2.120949
1	0	-3.079435	-4.360902	-2.140663
1	0	8.647964	-1.978208	0.435772
1	0	-10.029848	0.444626	2.998390
1	0	2.231624	-1.431699	-0.440000
1	0	5.259047	0.597487	-1.249899
1	0	3.656874	1.128487	-1.693759
1	0	4.112595	-1.134848	-2.576440
1	0	4.427126	-1.764632	-0.964996
1	0	1.172422	-0.252386	-1.871694
1	0	1.480566	1.587611	-3.253426
1	0	1.394598	2.024662	-1.540110
1	0	-0.589927	-0.376663	-0.725878
1	0	-1.800822	0.526911	1.140156
1	0	-2.098411	-1.160367	1.594867
1	0	-3.373104	-1.524677	-0.506877
1	0	-3.121814	0.163003	-0.974179
1	0	0.641750	-1.350969	0.864849
1	0	2.218863	-3.162952	2.337844
1	0	2.193582	-3.466533	0.616261
1	0	-0.441180	-3.228364	0.839873
1	0	-0.184922	-3.419127	2.561156
1	0	1.665776	4.837884	-1.062619
1	0	0.211522	8.651262	-2.451070
1	0	-2.124204	7.813206	-2.017270
1	0	-6.907459	-2.030573	1.330874

1	0	-8.891836	-1.792427	2.835445
1	0	-9.139353	2.346444	1.602072
1	0	-1.814908	-5.706546	-0.541005
1	0	-1.879027	-2.573827	-3.467513
1	0	1.787054	-3.926177	-1.628662
1	0	8.465840	2.281814	1.262228
1	0	9.842020	0.233194	0.629861
1	0	6.194849	-2.069285	0.887389
1	0	0.621810	-2.354665	-3.167160
1	0	6.054586	2.023391	1.619314
1	0	-7.155668	1.926468	0.133162
1	0	2.158153	7.105731	-1.931919
1	0	-2.421737	5.510032	-1.074107
1	0	-0.747263	-5.565533	1.608387
1	0	0.941944	-5.651496	2.130481
1	0	2.769273	0.557775	0.572921
1	0	4.023654	1.795570	0.570357
1	0	-1.487773	1.902251	-0.907885
1	0	-2.230108	3.225918	-1.778308
1	0	-4.378728	0.916712	1.072022
1	0	-4.551549	-0.771162	1.581728
1	0	-0.008652	3.433670	-3.134295
1	0	-0.999268	2.016630	-3.453065
6	0	0.722381	-5.655391	0.020003
1	0	0.494702	-6.714412	-0.130453
1	0	1.793454	-5.513277	-0.123645
6	0	-5.753576	-0.241353	-0.123733
1	0	-5.794578	0.510074	-0.915177
1	0	-5.839533	-1.235099	-0.559899
6	0	-0.610868	3.767596	-0.458091
1	0	-1.236118	3.881263	0.429324
1	0	0.372202	3.407957	-0.147320
6	0	4.570682	-0.107648	1.444833
1	0	4.352653	0.262339	2.450668
1	0	4.295454	-1.162020	1.406217

4. Molecular Dynamics (MD) simulations of $[HOC_4Py][NTf_2]$

We did NpT molecular dynamics simulation using GROMACS 5.0.6 [4–8] over a temperature range from $T = 300$–$400\,\mathrm{K}$ and a pressure of $p = 1\,\mathrm{bar}$. A cubic simulation box containing 512 ion pairs was first equilibrated for 2 ns at $T = 500\,\mathrm{K}$ employing the BERENDSEN thermostat as well as the BERENDSEN barostat [9] with coupling times of $\tau_\mathrm{T} = \tau_\mathrm{p} = 0.5\,\mathrm{ps}$. After that, another equlibration for 2 ns at the desired temperature of 300 K, 320 K, 340 K, 360 K, 380 K, or 400 K followed. Production runs of 100 ns length utilizing the NOSÉ-HOOVER thermostat [10, 11] with $\tau_\mathrm{T} = 1\,\mathrm{ps}$ and RAHMAN-PARRINELLO barostat [12, 13] with $\tau_\mathrm{p} = 2\,\mathrm{ps}$ were performed for each temperature.
All simulations were done with a 2.0 fs time step employing periodic boundary conditions and the LINCS algorithm [14] for fixed bond lengths. The smooth particle mesh EWALD summation [15] was applied with a mesh spacing of 0.12 nm, a real space cutoff of 0.9 nm and 4th order interpolation. The relative accuracy of the EWALD sum was set to 10^{-5} corresponding to a convergence factor $\alpha = 3.38\,\mathrm{nm}^{-1}$. The forcefield of the $[NTf_2]^-$ anion is published in reference [16]. The cation forcefield is derived from the OPLS forcefield for pyridine from Jorgensen [17, 18]. The diheadral potentials were fitted on ab initio calculations employing second order Møller-Plesset perturbation theory using the cc-pvtz basis set. The point charges were derived from the electostatic potential according to the CHelpG scheme [19]. All forcefield parameters for the cation can be found below.

Table 1: LENNARD-JONES parameter σ and ϵ for all interactions sites of the $[HOC_4Py]^+$ cation.

site	σ / Å	$\epsilon \cdot k_\mathrm{B}^{-1}$ / K
N	3.25	85.55
C_a	3.55	35.23
H_a	2.42	15.10
C_c	3.50	33.20
H_c	2.50	15.10
O	3.12	85.60
H_o	0.00	0.00

Table 2: Bond length $r^0_{\kappa\lambda}$ and angle parameters $\phi^0_{\kappa\lambda\omega}$ und $k^{\mathrm{a}}_{\kappa\lambda\omega}$ for the angle potential $V^{\mathrm{a}}_{\kappa\lambda\omega} = \frac{1}{2}k^{\mathrm{a}}_{\kappa\lambda\omega}(\phi_{\kappa\lambda\omega} - \phi^0_{\kappa\lambda\omega})^2$ in the force field of the $[HOC_4Py]^+$ cation.

bond	$r^0_{\kappa\lambda}$ / Å	angle	$\phi^0_{\kappa\lambda\omega}$ / °	$k^{\mathrm{a}}_{\kappa\lambda\omega}$ / kJ mol^{-1}rad^{-2}
C_a-N	1.339	C_a-C_a-C_a	120.0	527.20
C_a-H_a	1.080	C_a-C_a-N	124.0	585.80
C_a-C_a	1.400	C_a-N-C_a	117.0	585.80
N-C_c	1.339	C_a-C_a-H_a	120.0	292.90
C_c-C_c	1.529	N-C_a-H_a	116.0	292.90
C_c-H_c	1.090	C_a-N-C_c	121.5	585.80
C_c-O	1.410	N-C_c-C_c	112.7	487.43
O-H_o	0.945	H_c-C_c-N	110.7	313.26
		H_c-C_c-H_c	107.8	275.70
		H_c-C_c-C_c	110.7	313.26
		C_c-C_c-C_c	112.7	487.43
		H_o-O-C_c	108.5	460.55
		C_c-C_c-O	109.5	418.68
		H_c-C_c-O	109.5	293.08

Table 3: Parameters m_n, k_m^{dp} and ψ_m^0 for the torsion potential $V_{\kappa\lambda\omega\tau}^{\mathrm{dp}} = \sum_n k_m^{\mathrm{dp}}[1 + \cos(m_n\psi_m - \psi_m^0)]$ in the force field of the $[HOC_4Py]^+$ cation.

	$n(\kappa\lambda\omega\tau)$	m_n	k_m^{dp} / kJ mol^{-1}	ψ_m^0 / °
X-C_a-C_a-X	1	2	15.1780	180.0
X-C_a-N-X	1	2	15.1780	180.0
C_a-N-C_c-C_c	1	2	-0.3579	0
C_a-N-C_c-C_c	2	4	-0.4037	0
C_c-C_c-C_c-C_c	1	1	-0.2825	0.0
	2	2	0.6065	0.0
	3	3	4.6858	0.0
	4	4	0.7018	0.0
	5	5	0.4468	0.0
	6	6	0.4564	0.0
C_c-C_c-C_c-O	1	1	-2.3748	0.0
	2	3	6.8089	0.0
	3	4	0.9531	0.0
C_c-C_c-O-H_o	1	1	-3.5552	0.0
	2	2	0.5886	0.0
	3	3	2.5272	0.0
	4	4	0.1504	0.0
C_a-C_a-C_a-H_a	1	2	4.6060	180.0
C_a-N-C_a-H_a	1	2	4.6060	180.0
C_a-C_a-N-C_c	1	2	4.6060	180.0

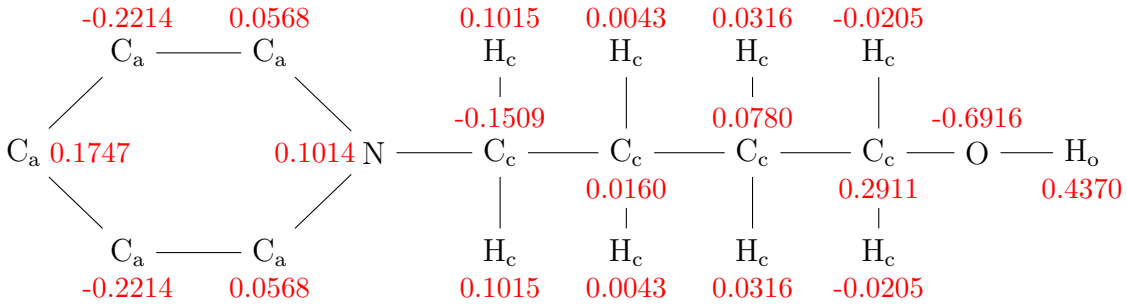

Figure 1: Structure of the $[HOC_4Py]^+$ cation with atom types and corresponding point charges in red.

5. Hydrogen bond criteria in MD and ND

In the MD as well as the ND experiments the hydrogen bonds were defined by geometric criteria: 1) By the intermolecular hydrogen-oxygen distance r_{OH} with $r_{\mathrm{OH}} < 2.7\,\text{Å}$ (2.8 Å for cation-anion hydrogen bonds) and 2) the hydrogen bond angle ($\angle$OHO) α with $\cos(\alpha) < -0.5$. These criteria were devised from the weighted logarithmic probability density shown in figures 2, 3, 6, and 7.
The figures 4 and 8 show the probability density of finding an intermolecular hydrogen-oxygen pair with a hydrogen bond angle α of $\cos(\alpha) < -0.5$ at a certain r_{OH} distance up to 5 Å. In both cases the cation-cation hydrogen bond is defined by smaller hydrogen bond lenghts suggesting a stronger hydrogen bond.
The figures 5 and 9 show the probability density of finding an intermolecular hydrogen-oxygen pair with a hydrogen bond length $r_{\mathrm{OH}} < 2.7\,\text{Å}$ for a cation-cation pair or $r_{\mathrm{OH}} < 2.8\,\text{Å}$ for a cation-anion pair respectively with a specific hydrogen bond angle α. Both hydrogen bonds favor a linear arrangement.However, the cation-anion hydrogen bond is characterized by a wider angle distribution.

5.1 MD

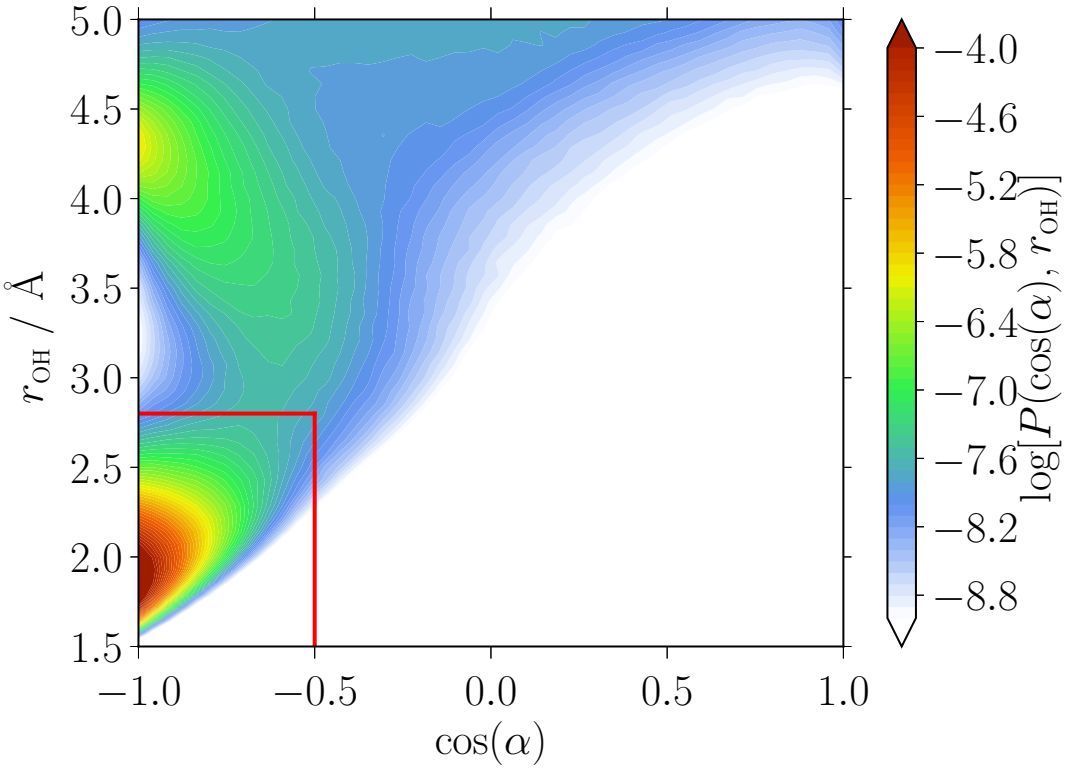

Figure 2: Logarithmic representation of the probability density of finding an intermolecular O-H distance r_{OH} between an anion and a cation and the cosine of the hydrogen bond angle α between the intermolecular O-H vector and the intramolecular O-H vector obtained at 300 K from molecular dynamics simulation and weighted with r^{-2}. The red solid line indicates the hydrogen bond criteria used in this work.

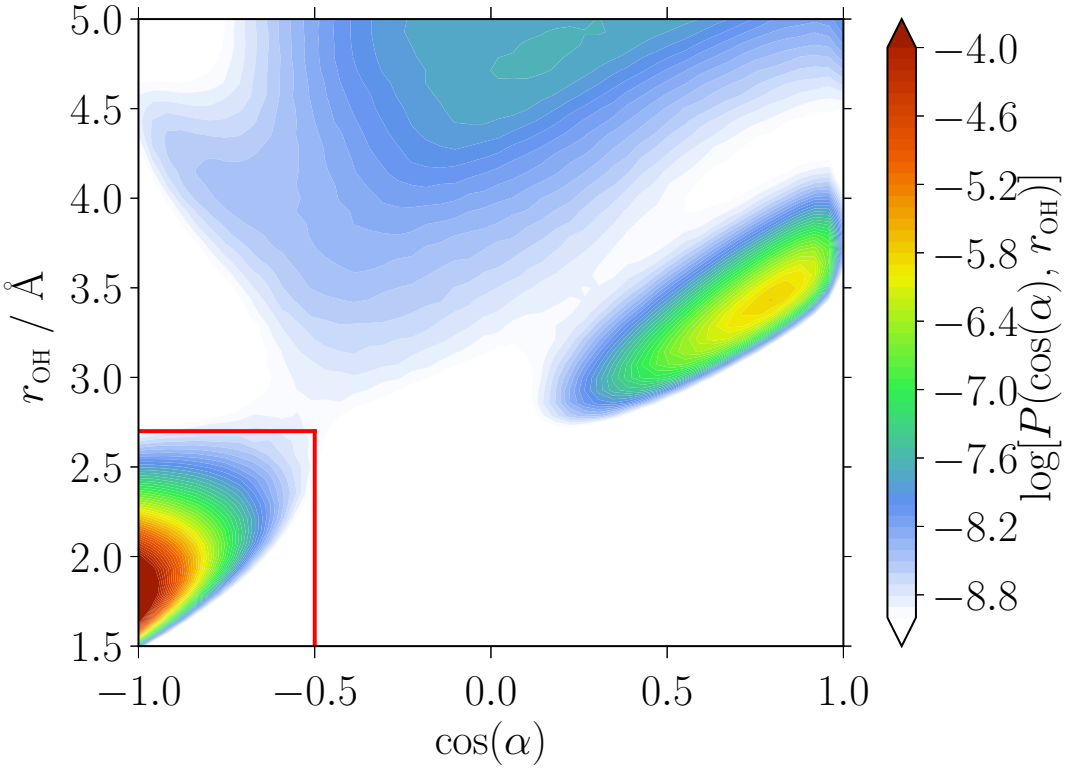

Figure 3: Logarithmic representation of the probability density of finding an intermolecular O-H distance r_{OH} between two cations and the cosine of the hydrogen bond angle α between the intermolecular O-H vector and the intramolecular O-H vector obtained at 300 K from molecular dynamics simulation and weighted with r^{-2}. The red solid line indicates the hydrogen bond criteria used in this work.

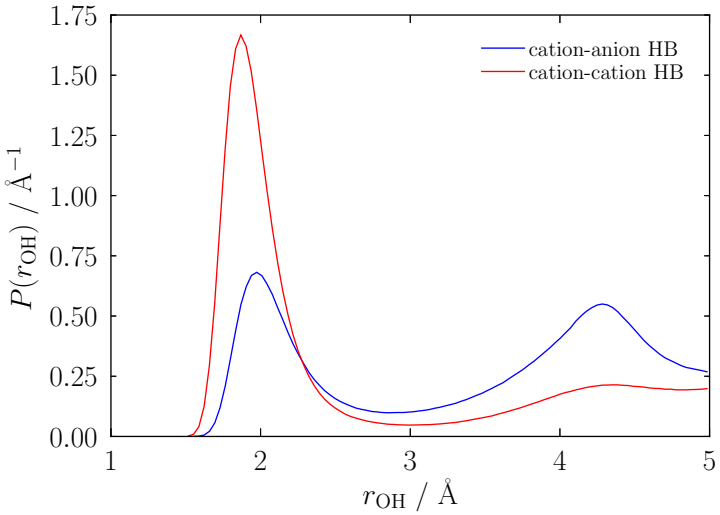

Figure 4: Probability density function of the intermolecular distances r_{OH} for $\cos(\alpha) < -0.5$ obtained from molecular dynamics simulations.

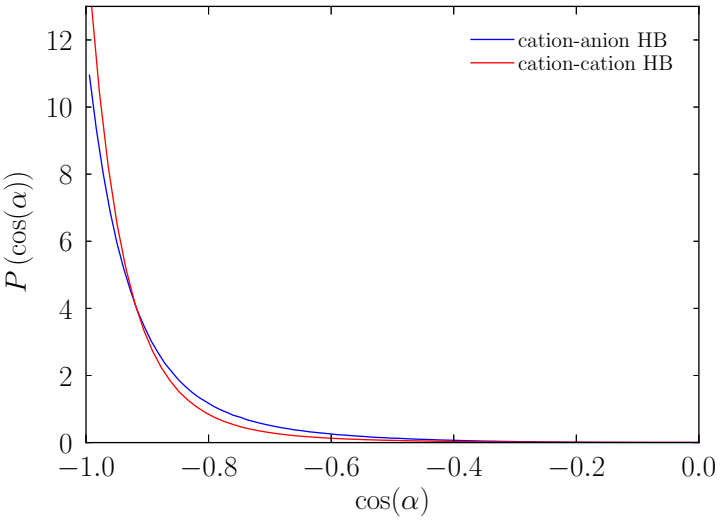

Figure 5: Probability density function of the hydrogen bond angles $\cos(\alpha)$ for $r_{OH} < 2.7\,\text{Å}$ for a cation-cation pair or $r_{OH} < 2.8\,\text{Å}$ obtained from molecular dynamics simulations.

5.2 ND

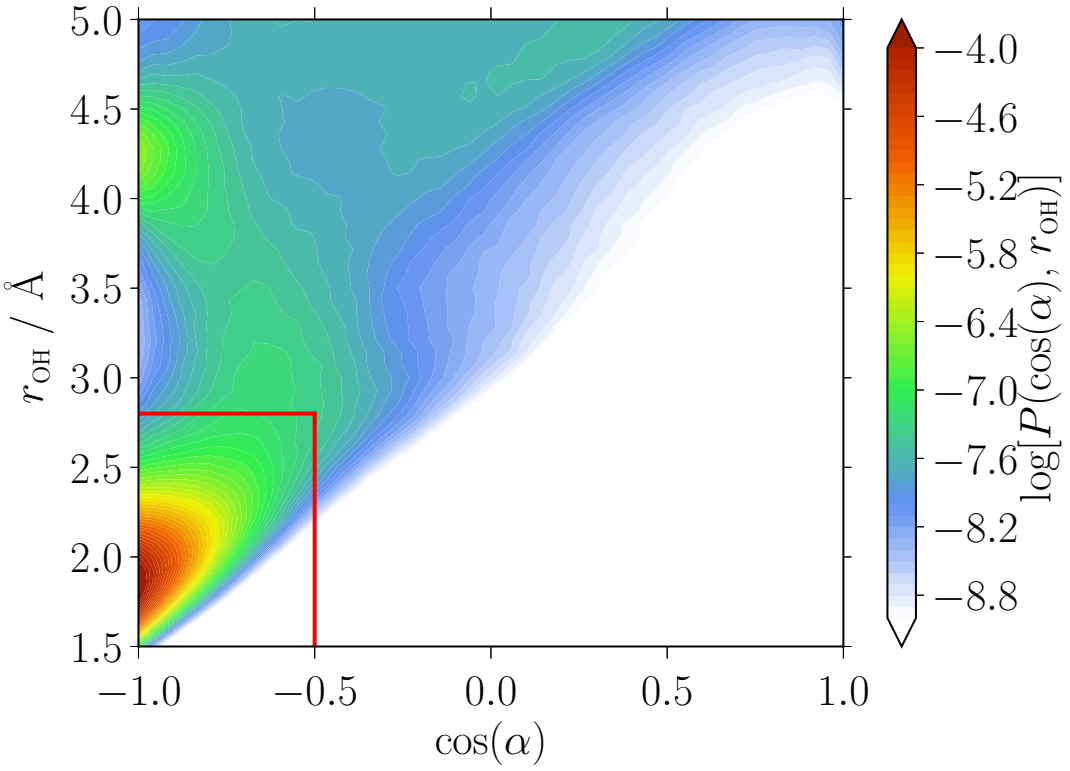

Figure 6: Logarithmic representation of the probability density of finding an intermolecular O-H distance r_{OH} between an anion and a cation and the cosine of the hydrogen bond angle α between the intermolecular O-H vector and the intramolecular O-H vector obtained at 300 K from the ND experiments and weighted with r^{-2}. The red solid line indicates the hydrogen bond criteria used in this work.

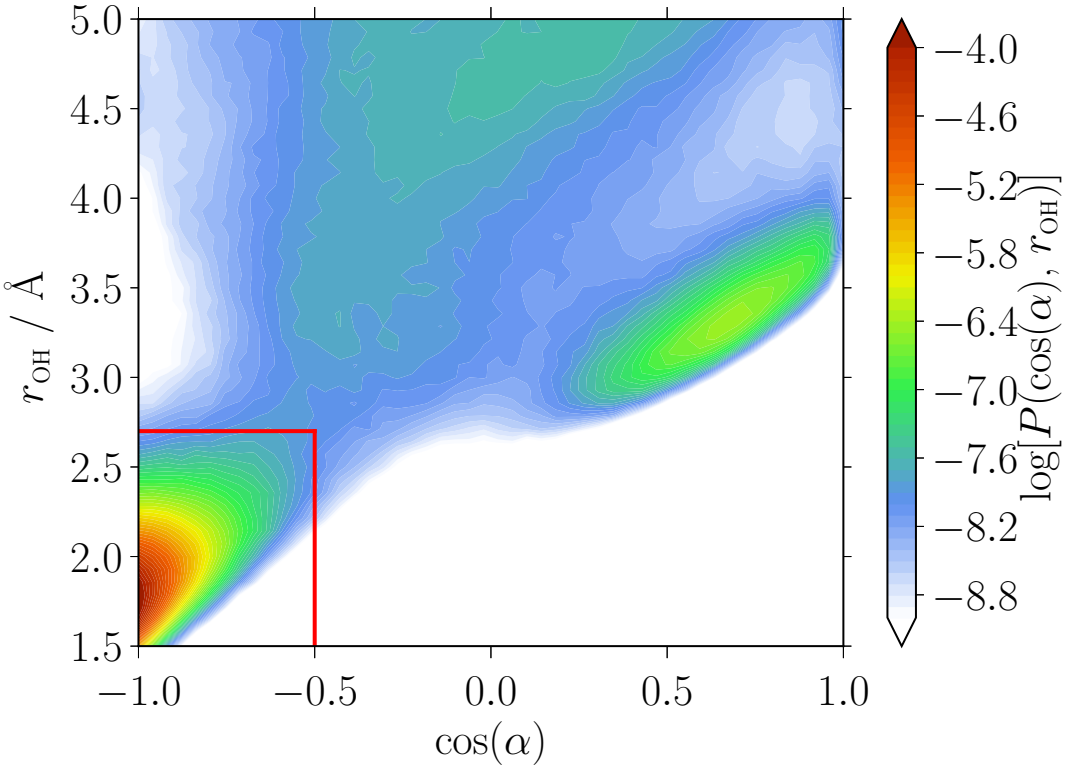

Figure 7: Logarithmic representation of the probability density of finding an intermolecular O-H distance r_{OH} between two cations and the cosine of the hydrogen bond angle α between the intermolecular O-H vector and the intramolecular O-H vector obtained at 300 K from the ND experiments and weighted with r^{-2}. The red solid line indicates the hydrogen bond criteria used in this work.

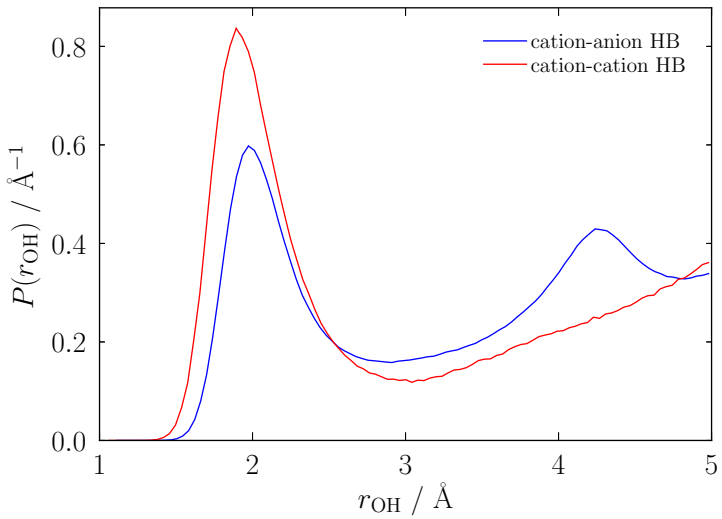

Figure 8: Probability density function of the intermolecular distances r_{OH} for $\cos(\alpha) < -0.5$ obtained from the ND experiments.

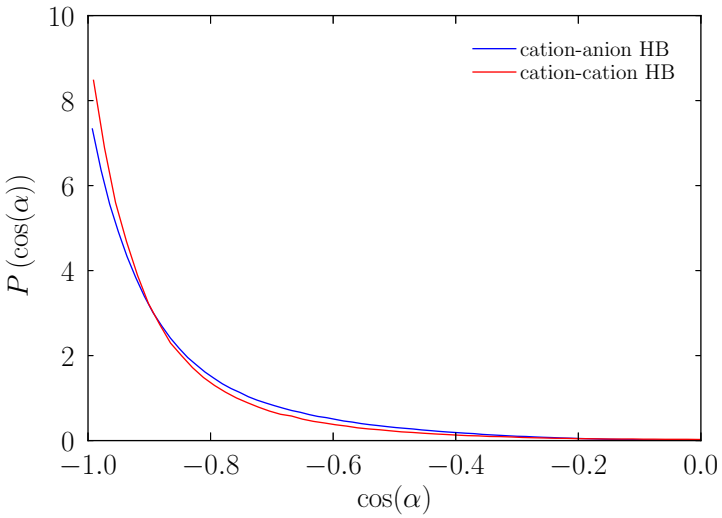

Figure 9: Probability density function of the hydrogen bond angles $\cos(\alpha)$ for $r_{OH} < 2.7\,\text{Å}$ for a cation-cation pair or $r_{OH} < 2.8\,\text{Å}$ obtained from the ND experiments.

References

[1] A. K. Soper, *GudruN and GudrunX: Programs for correcting raw neutron and x-ray total scattering data to differential cross section*, Rutherford Appleton Laboratory, Didcot, **2012**.

[2] A. K. Soper, D. Bowron, H. Thompson, F. Bruni, M. A. Ricci, S. McLain, S. Klotz, T. Staessle, S. Imberti, R. Rowan, Hargreaves, T. Youngs, S. Callear, C. Salzmann, *Empirical Potential Structure Refinement: A Users's Guide*, Rutherford Appleton Laboratory, Didcot, **2017**.

[3] S. Callear, T. Youngs, A. Scoper, T. Headen, S. Imberti, *EPSRgui Manual*, Rutherford Appleton Laboratory, Didcot, **2017**.

[4] E. Lindahl, B. Hess, D. van der Spoel, "Gromacs 3.0: A package for molecular simulation and trajectory analysis", *J. Mol. Mod.* **2001**, *7*, 306–317.

[5] H. J. C. Berendsen, D. van der Spoel, R. van Drunen, "Gromacs: A Message-Passing Parallel Molecular Dynamics Implementation", *Comp. Phys. Comm.* **1995**, *91*, 43–46.

[6] B. Hess, C. Kutzer, D. van der Spoel, E. Lindahl, "Gromacs 4: Algorithms for highly efficient, load-balanced, and scalable molecular simulation", *J. Chem. Theory Comput.* **2008**, *4*, 435–447.

[7] S. Pronk, S. Pall, R. Schulz, P. Larsson, P. Bjelkmar, R. Apostolov, M. R. Shirts, J. C. Smith, P. M. Kasson, D. van der Spoel, B. Hess, E. Lindahl, "Gromacs 4.5: A high-throughput and highly parallel open source molecular simulation toolkit", *Bioinformatics* **2013**, *29*, 845–54.

[8] M. Abraham, B. Hess, D. van der Spoel, E. Lindahl, E. Apol, R. Apostolov, H. J. C. Berendsen, A. van Buuren, P. Bjelkmar, R. van Drunen, A. Feenstra, S. Fritsch, G. Groenhof, C. Jungshans, J. Hub, P. Kasson, C. Kutzner, B. Lambeth, P. Larsson, J. A. Lemkul, E. Marklund, P. Meulenhoff, T. Murtola, S. Pall, S. Pronk, R. Schulz, M. Shirts, A. Sijbers, P. Tieleman, C. Wennberg, M. Wolf, Gromacs 5.0.6, **2015**.

[9] H. J. C. Berendsen, J. P. M. Postma, W. F. van Gunsteren, A. DiNola, J. R. Haak, "Molecular dynamics with coupling to an external bath", *J. Chem. Phys.* **1984**, *81*, 3684–3690.

[10] S. Nosé, "A molecular dynamics method for simulating in the canonical ensemble", *Mol. Phys.* **1984**, *52*, 255–268.

[11] W. G. Hoover, "Canonical Dynamics: Equilibrium Phase space distributions", *Phys. Rev. A* **1985**, *31*, 1695–1697.

[12] M. Parrinello, A. Rahman, "Polymorphic transitions in single crystals: A new molecular dynamics method", *J. Appl. Phys.* **1981**, *52*, 7182–7180.

[13] S. Nosé, M. L. Klein, "Constant pressure molecular dynamics for molecular systems", *Mol. Phys.* **1983**, *50*, 1055–1076.

[14] B. Hess, H. Bekker, H. J. C. Berendsen, J. G. E. M. Fraaije, "LINCS: A linear constraint solver for molecular simulations", *J. Comp. Chem.* **1997**, *18*, 1463–1472.

[15] U. Essmann, L. Perera, M. L. Berkowitz, T. A. Darden, H. Lee, L. G. Pedersen, "A smooth particle mesh Ewald method", *J. Chem. Phys.* **1995**, *103*, 8577–8593.

[16] J. Neumann, B. Golub, L.-M. Odebrecht, R. Ludwig, D. Paschek, "Revisiting imidazolium based ionic liquids: Effect of the conformation bias of the [ntf2] anion studied by molecular dynamics simulations", *The Journal of Chemical Physics* **2018**, *148*, 193828.

[17] W. L. Jorgensen, D. S. Maxwell, J. Tirado-Rives, "Development and testing of the OPLS all-atom force field on conformational energetics and properties of organic liquids", *Journal of the American Chemical Society* **1996**, *118*, 11225–11236.

[18] W. L. Jorgensen, N. A. McDonald, "Development of an all-atom force field for heterocycles. Properties of liquid pyridine and diazenes", *Journal of Molecular Structure: THEOCHEM* **1998**, *424*, 145–155.

[19] C. M. Breneman, K. B. Wiberg, "Determining atom-centered monopoles from molecular electrostatic potentials. The need for high sampling density in formamide conformational analysis", *Journal of Computational Chemistry* **1990**, *11*, 361–373.

III. Hydrogen Bonding Between Ions of Like Charge in Ionic Liquids Characterized by NMR Deuteron Quadropole Coupling Constants – Comparison with Salt Bridges and Molecular Systems

A. E. Khudozhitkov, J. Neumann, T. Niemann, D. Zaitsau, P. Stange, D. Paschek, A. G. Stepanov, D. I. Kolokolov, R. Ludwig, *Angew. Chem. Int. Ed.* **2019**, *58*, 17863.
DOI: 10.1002/anie.201912476

Contribution: I provided the force fields as well as the MD simulations of the ILs and the temperature dependent HB populations from those simulations to this publication. Some corrections of the draft of the manuscript were done by me and I participated in its revision. Around 15 % of the work for this publication were done by me.

Ionic Liquids

International Edition: DOI: 10.1002/anie.201912476
German Edition: DOI: 10.1002/ange.201912476

Hydrogen Bonding Between Ions of Like Charge in Ionic Liquids Characterized by NMR Deuteron Quadrupole Coupling Constants—Comparison with Salt Bridges and Molecular Systems

Alexander E. Khudozhitkov, Jan Neumann, Thomas Niemann, Dzmitry Zaitsau, Peter Stange, Dietmar Paschek, Alexander G. Stepanov, Daniil I. Kolokolov, and Ralf Ludwig**

Abstract: *We present deuteron quadrupole coupling constants (DQCC) for hydroxyl-functionalized ionic liquids (ILs) in the crystalline or glassy states characterizing two types of hydrogen bonding: The regular Coulomb-enhanced hydrogen bonds between cation and anion (c–a), and the unusual hydrogen bonds between cation and cation (c–c), which are present despite repulsive Coulomb forces. We measure these sensitive probes of hydrogen bonding by means of solid-state NMR spectroscopy. The DQCCs of (c–a) ion pairs and (c–c) H-bonds are compared to those of salt bridges in supramolecular complexes and those present in molecular liquids. At low temperatures, the (c–c) species successfully compete with the (c–a) ion pairs and dominate the cluster populations. Equilibrium constants obtained from molecular-dynamics (MD) simulations show van't Hoff behavior with small transition enthalpies between the differently H-bonded species. We show that cationic-cluster formation prevents these ILs from crystallizing. With cooling, the (c–c) hydrogen bonds persist, resulting in supercooling and glass formation.*

Introduction

Salt bridges play an important role in proteins and supramolecular chemistry.[1–14] They are characterized by the sum of two types of intermolecular interaction: ionic bonding and hydrogen bonding. Salt bridges are very strong because hydrogen bonding adds to the attractive Coulomb forces between the oppositely charged residues. Typical examples of salt bridges involve the interaction of negatively charged carboxylate groups, as found, for example, in glutamic acid and aspartic acid, with positively charged ammonium groups, as present, for example, in lysine or arginine. An important example is the salt bridge between primary ammonium and carboxylate groups in biological structures, $^{+}N{-}H\cdots O^{-}$.[7–14] The energetics of salt bridges are typically dominated by the Coulomb interaction between the charge centers, but the total interaction remains directional due to the hydrogen bonds. Thus, salt bridges are crucial for the structure, dynamics, and function of proteins. This type of Coulomb-enhanced hydrogen bonding is typical for ionic liquids, which consist solely of ions.[15–19] So-called "doubly ionic hydrogen bonds" (DIHB) usually result in the formation of ion pairs.[20–25] However, H-bonds in ionic liquids are manifold. They can also be present between ions of like charge.[26–36] This has recently been shown for cation–cation interaction by means of vibrational spectroscopy and neutron diffraction (ND).[37,38] In this case, the Coulomb forces are repulsive and need to be counterbalanced by hydrogen bonding. For hydroxyl-functionalized ILs, both types of ionic interaction are present in equilibrium: hydrogen bonding (O–H···O) between oppositely charged ions (c–a) and between like-charged ions, here cations (c–c). In principle, solid-state NMR spectroscopy allows to distinguish between (c–a) and (c–c) interactions if the proton exchange is slow on the NMR time scale.[39–42] Although very sensitive to the electronic environment and hydrogen bonding, deuteron quadrupole coupling constants (DQCCs) have been rarely used to characterize salt bridges in proteins, supramolecular complexes, and the related (c–a) type of interaction in ionic liquids.[43,44] DQCCs of OH groups that are involved in hydrogen bonding to like-charged ions (c–c) are completely unknown. The main challenge here is that in the liquid phase, the proton exchange between (c–a)- and (c–c)-bound species is usually fast on the NMR time scale, resulting in averaged coupling parameters and prohibiting to distinguish like-charge attraction (c–c) from the regular ion-

[*] A. E. Khudozhitkov, Prof. Dr. A. G. Stepanov, Dr. D. I. Kolokolov
Boreskov Institute of Catalysis
Siberian Branch of Russian Academy of Sciences
Prospekt Akademika Lavrentieva 5, Novosibirsk 630090 (Russia)
E-mail: kdi@catalysis.ru

J. Neumann, T. Niemann, P. Stange, Dr. D. Paschek, Prof. Dr. R. Ludwig
Universität Rostock, Institut für Chemie
Abteilung für Physikalische Chemie
Dr.-Lorenz-Weg 2, 18059 Rostock (Germany)
E-mail: ralf.ludwig@uni-rostock.de

Dr. D. Zaitsau, Prof. Dr. R. Ludwig
Department LL&M, University of Rostock
Albert-Einstein-Str. 25, 18059 Rostock (Germany)

Prof. Dr. R. Ludwig
Leibniz-Institut für Katalyse an der Universität Rostock e.V.
Albert-Einstein-Str. 29a, 18059 Rostock (Germany)

A. E. Khudozhitkov, Prof. Dr. A. G. Stepanov, Dr. D. I. Kolokolov
Novosibirsk State University
Pirogova Street 2, Novosibirsk 630090 (Russia)

Supporting information and the ORCID identification number(s) for the author(s) of this article can be found under: https://doi.org/10.1002/anie.201912476.

pair formation (c–a). This situation may change favorably in the supercooled or glassy state of ionic liquids.

It is the purpose of this work to show that the DQCCs and the related asymmetry parameters of the electric-field gradients provide valuable information about the strength and directionality of both types of hydrogen bonding present in hydroxyl-functionalized ionic liquids. We find one NMR coupling parameter for ILs exhibiting (c–a) ion pairing, but two if additional (c–c) cationic-cluster formation is present. We measure the first DQCCs describing hydrogen bonding between ions of like charge and show that they are unexpectedly smaller than those in the (c–a) ion pairs. Solid-state NMR spectroscopy allows for counting the (c–a)- and (c–c)-bound species and thus providing cluster populations. Overall, we show that cationic-cluster formation in well-suited ILs depends on the polarizability of the cations and the length of the hydroxyalkyl chain. If cationic-cluster formation is present, the ILs cannot be crystallized and form glasses. The solid-state NMR measurements are supported by density functional theory (DFT) calculations, differential scanning calorimetry (DSC) measurements, and MD simulations, which provide molecular insight into the H-bond patterns and the delicate balance between the two types of ion pairing.

Results and Discussion

Synthesis and Preparation of Suitable Hydroxyl-Functionalized ILs

We synthesized the ionic liquids 1-(2-hydroxyethyl)-1-methyl-piperidinium bis(trifluoromethylsulfonyl)imide [HOC_2MPip][NTf_2] (**I**), 1-(2-hydroxyethyl)pyridinium bis(trifluoromethylsulfonyl)imide [HOC_2Py][NTf_2] (**II**), 1-(3-hydroxypropyl)-1-methyl-piperidinium bis(trifluoromethylsulfonyl)imide [HOC_3MPip][NTf_2] (**III**), and 1-(3-hydroxybutyl)pyridinium bis(trifluoromethylsulfonyl)imide [HOC_3Py]-[NTf_2] (**IV**) using well-established protocols (see Supporting Information). The ILs were prepared in two steps: We synthesized the OH-functionalized onium halides, which were then used for the anion metathesis to create the desired cation/anion combinations. For the synthesis of the onium salts, we mixed equimolar amounts of the heterocyclic amine and the corresponding ω-halide alcohol and heated the mixture up to 110 °C for 1 h. Upon cooling, the mixture started to crystallize. The crude products were recrystallized from acetone/acetonitrile mixtures to obtain the colorless crystalline product. For the metathesis of the anion (bis(trifluoromethylsulfonyl)imide, [NTf_2]$^-$), we mixed equimolar amounts of the onium halide and lithium-bis(trifluoromethylsulfonyl)imide as aqueous solutions for 1 h. Two phases were obtained. The lower phase was washed several times with water until no residual bromine could be detected with silver nitrate solution. The resulting colorless ionic liquids were dried for several hours under vacuum at 60 °C. For detailed synthesis procedures and analytical data of each ILs see the Supporting Information.

As described, all ILs (**I**–**IV**) include the same [NTf_2]$^-$ counteranion and the same hydroxyl-functional groups at the cations. This set of hydroxyl-functionalized ILs allows studying cationic-cluster (c–c) formation depending on the polarizability of the cation and the hydroxyalkyl chain lengths (see Scheme 1). Hydrogen/deuterium (H/D) exchange was achieved by mixing the ILs with D_2O and removing water several times until nearly 100 % deuteration was reached as confirmed by ^{1}H NMR. All samples were dried under vacuum (at 3×10^{-3} mbar) for several days and the final water concentration (< 15 ppm) was checked by Karl-Fischer titration.

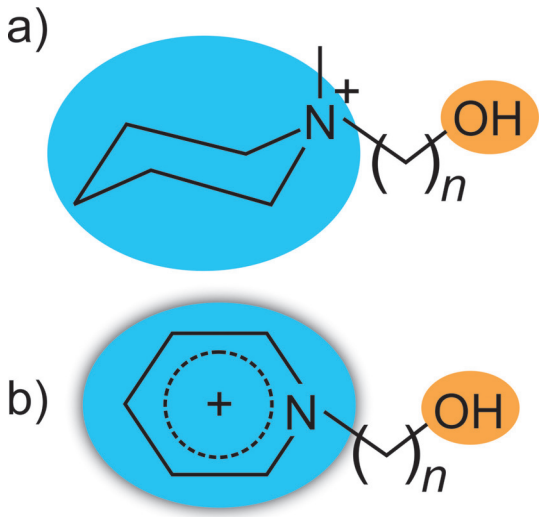

Scheme 1. a) 1-(*n*-hydroxyalkyl)-1-methyl-piperidinium and b) 1-(*n*-hydroxyalkyl)pyridinium cations as present in the ILs [HOC_nPip][NTf_2] with n = 2,3 (**I**, **III**) and [HOC_nPy][NTf_2] with n = 2,3 (**II**, **IV**). The two cations differ in polarizability. Moreover, we study (c–c) cluster formation by variation of the hydroxyalkyl chain length.

Deuteron Quadrupole Coupling Constants from Solid-State NMR Spectroscopy

The solid-state deuterium NMR spectrum is determined by two measurable parameters: the quadrupole coupling constant DQCC, $\chi_D = (e^2 q_{zz} Q/h)$, and the asymmetry parameter, $\eta = (q_{xx} - q_{yy})/q_{zz}$, which describes the principle elements q of the electric-field gradient tensor.[45–47] The DQCC is a measure of the magnitude of the electric-field gradient at the deuterium site, while the asymmetry parameter provides information about the shape of the electric-field gradient. For example, an asymmetry parameter of zero suggests a cylindrical symmetry of the electric-field gradient tensor along the O–D bond.[47] We determined the DQCCs from the solid-state deuterium NMR powder patterns for ILs **I**–**IV** at 183 K (see Supporting Information).

The ^{2}H NMR experiments were performed at a Larmor frequency of $\omega_z/2\pi = 61.42$ MHz on a Bruker Avance-400 spectrometer using a high-power probe with a 5 mm horizontal solenoid coil. All ^{2}H NMR spectra were obtained by Fourier transformation of the quadrature-detected phase-cycled quadrupole echo arising in the pulse sequence ($90°_x$–τ_1–$90°_y$–τ_2–acquisition–t), where $\tau_1 = 20$ μs, $\tau_2 = 21$ μs, and t is

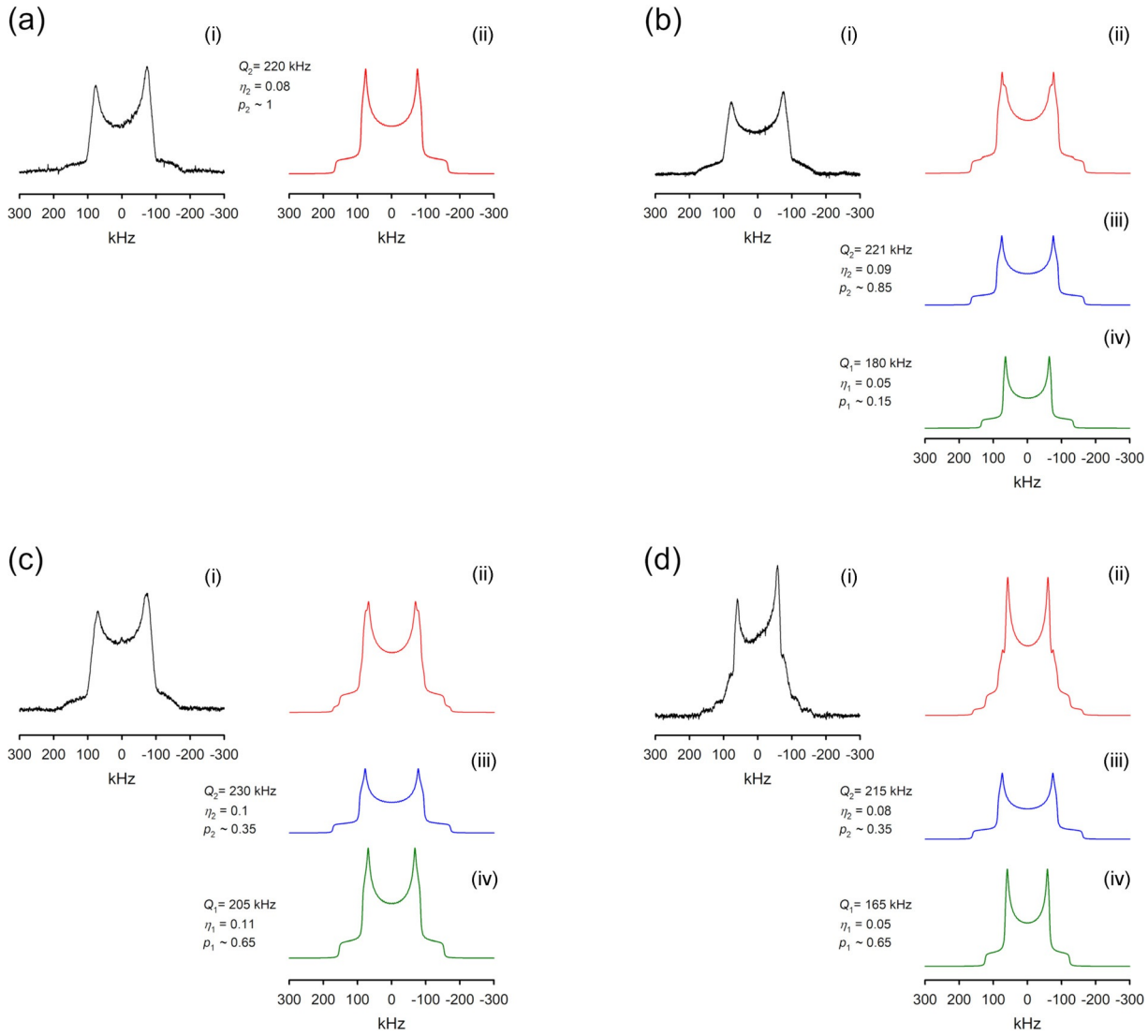

Figure 1. ^{2}H NMR spectra at 183 K and line-shape analysis for ILs **I** [HOC_2MPip][NTf_2] (a), **II** [HOC_2Py][NTf_2] (b), **III** [HOC_3MPip][NTf_2] (c), and **IV** [HOC_3Py][NTf_2] (d). i) measured spectra, ii) simulated spectra, iii) deconvoluted (c–a) spectra, iv) deconvoluted (c–c) spectra. Q denotes the DQCCs, η the asymmetry parameters, and p the relative populations (fractions) of the (c–c)- (index 1) and (c–a)-bound species (index 2).

a repetition time of the sequence during the accumulation of the NMR signal. The duration of the $\pi/2$ pulse was 1.6–1.7 μs. Spectra were typically obtained with 50–20 000 scans with a repetition time ranging from 0.5 to 15 s.

All spectra show purely Pake-powder patterns.[39,40] We obtained the DQCCs and the asymmetry parameters from a proper line-shape analysis. The deconvoluted spectra result from a parameter optimization guided by visual inspection. The measured, analyzed, and modelled spectra are shown in Figure 1. The experimental accuracy of χ_D and η is ± 3 kHz and ± 0.01, respectively, for the dominant component, and ± 5 kHz and ± 0.02, respectively, for the second component of the Pake spectra. For IL **I** we observed a single Pake-spectrum with $\chi_D = 220$ kHz and $\eta = 0.08$ (see Figure 1 a). In contrast, we could deconvolute the measured spectrum of IL **II** into two Pake patterns. One deconvoluted spectrum exhibits almost the same NMR parameters as IL **I** ($\chi_D =$ 221 kHz; $\eta = 0.09$), obviously describing the same type of O–D···O interaction in both ILs. However, the second deconvoluted spectrum is clearly different and shows a smaller DQCC and asymmetry parameter, namely $\chi_D = 180$ kHz and $\eta = 0.05$ (see Figure 1 b). Smaller DQCCs suggest that the O–D···O interaction is stronger. We know from recent IR and ND experiments that (c–c) hydrogen bonds are stronger than the (c–a) ones, resulting in significant IR red-shifts of the OH/OD stretching frequencies, lengthening of the R(O–H) bonds and shortening of the intermolecular R(O–H···O) and R(O···O) distances.[37,38] Thus, we conclude that the larger DQCC in both ILs of about 220 kHz can be related to the conventional (c–a) ion pairs, whereas the smaller DQCC of about 180 kHz characterizes the (c–c) interaction in cationic clusters. The smaller asymmetry parameter, 0.05 vs. 0.09, indicates that the hydrogen bond is more linear in (c–c) than in (c–a) hydrogen bonds, in accord with the above finding of stronger H-bonds in the cationic clusters. The fact that IL **I** shows (c–a) interactions only, whereas IL **II** includes both

types of H-bond interaction, (c–a) and (c–c), is related to the different polarizabilities of the piperidinium and pyridinium cations. The pyridinium cation is highly polarizable and thus interacts favorably with the $[NTf_2]^-$ anion, leaving the hydroxyl group free to interact with other OH bonds by forming cationic clusters. In contrast, the "hard" piperidinium cation in ILs **I** and **III** interacts less favorably with the counteranion, which is then available for interacting with the OH group of the cation, resulting in typical H-bond enhanced (c–a) ion pairs.

If we increase the hydroxyalkyl chain length from ethyl to propyl for both types of ILs, we measure two DQCCs with $\chi_D = 230$ kHz and $\chi_D = 205$ kHz for IL **III**, and $\chi_D = 215$ kHz and $\chi_D = 165$ kHz for IL **IV**. Again, the larger values $\chi_D =$ 230 kHz and $\chi_D = 215$ kHz can be assigned to (c–a) interactions, whereas the smaller values $\chi_D = 205$ kHz and $\chi_D =$ 165 kHz reflect stronger (c–c) cationic interactions. The fact that both ILs form cationic clusters despite the differently favorable cations is related to the increasing distance between the positively charged ring systems and the OH functional groups within the cations. The longer tethers allow for enhanced cationic-cluster formation (see Scheme 1). All DQCCs are shown in Figure 2, and values measured for salt

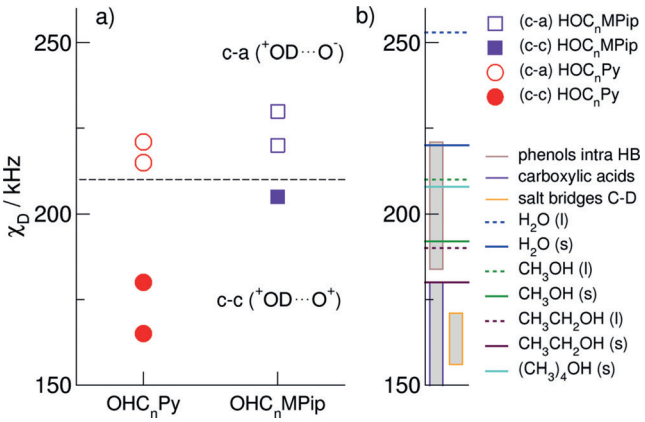

Figure 2. a) Measured and deconvoluted DQCCs for ILs **I**–**IV**. The DQCCs for the (c–a) hydrogen bonds above 210 kHz are given as open symbols, and the (c–c) hydrogen bonds below 210 kHz as filled symbols (with $n = 2,3$). b) Comparison of the (c–c) hydrogen-bond DQCCs with those for water, methanol, ethanol, and *tert*-butanol in the liquid and solid phases as well as in phenols.[49–57] The DQCCs for the (c–a) hydrogen bonds are related to those of salt bridges in proteins.[13,43–44]

bridges in supramolecular complexes or proteins are compared to (c–a) IL interactions and those measured for molecular liquids mimicking the (c–c) interaction in the ILs. Although the (c–c) DQCCs are slightly lower than those observed for solid methanol, ethanol, and *tert*-butanol, the (c–a) DQCCs range between the values of ice and liquid water.[48–57] The (c–a) DQCCs are significantly larger than the measured values for salt bridges, which range from 156 to 171 kHz, indicating that the H-bond-enhanced Coulomb interaction in (c–a) ion pairs of these ILs is weak. The molecular ions have low surface charge densities, resulting in strongly attenuated Coulomb attraction and DQCCs similar to those in H-bonded liquids. It should be noted that the (c–a) DQCCs in the hydroxyl-functionalized ILs considered in this study are about 30 kHz higher than those measured for the protic IL triethylammonium bis(trifluoromethylsulfonyl)-imide $[Et_3NH][NTf_2]$ due to weaker hydrogen bonding.[58]

Why Are (c–c) Hydrogen Bonds Stronger Than (c–a) Hydrogen Bonds?

So far, we showed that deuterons involved in (c–c) H-bonds exhibit smaller DQCCs than those bound in (c–a) species, indicating stronger binding. These results are in accord with stronger red-shifted IR bands and downfield-shifted NMR proton chemical shifts for hydrogen bonding between ions of like charge as observed experimentally.[36–38] At a first glance, it seems to be counterintuitive that the (c–c) hydrogen bonds are stronger than the (c–a) hydrogen bonds, although the first are weakened by repulsive, and the latter are enhanced by attractive Coulomb forces. To understand why hydrogen bonding is stronger in (c–c) than (c–a) clusters, we employed B3LYP-D3/6-31 + G* calculations performed with the Gaussian 09 program and analyzed with the NBO 6.0 program.[59–64] To calculate the (c–a) and (c–c) clusters using the same method, we have used the well-balanced but small 6-31 + G* basis set. It includes polarization as well as diffuse functions, and has been shown to be suitable for calculating hydrogen-bonded clusters of like-charged ions.[31,32,65,66] The 6-31 + G* basis set is also chosen for better comparison with earlier studies of molecular and ionic clusters.[17,67–69] We also show that the salient properties of these clusters can be robustly calculated with both smaller und larger basis sets. (see Supporting Information). Firstly, we fully optimized the cationic clusters of the IL **IV**, $[HOC_3Py][NTf_2]$, up to cyclic tetramers. The calculated vibrational frequencies were all positive, showing that we calculated at least local minimum structures. Additionally, we calculated the DQCC, χ_D, for each deuteron present in the (c–a) and (c–c) configurations. The DQCC describes the coupling between the nuclear quadrupole moment, eQ, and the principle component of the electric-field gradient tensor, eq_{zz}, at the deuteron nucleus. It could be shown that the relation between χ_D and eq_{zz} is given by the equation

$$\chi_D = \left(\frac{eQeq_{zz}}{h}\right)[\mathrm{kHz}] = 2.3496eQ\left(\frac{fm^2}{e}\right)eq_{zz}[\mathrm{a.u.}] \quad (1)$$

where the factor 2.3496 converts between the units. In principle, the DQCC can be obtained by multiplying the calculated principle component of the electric-field gradient tensor, eq_{zz}, of the OD hydroxyl groups in the (c–a) and (c–c) clusters of IL **IV** with a calibrated nuclear quadrupole moment, eQ. The calibrated eQ is obtained by plotting the measured gas-phase quadrupole coupling constants from microwave spectroscopy vs. the calculated electric-field gradients for small molecules, such as H_2O, CH_3OH, or formic acid, as described by Huber et al.[45,46,70] The slope gives a reasonable value of $eQ = 295.5\ \mathrm{fm}^2$, which should be used for calculating DQCCs with the B3LYP-D3/6-31 + G*

method. For this set of molecules, it could also be shown that the principal axis of the deuteron electric-field gradient is nearly axially symmetric and lies along the direction of the O–D bonds.[25] We cannot expect that the calculated DQCCs of (c–a) and (c–c) clusters represent the measured NMR values in the crystalline or glassy state of IL **IV**. Thus, we focus on the differences of the χ_D values in (c–c) clusters relative to those obtained for the (c–a) clusters, which can be compared to $\Delta\chi_D$((c–a)−(c–c)) obtained from the NMR experiment.

These spectroscopic features can be rationalized in the framework of natural bond orbital (NBO) analysis.[63,64] NBO analysis of the same (c–a) and (c–c) clusters shows a typical strong $n_o \rightarrow \sigma^*_{OH}$ donor–acceptor interaction with corresponding second-order stabilization energies $\Delta E^{(2)}_{n\rightarrow\sigma^*}$ and estimated total charge transfers of q_{CT} for OH···O hydrogen bonds.

The fact that the $^+$OH···OH$^+$ structural motif of the (c–c) species exhibits smaller DQCCs results from significant charge transfer from the non-bonding electron pair of the oxygen into the $^+$OH anti-bonding orbital, leading to strong IR red-shifts of ν_{OH}, enhanced downfield NMR chemical shifts, δ^1H, and, in our case, smaller deuteron quadrupole coupling constants, χ_D. This charge transfer is stronger than the one between cation and anion in the structural motif $^+$OH···O$^-$. This is true in particular for hydrophobic anions such as $[NTf_2]^-$, where the negative charge is distributed over the entire molecule, significantly reducing the surface charge density and thus the proton-acceptor ability of the anion. The results are summarized in Figure 3. The calculated second-order stabilization energies, $\Delta E^{(2)}_{n\rightarrow\sigma^*}$, and the transferred charges, q_{CT}, for the (c–c) clusters are plotted vs. the differences $\Delta\chi_D$((c–c)−(c–a)) with zero indicating the average DQCC calculated for (c–a) clusters. Figure 3 shows that both NBO parameters increase almost linearly with decreasing DQCCs for (c–c) hydrogen bonding, indicated by a negative $\Delta\chi_D$((c–c)−(c–a)). Obviously, both properties characterize hydrogen bonding and cooperativity in a similar way. The largest stabilization energies, $\Delta E^{(2)}_{n\rightarrow\sigma^*}$, and most intensive charge transfer, q_{CT}, is observed for the (c–c) cyclic tetramers due to cooperative effects.[64,65,67–69] Charge from the non-bonding electron-pair orbital of the oxygen of a first cation is donated into the OH anti-bonding orbital of a second cation. The larger negative charge at the OH oxygen at the second cation can now be transferred into the OH anti-bond of another cation, further enhancing hydrogen bonding. This process leads to stronger cooperativity in the (c–c) trimers and tetramers. This way, the short-range donor–acceptor covalency forces can overcome the strong long-range electrostatic repulsive forces, as expected for ions of like charge. The enhanced (c–c) hydrogen bonds are even stronger than those in (c–a) ion pairs despite the additional attractive Coulomb forces in the latter. Thus, cooperative stabilization energy and enhanced charge transfer lead to smaller DQCCs for (c–c) clusters. In Figure 3, we also show the experimentally measured $\Delta\chi_D$((c–c)−(c–a)) for IL **IV**. A difference of 50 kHz between the (c–c) and (c–a) DQCCs suggests that the fraction of (c–c) clusters consists of significant amounts of (c–c) trimers and tetramers at least in the glassy state.

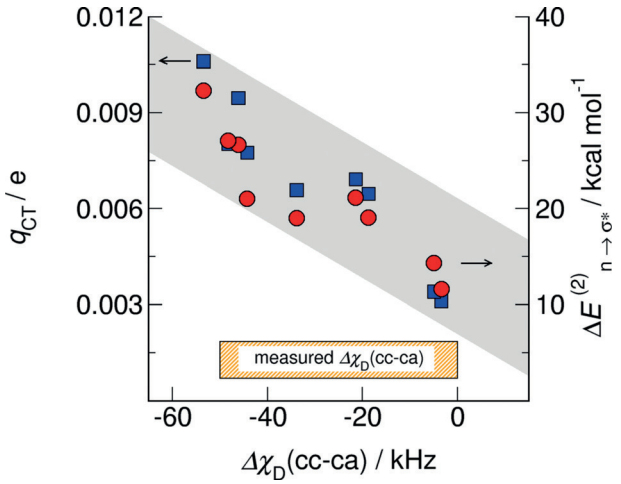

Figure 3. NBO second-order stabilization energies $\Delta E^{(2)}_{n\rightarrow\sigma^*}$, (red circles, right *y*-axis) and estimated total charge transfers q_{CT} (blue squares, left *y*-axis) for (c–c) clusters with $n = 2$–4 plotted vs. the calculated differences $\Delta\chi_D$((c–c)−(c–a)). The almost linear dependency indicates a strong relation between NBO stabilization energies and charge transfers with the spectroscopic descriptor DQCC. The NBO parameters in particular describe the different H-bond strength in both species. The measured $\Delta\chi_D$((c-c)−(c–a)) between (c–a) and (c–c) suggests that the glassy (c–c)-cluster populations consist of trimers/tetramers.

Populations of (c–a) and (c–c) Clusters from Solid-State NMR and MD Simulations

The NMR experiments in the crystalline or glassy states at 183 K allow a quantification of the populations of the local arrangements for $[HOC_2Py][NTf_2]$, $[HOC_3MPip][NTf_2]$, and $[HOC_3Py][NTf_2]$. In Figure 4, we show that 15 % (**II**) and 65 % (**IV**) of the cations are involved in (c–c) structural motifs. It should be noted that the experimental error for the determination of the second component is about ± 5 %. Thus, the existence of components can only be claimed for relative populations larger than 10 %. For comparison, we show the populations at 303 K as recently obtained from ND measurements for $[HOC_4Py][NTf_2]$ in the liquid phase.[38] Inspired by the solid-state NMR experiments, we also performed MD simulations using a recently improved version of the force field introduced by Köddermann et al.[71] The refined dihedral potentials for the $[NTf_2]^-$ anion are based on extensive ab initio calculations and are leading to a better representation of the conformational space of the anion.[72] In detail, we performed *NpT* molecular-dynamics simulation using Gromacs 5.0.6[73–77] at temperatures of 300 K, 320 K, 340 K, 360 K, 380 K, and 400 K and a pressure of $p = 1$ bar. The ILs were represented by a cubic simulation box containing 512 ion pairs. The box was first equilibrated for 2 ns at $T = 500$ K employing the Berendsen thermostat as well as the Berendsen barostat[78] with coupling times of $\tau_T = \tau_p = 0.5$ ps. After that, another equilibration run for 2 ns at the desired temperature followed. Production runs of 100 ns length utilizing the Nosé–Hoover thermostat[79,80] with $\tau_T = 1$ ps and the Rahman–Parrinello barostat[81,82] with $\tau_p = 2$ ps were performed for each temperature. All simulations were done with a 2.0 fs time step employing periodic boundary conditions and the

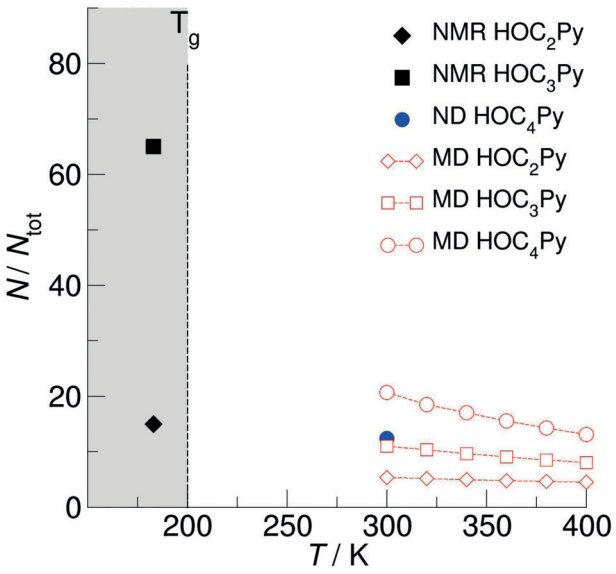

Figure 4. Analysis of (c–a)- and (c–c)-cluster populations in $[HOC_nPy][NTf_2]$ with $n = 2$–4 from MD simulations for the liquid phase between 300 and 400 K. The filled symbols show the cluster distribution obtained from the crystalline- and glassy-state NMR at 183 K (this study) and neutron diffraction (ND) experiments at 303 K.[38]

Table 1: Lennard-Jones parameters σ and ε for all interaction sites of the $[HOC_2Py]^+$, $[HOC_3Py]^+$, and $[HOC_4Py]^+$ cations. The assignment of the atoms is shown in Scheme 2.

site	σ [Å]	εk_B^{-1} [K]
N	3.25	85.55
Ca	3.55	35.23
Ha	2.42	15.10
Cc	3.50	33.20
Hc	2.50	15.10
Hm	2.50	15.10
O	3.12	85.60
Ho	0.00	0.00

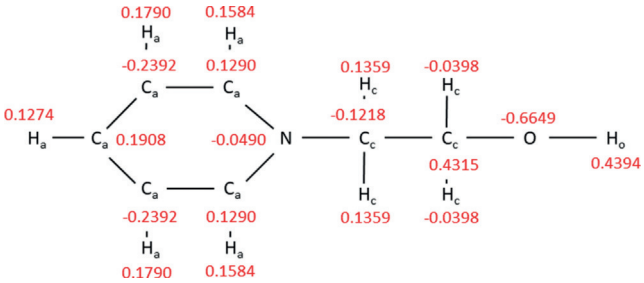

Scheme 2. Structure of the 1-(2-hydroxyethyl)pyridinium $[HOC_2Py]^+$ cation with atom types and corresponding point charges q/e (red).

LINCS algorithm[83] for fixed bond lengths. The smooth particle-mesh Ewald summation[84] was applied with a mesh spacing of 0.12 nm, a real-space cutoff 0.9 nm and fourth-order interpolation. The relative accuracy of the Ewald sum was set to 10^{-5} corresponding to a convergence factor of $\alpha = 3.38\ nm^{-1}$.

The force field of the $[NTf_2]^-$ anion has been published in refs. [71,85]. The pyridinium force fields were derived from the OPLS force field for pyridine from Jorgensen et al.[86,87] The dihedral potentials of the hydroxyalkyl chain were fitted to ab initio calculations employing second-order Møller–Plesset perturbation theory using the cc-pVTZ basis set. The point charges were derived from the electrostatic potential according to the CHelpG scheme.[88] The Lennard-Jones parameters for the cations can be found in Table 1, the point charges are given in Scheme 2. Further details on the simulations are given in the Supporting Information.

We performed MD simulations for $[HOC_2Py][NTf_2]$ and $[HOC_3Py][NTf_2]$ between 300 and 400 K to show the temperature dependence of the cluster populations. Although we obtained the cluster populations from NMR (183 K) and ND (303 K) measurements only at single temperatures, and those from MD simulations only above room temperature, we can clearly conclude: a) longer hydroxyalkyl chain lengths significantly enhance the formation of (c–c) cationic clusters; b) for longer alkyl chain lengths, the polarizability of the cation is less important; c) the temperature dependence of (c–c)-cluster formation in the liquid phase between 300 and 400 K can be described by van't Hoff plots. The ratios for the (c–c) and the (c–a) hydrogen-bonded species vs. the inverse temperature obtained from MD-simulation data result in transition enthalpies from (c–c) to (c–a) of about 31.24 kJ mol^{-1} (**II**), 9.42 kJ mol^{-1} (**IV**), and 3.75 kJ mol^{-1} (for $[HOC_4Py][NTf_2]$). The smaller transition enthalpy suggests that cationic clusters already exist at room temperature.

Crystallization or Supercooling—(c–c) Cluster Formation Prevents Crystallization

The DSC traces of ILs **I**–**IV** as shown in Figure 5 strongly support the interpretation of the NMR spectra at low temperatures (see also the Supporting Information). Thermograms were recorded during cooling (373–193 K) and heating (193–373 K) at cooling and heating rates of 1, 5, and 10 K min^{-1}. The glass-transition temperature (T_g, middle point of the heat capacity change), crystallization temperature (T_c), and melting temperature (T_{fus}) were determined from DSC thermograms during the heating scans. The summary of phase transitions is given in Table 2.

During cooling from 373 to 193 K at 5 and 10 K min^{-1} cooling rates, only a heat-capacity change corresponding to glass transitions (T_g) could be observed in the DSC profiles of ILs **II** (200 K), **III** (206 K), and **IV** (200 K). The supercooled state of the (c–c) cluster-forming ILs is obviously fairly stable. In contrast, the phase-transition behavior is complex for IL **I**, including melting ($T_{fus} = 276.2$ K) and solid/solid phase transitions ($T_{ss} = 266.2$ K and $T_{ss} = 251.6$ K). For the crystalline state of IL **I** at 183 K, we observed only one Pake pattern, indicating pure (c–a) hydrogen bonding. The strong formation of cationic clusters in ILs **II**, **III** and **IV** results in supercooling and glass transition. From the combined NMR and DSC experiments, we have clear evidence that the formation of cationic clusters prevents the ILs from crystallization and liquid/solid phase transition. The resulting material is a glass.[89] Our findings suggest that the phase

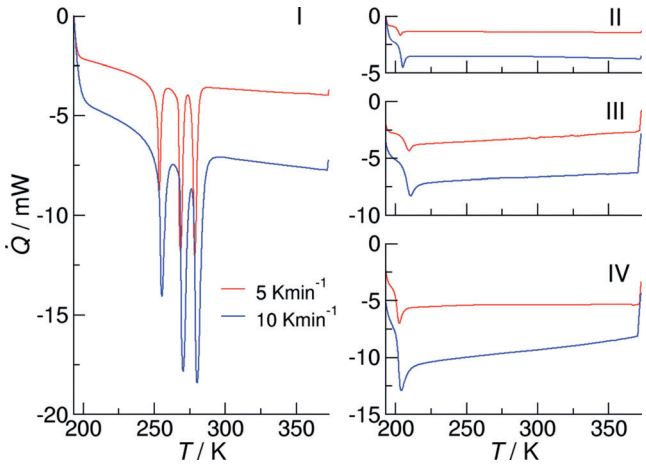

Figure 5. DSC traces for the ILs **I–IV**: For IL **I** we observe liquid/solid and several solid/solid phase transitions.[33] For the crystalline state at 183 K, we found a single Pake pattern indicating (c–a) hydrogen-bonded ion pairs only (see Figure 1). For ILs **II–IV** we observe supercooling and finally glass transition below 200 K. These ILs exhibit substantial cationic-cluster formation characterized by two distinguished Pake patterns. Obviously, cationic-cluster formation prevents the ILs from crystallizing.

Table 2: Thermodynamic parameters of the observed phase transitions for ILs **I–IV**.

Ionic liquid	Phase transition	T_{trs} [K]	$\Delta_{trs}H^{\circ}_{m}$ [kJ mol^{-1}]
[HOC_2MPip][NTf_2] (**I**)	crIII–crII	251.9 ± 1.3	2.7 ± 0.3
	crII–crI	266.7 ± 1.5	4.2 ± 0.2
	crI–liquid	276.6 ± 0.9	4.4 ± 0.3
[HOC_2Py][NTf_2] (**II**)	glass–liquid	200.4 ± 0.1	–
[HOC_3MPip][NTf_2] (**III**)	glass–liquid	204.4 ± 0.3 (1 K min^{-1})	–
		205.5 ± 0.1 (5 K min^{-1})	
		206.8 ± 0.1 (10 K min^{-1})	
[HOC_3Py][NTf2] (**IV**)	glass—liquid	197.6 ± 0.1 (1 K min^{-1})	–
		199.8 ± 0.1 (5 K min^{-1})	
		200.6 ± 0.1 (10 K min^{-1})	

behavior of this type of ILs can be controlled by cationic-cluster formation.

Conclusion

We measured DQCCs of hydroxyl-functionalized ionic liquids in the crystalline and glassy states. We observed two Pake patterns for deuterons involved in normal (c–a) Coulomb-enhanced hydrogen bonds, and in unusual (c–c) Coulomb-weakened hydrogen bonds between cations. The DQCCs in the (c–c) cationic clusters are smaller than in (c–a) ion-pairs, indicating stronger hydrogen bonding in accord with observed redshifts in IR spectra. These DQCCs are close to values for molecular liquids but larger than those known for salt bridges of supramolecular complexes. The (c–a) DQCCs are surprisingly large despite the additional attractive Coulomb forces. Depending on the polarizability of the cation and the alkyl chain length, the (c–c) clusters can be more strongly populated than the (c–a) ion pairs at low temperatures. The DSC traces clearly show that the ILs which form substantial amounts of (c–c) clusters do not tend to crystallize and rather form glasses.

Acknowledgements

This work has been supported by the Deutsche Forschungsgemeinschaft (DFG) within the projects LU 506/14-1 and LU 506/14-2 (286149019). R. L. also thanks the University of Rostock for a Baltic Mare Fellowship provided for D.I.K. D.I.K., A.G.S., and A.E.K. acknowledge financial support by the Ministry of Science and Higher Education of the Russian Federation (budget Project no. AAAA-A17-117041710084-2 for Boreskov Institute of Catalysis).

Conflict of interest

The authors declare no conflict of interest.

Keywords: DFT calculations · hydrogen bonding · ionic liquids · molecular-dynamics simulations · solid-state NMR

How to cite: *Angew. Chem. Int. Ed.* **2019**, *58*, 17863–17871
Angew. Chem. **2019**, *131*, 18027–18035

[1] *Ionic Interactions in Natural and Synthetic Macromolecules* (Eds.: A. Ciferri, A. Perico), Wiley, Hoboken, **2012**, p. 35.
[2] F. Biedermann, H. J. Schneider, *Chem. Rev.* **2016**, *116*, 5216–5300.
[3] H. J. Schneider, *Angew. Chem. Int. Ed.* **2009**, *48*, 3924–3977; *Angew. Chem.* **2009**, *121*, 3982–4036.
[4] M. Ikeda, Y. Tanaka, T. Hasegawa, Y. Furusho, E. Yashima, *J. Am. Chem. Soc.* **2006**, *128*, 6806–6807.
[5] B. Kuberski, A. Szumna, *Chem. Commun.* **2009**, 1959–1961.
[6] L. E. R. O'Leary, J. A. Fallas, E. L. Bakota, M. K. Kang, J. D. Hartgerink, *Nat. Chem.* **2011**, *3*, 821–828.
[7] S. Kumar, R. Nussinov, *J. Mol. Biol.* **1999**, *293*, 1241–1255.
[8] S. Kumar, R. Nussinov, *ChemBioChem* **2002**, *3*, 604–617.
[9] L. Cruz, B. Urbanc, J. M. Borreguero, N. D. Lazo, D. B. Teplow, H. E. Stanley, *Proc. Natl. Acad. Sci. USA* **2005**, *102*, 18258–18263.
[10] A. Moroni, G. Thiel, *Nat. Chem. Biol.* **2006**, *2*, 572–573.
[11] J. M. Christie, A. S. Arvai, K. J. Baxter, M. Heilmann, A. J. Pratt, A. O'Hara, S. M. Kelly, M. Hothorn, B. O. Smith, K. Hitomi, G. I. Jenkins, E. D. Getzoff, *Science* **2012**, *335*, 1492–1496.
[12] P. M. J. Szell, S. Zablotny, D. L. Bryce, *Nat. Commun.* **2019**, *10*, 916.
[13] X. Shi, C. M. Rienstra, *J. Am. Chem. Soc.* **2016**, *138*, 4105–4119.

[14] R. Manríquez, F. A. López-Dellamary, J. Frydel, T. Emmler, H. Breitzke, G. Buntkowsky, H.-H. Limbach, I. G. Shenderovich, *J. Phys. Chem.* **2009**, *113*, 934 – 940.
[15] H. Weingärtner, *Angew. Chem. Int. Ed.* **2008**, *47*, 654 – 670; *Angew. Chem.* **2008**, *120*, 664 – 682.
[16] N. V. Plechkova, K. R. Seddon, *Chem. Soc. Rev.* **2008**, *37*, 123 – 150.
[17] K. Fumino, S. Reimann, R. Ludwig, *Phys. Chem. Chem. Phys.* **2014**, *16*, 21903 – 21929.
[18] P. A. Hunt, C. R. Ashworth, R. P. Matthews, *Chem. Soc. Rev.* **2015**, *44*, 1257 – 1288.
[19] R. Hayes, G. Warr, R. Atkin, *Chem. Rev.* **2015**, *115*, 6357 – 6426.
[20] C. R. Ashworth, R. P. Matthews, T. Welton, P. A. Hunt, *Phys. Chem. Chem. Phys.* **2016**, *18*, 18145 – 18160.
[21] S. Grimme, W. Hujo, B. Kirchner, *Phys. Chem. Chem. Phys.* **2012**, *14*, 4875 – 4883.
[22] E. I. Izgorodina, Z. L. Seeger, D. L. A. Scarborough, S. Y. S. Tan, *Chem. Rev.* **2017**, *117*, 6696 – 6754.
[23] K. Fumino, V. Fossog, P. Stange, D. Paschek, R. Hempelmann, R. Ludwig, *Angew. Chem. Int. Ed.* **2015**, *54*, 2792 – 2795; *Angew. Chem.* **2015**, *127*, 2834 – 2837.
[24] R. Ludwig, *Phys. Chem. Chem. Phys.* **2015**, *17*, 13790 – 13793.
[25] D. H. Zaitsau, V. N. Emel'yanenko, P. Stange, C. Schick, S. P. Verevkin, R. Ludwig, *Angew. Chem. Int. Ed.* **2016**, *55*, 11682 – 11686; *Angew. Chem.* **2016**, *128*, 11856 – 11860.
[26] S. A. Katsyuba, M. V. Vener, E. E. Zvereva, Z. F. Fei, R. Scopelliti, G. Laurenczy, N. Yan, E. Paunescu, P. J. Dyson, *J. Phys. Chem. B* **2013**, *117*, 9094 – 9105.
[27] M. Fakhraee, B. Zandkarimi, H. Salari, M. R. Gholami, *J. Phys. Chem. B* **2014**, *118*, 14410 – 14428.
[28] S. K. Panja, B. Haddad, J. Kiefer, *ChemPhysChem* **2018**, *19*, 3061 – 3068.
[29] A. Knorr, R. Ludwig, *Sci. Rep.* **2015**, *5*, 17505.
[30] A. Strate, T. Niemann, D. Michalik, R. Ludwig, *Angew. Chem. Int. Ed.* **2017**, *56*, 496 – 500; *Angew. Chem.* **2017**, *129*, 510 – 514.
[31] A. Strate, T. Niemann, R. Ludwig, *Phys. Chem. Chem. Phys.* **2017**, *19*, 18854 – 18862.
[32] T. Niemann, D. Zaitsau, A. Strate, A. Villinger, R. Ludwig, *Sci. Rep.* **2018**, *8*, 14753.
[33] F. S. Menges, H. J. Zeng, P. J. Kelleher, O. Gorlova, M. A. Johnson, T. Niemann, A. Strate, R. Ludwig, *J. Phys. Chem. Lett.* **2018**, *9*, 2979 – 2984.
[34] T. Niemann, A. Strate, R. Ludwig, H. J. Zeng, F. S. Menges, M. A. Johnson, *Angew. Chem. Int. Ed.* **2018**, *57*, 15364 – 15368; *Angew. Chem.* **2018**, *130*, 15590 – 15594.
[35] A. Strate, V. Overbeck, V. Lehde, J. Neumann, A. M. Bonsa, T. Niemann, D. Paschek, D. Michalik, R. Ludwig, *Phys. Chem. Chem. Phys.* **2018**, *20*, 5617 – 5625.
[36] T. Niemann, A. Strate, R. Ludwig, H. J. Zeng, F. Menges, M. A. Johnson, *Phys. Chem. Chem. Phys.* **2019**, *21*, 18092 – 18098.
[37] A. Knorr, P. Stange, K. Fumino, F. Weinhold, R. Ludwig, *ChemPhysChem* **2016**, *17*, 458 – 462.
[38] T. Niemann, J. Neumann, P. Stange, S. Gärtner, T. G. A. Youngs, D. Paschek, R. Atkin, R. Ludwig, *Angew. Chem. Int. Ed.* **2019**, *58*, 12887 – 12892; *Angew. Chem.* **2019**, *131*, 13019 – 13024.
[39] J. G. Powles, J. H. Strange, *Proc. Phys. Soc. London* **1963**, *82*, 6 – 15.
[40] G. E. Pake, *J. Chem. Phys.* **1948**, *16*, 327 – 336.
[41] A. Abragam, *The Principles of Nuclear Magnetism*, Oxford Clarendon Press, Oxford, **1961**.
[42] T. C. Farrar, E. D. Becker, *Pulse and Fourier Transform NMR. Introduction to Theory and Methods*, Academic Press, New York, **1971**.
[43] J. W. Clymer, J. L. Ragle, *J. Chem. Phys.* **1982**, *77*, 4366 – 4373.
[44] J. M. Jackman, J. C. Trewella, R. C. Haddon, *J. Am. Chem. Soc.* **1980**, *102*, 2519 – 2525.
[45] H. Huber, *J. Chem. Phys.* **1985**, *83*, 4591 – 4598.
[46] R. Eggenberger, S. Gerber, H. Huber, D. Searles, M. Welker, *J. Chem. Phys.* **1992**, *97*, 5898 – 5904.
[47] P. L. Cummins, G. B. Bacskay, N. S. Hush, B. Halle, S. Engström, *J. Chem. Phys.* **1985**, *82*, 2002 – 2013.
[48] D. T. Emonds, A. L. Mackay, *J. Magn. Reson.* **1975**, *20*, 515 – 519.
[49] D. Lankhorst, J. Schriever, J. C. Leyte, *Ber. Bunsen-Ges.* **1982**, *86*, 215 – 221.
[50] R. Ludwig, F. Weinhold, T. C. Farrar, *J. Chem. Phys.* **1995**, *103*, 6941 – 6950.
[51] R. Ludwig, *Chem. Phys.* **1995**, *195*, 329 – 337.
[52] R. Ludwig, D. S. Gill, M. D. Zeidler, *Z. Naturforsch. A* **1991**, *46*, 89 – 94.
[53] R. Ludwig, M. D. Zeidler, *Mol. Phys.* **1994**, *82*, 313 – 323.
[54] R. Ludwig, M. D. Zeidler, T. C. Farrar, *Z. Phys. Chem.* **1995**, *189*, 19 – 27.
[55] M. A. Wendt, T. C. Farrar, *Mol. Phys.* **1998**, *95*, 1077 – 1081.
[56] T. D. Ferris, T. C. Farrar, *Mol. Phys.* **2002**, *100*, 303 – 309.
[57] A. M. Nishchenko, D. I. Kolokolov, A. G. Stepanov, *J. Phys. Chem.* **2011**, *115*, 7428 – 7438.
[58] A. E. Khudozhitkov, P. Stange, B. Golub, D. Paschek, A. G. Stepanov, D. I. Kolokov, R. Ludwig, *Angew. Chem. Int. Ed.* **2017**, *56*, 14310 – 14314; *Angew. Chem.* **2017**, *129*, 14500 – 14505.
[59] Gaussian 09, Revision A.02, M. J. Frisch, G. W. Trucks, H. B. Schlegel, G. E. Scuseria, M. A. Robb, J. R. Cheeseman, G. Scalmani, V. Barone, G. A. Petersson, H. Nakatsuji, X. Li, M. Caricato, A. Marenich, J. Bloino, B. G. Janesko, R. Gomperts, B. Mennucci, H. P. Hratchian, J. V. Ortiz, A. F. Izmaylov, J. L. Sonnenberg, D. Williams-Young, F. Ding, F. Lipparini, F. Egidi, J. Goings, B. Peng, A. Petrone, T. Henderson, D. Ranasinghe, V. G. Zakrzewski, J. Gao, N. Rega, G. Zheng, W. Liang, M. Hada, M. Ehara, K. Toyota, R. Fukuda, J. Hasegawa, M. Ishida, T. Nakajima, Y. Honda, O. Kitao, H. Nakai, T. Vreven, K. Throssell, J. A. Montgomery, Jr., J. E. Peralta, F. Ogliaro, M. Bearpark, J. J. Heyd, E. Brothers, K. N. Kudin, V. N. Staroverov, T. Keith, R. Kobayashi, J. Normand, K. Raghavachari, A. Rendell, J. C. Burant, S. S. Iyengar, J. Tomasi, M. Cossi, J. M. Millam, M. Klene, C. Adamo, R. Cammi, J. W. Ochterski, R. L. Martin, K. Morokuma, O. Farkas, J. B. Foresman, D. J. Fox, Gaussian, Inc., Wallingford CT, **2016**.
[60] S. Grimme, J. Antony, S. Ehrlich, H. Krieg, *J. Chem. Phys.* **2010**, *132*, 154104.
[61] S. Ehrlich, J. Moellmann, W. Reckien, T. Bredow, S. Grimme, *ChemPhysChem* **2011**, *12*, 3414 – 3420.
[62] S. Grimme, A. Jansen, J. G. Brandenburg, C. Bannwarth, *Chem. Rev.* **2016**, *116*, 5105 – 5154.
[63] NBO 6.0. E. D. Glendening, J. K. Badenhoop, A. E. Reed, J. E. Carpenter, J. A. Bohmann, C. M. Morales, C. R. Landis, F. Weinhold, Theoretical Chemistry Institute, University of Wisconsin, Madison, **2013**.
[64] F. Weinhold, C. R. Landis, *Valency and Bonding A Natural Bond Orbital Donor-Acceptor Perspective*, Cambridge, University Press, Cambridge, **2005**.
[65] A. Knorr, K. Fumino, A.-M. Bonsa, R. Ludwig, *Phys. Chem. Chem. Phys.* **2015**, *17*, 30978 – 30982.
[66] T. Niemann, P. Stange, A. Strate, R. Ludwig, *Phys. Chem. Chem. Phys.* **2019**, *21*, 8215 – 8220.
[67] R. Ludwig, *Phys. Chem. Chem. Phys.* **2002**, *4*, 5481 – 5487.
[68] K. M. Murdoch, T. D. Ferris, J. C. Wright, T. C. Farrar, *J. Chem. Phys.* **2002**, *116*, 5717.
[69] R. Ludwig, *ChemPhysChem* **2005**, *6*, 1369 – 1375.
[70] "Accurate Determination of Nuclear Quadrupole Coupling Constants and other NMR Parameters in Liquids from the Combination of Molecular Dynamics Simulations and ab initio Calculations": D. J. Searles, H. Huber in *Encyclopedia of Nuclear Magnetic Resonance*, *Vol. 9* (Eds.: D. M. Grant, R. K. Harris), Wiley, New York, **2002**.

[71] T. Köddermann, D. Paschek, R. Ludwig, *ChemPhysChem* **2007**, *8*, 2464 – 2470.
[72] D. Paschek, B. Golub, R. Ludwig, *Phys. Chem. Chem. Phys.* **2015**, *17*, 8431 – 8440.
[73] E. Lindahl, B. Hess, D. van der Spoel, *J. Mol. Model.* **2001**, *7*, 306 – 317.
[74] H. J. C. Berendsen, D. van der Spoel, R. van Drunen, *Comput. Phys. Commun.* **1995**, *91*, 43 – 46.
[75] B. Hess, C. Kutzer, D. van der Spoel, E. Lindahl, *J. Chem. Theory Comput.* **2008**, *4*, 435 – 447.
[76] S. Pronk, S. Pall, R. Schulz, P. Larsson, P. Bjelkmar, R. Apostolov, M. R. Shirts, J. C. Smith, P. M. Kasson, D. van der Spoel, B. Hess, E. Lindahl, *Bioinformatics* **2013**, *29*, 845 – 854.
[77] M. Abraham, B. Hess, D. van der Spoel, E. Lindahl, E. Apol, R. Apostolov, H. J. C. Berendsen, A. van Buuren, P. Bjelkmar, R. van Drunen, A. Feenstr, S. Fritsch, G. Groenhof, C. Jungshans, J. Hub, P. Kasson, C. Kutzner, B. Lambeth, P. Larsson, J. A. Lemkul, E. Marklund, P. Meulenho, T. Murtola, S. Pall, S. Pronk, R. Schulz, M. Shirts, A. Sijbers, P. Tieleman, C. Wennberg, M. Wolf, Gromacs 5.0.6, **2015**.
[78] H. J. C. Berendsen, J. P. M. Postma, W. F. van Gunsteren, A. DiNola, J. R. Haak, *J. Chem. Phys.* **1984**, *81*, 3684 – 3690.
[79] S. Nosé, *Mol. Phys.* **1984**, *52*, 255 – 268.
[80] W. G. Hoover, *Phys. Rev. A* **1985**, *31*, 1695 – 1697.
[81] M. Parrinello, A. Rahman, *J. Appl. Phys.* **1981**, *52*, 7182 – 7190.
[82] S. Nosé, M. L. Klein, *Mol. Phys.* **1983**, *50*, 1055 – 1076.
[83] B. Hess, H. Bekker, H. J. C. Berendsen, J. G. E. M. Fraaije, *J. Comput. Chem.* **1997**, *18*, 1463 – 1472.
[84] U. Essmann, L. Perera, M. L. Berkowitz, T. A. Darden, H. Lee, L. G. Pedersen, *J. Chem. Phys.* **1995**, *103*, 8577 – 8593.
[85] J. Neumann, B. Golub, L.-M. Odebrecht, R. Ludwig, D. Paschek, *J. Chem. Phys.* **2018**, *148*, 193828.
[86] W. L. Jorgensen, D. S. Maxwell, J. Tirado-Rives, *J. Am. Chem. Soc.* **1996**, *118*, 11225 – 11236.
[87] W. L. Jorgensen, N. A. McDonald, *J. Mol. Struct. THEOCHEM* **1998**, *424*, 145 – 155.
[88] C. M. Breneman, K. B. Wiberg, *J. Comput. Chem.* **1990**, *11*, 361 – 373.
[89] P. G. Debenedetti, F. H. Stillinger, *Nature* **2001**, *410*, 259 – 267.

Manuscript received: September 30, 2019
Accepted manuscript online: October 6, 2019
Version of record online: October 31, 2019

Angewandte Chemie
Eine Zeitschrift der Gesellschaft Deutscher Chemiker

Supporting Information

Hydrogen Bonding Between Ions of Like Charge in Ionic Liquids Characterized by NMR Deuteron Quadrupole Coupling Constants—Comparison with Salt Bridges and Molecular Systems

Alexander E. Khudozhitkov, Jan Neumann, Thomas Niemann, Dzmitry Zaitsau, Peter Stange, Dietmar Paschek, Alexander G. Stepanov, Daniil I. Kolokolov, and Ralf Ludwig**

anie_201912476_sm_miscellaneous_information.pdf

Contents

1 Materials and Synthesis

Sample preparation

Synthesis of the onium salts: Equimolar amounts of the heterocyclic amine and the corresponding ω-halide-alcohol were mixed and heated up to 110 °C for 1h. Upon cooling, the mixture began to crystallize. The crude product was recrystallized from acetone/acetonitrile mixtures to obtain the colorless crystalline product.
Synthesis of the bis(trifluoromethanesulfonyl)imide: Equimolar amounts of the onium halide and lithium-bis(trifluoromethanesulfonyl)imide were mixed as aqueous solutions for 1h. Two phases were obtained, the lower one was washed several times with water until no residual bromine could be detected with silver nitrate solution. The obtained colorless liquids were dried for several hours in vacuum at 60 °C.

Synthesis of the specific compounds

Apart from the reactions in aqueous solutions all reactions were performed in a moisture-guarded assembly and reflux condenser was used while heating. The used solvents were dried with molecular sieves to a water content less than 50 ppm and distilled freshly. All starting materials used in the synthesis were purchased from Sigma Aldrich and dried by conventional methods for the use in moisture-free reactions.

1-(2-Hydroxyethyl)-1-methylpiperidinium-bromide [HOC$_2$MPip][Br]

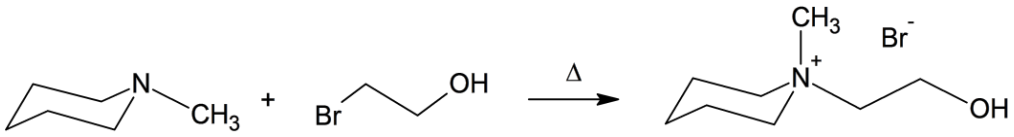

32.661 g of 2-bromoethanol (261 mmol, 19 ml) were added to a solution of 16.378 g of N-methylpiperidine (165 mmol, 20 ml) and 40 ml ethanol at room temperature. The mixture was refluxed for 2 h. After cooling to room temperature the ethanol and the residual 2-bromoethanol were removed in vacuum. The liquid crude product begins to crystallize by addition of 40 ml of acetone. The white precipitate was washed three times with dry acetone. The product was dried for 4 h in vacuum at 60 °C. (**[HOC$_2$MPip][Br]**) was obtained in 89 % yield.
EA % cal. (exp.): C 42.87 (42.65); H 8.10 (8.06); N 6.25 (6.11). ^{1}**H-NMR**(298.2 K, DMSO-d6, 300.13 MHz, [ppm]): δ = 1.48-1.58 (m, 2H, C(4)*H*2); 1.74-1.84 (m, 4H, C(2; 6)*H*2); 3.08 (s, 3H, C*H*3); 3.30-3.47 (m, 6H, C(3; 5)*H*2 +CH2−C*H*2−OH); 3.81-3.88 (m, 2H, C*H*2−CH2−OH), 5.26 (t, 1H, O*H*). ^{13}**C-NMR** (298 K, DMSO-d6, 75.46 MHz, [ppm]): δ = 20.48 (s, *C*(4)); 19.24 (s, *C*(3; 5)); 48.07 – 48.27 (m, *C*H3); 54.49 (s, *C* H2−CH2−OH); 60.77 – 60.92 (m, CH2−*C*H2−OH); 63.72 – 63.93 (m, *C*(2; 6)).

1-(2-Hydroxyethyl)-1-methylpiperidinium-bis(trifluoromethanesulfonyl)imide [HOC$_2$MPip][NTf$_2$]

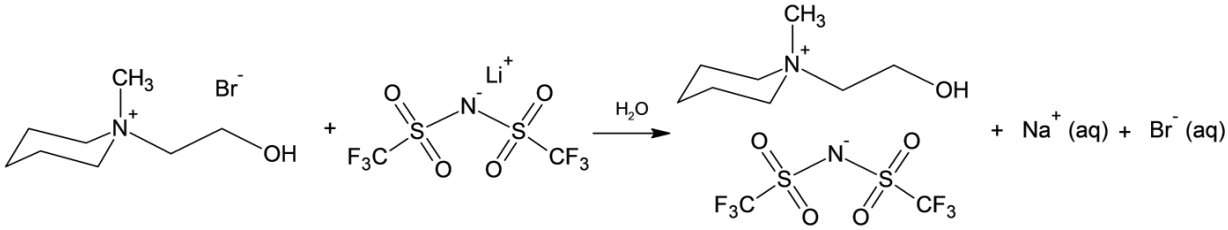

9.030 g **[HOC$_2$MPip][Br]** (40 mmol) were solved in 10 ml H_2O and added to a solution of 11.518 g $LiNTf_2$ (40 mmol) in 10 ml H_2O. The mixture was stirred for 1h. During this time two phases were formed. The lower phase was washed several times with water until no residual bromine could be detected with silver nitrate solution. The thus obtained colorless liquid was dried for 6 h at 110 °C in vacuum. Yield: 68 %.

^{1}**H-NMR**(300 K, DMSO-d6, 250.13 MHz, [ppm]): δ = 1.46-1.57 (m, 2H, C(4)*H*2); 1.71-1.82 (m, 4H, C(2; 6)*H*2); 3.05 (s, 3H, C*H*3); 3.26-3.44 (m, 6H, C(3; 5)*H*2 CH2−C*H*2−OH); 3.78-3.86 (m, 2H, C*H*2−CH2−OH), 5.24 (t, 1H, O*H*). ^{13}**C-NMR**(298 K, DMSO-d6, 75.6 MHz, [ppm]): δ = 20.48 (s, *C*(4)); 19.24 (s, *C*(3; 5)); 48.07 – 48.27 (m, *C*H3); 54.49 (s, *C*H2−CH2−OH); 60.77 – 60.92 (m, CH2−*C*H2−OH); 63.72 – 63.93 (m, *C*(2; 6)); 119.21 (q, *C*F3). ^{19}**F-NMR**(300 K, DMSO-d6, 235.36 MHz, [ppm]): δ = −78.79 (s, C*F*3). **IR** (Transm., CaF2-Window, 12 μm- Spacer, 20 °C, 128 Scans, [cm^{-1}]): 3536 (w); 2958 (w); 2882 (w); 1846 (vw); 1797 (vw); 1471 (w); 1349 (s); 1332 (m); 1195 (s); 1138 (s); 1086 (w); 1056 (s); 986 (w).

1-(2-Hydroxyethyl)pyridinium-bromide [HOC$_2$Py][Br]

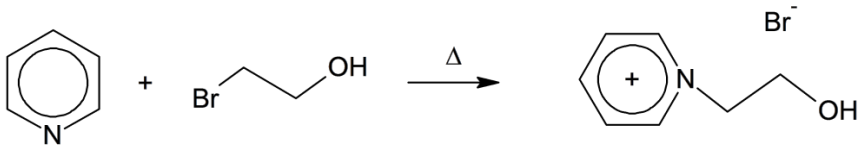

At room temperature equimolar amounts of pyridine (8.977 g; 113 mmol; 9.6 ml) and 2-bromoethanol (14.929 g; 113 mmol; 14.9 ml) were mixed and heated slowly up to 110 °C. When the reaction begins, the solution turns brown and starts to crystallize. The mixture was cooled to room temperature. The crude product was recrystallized from about 330 ml acetonitrile. The product (**[HOC$_2$Py][Br]**) was obtained as rod-shaped colorless crystals. Yield 89 %.

EA % cal. (exp.): C 41.20 (41.22); H 4.94 (4.92); N 6.86 (6.76). ^{1}**H-NMR**(298.2 K, DMSO-d6, 300.13 MHz, [ppm]): δ = 3.86 (dd, 2H, CH2−C*H*2−OH); 4.67-4.74 (m, 2H, C*H*2−CH2−OH); 5.25(t, 1H, O*H*); 8.14-8.21 (m, 2H, *m*-C*H*); 8.60-8.67 (m, 1H, *p*-C*H*); 9.03-9.09 (m, 2H, *o*-C*H*). ^{13}**C-NMR**(298 K, DMSO-d6, 75.46 MHz, [ppm]): δ = 59.98 (s, CH2−*C*H2−OH); 63.04 (s, *C*H2−CH2−OH); 127.67 (s, *m*-*C*H); 145.15 (s, *p*-*C*H); 145.53 (s, *o*-*C*H).

1-(2-Hydroxyethyl)pyridinium-bis(trifluoromethanesulfonyl)imide [HOC_2Py][NTf_2]

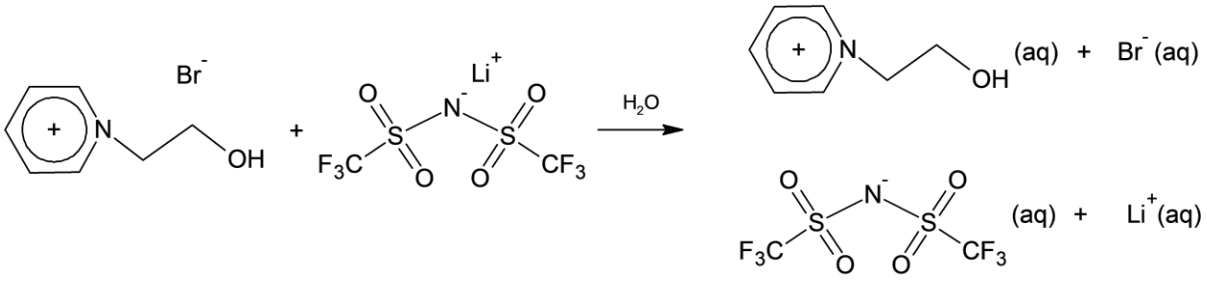

3.220 g (**[HOC_2Py][Br]**) (16 mmol) solved in 2 ml H_2O were added to a solution of 4.576 g lithium- bis(trifluoromethylsulfonyl)imide $LiNTf_2$ (16 mmol) in 2.5 ml H_2O. The mixture was stirred for 1 h. Two phases were obtained, the lower one was washed several times with water until no residual bromine could be detected with silver nitrate solution. The obtained colorless liquid of (**[HOC_2Py][NTf_2])** was dried for 8 h in vacuum at 60 °C. Yield 57 %.

EA % cal. (exp.): C 26.73 (26.14); H 2.49 (2.41); N 6.93 (6.54); S 15.86 (15.50).

^{1}**HNMR**(298.2 K, DMSO-d6, 300.13 MHz, [ppm]): δ = 3.88 (dd, 2H, CH_2-CH_2-OH); 4.65- 4.71 (m, 2H, CH_2-CH_2-OH); 5.22(t, 1H, O*H*); 8.12-8.20 (m, 2H, *m*-C*H*); 8.57-8.64 (m, 1H, *p*-C*H*); 9.00-9.05 (m, 2H, *o*-C*H*). ^{13}**C-NMR**(298 K, DMSO-d6, 75.46 MHz, [ppm]): δ = 59.95 (s, CH_2-CH_2-OH); 63.01 (s, CH_2-CH_2-OH); 119.43 (q, CF_3); 127.65 (s, *m*-CH); 145.12 (s, *p*-CH); 145.50 (s, *o*-CH). ^{19}**F-NMR**(298 K, DMSO-d6, 282.40 MHz, [ppm]): δ = −78.81 (s, CF_3).

IR (Transm., CaF_2-Window, 12 μm Spacer, 20 °C, 128 Scans, [cm^{-1}]): 3528 (vw); 3141 (vw); 3097 (vw); 3074 (vw); 2972 (vw); 2951 (vw); 2893 (vw); 2857 (vw); 1936 (vw); 1850 (vw); 1741 (vw); 1638 (w); 1585 (vw); 1502 (vw); 1491 (m); 1451 (vw); 1352 (vs); 1200 (s); 1136 (s); 1060 (s).

1-(3-Hydroxypropyl)-1-methylpiperidinium-chloride [HOC_3MPip][Cl]

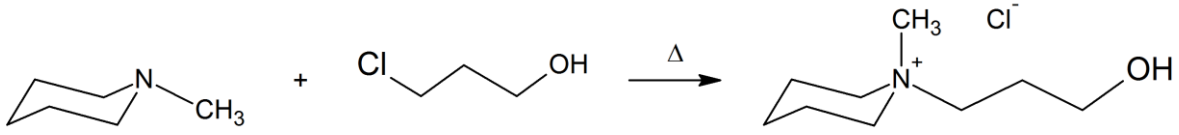

At room temperature equimolar amounts of N- methylpiperidine (8.286 g; 105 mmol; 8.9 ml) and 3-chloropropanol (14.600 g; 105 mmol; 8.8 ml) were mixed and heated slowly up to 110 °C. When the reaction begins, the solution turns yellow and starts to crystallize upon cooling to room temperature . The crude product was recrystallized from about 400 ml of an acetonitrile/acetone mixture. The product was obtained as needle-shaped colorless crystals. Yield 87 %.

^{1}**H-NMR**(298.2 K, DMSO-d6, 300.13 MHz, [ppm]): δ = 1.48-1.58 (m, 2H, C(4)H_2); 1.71-1.88 (m, 4H, C(2; 6)H_2 + 2H, CH_2-CH_2-OH); 3.01 (s, 3H, CH_3); 3.28-3.43 (m, 6H, C(3; 5)H_2 + $CH_2-CH_2-CH_2-OH$); 3.47 (td, 2H, $CH_2-CH_2-CH_2-OH$); 5.06 (t, 1H, O*H*). ^{13}**C-**

NMR (298 K, DMSO-d6, 75.46 MHz, [ppm]): δ = 19.27 (s, *C*(3; 5)); 20.58 (s, *C*(4)); 24.59 (s, *C*H2−CH2− OH); 47.07 (s, *C*H3); 57.58 (s, CH2−*C*H2−OH); 59.87 (s, *C*(2; 6)) 60.24 (s, *C*H2−CH2−CH2− OH).

1-(3-Hydroxypropyl)-1-methylpiperidinium-bis(trifluoromethanesulfonyl)imide [HOC$_3$MPip][NTf$_2$]

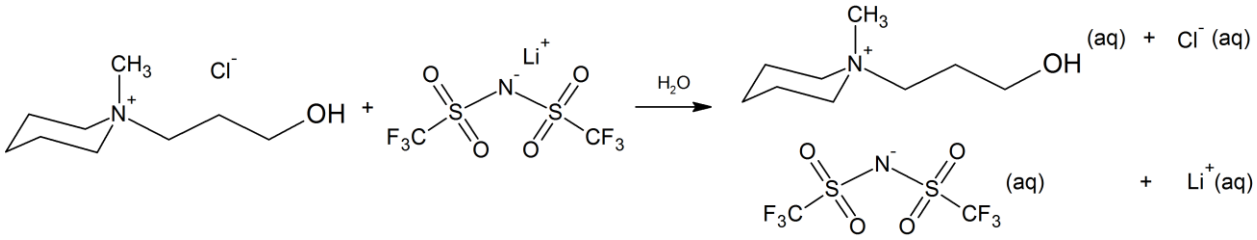

10 g (**[HOC$_2$MPip][Cl]**) (52 mmol) were solved in 10 ml H_2O and added to a solution of 14.821g $LiNTf_2$ (52 mmol) and 10 ml H_2O. The mixture was stirred for 1h. During this time two phases were formed. The lower phase was washed several times with water until no residual chlorine could be detected with silver nitrate solution. The thus obtained colorless liquid was dried for 6 h at 110 °C in vacuum. Yield: 74 %.
^{1}**H-NMR**(298.2 K, DMSO-d6, 300.13 MHz, [ppm]): δ = 1.47-1.60 (m, 2H, C(4)*H*2); 1.71-1.88 (m, 4H, C(2; 6)*H*2 + 2H, C*H*2−CH2−OH); 2.98 (s, 3H, C*H*3); 3.26-3.39 (m, 6H, C(3; 5)*H*2 + C*H*2−CH2−CH2−OH); 3.49 (td, 2H, CH2−CH2−*CH2*−OH); 4.77 (t, 1H, O*H*). ^{13}**C-NMR** (298 K, DMSO-d6, 75.46 MHz, [ppm]): δ = 19.27 (s, *C*(3; 5)); 20.58 (s, *C*(4)); 24.59 (s, *C*H2−CH2− OH); 47.07 (s, *C*H3); 57.58 (s, CH2−*C*H2−OH); 59.87 (s, *C*(2; 6)) 60.24 (s, *C*H2−CH2−CH2 −OH); 119.44 (q, *C*F3). ^{19}**F-NMR**(300 K, DMSO-d6, 235.36 MHz, [ppm]): δ = −78.79 (s, C*F*3). **IR** (Transm., CaF2-Window, 12 μm- Spacer, 20 °C, 128 Scans, [cm^{-1}]): 3539 (w); 2952 (w); 2882 (w); 1841 (vw); 1800 (vw); 1470 (w); 1349 (s); 1332 (m); 1194 (s); 1136 (s); 1086 (w); 1056 (s); 985 (w).

1-(3-Hydroxypropyl)pyridinium chloride [HOC$_2$Py][Cl]

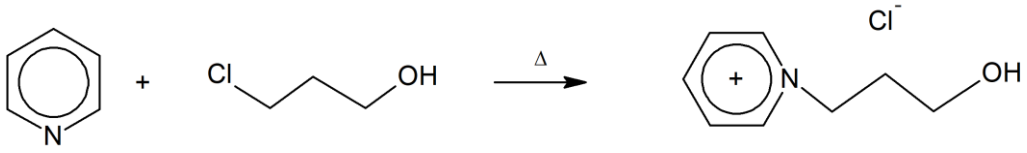

At room temperature equimolar amounts of pyridine (12.231 g; 155 mmol; 13.1 ml) and 3-chloropropanol (14.600 g; 154 mmol; 12.9 ml) were mixed and heated slowly up to 100 °C. When the reaction begins, the solution turns slightly brown and starts to crystallize upon cooling to room temperature . The crude product was recrystallized from about 450 ml acetonitrile. The product was obtained as rod-shaped colorless crystals. Yield 92 %.
^{1}**H-NMR**(298.2 K, DMSO-d$_6$, 300.13 MHz, [ppm]): δ = 2.03-2.13 (tt, 2H, CH$_2$−C*H*$_2$−CH$_2$−OH); 3.38-3.45 (dt, 2H, CH$_2$−CH$_2$− C*H*$_2$−OH); 4.76 (t, 2H, C*H*$_2$−CH$_2$− CH$_2$−OH); 5.12 (t, 1H, O*H*); 8.13-8.19 (m, 2H, *m*-C*H*); 8.58-8.65 (m, 1H, *p*-C*H*); 9.25-9.29 (m, 2H, *o*-

C*H*). ^{13}**C-NMR** (298 K, DMSO-d_6, 75.46 MHz, [ppm]): δ = 33.46 (s, $CH_2-CH_2-CH_2-OH$); 56.88 (s, $CH_2-CH_2-CH_2-OH$); 58.42 (s, $CH_2-CH_2-CH_2-OH$); 127.87 (s, *m*-C*H*); 145.05 (s, *p*-C*H*); 145.38 (s, *o*-C*H*). **IR** (ATR, 30°C, 128 Scans, [cm^{-1}]): 3277 (m); 3128 (w); 3093 (w); 3071 (w); 3043 (w); 3019 (w); 2969 (w); 2939 (w); 2905 (w); 2868 (w); 2804 (w); 1636 (w); 1626 (m); 1579 (vw); 1505 (w); 1484 (s); 1470(m); 1421 (w); 1379 (vw); 1360 (w); 1304 (m); 1265 (w); 1233 (w); 1174 (m); 1150 (w); 1083 (m); 1050 (s); 957 (w); 934(m); 872(vw); 819 (w); 774 (s); 6855 (vs); 638 (s).

1-(3-Hydroxypropyl)pyridinium-bis(trifluoromethanesulfonyl)imide [HOC_3Py][NTf_2]

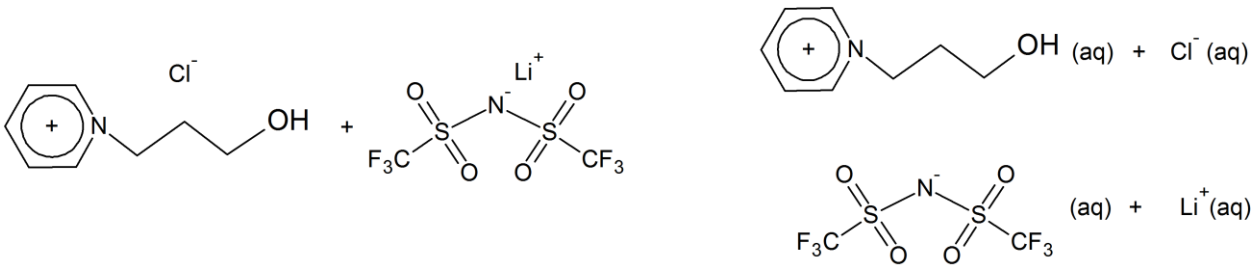

9.653 g (**[HOC_3Py][Cl]**) (56 mmol) solved in 10 ml H_2O were added to a solution of 16.125 g lithium- bis(trifluoromethylsulfonyl)imide $LiNTf_2$ (56 mmol) in 10 ml H_2O. The mixture was stirred for 1 h. Two phases were obtained, the lower one was washed several times with water until no residual chlorine could be detected with silver nitrate solution. The obtained colorless liquid of (**[HOC_3Py][NTf_2])** was dried for 8 h in vacuum at 60 °C. Yield 77 %.
^{1}**H-NMR**(298.2 K, DMSO-d_6, 300.13 MHz, [ppm]): δ = 2.03-2.13 (tt, 2H, $CH_2-CH_2-CH_2-OH$); 3.41-3.48 (dt, 2H, $CH_2-CH_2-CH_2-OH$); 4.71 (t, 2H, $CH_2-CH_2-CH_2-OH$); 4,88 (t, 1H, O*H*); 8.11-8.19 (m, 2H, *m*-C*H*); 8.56-8.64 (m, 1H, *p*-C*H*); 9.10-9.17 (m, 2H, *o*-C*H*). ^{13}**C-NMR**(298 K, DMSO-d_6, 75.46 MHz, [ppm]): δ = 33.27 (s, $CH_2-CH_2-CH_2-OH$); 57.04 (s, $CH_2-CH_2-CH_2-OH$); 58.59 (s, $CH_2-CH_2-CH_2-OH$); 119.43 (q, CF_3); 127.87 (s, *m*-C*H*); 144.99 (s, *p*-C*H*); 145.37 (s, *o*-C*H*). ^{19}**F-NMR**(298 K, DMSO-d_6, 282.40 MHz, [ppm]): δ = −78.81 (s, CF_3). **IR** (Transm., CaF_2-Window, 12 μm Spacer, 20 °C, 128 Scans, [cm^{-1}]): 3552 (w); 3299 (m); 3139 (w); 3097 (w); 3071 (w); 2943 (w); 2881 (w); 1637 (m); 1491 (m); 1318 (w); 1286 (w); 1221 (w); 1170 (w); 1060 (vs); 953 (w).

2 Sample preparation

In order to prepare the samples for the NMR experiments, the deuterated ionic liquids $[DOC_2MPip]NTf_2$, $[DOC_2Py]NTf_2$, $[DOC_3MPip]NTf_2$, and $[DOC_3Py]NTf_2$, were loaded into a glass tube (5 mm o.d.; 20 mm long), connected to a high vacuum grade valve (HI-VAC). All manipulations were performed in argon atmosphere. The samples were then attached to a vacuum line and the argon was pumped off under vacuum to a final pressure above the samples of 10^{-2} Pa. To fully degas the material the samples were slowly introduced into liquid nitrogen 2-3 times, while being connected to vacuum line. After degassing, the necks of the tubes were sealed off, while the material samples were maintained in liquid nitrogen in order to prevent their heating by the flame. The sealed samples were then transferred into an NMR probe for analysis with ^2H NMR spectroscopy.

3 Solid State NMR

In order to prepare sample for the NMR experiments, the OH-deuterated ionic liquid was loaded into a glass tube (5 mm o.d.; 20 mm long), connected to a high vacuum grade valve (HI-VAC). All manipulations were performed in argon atmosphere. The sample was then attached to a vacuum line and the argon was pumped off under vacuum to a final pressure above the sample of 10^{-2} Pa. To fully degas the material, the sample was slowly introduced into liquid nitrogen 2-3 times, while being connected to vacuum line. After degassing, the neck of the tube was sealed off, while the material sample was maintained in liquid nitrogen in order to prevent its heating by the flame. The sealed sample was then transferred into an NMR probe for analysis with ^{2}H NMR spectroscopy. The temperature of the samples was controlled with a flow of nitrogen gas by a variable-temperature unit BVT-3000 with a precision of about 1 K.

It should be noted that in each the NMR experiments were conducted by first cooling the sample in the liquid nitrogen, rapidly transferring the sample in the pre-cooled probe and then heating it up to the required temperature. Such procedure allowed a perfect reproducibility of the experimental results in the solid phase.

^{2}H NMR experiments were performed at Larmor frequency $\omega_z / 2\pi = 61.42$ MHz on a Bruker Avance-400 spectrometer, using a high power probe with 5 mm horizontal solenoid coil. All ^{2}H NMR spectra were obtained by Fourier transformation of quadrature-detected phase-cycled quadrupole echo arising in the pulse sequence ($90°_x - \tau_1 - 90°_y - \tau_2$ – acquisition – t), where τ_1 = 20 μs, τ_2 = 21 μs and t is a repetition time of the sequence during the accumulation of the NMR signal. The duration of the π/2 pulse was 1.6-1.7 μs. Spectra were typically obtained with 50 - 20000 scans with repetition time ranging from 0.5 to 15 seconds.

4. DSC

Differential scanning calorimetry (DSC) measurements were carried out by using a Mettler Toledo DSC 822e with a Huber TC100MT cooler under N_2 atmosphere. The samples for DSC measurements were tightly sealed in Al pans of 40 μl volume. All handling operations with sample were carried out in a glove-box under a nitrogen atmosphere (residual concentrations of oxygen 1.0 ppm and water 0.3 ppm). Pans and samples were weighted with Sartorius MSE3.6P-000-DM microbalances with the standard uncertainty of $5 \cdot 10^{-6}$ g. The calibration of Mettler Toledo DSC 822e was checked with melting behavior of the reference samples of indium, *n*-octane, and twice distilled water. The temperature of fusion agreed with recommended value better than 0.3 K and the fusion enthalpy within 0.2 $kJ \cdot mol^{-1}$.

Thermograms were recorded during cooling (373-193 K) and heating (193-373 K) at cooling and heating rates of 1, 5, and 10 $K \cdot min^{-1}$. The glass transition temperature (T_g, middle point of the heat capacity change), crystallization temperature (T_c), and melting temperature (T_{fus}) were determined from DSC thermograms during the heating scans. The summary of phase transitions is given in Table S1.

[HOC$_2$MPip][NTf$_2$] (I) [1]

For this IL the crystallization of the sample was observed on cooling. Changing the heating and cooling rates doesn't change the temperature of the observed phase transitions. That obviously shows the thermodynamic nature of the recorded transitions.

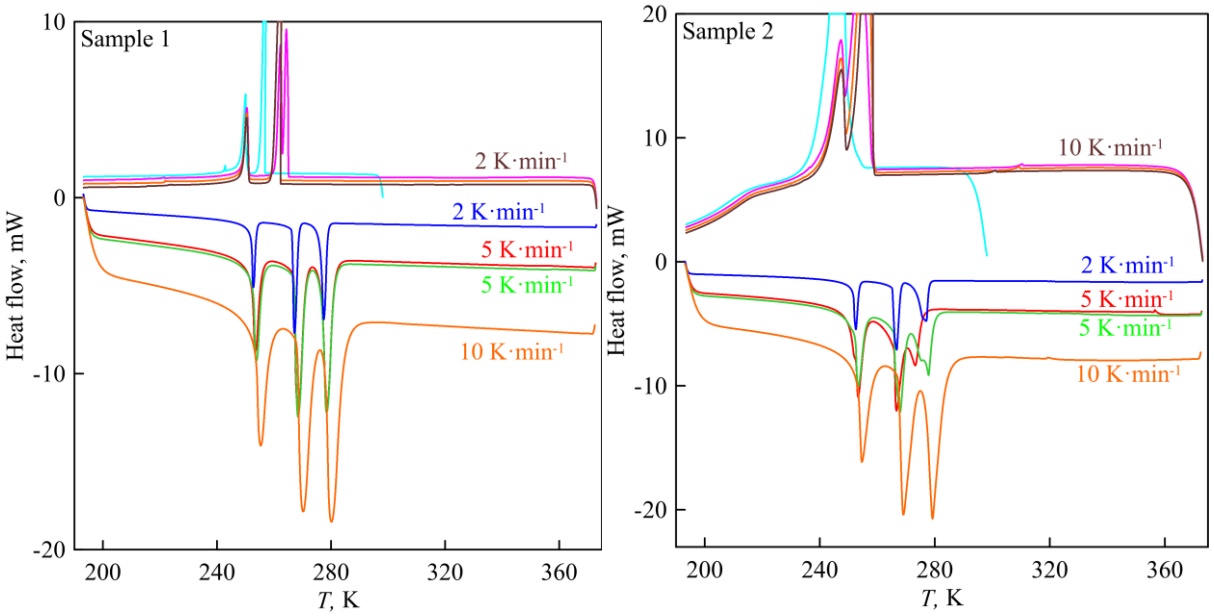

SI Fig. S1 The DSC profile for [HOC$_2$MPip][NTf$_2$] (**II**) samples; blue line is heating with 2 K·min^{-1}, green and read lines – heating with 5 K·min^{-1}, orange line - heating with 10 K·min^{-1}. The curves with the same heating or cooling rate are shifted for 0.1 mW for better illustration.

[HOC$_2$Py][NTf$_2$] (II) [1]

No phase transition was observed during cooling down to 193 K. During heating the glass transition at 200.4 K was observed and reproduced for both samples. No fusion or crystallization peak has been seen for both samples at heating rates from 2 to 10 K·min^{-1}.

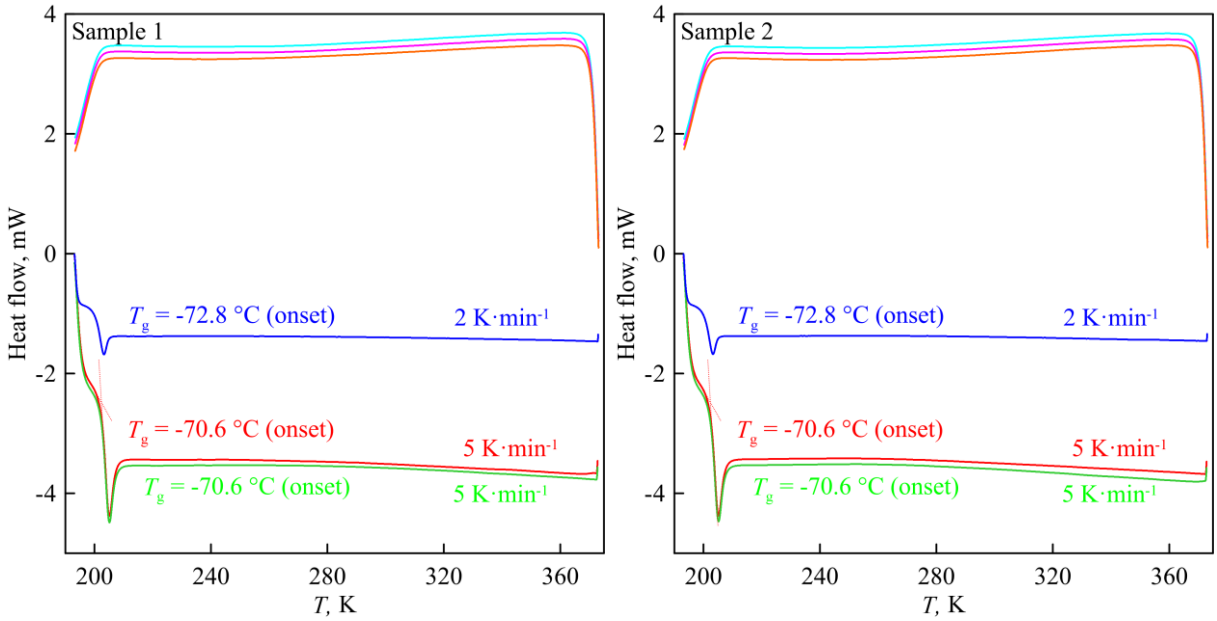

SI Fig. S2 The DSC profile for $[HOC_2Py][NTf_2]$ (**II**) samples; blue line is the heating with 2 K·min^{-1}, green and red lines – heating with 5 K·min^{-1}. No peak of fusion was observed. The curves with the same heating or cooling rate are shifted for 0.1 mW for better illustration.

$[HOC_3Pip][NTf_2]$ (III), $[HOC_3Py][NTf_2]$ (IV)

For all these samples no crystallization has been during cooling and heating runs. According to Beaman−Kauzmann rule one can expect $T_g \approx 2/3\ T_{fus}$ and evaluate the fusion temperature for studied ILs. As a matter of fact, the highest rate of crystallization can be obtained at temperatures 20 - 30 K lower than T_{fus}. We have annealed the samples at these temperatures to obtain the crystal phase of the studied compounds.

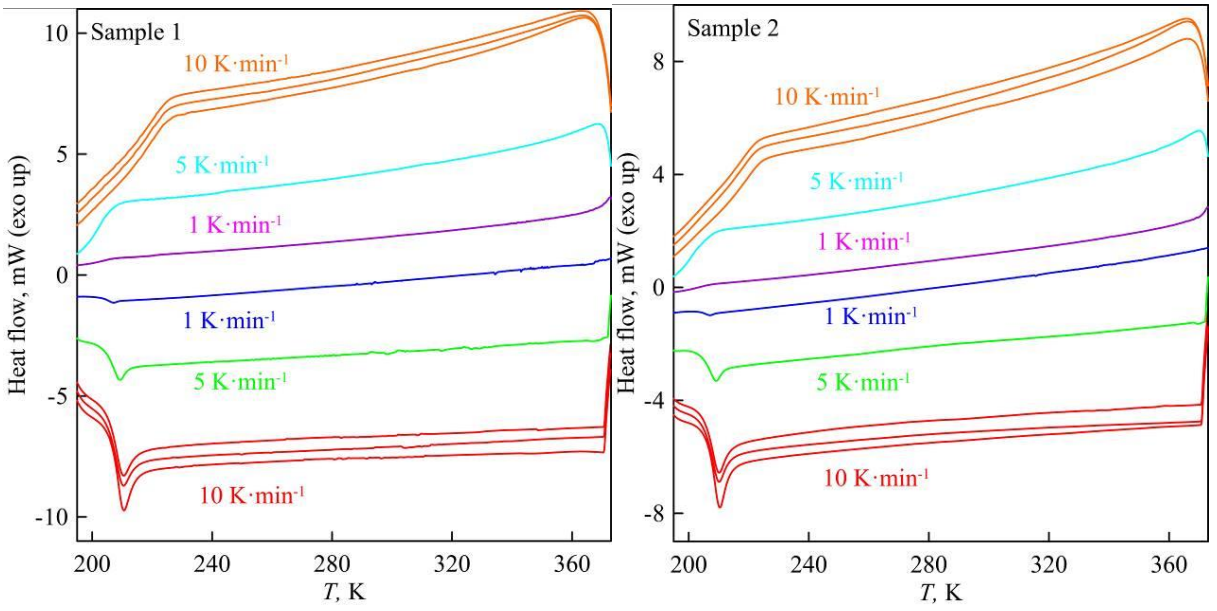

SI Fig. S3 The DSC profile for $[HOC_3MPip][NTf_2]$(**III**) samples; blue line is the heating with 1 $K \cdot min^{-1}$, green and red lines – heating with 5 and 10 $K \cdot min^{-1}$, correspondingly. The cooling curves are marked as follows: magenta – 1 $K \cdot min^{-1}$; cyan - 5 $K \cdot min^{-1}$, and orange - 10 $K \cdot min^{-1}$. The curves with the same heating or cooling rate are shifted for 0.2 mW for better illustration.

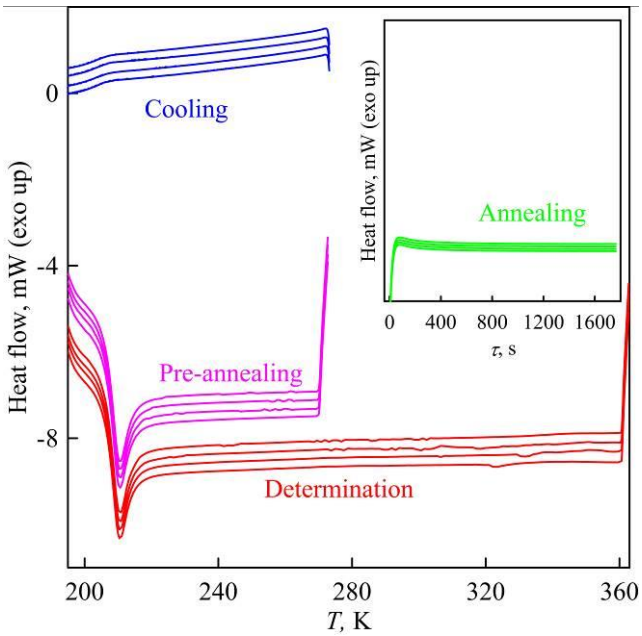

SI Fig. S4 The DSC profile for $[HOC_3MPip][NTf_2]$(**III**) samples with annealing procedure; blue lines are the cooling after annealing, green lines show the heat flow during annealing, magenta corresponds to heating before annealing and red lines correspond to heating with 10 $K \cdot min^{-1}$ after annealing. The curves with the same heating or cooling rate are shifted for 0.3 mW for better illustration.

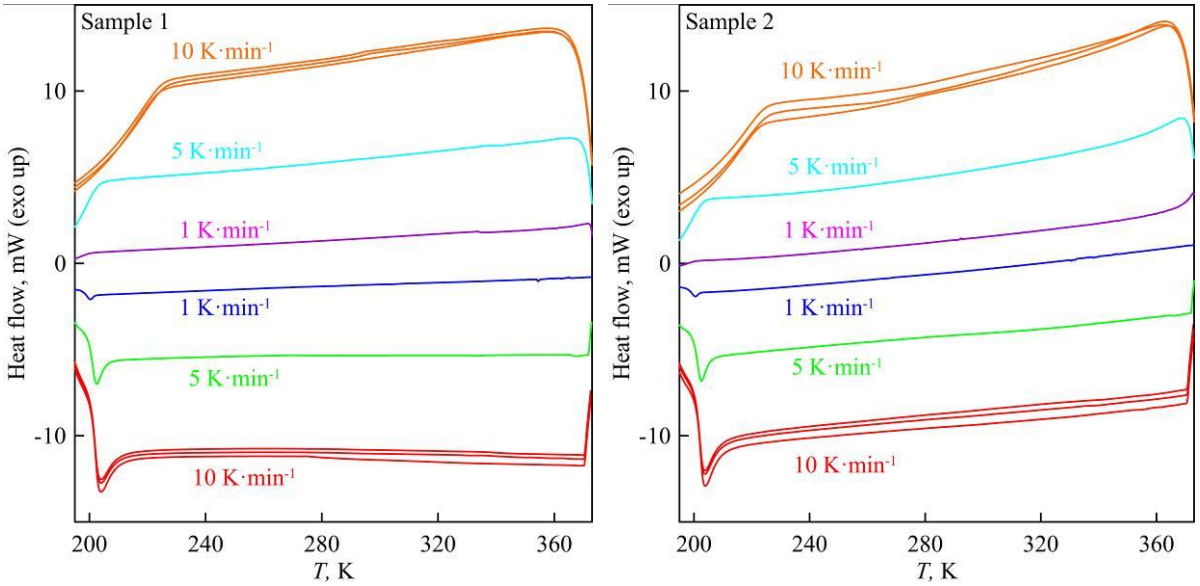

SI Fig. S5 The DSC profile for $[HOC_3Py][NTf_2]$(**IV**) samples; blue line is the heating with 1 $K \cdot min^{-1}$, green and red lines – heating with 5 and 10 $K \cdot min^{-1}$, correspondingly. The cooling curves are marked as follows: magenta – 1 $K \cdot min^{-1}$; cyan - 5 $K \cdot min^{-1}$, and orange - 10 $K \cdot min^{-1}$. The curves with the same heating or cooling rate are shifted for 0.2 mW for better illustration.

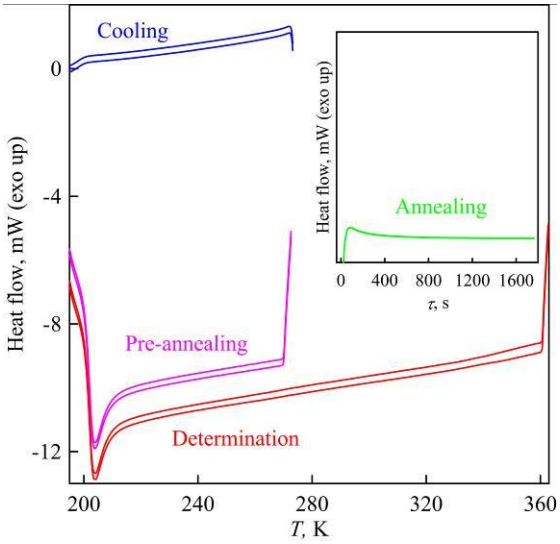

SI Fig. S6 The DSC profile for $[HOC_3Py][NTf_2]$(**IV**) samples with annealing procedure; blue lines are the cooling after annealing, green lines show the heat flow during annealing procedure, magenta corresponds to heating before annealing and red lines correspond to heating with 10 $K \cdot min^{-1}$ after annealing. The curves with the same heating or cooling rate are shifted for 0.3 mW for better illustration.

Table S1. The thermodynamic parameters of observed phase transitions for studied ILs.

Ionic liquid	Phase transition	T_{trs}, K	$\Delta_{trs}H^{o}_{m}$, kJ·mol^{-1}	Comments
[HOC_2MPip][NTf_2] (I)	crIII-crII	251.9 ± 1.3	2.7 ± 0.3	Ref. 1
	crII-crI	266.7 ± 1.5	4.2 ± 0.2	
	crI – liquid	276.6 ± 0.9	4.4 ± 0.3	
[HOPy][NTf_2] (**II**)	glass - liquid	200.4 ± 0.1	-	Ref. 1
[HOC_3MPip][NTf_2] (**III**)	glass-liquid	204.4 ± 0.3 (1 K·min^{-1})	-	
		205.5 ± 0.1 (5 K·min^{-1})		
		206.8 ± 0.1 (10 K·min^{-1})		
[HOC3Py][NTf2] (**IV**)	glass-liquid	197.6 ± 0.1 (1 K·min-1)	-	
		199.8 ± 0.1 (5 K·min-1)		
		200.6 ± 0.1 (10 K·min-1)		

References:

[1] T. Niemann, D. Zaitsau, A. Strate, A. Villinger, R. Ludwig, *Sci. Rep.* **2018**, *8*, 14753.

7. Density functional theory (DFT) calculations on [HOC_3Py][NTf_2] clusters

***** pyridinium_C3_NTf2_b3lyp_6-31+Gp_monomer_D3.g09 (c-a)**

6	0	4.434121	-0.291884	-0.470492
7	0	3.384067	0.551822	-0.596495
6	0	2.290456	0.195540	-1.304270
6	0	2.208278	-1.055110	-1.899906
6	0	3.274018	-1.941416	-1.769207
6	0	4.410136	-1.543471	-1.055564
6	0	3.447541	1.677646	1.667366
6	0	2.293102	0.870967	2.258689
8	0	2.421148	-0.476511	1.812394
9	0	-3.519859	1.189383	-0.533543
6	0	-2.481299	2.006069	-0.750612
9	0	-2.776216	3.223510	-0.272091
16	0	-0.941296	1.359715	0.126700
7	0	-0.761637	-0.074522	-0.612246
16	0	-0.760947	-1.507454	0.135273
6	0	-2.572174	-1.959505	0.422224
9	0	-2.640934	-3.188270	0.953422
9	0	-2.268025	2.098683	-2.070565
8	0	0.132221	2.259409	-0.350353
8	0	-1.257195	1.349967	1.556871
8	0	-0.281744	-2.495537	-0.837910
8	0	-0.180072	-1.502572	1.492111
9	0	-3.146383	-1.087859	1.258153
9	0	-3.236282	-1.951075	-0.742127
1	0	1.290617	-1.329364	-2.404461
1	0	1.544577	-0.910920	1.841940
1	0	3.438747	2.689276	2.092783
1	0	4.397398	1.216634	1.968115
1	0	2.348020	0.923200	3.356613
1	0	1.330781	1.299890	1.955675
1	0	5.261563	-2.203019	-0.929192
1	0	3.216636	-2.934377	-2.204197
1	0	1.481312	0.913256	-1.338736
1	0	5.265481	0.061199	0.126397
6	0	3.392562	1.852034	0.142505
1	0	2.480523	2.376144	-0.144998
1	0	4.257211	2.418195	-0.218849

***** pyridinium_C3_NTf2_cation_cation_b3lyp_6-31+Gp_dimer_D3.g09 (c-c)**

6	0	-0.065823	-3.195163	0.135749
7	0	-1.410858	-3.037518	0.041377

6	0	-2.073852	-2.225734	0.895003
6	0	-1.392217	-1.533799	1.885769
6	0	-0.013810	-1.695709	2.006322
6	0	0.656267	-2.543303	1.115920
6	0	-1.882137	-3.221561	-2.444608
6	0	-2.585546	-1.906427	-2.761109
8	0	-2.071286	-0.912999	-1.872608
8	0	2.908703	-1.561278	3.230295
16	0	3.910264	-0.871775	2.407915
8	0	5.313002	-0.817332	2.820311
6	0	3.327011	0.921773	2.471780
9	0	3.998721	1.680709	1.571145
7	0	3.640506	-1.199765	0.846870
16	0	4.811484	-1.612581	-0.190308
8	0	5.278592	-0.465401	-1.003195
9	0	2.014065	1.014924	2.189034
9	0	3.538971	1.433415	3.688181
8	0	5.800621	-2.580029	0.280345
6	0	3.690300	-2.555099	-1.380679
9	0	2.706142	-1.771248	-1.851815
9	0	4.420817	-2.995010	-2.413110
9	0	3.126435	-3.617947	-0.772546
8	0	0.380675	0.305527	-2.157576
6	0	0.654691	0.755108	-0.834603
6	0	1.575912	1.968163	-0.934067
7	0	3.817094	2.705253	-1.771552
6	0	3.512398	3.869223	-2.394064
6	0	4.398022	4.932156	-2.385431
6	0	5.621698	4.793483	-1.719959
6	0	5.919489	3.585273	-1.092858
6	0	4.997279	2.546075	-1.131985
9	0	-7.169000	1.071558	0.256295
6	0	-6.920264	-0.241801	0.183607
9	0	-7.780400	-0.801179	-0.680030
16	0	-5.160446	-0.549167	-0.422343
7	0	-4.281933	0.149207	0.746713
16	0	-3.295760	1.412844	0.534013
6	0	-4.371850	2.949380	0.741537
9	0	-3.585626	4.037973	0.750807
9	0	-7.099920	-0.787669	1.392432
8	0	-5.007371	-2.013459	-0.306602
8	0	-5.079276	0.048296	-1.762536
8	0	-2.378651	1.452565	1.677448
8	0	-2.735460	1.555620	-0.823714
9	0	-5.239985	3.051410	-0.272437
9	0	-5.050380	2.894882	1.894947
1	0	-1.951839	-0.858046	2.520853
1	0	-2.626812	-0.107103	-1.869657
1	0	-2.236351	-3.982840	-3.151228
1	0	-0.801645	-3.115737	-2.607640
1	0	-2.392988	-1.625784	-3.806538

1	0	-3.667638	-2.005168	-2.622906
1	0	-0.467625	-0.187789	-2.139940
1	0	1.156201	-0.032549	-0.253939
1	0	-0.264899	1.041507	-0.311289
1	0	1.029151	2.794893	-1.404330
1	0	1.878947	2.282270	0.069252
1	0	5.177889	1.570603	-0.692894
1	0	6.330231	5.616002	-1.697887
1	0	4.128264	5.851585	-2.893319
1	0	1.728776	-2.672933	1.175070
1	0	0.553856	-1.176784	2.770577
1	0	-3.142095	-2.141862	0.750759
1	0	0.396715	-3.852358	-0.590969
1	0	6.857754	3.427821	-0.572419
1	0	2.547744	3.907115	-2.886343
6	0	-2.155990	-3.759594	-1.031179
1	0	-3.217297	-3.679262	-0.789571
1	0	-1.859349	-4.810141	-0.956765
6	0	2.808168	1.599652	-1.762833
1	0	3.311846	0.724593	-1.359221
1	0	2.535429	1.391584	-2.799303

***** pyridinium_C3_NTf2_cation_cation_b3lyp_6-31+Gp_trimer_D3.g09 (c-c)**

6	0	-0.342511	0.143526	3.215786
7	0	-1.643486	0.431472	2.966927
6	0	-2.569121	-0.555227	2.868318
6	0	-2.195893	-1.884711	2.991795
6	0	-0.853494	-2.201695	3.216589
6	0	0.078687	-1.168991	3.343703
6	0	-2.078415	2.056753	1.154194
6	0	-2.294929	3.525211	0.785099
8	0	-2.129544	3.714588	-0.628663
8	0	-2.125435	1.659582	-2.405797
6	0	-3.212776	1.569414	-3.331536
6	0	-3.271408	0.157243	-3.911136
7	0	-2.306551	-1.393390	-2.168368
6	0	-1.958179	-0.793616	-1.012235
6	0	-0.792423	-1.147101	-0.356599
6	0	0.011729	-2.156325	-0.877293
6	0	-0.379628	-2.789330	-2.063015
6	0	-1.544047	-2.386213	-2.689304
8	0	0.253906	1.763747	-3.836049
6	0	0.692216	0.431479	-3.624968
6	0	1.846360	0.341158	-2.623051
7	0	4.238833	1.032598	-2.243780
6	0	4.830505	2.168524	-1.810298
6	0	5.937416	2.109938	-0.976833
6	0	6.431509	0.867980	-0.577542

6	0	5.806877	-0.295010	-1.034923
6	0	4.711768	-0.182720	-1.874532
8	0	2.590138	4.441598	-2.254501
16	0	1.924139	4.378738	-0.949078
7	0	2.372471	2.980303	-0.277245
16	0	1.737860	2.328670	1.050116
8	0	0.782696	3.142893	1.820309
6	0	2.786475	5.723997	0.057896
9	0	2.308076	5.769099	1.305150
9	0	4.106637	5.463429	0.106690
9	0	2.600687	6.909500	-0.530647
8	0	0.494511	4.703272	-0.838698
8	0	1.387934	0.922933	0.794895
6	0	3.258885	2.232587	2.159125
9	0	4.237171	1.521044	1.583005
9	0	3.721617	3.458199	2.431756
9	0	2.906826	1.635933	3.312599
8	0	1.854219	-3.649567	2.561290
16	0	3.102845	-3.676703	1.786491
8	0	4.100243	-4.719159	2.017333
6	0	3.930330	-2.056709	2.292978
9	0	5.097320	-1.868596	1.660419
7	0	2.686607	-3.399784	0.240013
16	0	3.623506	-3.631592	-1.049006
8	0	2.963311	-2.929496	-2.170093
9	0	3.115377	-1.026588	2.000238
9	0	4.153031	-2.058422	3.617131
8	0	5.068618	-3.436390	-0.869608
6	0	3.392332	-5.452882	-1.493358
9	0	2.084809	-5.697205	-1.703425
9	0	4.065315	-5.720268	-2.622109
9	0	3.831148	-6.248044	-0.518583
9	0	-4.881615	2.446118	-0.645401
6	0	-6.097485	1.980757	-0.298304
9	0	-6.828189	3.000043	0.163668
9	0	-6.688167	1.475904	-1.390147
16	0	-5.947061	0.681188	1.058437
7	0	-5.096194	-0.405399	0.175335
16	0	-5.074771	-1.970581	0.579747
6	0	-6.600018	-2.742897	-0.230955
9	0	-6.521704	-4.076655	-0.116785
8	0	-5.099960	1.324884	2.082138
8	0	-7.314831	0.300225	1.405800
8	0	-3.964320	-2.591256	-0.158004
8	0	-5.207808	-2.232026	2.020867
9	0	-7.730012	-2.319132	0.328505
9	0	-6.611226	-2.423849	-1.541273
1	0	1.127297	-1.382635	3.503675
1	0	-0.510033	-0.625893	0.547270
1	0	-2.248358	2.421081	-1.783126
1	0	-4.092115	0.129865	-4.639168

1	0	-2.349491	-0.058490	-4.466034
1	0	-3.077178	2.292975	-4.147717
1	0	-4.155705	1.800664	-2.823160
1	0	-0.546237	1.897486	-3.284232
1	0	1.010188	0.023649	-4.595848
1	0	-0.131432	-0.193305	-3.263275
1	0	1.544190	0.759298	-1.659150
1	0	2.087442	-0.715792	-2.467906
1	0	-1.234515	4.075355	-0.786106
1	0	-3.311926	3.838854	1.039993
1	0	-1.581489	4.160589	1.320939
1	0	-1.132672	1.724369	0.719281
1	0	-2.890041	1.458174	0.734065
1	0	4.187614	-1.049257	-2.258654
1	0	7.285365	0.804341	0.090330
1	0	6.380986	3.038067	-0.633612
1	0	0.329672	0.987886	3.274846
1	0	-0.517927	-3.231833	3.275833
1	0	-3.587149	-0.238415	2.677445
1	0	0.229436	-3.573470	-2.498397
1	0	0.926609	-2.458216	-0.375288
1	0	-2.640214	-0.044976	-0.648500
1	0	-2.964399	-2.641214	2.885094
1	0	-1.900536	-2.825629	-3.613671
1	0	6.132184	-1.288646	-0.748898
1	0	4.381459	3.098520	-2.134561
6	0	3.054523	1.109802	-3.155353
1	0	3.380821	0.709793	-4.122094
1	0	2.806785	2.164600	-3.276067
6	0	-3.538492	-0.953237	-2.879648
1	0	-4.250230	-0.634599	-2.116022
1	0	-3.949478	-1.844307	-3.359283
6	0	-2.038872	1.840530	2.668792
1	0	-1.294002	2.486741	3.135270
1	0	-3.015805	2.013614	3.122013

***** pyridinium_C3_NTf2_b3lyp_6-31+Gp_cation_cation_tetramer_D3.g09 (c-c)**

C	-5.538088	-3.197406	-1.003359
N	-4.545942	-2.943787	-1.883581
C	-3.840967	-3.945630	-2.461119
C	-4.135073	-5.266092	-2.169466
C	-5.176240	-5.553124	-1.277702
C	-5.884949	-4.504196	-0.695002
C	-4.194372	-1.524276	-2.168963
C	-3.158852	-0.994397	-1.181711
C	-1.777378	-1.603686	-1.328125
O	-1.339617	-1.446506	-2.691665
O	1.193661	-1.487385	-2.088820
C	1.703521	-2.680153	-1.495917

C	1.642245	-3.869797	-2.455813
C	1.918746	-5.224356	-1.781874
N	3.182202	-5.257726	-0.986590
C	4.361702	-5.532760	-1.595819
C	5.540265	-5.556654	-0.872205
C	5.512253	-5.259402	0.493242
C	4.292859	-4.958530	1.096824
C	3.136446	-4.967549	0.335701
O	-0.801861	1.185851	-2.792174
C	-1.879776	1.935861	-3.366595
C	-1.868110	3.332102	-2.759816
C	-2.328086	3.450178	-1.299477
N	-1.610693	2.560439	-0.335848
C	-0.262161	2.545076	-0.293331
C	0.411014	1.736479	0.604677
C	-0.314511	0.933559	1.485585
C	-1.707989	0.990910	1.449857
C	-2.332134	1.817252	0.529395
O	1.809976	0.673864	-3.622317
C	2.796265	1.692183	-3.483095
C	3.109771	1.990739	-2.010570
C	4.246421	3.004866	-1.878055
N	4.485895	3.397561	-0.453353
C	3.944545	4.540801	0.028941
C	4.127032	4.914017	1.349974
C	4.862589	4.091021	2.201111
C	5.402551	2.909574	1.689963
C	5.207092	2.583388	0.356929
O	-1.288994	4.750411	1.519190
S	-0.223009	5.745723	1.706233
O	-0.573648	7.109059	2.099666
N	0.961758	5.639311	0.568512
S	0.623917	5.954487	-0.970358
C	1.491811	7.607343	-1.245834
F	2.821670	7.459222	-1.049724
O	1.381582	5.021433	-1.842025
O	-0.792639	6.191601	-1.278500
C	0.818326	5.059956	3.123076
F	1.883312	5.842805	3.375001
F	0.056763	5.012337	4.218881
F	1.261281	3.817505	2.849520
F	1.292423	8.024447	-2.500944
F	1.035874	8.524401	-0.393587
O	2.361950	-4.015058	3.124404
S	1.269120	-3.805500	4.092968
O	1.264536	-4.527092	5.360263
N	-0.210877	-3.887606	3.444244
S	-0.504296	-3.557030	1.902531
O	-0.028018	-4.572377	0.932356
C	-2.366524	-3.831412	2.012636
F	-2.927838	-2.998760	2.892571

F	-2.663553	-5.093948	2.331931
F	-2.897869	-3.571616	0.790813
O	-0.346965	-2.151474	1.483995
C	1.458713	-1.989061	4.594202
F	1.481709	-1.183037	3.515238
F	0.446524	-1.609239	5.384946
F	2.614008	-1.835452	5.258281
F	3.687968	-2.086363	1.560839
C	4.259069	-0.994093	1.066800
F	4.561058	-0.159314	2.082179
S	5.850684	-1.397857	0.127473
N	5.315941	-2.380057	-1.042259
S	5.282690	-1.964191	-2.606947
C	7.076056	-2.137046	-3.179408
F	7.488856	-3.403580	-2.984733
O	6.333910	-0.087490	-0.347121
O	6.629560	-2.159934	1.103725
F	3.372216	-0.367601	0.267711
O	4.600331	-3.057103	-3.315221
O	4.898424	-0.578615	-2.899777
F	7.151939	-1.852801	-4.485558
F	7.885808	-1.315002	-2.502793
O	-5.196678	1.256426	-0.639897
S	-6.475836	1.035913	0.070939
O	-7.495104	2.079758	0.037796
N	-6.956101	-0.499157	-0.157009
S	-8.451777	-0.944974	-0.622326
C	-8.398590	-0.655141	-2.489525
F	-7.390461	-1.377780	-3.041515
O	-8.481021	-2.410721	-0.507959
O	-9.566141	-0.133450	-0.148490
C	-5.926491	0.879634	1.868430
F	-5.356785	2.033818	2.256698
F	-6.949320	0.601711	2.673515
F	-4.996450	-0.100303	1.989680
F	-9.546791	-1.038810	-3.054717
F	-8.178201	0.637412	-2.764491
H	6.470562	-5.761468	-1.390204
H	-3.557742	-6.055289	-2.638425
H	4.999826	4.358474	3.244492
H	-0.354402	-1.601192	-2.655981
H	-3.522165	-1.114869	-0.155205
H	-3.101938	0.081420	-1.361157
H	-1.086004	-1.099309	-0.647231
H	-1.759890	-2.668183	-1.063055
H	-1.028463	0.219632	-2.813376
H	-2.838595	1.436058	-3.164605
H	-1.756355	1.997621	-4.456955
H	-0.866196	3.762515	-2.875929
H	-2.542254	3.985632	-3.327295
H	0.920242	1.025652	-3.388296

H	2.470840	2.611136	-3.993354
H	3.691605	1.317392	-3.984745
H	3.386542	1.056974	-1.521655
H	2.218233	2.395895	-1.527692
H	1.626817	-0.850168	-2.702059
H	1.067045	-2.862328	-0.625558
H	2.721611	-2.519316	-1.137931
H	2.330538	-3.708306	-3.288877
H	0.625118	-3.934300	-2.864640
H	-3.406788	1.880883	0.431233
H	0.191049	0.265977	2.174501
H	1.493815	1.734381	0.606981
H	5.618555	1.671642	-0.066768
H	5.973998	2.225579	2.307028
H	3.658422	5.827100	1.690869
H	4.324683	-5.703042	-2.663936
H	6.432036	-5.223770	1.067569
H	2.160896	-4.740889	0.751758
H	-6.709711	-4.668566	-0.010913
H	-5.425333	-6.583746	-1.043277
H	-3.052961	-3.638281	-3.140015
H	4.178884	-4.651817	2.128222
H	-6.031647	-2.331192	-0.578390
H	3.332416	5.130644	-0.635063
H	-2.318713	0.391345	2.114717
H	0.235789	3.195793	-0.997373
H	1.999369	-6.017024	-2.529399
H	1.115519	-5.480880	-1.087286
H	-3.818932	-1.485002	-3.193229
H	-5.111606	-0.942787	-2.098752
H	-3.386548	3.205435	-1.195135
H	-2.154667	4.486079	-0.999714
H	4.013890	3.925045	-2.418464
H	5.186199	2.594315	-2.256907

6 Molecular Dynamics Simulations

SI Tab. S2: Lennard-Jones parameters σ and ϵ for all interaction sites of the $[HOC_2Py]^+$, $[HOC_3Py]^+$ and $[HOC_4Py]^+$ cation.

site	σ / Å	$\epsilon \cdot k_B^{-1}$ / K
N	3.25	85.55
C_a	3.55	35.23
H_a	2.42	15.10
C_c	3.50	33.20
H_c	2.50	15.10
H_m	2.50	15.10
O	3.12	85.60
H_o	0.00	0.00

SI Tab. S3: Bond length $r^0_{\kappa\lambda}$ and angle parameters $\phi^0_{\kappa\lambda\omega}$ und $k^a_{\kappa\lambda\omega}$ for the angle potential $V^a_{\kappa\lambda\omega} = \frac{1}{2}k^a_{\kappa\lambda\omega}(\phi_{\kappa\lambda\omega} - \phi^0_{\kappa\lambda\omega})^2$ in the force field of the $[HOC_2Py]^+$, $[HOC_3Py]^+$ and $[HOC_4Py]^+$ cation.

bond	$r^0_{\kappa\lambda}$ / Å	angle	$\phi^0_{\kappa\lambda\omega}$ / °	$k^a_{\kappa\lambda\omega}$ / kJ mol^{-1}rad^{-2}
C_a-N	1.339	C_a-C_a-C_a	120.0	527.20
C_a-H_a	1.080	C_a-C_a-N	124.0	585.80
C_a-C_a	1.400	C_a-N-C_a	117.0	585.80
N-C_c	1.339	C_a-C_a-H_a	120.0	292.90
C_c-C_c	1.529	N-C_a-H_a	116.0	292.90
C_c-H_c	1.090	C_a-N-C_c	121.5	585.80
C_c-O	1.410	N-C_c-C_c	112.7	487.43
O-H_o	0.945	H_c-C_c-N	110.7	313.26
C_c-H_m	1.090	H_c-C_c-H_c	107.8	275.70
		H_c-C_c-C_c	110.7	313.26
		H_m-C_c-C_c	110.7	313.26
		H_m-C_c-H_m	107.8	275.70
		C_c-C_c-C_c	112.7	487.43
		H_o-O-C_c	108.5	460.55
		C_c-C_c-O	109.5	418.68
		H_c-C_c-O	109.5	293.08

SI Tab. S4: Parameters m_n, k_m^{dp} and ψ_m^0 for the improper dihedral potential $V_{\kappa\lambda\omega\tau}^{\mathrm{dp}} = \sum_n k_m^{\mathrm{dp}}[1 + \cos(m_n\psi_m - \psi_m^0)]$ in the force field of the $[HOC_2Py]^+$, $[HOC_3Py]^+$ and $[HOC_4Py]^+$ cation. The central atom is the first in the list.

	m_n	k_m^{dp} / kJ mol^{-1}	ψ_m^0 / $^\circ$
N-C_a-C_a-C_c	2	4.6060	180.0
C_a-N-C_a-H_a	2	4.6060	180.0
C_a-C_a-C_a-H_a	2	4.6060	180.0

SI Tab. S5: Parameters m_n, k_m^{dp} and ψ_m^0 for the torsion potential $V_{\kappa\lambda\omega\tau}^{\mathrm{dp}} = \sum_n k_m^{\mathrm{dp}}[1+\cos(m_n\psi_m - \psi_m^0)]$ in the force field of the $[HOC_2Py]^+$ cation.

	$n(\kappa\lambda\omega\tau)$	m_n	k_m^{dp} / kJ mol^{-1}	ψ_m^0 / $^\circ$
X-C_a-C_a-X	1	2	15.1780	180.0
X-C_a-N-X	1	2	15.1780	180.0
C_a-N-C_c-C_c	1	2	0.0802	0
	2	4	-0.4693	0
N-C_c-C_c-O	1	1	-0.7375	0.0
	2	2	1.8576	0.0
	3	3	7.2898	0.0
C_c-C_c-O-H_o	1	1	-5.8097	0.0
	2	2	1.8939	0.0
	3	3	2.5150	0.0

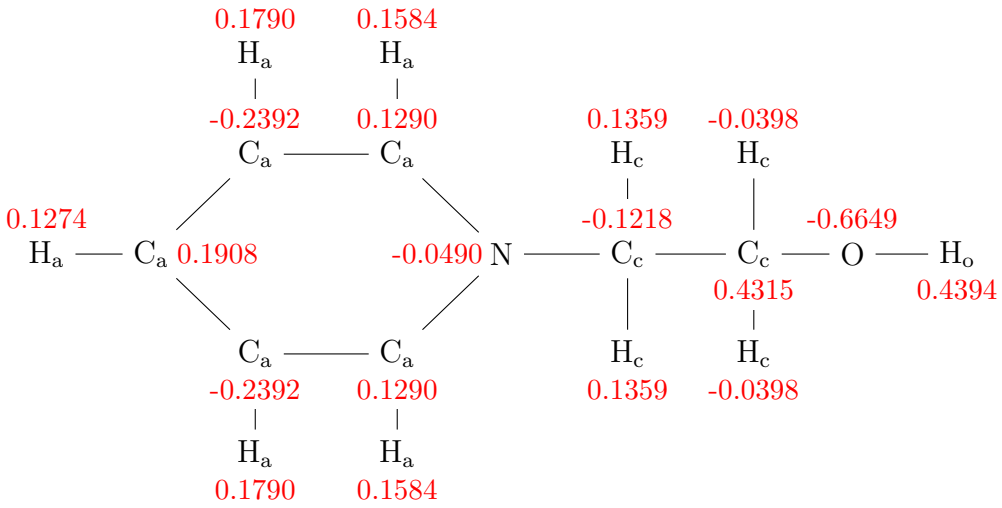

SI Fig. S7: Structure of the $[HOC_2Py]^+$ cation with atom types and corresponding point charges q/e in red.

SI Tab. S6: Parameters m_n, k_m^{dp} and ψ_m^0 for the torsion potential $V_{\kappa\lambda\omega\tau}^{\mathrm{dp}} = \sum_n k_m^{\mathrm{dp}}[1+\cos(m_n\psi_m - \psi_m^0)]$ in the force field of the $[HOC_3Py]^+$ cation.

	$n(\kappa\lambda\omega\tau)$	m_n	k_m^{dp} / kJ mol^{-1}	ψ_m^0 / °
X-C_a-C_a-X	1	2	15.1780	180.0
X-C_a-N-X	1	2	15.1780	180.0
C_a-N-C_c-C_c	1	2	-0.7379	0
	2	4	-0.2237	0
N-C_c-C_c-C_c	1	1	-3.0206	0.0
	2	2	0.6685	0.0
	3	3	5.1206	0.0
	4	4	0.4708	0.0
C_c-C_c-C_c-O	1	1	4.1980	0.0
	2	3	5.2448	0.0
	3	4	1.0859	0.0
C_c-C_c-O-H_o	1	1	-1.8926	0.0
	2	2	1.0349	0.0
	3	3	2.5840	0.0
	4	4	0.0316	0.0

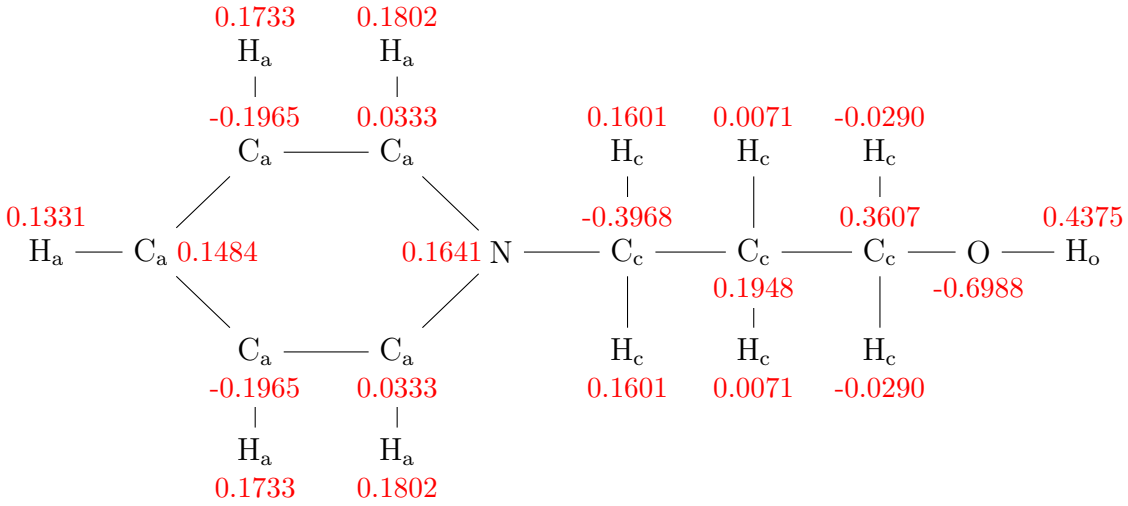

SI Fig. S8: Structure of the $[HOC_3Py]^+$ cation with atom types and corresponding point charges q/e in red.

SI Tab. S7: Parameters m_n, k_m^{dp} and ψ_m^0 for the torsion potential $V_{\kappa\lambda\omega\tau}^{dp} = \sum_n k_m^{dp}[1+\cos(m_n\psi_m - \psi_m^0)]$ in the force field of the $[HOC_4Py]^+$ cation.

	$n(\kappa\lambda\omega\tau)$	m_n	k_m^{dp} / kJ mol^{-1}	ψ_m^0 / °
X-C_a-C_a-X	1	2	15.1780	180.0
X-C_a-N-X	1	2	15.1780	180.0
C_a-N-C_c-C_c	1	2	-0.3579	0
C_a-N-C_c-C_c	2	4	-0.4037	0
C_c-C_c-C_c-C_c	1	1	-0.2825	0.0
	2	2	0.6065	0.0
	3	3	4.6858	0.0
	4	4	0.7018	0.0
	5	5	0.4468	0.0
	6	6	0.4564	0.0
C_c-C_c-C_c-O	1	1	-2.3748	0.0
	2	3	6.8089	0.0
	3	4	0.9531	0.0
C_c-C_c-O-H_o	1	1	-3.5552	0.0
	2	2	0.5886	0.0
	3	3	2.5272	0.0
	4	4	0.1504	0.0

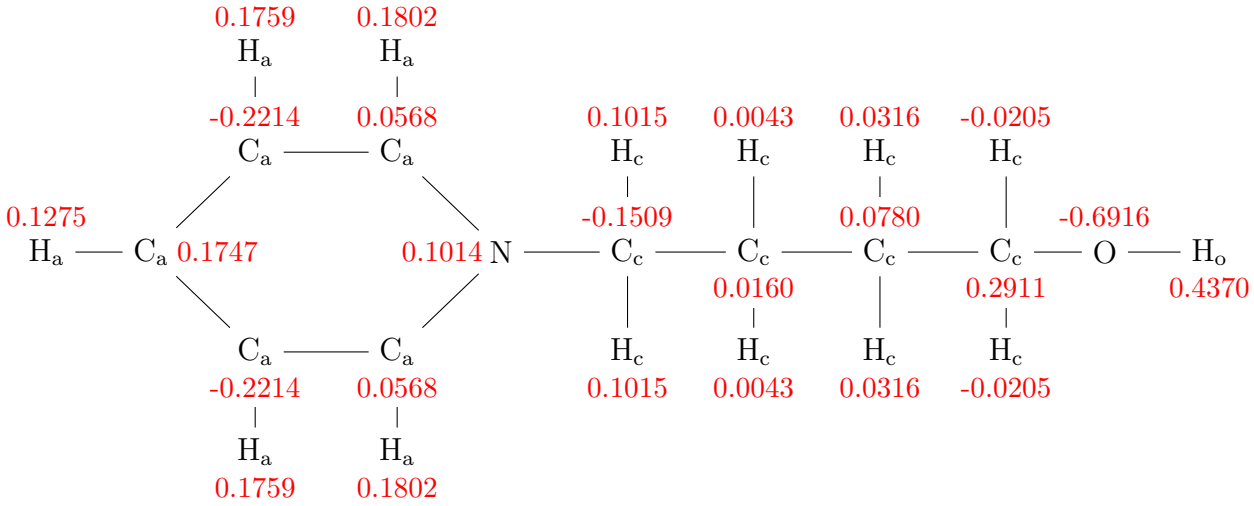

SI Fig. S9: Structure of the $[HOC_4Py]^+$ cation with atom types and corresponding point charges in red.

IV. Isolating the role of hydrogen bonding in hydroxyl-functionalized ionic liquids by means of vaporization enthalpies, infrared spectroscopy and molecular dynamics simulations

D. H. Zaitsau, J. Neumann, T. Niemann, A. Strate, D. Paschek, S. P. Verevkin, R. Ludwig, *Phys. Chem. Chem. Phys.* **2019**, *21*, 20308.
DOI: 10.1039/c9cp04337c

Contribution:
In earlier works I developed the force fields of the imidazolium- as well as pyridinium-based cations. The MD simulation in the gas and liquid phases of the investigated ILs were performed by me as well as the related analysis, such as the separation of the interaction energy contributions. I contributed to the draft of the manuscript and aided in its revision. Overall, my part of the publication sums up to approximately 20 %.

PCCP

PAPER

View Article Online
View Journal | View Issue

Cite this: *Phys. Chem. Chem. Phys.*, 2019, **21**, 20308

Isolating the role of hydrogen bonding in hydroxyl-functionalized ionic liquids by means of vaporization enthalpies, infrared spectroscopy and molecular dynamics simulations†

Dzmitry H. Zaitsau, [ab] Jan Neumann,[ab] Thomas Niemann,[a] Anne Strate,[ab] Dietmar Paschek, *[ab] Sergey P. Verevkin *[ab] and Ralf Ludwig *[abc]

Received 5th August 2019,
Accepted 28th August 2019

DOI: 10.1039/c9cp04337c

rsc.li/pccp

The enthalpy of vaporization is mainly the amount of the energy needed for transferring quantities from the liquid into the gas phase. It simply describes the energy required to overcome the interaction energy between quantities if those evaporate as monomers as is the case for molecular liquids. The situation for ionic liquids (ILs) is more complex. We do not know the delicate composition of different types of interaction, neither for the liquid nor for the gas phase. Additionally, we have to consider that ILs evaporate as ion pairs which carry substantial interaction energy of all kind into the vapor phase. In this study, we measured the vaporization enthalpies of well-selected hydroxyl-functionalized and non-hydroxyfunctionalized ILs. In particular, we focussed on the case of hydroxyl-functionalized ILs providing possible hydrogen bonding between cation and anion in the liquid as well as in the gas phase. With infrared spectroscopy, we showed that all the hydroxyl groups are involved in hydrogen bonding in the liquid state of the ILs. However, molecular dynamics simulations showed that the evaporating ion pairs also include this hydrogen bond. A detailed analysis of the potential energies for all IL constituents showed that the hydrogen bond hinders favourable interaction between the polarizable ring of the cations and the anions leading to higher vaporization enthalpies for the hydroxyl-functionalized ILs.

Introduction

The secret of ionic liquids (ILs) lies in the mélange of Coulomb interaction, hydrogen bonding and dispersion forces between cations and anions.[1–4] The delicate balance of these differently strong and directional types of interaction results in the unique properties of these liquid salts, which attracted increasing interest in science and technology since more than a decade.[5–8] In principle, vaporization enthalpies provide information about the energy, which is required to overcome the overall interaction energy between the liquid constituents. For molecular liquids the situation is easy because the gas phase species are represented by isolated molecules. Thus, hydrogen bond energy is accessible from the differences of the vaporization enthalpies of *n*-alkanes and *n*-alcohols, because monomeric species dominate the gas phase.[9–12] Beside the difficulty to measure vapor pressures for unstable ILs, the challenge to dissect their overall interaction energy from vaporization enthalpies only is twofold: neither the liquid nor the gas-phase species are known. Thus, the sole knowledge of transfer energies is insufficient. If the gas phase species can be identified as ion pairs, then ILs including functionalized groups usually exhibit lower vaporization energies because the H-bond energy is carried into the gas phase.[13–19] Here, we show that vaporization enthalpies alone are not suitable to explain structure and interaction at molecular level. Supporting infrared (IR) spectroscopy and molecular dynamics (MD) simulations allow dissecting vaporization enthalpies, and isolating the role of hydrogen bonding.

Strategy of this study

In this study, we measured the vaporization enthalpies for well-selected sets of hydroxyl-functionalized (IL-OH) and non-hydroxyl-functionalized (IL-CH_3) ionic liquids including differently strong interacting anions such as bis(trifluoromethylsulfonyl)imide (NTf_2), trifluoromethylsulfonate (OTf), and metyhlsulfonate (OMs).

[a] *Universität Rostock, Institut für Chemie, Abteilung für Physikalische Chemie, Dr-Lorenz-Weg 2, 18059, Rostock, Germany. E-mail: Dietmar.Paschek@uni-rostock.de, Sergey.Verevkin@uni-rostock.de, Ralf.Ludwig@uni-rostock.de*

[b] *Department LL&M, University of Rostock, Albert-Einstein-Str. 25, 18059, Rostock, Germany*

[c] *Leibniz-Institut für Katalyse an der Universität Rostock e.V., Albert-Einstein-Str. 29a, 18059 Rostock, Germany*

† Electronic supplementary information (ESI) available. See DOI: 10.1039/c9cp04337c

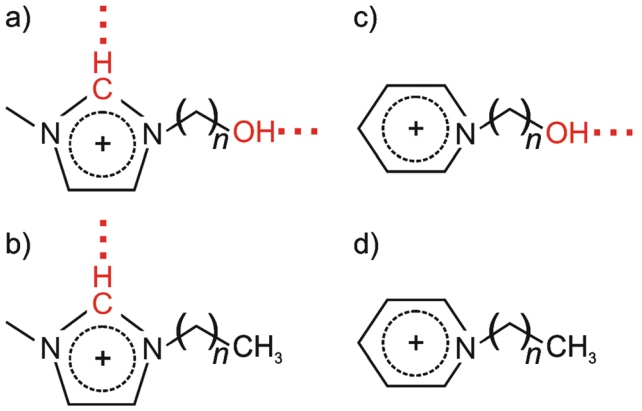

Scheme 1 Four cations providing different interaction sites for possible hydrogen bonding in ILs. (a) 1-(2-Hydroxyethyl)-3-methylimidazolium (HEMIm) with interaction sites C(2)H and OH, (b) 1-methyl-3-propyl-imidazolium (PMIm) with interaction site C(2)H, (c) 1-(2-hydroxyalkyl)-pyridinium (HEPy) with interaction site OH, and finally (d) 1-alkylpyridinium (PPy) without any H-bond donor function.

As shown in Scheme 1 four different types of cations are used, each providing different types and numbers of proton donor functions: (a) C(2)H and OH in the 1-(2-hydroxyethyl)-3-methylimidazolium (HEMIm) cation, (b) C(2)H in the 1-methyl-3-propyl-imidazolium (PMIm) cation, (c) OH in the 1-(2-hydroxyethyl)pyridinium (HEPy) and 1-(2-hydroxypropyl)pyridinium (HPPy) cations, and finally (d) with none of two interaction sites, 1-propylpyridinium (PPy) and 1-butylpyridinium (BPy) cations.

Most of the ILs were synthesized using well-established protocols (see ESI†). The other ILs were purchased from Iolitec. All samples have been dried under vacuum (at 3×10^{-3} mbar) for several days and the final water concentration (<15 ppm) has been checked by Karl–Fischer titration.

Differences in enthalpies of vaporization for functionalized and non-functionalized ILs

We measured the vaporization enthalpies, $\Delta_l^g H_m^0$, for two sets of ILs showing characteristic cation–anion combinations. The main idea is to compare the vaporization enthalpies of ILs of type IL-CH_3 and IL-OH for isolating the role of hydrogen bonding in the hydroxyl-functionalized ILs. The first set of ionic liquids includes 1-methyl-3-propyl-imidazolium (PMIm) and 1-(2-hydroxyethyl)-3-methylimidazolium (HEMIm) cations each in combination with the anions bis(trifluoromethylsulfonyl)imide (NTf_2), trifluoromethylsulfonate (OTf), and metyhlsulfonate (OMs), which are supposed to have increasing interaction potential in this sequence. As shown in Fig. 1a the vaporization enthalpies are 127.1 kJ mol^{-1}, 132.6 kJ mol^{-1}, and 146.4 kJ mol^{-1} for ILs-CH_3 as well as 127.5 kJ mol^{-1}, 136.0 kJ mol^{-1} and 145.2 kJ mol^{-1} for ILs-OH, indicating the increasing interaction strength of the selected anions. However, the differences of vaporization enthalpies $\Delta(\Delta_l^g H_m^0)$ for ILs-CH_3 and ILs-OH are only −0.4 kJ mol^{-1}, −3.4 kJ mol^{-1} and +1.2 kJ mol^{-1},

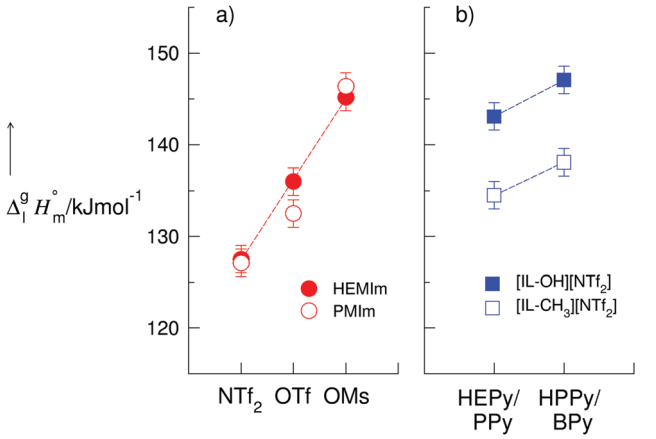

Fig. 1 $\Delta_l^g H_m^0$ vaporization enthalpies measured for IL-CH_3 and IL-OH types of ionic liquids. (a) 1-Methyl-3-propylimidazolium (PMIm) and 1-(2-hydroxyethyl)-3-methylimidazolium (HEMIm) cations with bis(trifluoromethylsulfonyl)imide (NTf_2), trifluoromethylsulfonate (OTf), and metyhlsulfonate (OMs) anions. (b) 1-(2-Hydroxyethyl)pyridinium (HEPy) and 1-propylpyridinium (PPy), 1-(2-hydroxypropyl)pyridinium (HPPy) and 1-butylpyridinium (BPy) cations with the same bis(trifluoromethylsulfonyl)-imide (NTf_2) anion. This interaction energy can be referred to H-bonding as present in the liquid phase of the hydroxyl-functionalized ILs.

respectively, and almost zero within the experimental error (±1.5 kJ mol^{-1}) (Fig. 2). Instead, we expected somewhat lower enthalpies of vaporization for ILs-OH for the case that the hydrogen bond is also present in the gas phase species. This could be shown earlier for ionic liquids including alkyl ammonium cations. The differences in vaporization enthalpies of tetraalkyl and trialkyl ammonium-based ILs were positive and could be clearly related to hydrogen bonding, which is transferred into the gas phase through ion pairs.[13–19]

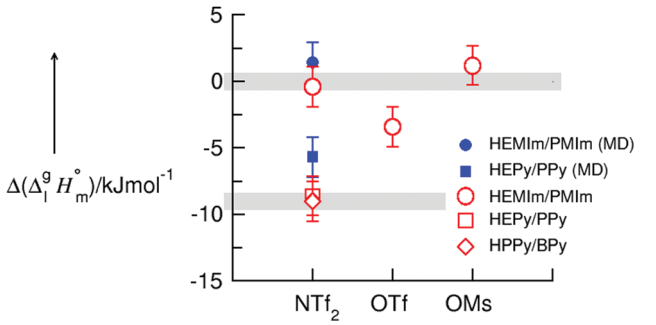

Fig. 2 $\Delta(\Delta_l^g H_m^0)$ differences of vaporization enthalpies measured for IL-CH_3 and IL-OH types of ionic liquids. The differences for ILs including 1-methyl-3-propylimidazolium (PMIm) and 1-(2-hydroxyethyl)-3-methyl-imidazolium (HEMIm) cations are almost zero, regardless the increasing interaction strength of the counter anions bis(trifluoromethylsulfonyl)imide (NTf_2), trifluoromethylsulfonate (OTf), and metyhlsulfonate (OMs). If the C(2)H interaction site is removed by using 1-(2-hydroxyethyl)pyridinium (HEPy) and 1-propylpyridinium (PPy), 1-(2-hydroxypropyl)pyridinium (HPPy) and 1-butylpyridinium (BPy) cations with the same bis(trifluoromethyl-sulfonyl)imide (NTf_2) anion, $\Delta(\Delta_l^g H_m^0)$ is −9 kJ mol^{-1}. The $\Delta(\Delta_l^g H_m^0)$ values from MD simulations (blue filled symbols) are in good agreement with the differences obtained for the measured vaporization enthalpies (red open symbols).

In the second set of ILs, we considered 1-(2-hydroxyethyl)-pyridinium (HEPy), 1-propylpyridinium (PPy), 1-(2-hydroxypropyl)pyridinium (HPPy) and 1-butylpyridinium (BPy) cations with always the same counter anion, bis(trifluoromethylsulfonyl)-imide (NTf_2). In the hydroxyl-functionalized pyridinium cations we eliminate the acidic C(2)H position and only the OH group is available for hydrogen bonding (see Scheme 1). We measured vaporization enthalpies of 134.5 kJ mol^{-1}, and 138.1 kJ mol^{-1} for ILs-CH_3, and 143.1 kJ mol^{-1} and 147.1 kJ mol^{-1} for ILs-OH, respectively (see Fig. 1b). The lengthening of alkyl chain from ethyl to propyl results in larger vaporization enthalpies of about 3.6 and 4.0 kJ mol^{-1}, simply explained by dispersion interaction for the additional methylene group.[9–12,20–30] In this case, the differences in vaporization enthalpies for ILs-CH_3 and ILs-OH are surprisingly negative, −8.6 kJ mol^{-1} and −9.0 kJ mol^{-1}, respectively (see Fig. 2). In other studies we could show that, if the H-bond is transferred into the gas phase, the vaporization energies of ILs-OH are significantly smaller, and $\Delta(\Delta_l^g H_m^0)$ becomes strongly positive. That is in stark contrast to what we observe here for the hydroxyl-functionalized ILs.

Obviously, both type of ILs evaporate as ion pairs and transfer the cation–anion interaction energy into the gas phase. That the differences between the vaporization enthalpies for the ILs-CH_3 and ILs-OH, are zero for the first set of ILs and even negative for the second set, may be explained with two possible scenarios: Firstly, the OH hydrogen bonding is almost negligible and does not play a role, neither in the liquid nor in the gas phase. This possibility can be ruled out by infrared (IR) measurements, which clearly show that the cation–anion hydrogen bonds between the hydroxyl groups and the anion are present throughout in the liquid phase for all hydroxyl-functionalized ILs. Thus, a second scenario seems to be more reasonable. Hydrogen between the acidic C(2)H group of the imidazolium ring and the corresponding anions plays the dominant role. This interaction is present in both types of ILs and in both phases, respectively, whereas the hydrogen bond between the OH group and the anion is almost negligible. That the acidic C(2)H group on the imidazolium ring rather than the OH group favorably interacts with the NTf_2^- anion has been shown recently by mass-selective, cryogenic ion trapping techniques accompanied by isomer-selective, two-color IR–IR double resonance spectroscopy.[31,32] In their study, Menges *et al.* characterized the structures of the ternary complexes $(HEMIm^+)_2NTf_2$ with two cations and one anion from the ionic liquid [HEMIm][NTf_2]. Although expected, they could not observe complexes wherein the OH groups of both cations form Coulomb enhanced hydrogen bonds to the oxygens of the sulfonyl groups of the NTf_2^- anion. Instead, they could isolate a complex wherein only one of the two cations interacts *via* the OH groups, while the other cation forms a hydrogen bond *via* the acidic C(2)H group leaving a free hydroxyl group as indicated by a high frequency band. Although observed for charged gas phase complexes, these studies provide strong evidence that the C(2)H···OS is stronger than the OH···OS hydrogen bond. This H-bond can be transferred into the gas phase for both species, IL-OH and IL-CH_3, finally resulting in similar vaporization enthalpies. To test both scenarios, we measured IR spectra in the bulk liquid phase and performed MD simulations for analyzing the subtle interaction energies of the ion-pair species present in the liquid and in the gas phase as well.

Hydrogen bonding of OH-functionalized ILs in the liquid state shown by IR spectrocopy

For both sets of ILs we measured the infrared (IR) spectra in the OH-stretch region at 353 K. In principle the OH functional groups in the [HEMIm], [HEPy] and [HPPy] cations can form both, hydrogen bonds with the anions, but also hydrogen bonds with hydroxyl groups of other cations resulting in H-bonded cationic clusters as known for molecular liquids.[31–44] However the latter are mainly kinetically stabilized at low temperatures and disappear at higher temperatures as chosen here. In Fig. 3 we show the IR spectra of the ILs [HEMIm][NTf_2], [HEPy][NTf_2] and [HPPy][NTf_2]. We clearly observe single OH vibrational bands for all ILs around 3550 cm^{-1} with similar intensity indicating that all OH groups are involved in hydrogen bonding with the same NTf_2 anion. From recent work we know, that the broad but small vibrational band at 3400 cm^{-1} indicates hydrogen bonding between cations wherein the OH-functionalized groups act as donors and acceptors, respectively. Considering the larger transition dipole moments of the OH stretch frequencies for the stronger c–c H-bonded species, we conclude that the c–a H-bonds absolutely dominate and that the c–c H-bonds are almost negligible. In any case, all OH groups are involved in hydrogen bonding.

In Fig. 4 we show the IR spectra of the ILs [HEMIm][NTf_2], [HEMIm][OTf], and [HEMIm][OMs]. Again, we observe single, symmetric OH vibrational bands, which are now strongly shifted

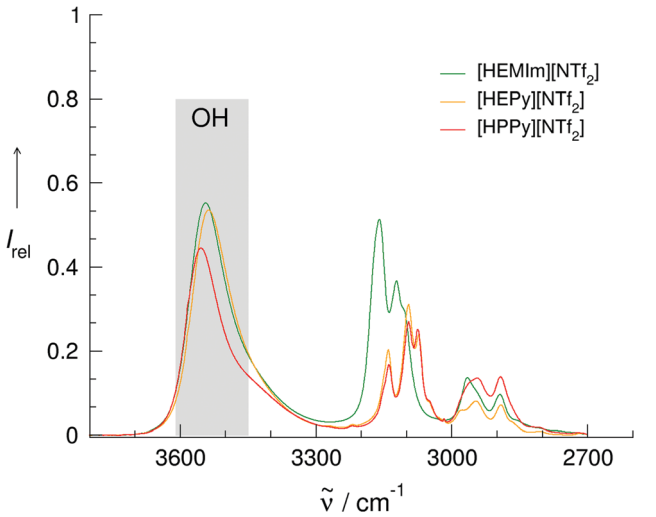

Fig. 3 Infrared spectra in the OH stretching region recorded for the ionic liquids [HEPy][NTf_2] and [HPPy][NTf_2] along with the earlier shown spectrum of [HEMIm][NTf_2] at 353 K. The IR spectra provide clear evidence, that the OH group of the hydroxyl-functionalized ILs forms hydrogen bonds to the NTf_2^- anion.

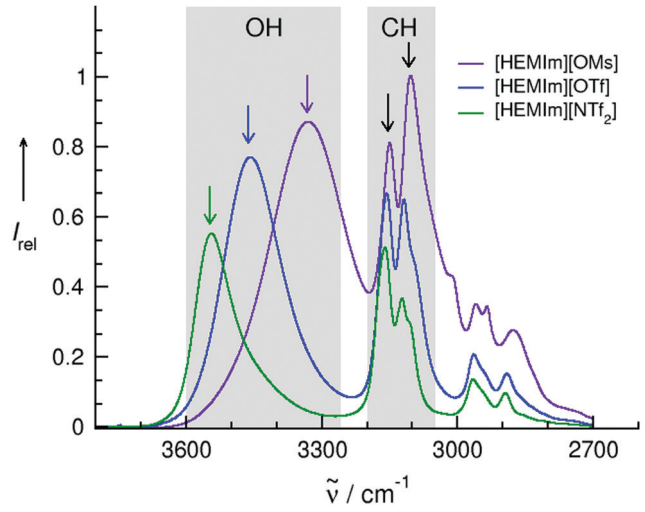

Fig. 4 Infrared spectra in the OH stretching region recorded for the ionic liquids [HEMIm][NTf_2], [HEMIm][OTf], and [HEMIm][OMs] at 353 K. We observe a red shift and an increase in intensity of OH stretch vibrational bands with increasing interaction strength of the anions I–III. The spectra show similar behavior for the C(2)H stretching bands. Both vibrational signatures indicate that the OH as well as the C(2)H bonds of the cation are involved in hydrogen bonding with the anion in the liquid phase.

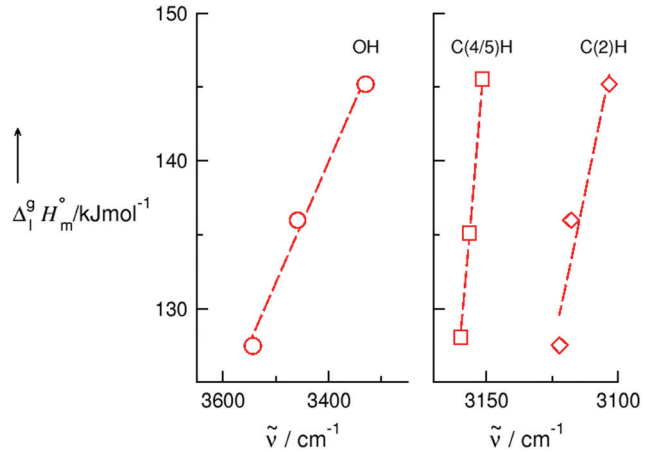

Fig. 5 $\Delta_l^g H^0_m$ vaporization enthalpies plotted *versus* OH, C(4/5)H and C(2)H stretching frequencies as recorded for the ionic liquids [HEMIm][NTf_2], [HEMIm][OTf], and [HEMIm][OMs] at 353 K. We observe a red shift of all vibrational bands with increasing interaction strengths of the anions indicating hydrogen bonding between cation and anion in the liquid phase.

to the red, and gaining substantial intensity with increasing interaction strength of the anion in the order NTf_2^-, OTf^- and OMs^-. In Fig. 5 it is shown that the measured frequencies for all H-bond sensitive bonds OH, C(2)H and C(4/5)H reflect the interaction strength of the anions indicating again that all the hydroxyl groups are involved in hydrogen bonding in the liquids phase of the ILs.[37–39] So far, enthalpies of vaporization and IR spectra of the hydroxyl-functionalized ILs suggest that hydrogen bonding is present in both phases, the liquid as well as in the gas phase.

Competing hydrogen bonding and dispersion forces analyzed by MD simulations

To elucidate the mechanism underlying the observed thermal effects we have performed molecular dynamics (MD) simulations of four ionic liquids: [HEMIm][NTf_2], [PMIm][NTf_2], [HEPy][NTf_2], and [PPy][NTf_2].[26,38,39] For each IL we have studied both, the liquid and the gas phase using MD at a temperature of 300 K. Each liquid phase was represented by a system of 512 ion pairs applying periodic boundary conditions, whereas the gas phase was represented by one single ion pair. Details about the simulation setup and employed forcefield models have been included in the ESI.†

To validate whether the simulations are capable of reproducing the experimentally observed scenario as outlined in Fig. 1, we have computed the difference between the molar vaporization enthalpies between the hydroxylated and non-hydydroxylated species according to $\Delta\left(\Delta_l^g H^\circ_m\right) = \Delta_l^g H^\circ_m([PX][NTf_2]) - \Delta_l^g H^\circ_m([HEX][NTf_2])$. Since the the P·V-contributions to the heat of vaporization for both ILs cancel each other out, their value is solely determined by the difference of the potential energy differences between their liquid and gas phases $\Delta\left(\Delta_l^g H^\circ_m\right) = \Delta\Delta\langle E_{pot}\rangle$ as listed in Tables 1 and 2. The computed value for X = Mim is $\Delta\left(\Delta_l^g H^\circ_m\right) = +1.4$ kJ mol^{-1}, and for X = Py is $\Delta\left(\Delta_l^g H^\circ_m\right) = -5.6$ kJ mol^{-1}, as shown in Fig. 2. For both cases, the simulation data are semiquantitatively mimicking the experimentally observed behavior.

Having shown that the MD data emulate the experimental data, we can use the simulations to dissect the different contributions to the corresponding energetical changes. First, we would like to address the question whether the observed effects are predominantly caused by changes between inter- or intramolecular interactions. Fig. 6 shows the intramolecular energy distribution for all four studied ILs for both, the gas and

Table 1 Potential energies E_{pot}, intramolecular interaction energies of the cation $E_{intra,cat}$, intramolecular interaction energies of the anion $E_{intra,an}$, and intermolecular interaction energies per ion pair E_{inter} for [HEMIm][NTf_2] and [PMIm][NTf_2] in the gaseous and liquid phase

	[HEMIm][NTf_2]	[PMIm][NTf_2]
	$\langle E\rangle$/kJ mol^{-1}	
Gas phase		
$\langle E_{pot}\rangle$	169.8	203.4
$\langle E_{intra,cat}\rangle$	192.8	201.1
$\langle E_{intra,an}\rangle$	323.5	323.0
$\langle E_{inter}\rangle$	−346.5	−320.7
Liquid phase		
$\langle E_{pot}\rangle$	46.8	79.0
$\langle E_{intra,cat}\rangle$	190.6	199.1
$\langle E_{intra,an}\rangle$	318.5	318.1
$\langle E_{inter}\rangle$	−462.3	−438.2
$\Delta\langle E_{pot}\rangle$	123.0	124.4
$\Delta\langle E_{intra,cat}\rangle$	2.2	2.0
$\Delta\langle E_{intra,an}\rangle$	5.0	4.9
$\Delta\langle E_{inter}\rangle$	115.8	117.5

Table 2 Potential energies E_{pot}, intramolecular interaction energies of the cation $E_{intra,cat}$, intramolecular interaction energies of the anion $E_{intra,an}$ and intermolecular interaction energies per ion pair E_{inter} for [HEPy][NTf_2] and [PPy][NTf_2] in the gaseous and liquid phase

	[HEPy][NTf_2]	[PPy][NTf_2]
	$\langle E\rangle$/kJ mol^{-1}	
Gas phase		
$\langle E_{pot}\rangle$	157.7	218.2
$\langle E_{intra,cat}\rangle$	159.7	193.9
$\langle E_{intra,an}\rangle$	323.9	323.6
$\langle E_{inter}\rangle$	−325.9	−299.3
Liquid phase		
$\langle E_{pot}\rangle$	13.0	79.1
$\langle E_{intra,cat}\rangle$	158.3	191.4
$\langle E_{intra,an}\rangle$	318.5	318.3
$\langle E_{inter}\rangle$	−463.8	−430.6
$\Delta\langle E_{pot}\rangle$	144.7	139.1
$\Delta\langle E_{intra,cat}\rangle$	1.4	2.5
$\Delta\langle E_{intra,an}\rangle$	5.4	5.3
$\Delta\langle E_{inter}\rangle$	137.9	131.3

the liquid phases: In all cases we find that the ions adopt energetically less favorable configurations in the gas phase. This behavior is not unexpected since the environment found in the gas phase is highly anisotropic. The ions are thus preferring conformations allowing for a better matching of intermolecular interactions. For the case of the NTf_2^- anion in the gas phase it is observed that the anion predominantly adopts a *gauche*-like conformation (as discussed in ref. 28) to allow close contact interactions of all of the four negatively polarized oxygen-sites with the positively charged cation–core. However, this is resulting in an intramolecular energy penalty of about 5 kJ mol^{-1} to 5.5 kJ mol^{-1} (see Tables 1 and 2) irrespective of the actual corresponding counter ion. Similarly, the cations also adopt energetically less favorable conformations in the gas phase, resulting in an overall energy penalty between 1.4 kJ mol^{-1} to 2.5 kJ mol^{-1}. When comparing the differences between hydroxylated and non-hydroxylated species, however, these intramolecular energy changes roughly cancel each other out (see Tables 1 and 2) and, hence, do not seem to be the root of the observed thermal effects. Instead, as shown in Tables 1 and 2, the dominant effect has to be attributed to the differences between their intermolecular interactions.

To further investigate the mechanism leading to respective changes in their intermolecular interaction, we first discuss the distribution of intermolecular energies between ion pairs in the gas phase as shown in Fig. 7. Here, the main difference of the distribution between hydroxylated and non-hydroxylated species is that the hydroxylated cations exhibit an overall stronger interaction with the anion due to their ability to form a hydrogen bond. However, the energy distribution of the two shown hydroxylated species are also significantly broader, thus suggesting the presence of a larger variety of possible modes of interaction. The formation of hydrogen bonds in the gas phase can also be deduced geometrically from the distribution of intermolecular H···O distances of closest approach between the cationic hydroxyl hydrogen atoms and [NTf_2]–oxygen in anion/cation ion-pairs shown in Fig. 8. We choose this representation instead of pair distribution functions since the normalization density is not available for the gas phase. The peak centered around 2 Å indicates the presence of hydrogen bonds in both, liquid and gas phase. However, the lowered peak for the gas phase indicates slightly weaker hydrogen bonds. Nevertheless, still in about between 80% and 90% of the configurations an inter-ionic hydrogen bond is present in the gas phase. As a result, the apparent necessity to form a

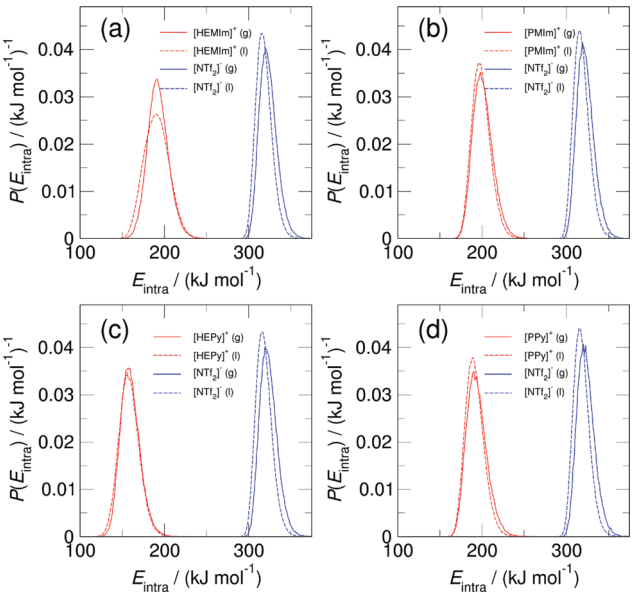

Fig. 6 Distribution of intramolecular energies per ion E_{pair} computed separately for anions and cations at a temperature of 300 K for (a) [HEMIm][NTf_2], (b) [PMIm][NTf_2], (c) [HEPy][NTf_2] and (d) [PPy][NTf_2]. Dashed lines indicate data obtained from liquid phase simulations, whereas the solid lines represent data computed from simulations an ion pair in the gas phase.

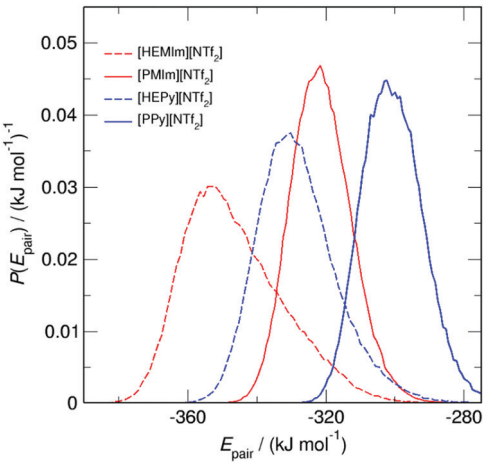

Fig. 7 Distribution of intermolecular pair interaction energies E_{inter} computed for all four indicated ion pairs in the gas phase at a temperature of 300 K.

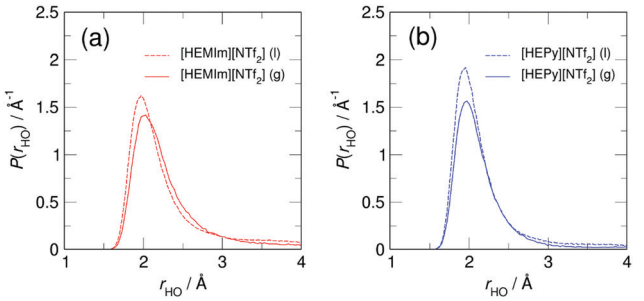

Fig. 8 Distribution of intermolecular H···O distances of closest approach between the cationic hydroxyl hydrogen atoms and [NTf_2]–oxygen in anion/cation ion pairs in both, the gas and liquid phase for (a) [HEMIm][NTf_2], and (b) [HEPy][NTf_2].

hydrogen bond in the gas phase somewhat constraints the interaction between the charge centers, which is illustrated in Fig. 9. The matching of the anion-cation "chargecenter" interaction has been monitored in two exemplary ways: (1) The distances of closest approach between the nitrogen sites in the imidazolium and pyridinium ring systems and the [NTf_2]–oxygen, shown in Fig. 9a, and (2) the smallest angle φ between the normal vectors of the imidazolium- or pyridinium-ring and a plane formed by three oxygen-atoms of the [NTf_2]–anion. In both cases the presence of an interionic hydrogen bond seems to perturb the matching of the charge centers, leading to larger N···O distances for the hydroxylated species, as shown in Fig. 9a and a larger tilt angle between the plane formed by the oxygen sites and the ring, as shown in Fig. 9b. As a consequence, the matching of the charge centers is more strongly perturbed in the presence of an hydroxylated cation, as it is outlined from a pair of selected snapshots shown in Fig. 10. Fig. 9 also points to an explanation as to why the thermal effect is more strongly pronounced in case of the pyridium–cations: apparently, in the case of the pyridium-cations the presence of a hydrogen bonds leads to a somewhat larger perturbation compared to the Imidazolium system. Finally, we are able to explain the vaporization enthalpies at molecular level by means of IR spectroscopy and MD simulations.

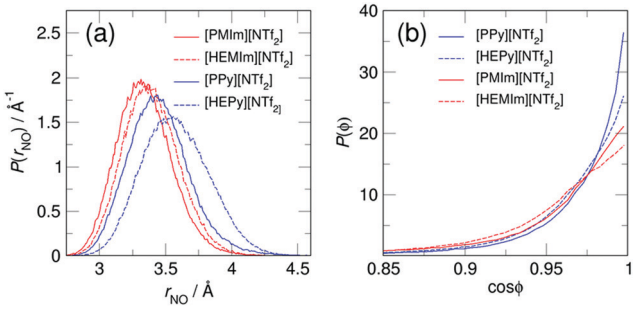

Fig. 9 Local matching of anion–cation interaction *via* the "charge center" of the cations with the negatively charged oxygen atoms on the anions: (a) distances of closest approach between the nitrogen sites in the imidazolium and pyridinium ring systems and the [NTf_2]–oxygen. (b) Smallest angle φ between the normal vectors of the Imidazolium or Pyridinium-ring and a plane formed by three oxygen-atoms of the NTf_2^- anion.

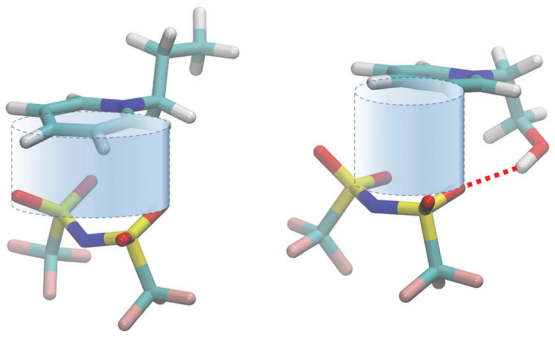

Fig. 10 Gas phase ion-pairs of [PPy][NTf_2] (left) and [HEPy][NTf_2] (right) from snapshots of MD simulations. The existing hydrogen bond in the [HEPy][NTf_2] ion pair (red dotted line) hinders favorable interaction between the pyridinium ring and the oxygens of the NTf_2^- anion, which is perfectly possible in the [PPy][NTf_2] ion pairs (see distances and contact areas).

Conclusion

In this work, we showed that the mélange of different types of interactions between cations and anions in the gaseous and the liquid phases of ILs can be fully understood by means of calorimetry, IR spectroscopy and MD simulations. In particular, we focused on the specific role of hydrogen bonding for hydroxyl-functionalized ILs-OH. Usually, the differences of vaporization enthalpies for ILs-CH_3 and ILs-NH are strongly positive because the hydrogen bond NH···O bond is transferred into the gas phase, thus significantly reducing the vaporization energies for ILs-NH. However, for ILs including hydroxyalkyl imidazolium and hydroxyalkyl pyridinium cations, we obtained zero or negative $\Delta(\Delta H_{vap})$ values which is not in agreement with this simple assumption. IR spectra of the hydroxyl-functionalized ILs suggested that all OH groups are involved in hydrogen bonding. The measured vaporization enthalpies than provided evidence that all ionic liquids evaporate as ion pairs. MD simulations showed that the OH···O hydrogen bonds are also present in the gas phase ion-pairs. A detailed analysis of the mean potential energies for cations, anions and ion pairs in the liquid and the gaseous phases showed that the H-bond in the gaseous phase hinders favorable interaction between the polarizable ring system and the anion. As a result the enthalpies of vaporization of the non-functionalized ILs are similar or even lower than those of the similar hydroxyl-functionalized ILs.

Conflicts of interest

There are no conflicts to declare.

Acknowledgements

This work has been supported by the DFG Priority Programme SPP 1807 "Control of London dispersion interaction in molecular chemistry". R. L. and S. P. V. acknowledge support by the research grants LU-506/12-2 and VE-265/9-2, respectively.

References

1 H. Weingärtner, *Angew. Chem.*, 2010, **120**, 664–682 (*Angew. Chem., Int. Ed.*, 2010, **47**, 654–670).
2 R. Hayes, G. Warr and R. Atkin, *Chem. Rev.*, 2015, **115**, 6357–6426.
3 K. Fumino and R. Ludwig, *J. Mol. Liq.*, 2014, **192**, 94–102.
4 K. Fumino, S. Reimann and R. Ludwig, *Phys. Chem. Chem. Phys.*, 2014, **40**, 21903–21929.
5 N. V. Plechkova and K. R. Seddon, *Chem. Soc. Rev.*, 2008, **37**, 123–150.
6 P. Wasserscheid and T. Welton, *Ionic Liquids in Synthesis*, 2nd edn, Wiley-VCH, Weinheim, 2008.
7 R. D. Rogers and K. R. Seddon, *Science*, 2003, **302**, 792–793.
8 F. Endres and S. Z. E. Abedin, *Phys. Chem. Chem. Phys.*, 2006, **8**, 2101.
9 J. S. Chickos and W. E. Acree, Jr., *J. Phys. Chem. Ref. Data*, 2003, **32**, 1–361.
10 D. Matulis, *Biophys. Chem.*, 2001, **93**, 67–82.
11 D. Kulikov, S. P. Verevkin and A. Heintz, *Fluid Phase Equilib.*, 2001, **192**, 187–207.
12 J. B. Pedley, *Thermochemical Data and Structures of Organic Compounds*, TRC Data Series, Texas, 1994, vol. 1.
13 J. M. S. S. Esperança, J. N. Canongia Lopes, M. Tariq, L. M. N. B. F. Santos, J. W. Magee and L. P. N. Rebelo, *J. Chem. Eng. Data*, 2010, **55**, 3–12.
14 J. Vitorino, C. E. S. Bernardes and M. E. Minas da Piedade, *Phys. Chem. Chem. Phys.*, 2012, **14**, 4440–4446.
15 V. N. Emel'yanenko, G. Boeck, S. P. Verevkin and R. Ludwig, *Chem. – Eur. J.*, 2014, **20**, 11640–11645.
16 K. Fumino, A. Wulf, S. P. Verevkin, A. Heintz and R. Ludwig, *ChemPhysChem*, 2010, **11**, 1623–1626.
17 D. H. Zaitsau, V. N. Emel'yanenko, P. Stange, C. Schick, S. P. Verevkin and R. Ludwig, *Angew. Chem., Int. Ed.*, 2016, **55**, 11682–11686 (*Angew. Chem.*, 2016, **128**, 11856–11860).
18 S. P. Verevkin, *Angew. Chem.*, 2008, **120**, 5149–5152 (*Angew. Chem., Int. Ed.*, 2008, **47**, 5071–5074).
19 S. P. Verevkin, D. H. Zaitsau, V. N. Emel'yanenko, A. V. Yermalayeu, C. Schick, H. Liu, E. J. Maginn, S. Bulut, I. Krossing and R. Kalb, *J. Phys. Chem. B*, 2013, **117**, 6473–6486.
20 K. Fumino, A. Wulf and R. Ludwig, *Phys. Chem. Chem. Phys.*, 2009, **11**, 8790–8794.
21 K. Fumino, E. Reichert, K. Wittler, R. Hempelmann and R. Ludwig, *Angew. Chem., Int. Ed.*, 2012, **51**, 6236–6240 (*Angew. Chem.*, 2012, **124**, 6340–6344).
22 E. I. Izgorodina, Z. L. Seeger, D. L. A. Scarborough and S. Y. S. Tan, *Chem. Rev.*, 2017, **117**, 6696–6754.
23 R. Ludwig, *Phys. Chem. Chem. Phys.*, 2008, **10**, 4333–4339.
24 J. Ingenmey, M. von Domaros, E. Perlt, S. P. Verevkin and B. Kirchner, *J. Chem. Phys.*, 2018, **148**, 193822.
25 S. Zahn, M. Brehm, M. Brüssel, O. Hollóczki, M. Kohagen, S. Lehmann, F. Malberg, A. S. Pensado, M. Schöppke, H. Weber and B. Kirchner, *J. Mol. Liq.*, 2014, **192**, 71–76.
26 T. Köddermann, D. Paschek and R. Ludwig, *ChemPhysChem*, 2007, **8**, 2464–2470.
27 T. Köddermann, D. Paschek and R. Ludwig, *ChemPhysChem*, 2008, **9**, 549–555.
28 J. Neumann, B. Golub, L.-M. Odebrecht, R. Ludwig and D. Paschek, *J. Chem. Phys.*, 2018, **148**, 193828.
29 F. Dommert, K. Wendler, B. Qiao, L. Delle Site and C. Holm, *J. Mol. Liq.*, 2014, **192**, 32–37.
30 C. Schröder, *Phys. Chem. Chem. Phys.*, 2012, **14**, 3089–3102.
31 F. S. Menges, H. J. Zeng, P. J. Kelleher, O. Gorlova, M. A. Johnson, T. Niemann, A. Strate and R. Ludwig, *J. Phys. Chem. Lett.*, 2018, **9**, 2979–2984.
32 T. Niemann, A. Strate, R. Ludwig, F. Menges, H. Zeng, P. Kelleher, O. Gorlova and M. Johnson, *Angew. Chem., Int. Ed.*, 2018, **57**, 15364–15369 (*Angew. Chem.*, **130**, 15590–15594).
33 S. A. Katsyuba, M. V. Vener, E. E. Zvereva, Z. F. Fei, R. Scopelliti, G. Laurenczy, N. Yan, E. Paunescu and P. J. Dyson, *J. Phys. Chem. B*, 2013, **117**, 9094–9105.
34 M. Fakhraee, B. Zandkarimi, H. Salari and M. R. Gholami, *J. Phys. Chem. B*, 2014, **118**, 14410–14428.
35 S. K. Panja, B. Haddad and J. Kiefer, *ChemPhysChem*, 2018, **19**, 3061–3068.
36 A. Knorr, K. Fumino, A.-M. Bonsa and R. Ludwig, *Phys. Chem. Chem. Phys.*, 2015, **17**, 30978–30982.
37 A. Knorr and R. Ludwig, *Sci. Rep.*, 2015, **5**, 17505.
38 A. Knorr, P. Stange, K. Fumino, F. Weinhold and R. Ludwig, *ChemPhysChem*, 2016, **17**, 458–462.
39 A. Strate, T. Niemann, P. Stange, D. Michalik and R. Ludwig, *Angew. Chem., Int. Ed.*, 2017, **56**, 496–500 (*Angew. Chem.*, 2017, **129**, 510–514).
40 T. Niemann, D. Zaitsau, A. Strate, A. Villinger and R. Ludwig, *Sci. Rep.*, 2018, **8**, 14753.
41 R. Ludwig, *Chem. Phys. Chem.*, 2000, **1**, 53–56.
42 R. Ludwig, *Phys. Chem. Chem. Phys.*, 2002, **4**, 5481–5487.
43 W. L. Jorgensen, D. S. Maxwell and J. Tirado-Rives, *J. Am. Chem. Soc.*, 1996, **118**, 11225–11236.
44 W. L. Jorgensen and N. A. McDonald, *J. Mol. Struct.: THEOCHEM*, 1998, **424**, 145–155.

Electronic Supplementary Material (ESI) for Physical Chemistry Chemical Physics.

Isolating the role of hydrogen bonding in hydroxyl-functionalized ionic liquids by means of vaporization enthalpies, infrared spectroscopy and molecular dynamics simulations

Dzmitry H. Zaitsau,[a,b] Jan Neumann, Thomas Niemann,[a] Anne Strate,[a,b] Dietmar Paschek,[a,b*] Sergey P. Verevkin,[a,b*] and Ralf Ludwig,[a,b,c*]

[a] Universität Rostock, Institut für Chemie, Abteilung für Physikalische Chemie, Dr.-Lorenz-Weg 2, 18059, Rostock, Germany

[b] Department LL&M, University of Rostock, Albert-Einstein-Str. 25, 18059, Rostock, Germany

[c] Leibniz-Institut für Katalyse an der Universität Rostock e.V., Albert-Einstein-Str. 29a, 18059 Rostock, Germany

Contents

1. Materials and Synthesis

Sample preparation

Synthesis of the onium salts: Equimolar amounts of the heterocyclic amine and 2-bromoethanol, 3-chloropropanol or 1-bromopropane respectively were mixed and heated up to 110 °C for 1h. Upon cooling, the mixture began to crystallize. The crude product was recrystallized from acetone/acetonitrile mixtures to obtain the colorless crystalline product.
Synthesis of the bis(trifluoromethanesulfonyl)imide: Equimolar amounts of the onium halide and lithium-bis(trifluoromethanesulfonyl)imide were mixed as aqueous solutions for 1h. Two phases were obtained, the lower one was washed several times with water until no residual bromine could be detected with silver nitrate solution. The obtained colorless liquids were dried for several hours in vacuum at 60 °C.
All 3-methylimidazolium based ILs were purchased from IoLiTec and dried for several hours in vacuum at 60 °C.

Synthesis of the specific compounds

Apart from the reactions in aqueous solutions all reactions were performed in a moisture-guarded assembly and reflux condenser was used while heating. The used solvents were dried with molecular sieves to a water content less than 50 ppm and distilled freshly. All starting materials used in the synthesis were purchased from Sigma Aldrich and dried by conventional methods for the use in moisture-free reactions.

1-(2-Hydroxyethyl)pyridinium-bromide [HEPy][Br]

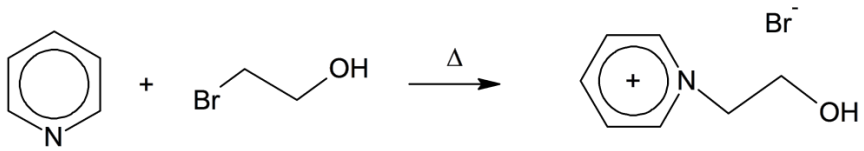

At room temperature equimolar amounts of pyridine (8.977 g; 113 mmol; 9.6 ml) and 2-bromoethanol (14.929 g; 113 mmol; 14.9 ml) were mixed and heated slowly up to 110 °C. When the reaction begins, the solution turns brown and starts to crystallize. The mixture was cooled to room temperature. The crude product was recrystallized from about 330 ml acetonitrile. The product (**[HEPy][Br]**) was obtained as rod-shaped colorless crystals. Yield 89 %.
EA % cal. (exp.): C 41.20 (41.22); H 4.94 (4.92); N 6.86 (6.76). ^{1}**H-NMR**(298.2 K, DMSO-d6, 300.13 MHz, [ppm]): δ = 3.86 (dd, 2H, CH_2-CH_2-OH); 4.67-4.74 (m, 2H, CH_2-CH_2-OH); 5.25(t, 1H, O*H*); 8.14-8.21 (m, 2H, *m*-C*H*); 8.60-8.67 (m, 1H, *p*-C*H*); 9.03-9.09 (m, 2H, *o*-C*H*).
^{13}**C-NMR**(298 K, DMSO-d6, 75.46 MHz, [ppm]): δ = 59.98 (s, CH_2-CH_2-OH); 63.04 (s, CH_2-CH_2-OH); 127.67 (s, *m*-*C*H); 145.15 (s, *p*-*C*H); 145.53 (s, *o*-*C*H).

1-(2-Hydroxyethyl)pyridinium-bis(trifluoromethanesulfonyl)imide [HEPy][NTf_2]

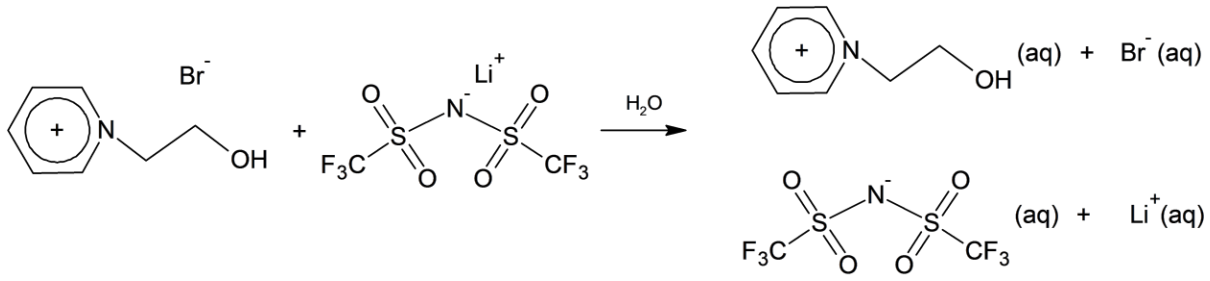

3.220 g (**[HEPy][Br]**) (16 mmol) solved in 2 ml H_2O were added to a solution of 4.576 g lithium- bis(trifluoromethylsulfonyl)imide $LiNTf_2$ (16 mmol) in 2.5 ml H_2O. The mixture was stirred for 1 h. Two phases were obtained, the lower one was washed several times with water until no residual bromine could be detected with silver nitrate solution. The obtained colorless liquid of (**[HEPy][NTf_2]**) was dried for 8 h in vacuum at 60 °C. Yield 57 %.

EA % cal. (exp.): C 26.73 (26.14); H 2.49 (2.41); N 6.93 (6.54); S 15.86 (15.50). ^{1}**HNMR**(298.2 K, DMSO-d_6, 300.13 MHz, [ppm]): δ = 3.88 (dd, 2H, CH_2-CH_2-OH); 4.65- 4.71 (m, 2H, CH_2-CH_2-OH); 5.22(t, 1H, O*H*); 8.12-8.20 (m, 2H, *m*-C*H*); 8.57-8.64 (m, 1H, *p*-C*H*); 9.00-9.05 (m, 2H, *o*-C*H*). ^{13}**C-NMR**(298 K, DMSO-d_6, 75.46 MHz, [ppm]): δ = 59.95 (s, CH_2-CH_2-OH); 63.01 (s, CH_2-CH_2-OH); 119.43 (q, CF_3); 127.65 (s, *m*-CH); 145.12 (s, *p*-CH); 145.50 (s, *o*-CH). ^{19}**F-NMR**(298 K, DMSO-d_6, 282.40 MHz, [ppm]): δ = −78.81 (s, CF_3). **IR** (Transm., CaF_2-Window, 12 μm Spacer, 20 °C, 128 Scans, [cm^{-1}]): 3528 (vw); 3141 (vw); 3097 (vw); 3074 (vw); 2972 (vw); 2951 (vw); 2893 (vw); 2857 (vw); 1936 (vw); 1850 (vw); 1741 (vw); 1638 (w); 1585 (vw); 1502 (vw); 1491 (m); 1451 (vw); 1352 (vs); 1200 (s); 1136 (s); 1060 (s).

1-(3-Hydroxypropyl)pyridinium chloride [HPPy][Cl]

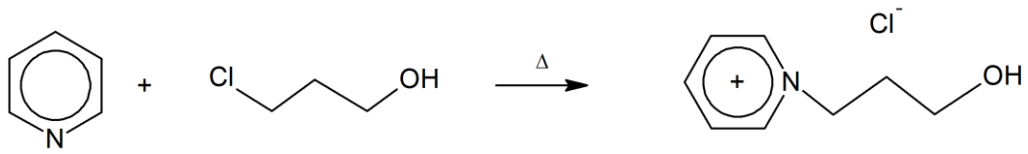

At room temperature equimolar amounts of pyridine (12.231 g; 155 mmol; 13.1 ml) and 3-chloropropanol (14.600 g; 154 mmol; 12.9 ml) were mixed and heated slowly up to 100 °C. When the reaction begins, the solution turns slightly brown and starts to crystallize upon cooling to room temperature . The crude product was recrystallized from about 450 ml acetonitrile. The product was obtained as rod-shaped colorless crystals. Yield 92 %.

^{1}**H-NMR**(298.2 K, DMSO-d_6, 300.13 MHz, [ppm]): δ = 2.03-2.13 (tt, 2H, $CH_2-CH_2-CH_2-OH$); 3.38-3.45 (dt, 2H, $CH_2-CH_2-CH_2-OH$); 4.76 (t, 2H, $CH_2-CH_2-CH_2-OH$); 5.12 (t, 1H, O*H*); 8.13-8.19 (m, 2H, *m*-C*H*); 8.58-8.65 (m, 1H, *p*-C*H*); 9.25-9.29 (m, 2H, *o*-C*H*). ^{13}**C-NMR** (298 K, DMSO-d_6, 75.46 MHz, [ppm]): δ = 33.46 (s, $CH_2-CH_2-CH_2-OH$); 56.88 (s, $CH_2-CH_2-CH_2-OH$); 58.42 (s, $CH_2-CH_2-CH_2-OH$); 127.87 (s, *m*-CH); 145.05 (s, *p*-CH); 145.38 (s, *o*-CH). **IR** (ATR, 30°C, 128 Scans, [cm^{-1}]): 3277 (m); 3128 (w); 3093 (w); 3071 (w); 3043 (w); 3019 (w); 2969 (w); 2939 (w); 2905 (w); 2868 (w); 2804 (w); 1636 (w); 1626 (m); 1579 (vw); 1505 (w); 1484 (s); 1470(m); 1421 (w); 1379 (vw); 1360 (w); 1304 (m); 1265 (w); 1233 (w); 1174 (m); 1150 (w); 1083 (m); 1050 (s); 957 (w); 934(m); 872(vw); 819 (w); 774 (s); 6855 (vs); 638 (s).

1-(3-Hydroxypropyl)pyridinium-bis(trifluoromethanesulfonyl)imide [HPPy][NTf$_2$]

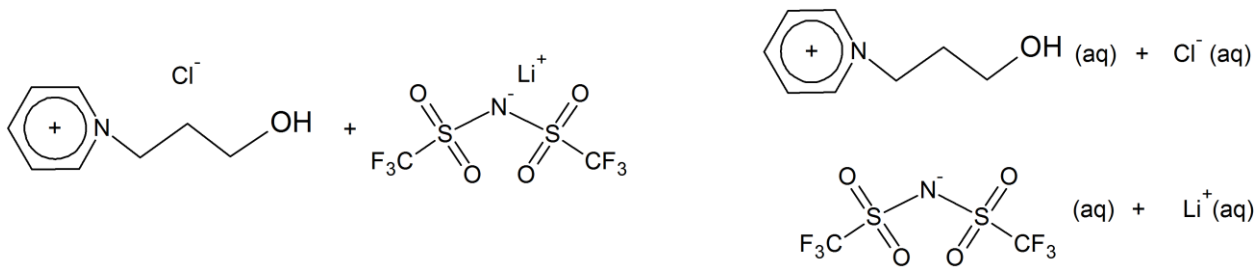

9.653 g (**[HPPy][Cl]**) (56 mmol) solved in 10 ml H_2O were added to a solution of 16.125 g lithium- bis(trifluoromethylsulfonyl)imide $LiNTf_2$ (56 mmol) in 10 ml H_2O. The mixture was stirred for 1 h. Two phases were obtained, the lower one was washed several times with water until no residual chlorine could be detected with silver nitrate solution. The obtained colorless liquid of (**[HPPy][NTf$_2$])** was dried for 8 h in vacuum at 60 °C. Yield 77 %.
^{1}**H-NMR**(298.2 K, DMSO-d$_6$, 300.13 MHz, [ppm]): δ = 2.03-2.13 (tt, 2H, $CH_2-CH_2-CH_2-OH$); 3.41-3.48 (dt, 2H, $CH_2-CH_2-CH_2-OH$); 4.71 (t, 2H, $CH_2-CH_2-CH_2-OH$); 4,88 (t, 1H, O*H*); 8.11-8.19 (m, 2H, *m*-C*H*); 8.56-8.64 (m, 1H, *p*-C*H*); 9.10-9.17 (m, 2H, *o*-C*H*). ^{13}**C-NMR**(298 K, DMSO-d$_6$, 75.46 MHz, [ppm]): δ = 33.27 (s, $CH_2-CH_2-CH_2-OH$); 57.04 (s, $CH_2-CH_2-CH_2-OH$); 58.59 (s, $CH_2-CH_2-CH_2-OH$); 119.43 (q, CF_3); 127.87 (s, *m*-C*H*); 144.99 (s, *p*-C*H*); 145.37 (s, *o*-C*H*). ^{19}**F-NMR**(298 K, DMSO-d$_6$, 282.40 MHz, [ppm]): δ = −78.81 (s, CF_3). **IR** (Transm., CaF_2-Window, 12 μm Spacer, 20 °C, 128 Scans, [cm^{-1}]): 3552 (w); 3299 (m); 3139 (w); 3097 (w); 3071 (w); 2943 (w); 2881 (w); 1637 (m); 1491 (m); 1318 (w); 1286 (w); 1221 (w); 1170 (w); 1060 (vs); 953 (w).

1-Propylpyridinium-bromide [PPy][Br]

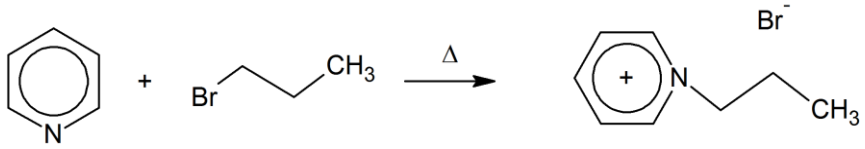

At room temperature equimolar amounts of pyridine (19.57 g; 247 mmol; 20 ml) and 1-bromopropane (30.378 g; 247 mmol; 22.5 ml) were mixed and heated slowly up to 100 °C. When the reaction begins, the solution turns brown and begins to crystallize while cooling to room temperature. The crude product was dispersed in 300 ml ethyl acetate and filtered. The product (**[PPy][Br]**) was obtained as white powder. Yield 91 %.
^{1}**H-NMR**(298.2 K, DMSO-d6, 300.13 MHz, [ppm]): δ = 0.90 (t, 2H, $CH_2-CH_2-CH_3$); 1.86-2.09 (m, 2H, $CH_2-CH_2-CH_3$); 4.61-4.72 (m, 2H, $CH_2-CH_2-CH_3$);
8.19-8.26 (m, 2H, *m*-C*H*); 8.66-8.72 (m, 1H, *p*-C*H*); 9.21-9.30 (m, 2H, *o*-C*H*).
^{13}**C-NMR**(298 K, DMSO-d6, 75.46 MHz, [ppm]): δ = 10.23 (s, $CH_2-CH_2-CH_3$); 23.98 (s, $CH_2-CH_2-CH_3$); 62.04 (s,$CH_2-CH_2-CH_3$); 127.67 (s, *m*-C*H*); 145.19 (s, *p*-C*H*); 145.55 (s, *o*-C*H*).

1-Propylpyridinium-bis(trifluoromethanesulfonyl)imide [PPy][NTf$_2$]

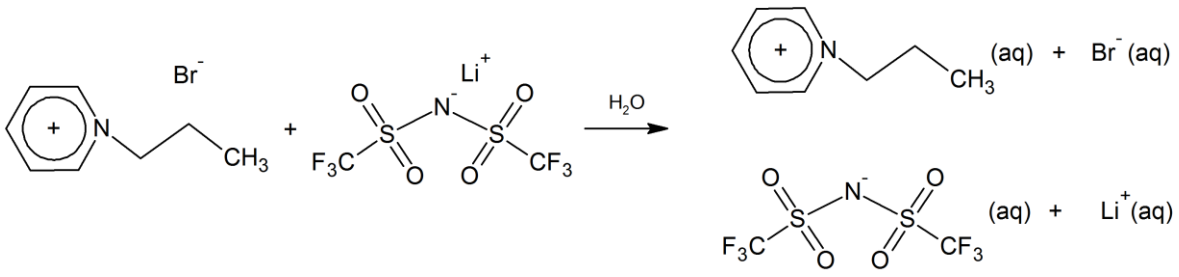

22.10 g (**[PPy][Br]**) (109 mmol) solved in 20 ml H_2O were added to a solution of 31.811g lithium- bis(trifluoromethylsulfonyl)imide $LiNTf_2$ (109 mmol) in 20 ml H_2O. The mixture was stirred for 1 h. Two phases were obtained, the lower one was washed several times with water until no residual bromine could be detected with silver nitrate solution. The obtained colorless liquid of (**[PPy][NTf_2])** was dried for 8 h in vacuum at 60 °C. Yield 83 %.

^{1}**H-NMR**(298.2 K, DMSO-d6, 300.13 MHz, [ppm]): δ = 0.92 (t, 2H, $CH_2-CH_2-CH_3$); 1.87-2.10 (m, 2H, $CH_2-CH_2-CH_3$); 4.61-4.72 (m, 2H, $CH_2-CH_2-CH_3$); 8.19-8.27 (m, 2H, *m*-C*H*); 8.66-8.73 (m, 1H, *p*-C*H*); 9.21-9.31 (m, 2H, *o*-C*H*).

^{13}**C-NMR**(298 K, DMSO-d6, 75.46 MHz, [ppm]): δ = 10.22 (s, $CH_2-CH_2-CH_3$); 24.01 (s, $CH_2-CH_2-CH_3$); 62.10 (s,$CH_2-CH_2-CH_3$); 119.44 (q, CF_3); 127.66 (s, *m*-CH); 145.19 (s, *p*-CH); 145.57 (s, *o*-CH). ^{19}**F-NMR**(298 K, DMSO-d_6, 282.40 MHz, [ppm]): δ = −78.85 (s, CF_3).

2. Vapor pressure and enthalpy of vaporization determiation by usin Quartz-Crystal-Microbalance Langmuir technique.

Vapor pressures and standard molar enthalpies of vaporization of stuied series of ILs were determined by using the QCM method.[1] Vaporization enthalpies were derived from the temperature dependencies of the experimentally measured shift in the vibrational frequency of the quartz crystal. In our method a sample of an IL is placed in an open cavity (Langmuir evaporation) inside of the thermostat block and it is exposed to vacuum (10^{-5} Pa) with the whole open surface of the loaded compound. The QCM is placed directly above the measuring cavity containing the sample. During the vaporization into a vacuum, a certain amount of sample is deposited on the quartz crystal. The change of the vibrational frequency Δf was directly related to the mass deposition Δm on the crystal according to the Sauerbrey equation:[2]

$$\Delta f = - C \cdot f^2 \cdot \Delta m \cdot S_C^{-1} \quad (1)$$

where f is the fundamental frequency of the crystal (6 MHz in this case) with $\Delta f << f$, S_C is the surface of the crystal, and C is a constant.[3] The measured frequency change rates ($df \cdot dt^{-1}$) can be used for calculation of absolute vapor pressures p_{sat} according to the equation:

$$p_{sat} = K' \frac{df}{dt} \sqrt{\frac{T}{M}}. \quad (2)$$

where the $K' = (9.5 \pm 1.1) \times 10^{-6}$ Pa·s·kg$^{1/2}$·Hz^{-1}·K$^{-1/2}$·mol$^{-1/2}$ is the empirical constant containing all parameters of the Sauerbrey equation as well as the parameters specific for the geometry of the experimental setup.[3] The K'-value for our apparatus was evaluated with the help of reliable vapor pressure data available for imidazolium and pyridinium based Ils.[3] Using the experimental vapor pressures p_{sat} measured with the QCM technique the molar enthalpy of vaporization, $\Delta_l^g H_m^o(T)$ at experimental temperatures is obtained according to the Clarke-Glew equation:[4]

$$R\ln(p_{sat}/p^o) = -\frac{\Delta_l^g G_m^\circ(T_{av})}{T_{av}} + \Delta_l^g H_m^\circ(T_{av})\left(\frac{1}{T_{av}} - \frac{1}{T}\right) + \Delta_l^g C_{p,m}^\circ\left(\frac{T_{av}}{T} - 1 + \ln\left(\frac{T}{T_{av}}\right)\right) \quad (3),$$

where T_{av} is the average temperature interval of the study. The value $\Delta_l^g C_{p,m}^o = C_{p,m}^o(g) - C_{p,m}^o(liq)$ is the difference between the molar heat capacities of the gaseous, $C_{p,m}^o(g)$, and the liquid phase, $C_{p,m}^o(liq)$, respectively. The vaporization enthalpy $\Delta_l^g H_m^o(298.15\ K)$ at the reference temperature is calculated according to the Kirchhoff´s equation:

$$\Delta_l^g H_m^o(298.15\ K) = \Delta_l^g H_m^o(T_{av}) + \Delta_l^g C_{p,m}^o\ (298.15 - T_{av}) \quad (4),$$

To detect and avoid any possible effect of impurities on the measured frequency loss rate ($df \cdot dt^{-1}$), a typical experiment was performed in a few consequent series with increasing and decreasing temperature steps. Every series consisted of 5 to 8 temperature points of mass loss rate determination. Several runs have been performed to test the reproducibility of the results. The study

was finished when the enthalpy of vaporization, $\Delta_l^g H_m^o(T_{av})$, obtained in the sequential runs by adjusting Eq. 3 to the temperature dependent rates ($df \cdot dt^{-1}$) agreed within the assessed experimental uncertainty of about ± 1 kJ·mol^{-1}. In order to confirm the absence of decomposition of IL under the experimental conditions, the residual IL in the crucible and the IL-deposit on QCM were analyzed by ATR-FTIR spectroscopy. No changes in the spectra have been detected. Primary experimental results of the QCM studies are given in Table S1. The final uncertainty of the absolute vapor pressure determination is estimated to be 50 % and mostly determined by the uncertainty of *K′* coefficient.

Table S1. The results of the temperature dependence of frequency shift velocity *df/dt* of the QCM for studied Ionic Liquids and, corresponding vaporization enthalpies $\Delta_l^g H^o_m(T)$.[a]

Run	T / K	df/dt / Hz·s^{-1}	$10^6 \cdot p_{sat}$ / Pa	T^{-1} / K^{-1}	$R\cdot\ln(p_{sat}/p^o)$	$\frac{\Delta_l^g H_m^o(T)}{\text{kJ·mol}^{-1}}$
[PMIm][NTf$_2$]						
$\ln(p^*_{sat}/p^o) = -\frac{69296}{RT_0} - \frac{121408}{R}\left(\frac{1}{T} - \frac{1}{T_0}\right) - \frac{76}{R}\left(\frac{T_0}{T} - 1 - \ln\left(\frac{T}{T_0}\right)\right)$, T_0 = 380.2 K, p^o = 10^5 Pa						
1	401.66	0.7738	231	0.002490	-165.3	119.8
	396.77	0.4986	148	0.002520	-169.0	120.2
	391.91	0.3211	95	0.002552	-172.7	120.5
	386.93	0.2010	59	0.002584	-176.7	120.9
	381.95	0.1237	36	0.002618	-180.8	121.3
	376.96	0.07469	22	0.002653	-185.0	121.7
	371.65	0.04272	12	0.002691	-189.7	122.1
	366.36	0.02447	7.0	0.002730	-194.4	122.5
2	394.39	0.3939	117	0.002536	-171.0	120.3
	389.43	0.2529	74.5	0.002568	-174.8	120.7
	384.48	0.1577	46	0.002601	-178.7	121.1
	379.47	0.09743	28	0.002635	-182.8	121.5
	374.49	0.05970	17	0.002670	-186.9	121.8
	369.51	0.03392	10	0.002706	-191.7	122.2
	364.53	0.02072	5.9	0.002743	-195.8	122.6

	359.55	0.01125	3.2	0.002781	-201.0	123.0

[PMIm][OTf]

$\ln(p^*_{sat}/p^o) = -\frac{76900}{RT_0} - \frac{125184}{R}\left(\frac{1}{T} - \frac{1}{T_0}\right) - \frac{70}{R}\left(\frac{T_0}{T} - 1 - \ln\left(\frac{T}{T_0}\right)\right)$, T_0 = 403.7 K, p^o = 10^5 Pa

1	428.09	0.2486	93	0.002336	-172.9	123.5
	423.06	0.1663	62	0.002364	-176.3	123.8
	418.03	0.10827	40	0.002392	-179.9	124.2
	413.00	0.06999	26	0.002421	-183.6	124.5
	407.96	0.04442	16	0.002451	-187.4	124.9
	402.94	0.02848	10	0.002482	-191.1	125.2
	397.91	0.01801	6.5	0.002513	-195.0	125.6
	392.90	0.01105	4.0	0.002545	-199.1	125.9
	387.94	0.006890	2.5	0.002578	-203.1	126.3
	383.04	0.004238	1.5	0.002611	-207.2	126.6
2	425.57	0.2050	77	0.002350	-174.5	123.7
	420.55	0.1339	50	0.002378	-178.1	124.0
	415.52	0.08687	32	0.002407	-181.7	124.4
	410.49	0.05618	21	0.002436	-185.4	124.7
	405.44	0.03565	13	0.002466	-189.3	125.1
	400.43	0.02260	8.2	0.002497	-193.1	125.4
	395.39	0.01390	5.0	0.002529	-197.2	125.8
	390.37	0.008873	3.2	0.002562	-201.0	126.1
	385.38	0.005367	1.9	0.002595	-205.2	126.5
	380.43	0.003196	1.1	0.002629	-209.6	126.8

[PMIm][OMs]

$\ln(p^*_{sat}/p^o) = -\frac{78930}{RT_0} - \frac{135784}{R}\left(\frac{1}{T} - \frac{1}{T_0}\right) - \frac{75}{R}\left(\frac{T_0}{T} - 1 - \ln\left(\frac{T}{T_0}\right)\right)$, T_0 = 399.2 K

1	413.33	0.04559	19	0.002419	-186.2	134.7
	408.36	0.02926	12	0.002449	-190.0	135.1
	403.37	0.01760	7.2	0.002479	-194.2	135.5
	398.43	0.01087	4.4	0.002510	-198.3	135.8
	393.48	0.006262	2.5	0.002541	-202.9	136.2
	388.54	0.003720	1.5	0.002574	-207.3	136.6
	383.62	0.002216	0.88	0.002607	-211.7	137.0
	378.68	0.001275	0.50	0.002641	-216.3	137.3
	373.72	0.0007515	0.29	0.002676	-220.8	137.7
	368.75	0.0004121	0.16	0.002712	-225.8	138.1
2	425.55	0.1417	59	0.002350	-176.7	133.8
	420.51	0.0895	37	0.002378	-180.5	134.2
	415.48	0.05611	23	0.002407	-184.5	134.6
	410.45	0.03518	14	0.002436	-188.4	134.9
	405.42	0.02140	8.7	0.002467	-192.6	135.3
	400.40	0.01297	5.3	0.002498	-196.8	135.7
	395.36	0.007835	3.2	0.002529	-201.0	136.1
	390.34	0.004578	1.8	0.002562	-205.6	136.4
	385.36	0.002748	1.1	0.002595	-209.9	136.8
	380.42	0.001545	0.61	0.002629	-214.7	137.2
3	428.08	0.1766	74	0.002336	-174.8	133.6
	423.05	0.1118	47	0.002364	-178.7	134.0
	418.03	0.07124	29	0.002392	-182.5	134.4
	413.00	0.04503	19	0.002421	-186.3	134.7
	407.99	0.02758	11	0.002451	-190.4	135.1
	402.98	0.01651	6.7	0.002482	-194.8	135.5
	397.96	0.01026	4.1	0.002513	-198.8	135.9

	392.95	0.006134	2.5	0.002545	-203.1	136.3
	387.99	0.003562	1.4	0.002577	-207.7	136.6
	383.08	0.002121	0.84	0.002610	-212.0	137.0

[PPy][NTf$_2$]

$$\ln(p^*_{\mathrm{sat}}/p^{\mathrm{o}}) = -\frac{73530}{RT_0} - \frac{127931}{R}\left(\frac{1}{T} - \frac{1}{T_0}\right) - \frac{66}{R}\left(\frac{T_0}{T} - 1 - \ln\left(\frac{T}{T_0}\right)\right),\ T_0 = 398.2\ \mathrm{K}$$

1	419.89	0.5316	163	0.002382	-168.2	126.5
	414.87	0.3452	105	0.002410	-171.9	126.8
	409.86	0.2220	67	0.002440	-175.6	127.2
	404.90	0.1426	43	0.002470	-179.3	127.5
	399.92	0.08893	27	0.002501	-183.3	127.8
	394.99	0.05599	17	0.002532	-187.2	128.1
	390.04	0.03413	10	0.002564	-191.4	128.5
	385.07	0.02065	6.1	0.002597	-195.6	128.8
	380.09	0.01213	3.5	0.002631	-200.1	129.1
	375.10	0.007137	2.1	0.002666	-204.5	129.5
2	422.39	0.6584	203	0.002367	-166.4	126.3
	417.38	0.4292	131	0.002396	-170.0	126.7
	412.40	0.2793	85	0.002425	-173.7	127.0
	407.44	0.1800	54	0.002454	-177.4	127.3
	402.49	0.1147	34	0.002485	-181.2	127.6
	397.54	0.07232	22	0.002515	-185.0	128.0
	392.59	0.04451	13	0.002547	-189.1	128.3
	387.61	0.02685	7.9	0.002580	-193.4	128.6
	382.62	0.01577	4.6	0.002614	-197.9	129.0
	377.65	0.009051	2.6	0.002648	-202.5	129.3

[BPy][NTf$_2$]

$\ln(p^*_{sat}/p^o) = -\frac{73466}{RT_0} - \frac{131039}{R}\left(\frac{1}{T} - \frac{1}{T_0}\right) - \frac{70}{R}\left(\frac{T_0}{T} - 1 - \ln\left(\frac{T}{T_0}\right)\right)$, T_0 = 399.5 K

1	422.34	0.6840	207	0.002368	-166.3	129.4
	417.37	0.4395	132	0.002396	-170.0	129.8
	412.37	0.2809	84	0.002425	-173.8	130.1
	407.40	0.1785	53	0.002455	-177.6	130.5
	402.45	0.1121	33	0.002485	-181.5	130.8
	397.50	0.07015	21	0.002516	-185.4	131.2
	392.53	0.04233	12	0.002548	-189.7	131.5
	387.56	0.02585	7	0.002580	-193.8	131.9
	382.58	0.01472	4	0.002614	-198.6	132.2
	377.61	0.008651	2	0.002648	-203.1	132.6
2	419.87	0.5557	168	0.002382	-168.0	129.6
	414.88	0.3549	106	0.002410	-171.8	130.0
	409.89	0.2254	67	0.002440	-175.6	130.3
	404.89	0.1410	42	0.002470	-179.6	130.7
	399.95	0.08834	26	0.002500	-183.5	131.0
	394.99	0.05354	16	0.002532	-187.7	131.4
	390.03	0.03283	10	0.002564	-191.8	131.7
	385.06	0.01946	5.6	0.002597	-196.2	132.1
	380.08	0.01132	3.2	0.002631	-200.8	132.4

[HEMIm][OTf]

$\ln(p^*_{sat}/p^o) = -\frac{72890}{RT_0} - \frac{129625}{R}\left(\frac{1}{T} - \frac{1}{T_0}\right) - \frac{71}{R}\left(\frac{T_0}{T} - 1 - \ln\left(\frac{T}{T_0}\right)\right)$, T_0 = 387.4 K

1	408.05	0.08510	124	0.002451	-170.5	128.2
	403.05	0.04998	73	0.002481	-175.0	128.5
	398.08	0.03027	44	0.002512	-179.2	128.9
	393.12	0.01851	27	0.002544	-183.3	129.2

	388.19	0.01095	16	0.002576	-187.8	129.6
	383.23	0.00673	10	0.002609	-191.9	129.9
	378.28	0.00386	5.4	0.002644	-196.5	130.3
	373.34	0.00213	3.0	0.002678	-201.5	130.6
	368.37	0.00124	1.7	0.002715	-206.1	131.0
	363.43	0.0007966	1.1	0.002752	-209.8	131.3
2	410.47	0.09862	144	0.002436	-169.2	128.0
	405.42	0.06012	88	0.002467	-173.4	128.3
	400.39	0.03619	52	0.002498	-177.7	128.7
	395.37	0.02236	32	0.002529	-181.7	129.1
	390.35	0.01368	20	0.002562	-185.9	129.4
	385.31	0.008126	12	0.002595	-190.3	129.8
	380.31	0.004905	6.9	0.002629	-194.5	130.1
	375.31	0.002843	4.0	0.002664	-199.1	130.5
	370.32	0.001718	2.4	0.002700	-203.3	130.8
	365.36	0.001013	1.4	0.002737	-207.8	131.2
3	413.00	0.1239	182	0.002421	-167.3	127.8
	407.95	0.07985	117	0.002451	-171.0	128.2
	402.92	0.04743	69	0.002482	-175.4	128.5
	397.90	0.02844	41	0.002513	-179.7	128.9
	392.87	0.01787	26	0.002545	-183.6	129.2
	387.84	0.01063	15	0.002578	-188.0	129.6
	382.80	0.006190	8.8	0.002612	-192.6	130.0
	377.81	0.003682	5.2	0.002647	-196.9	130.3
	372.81	0.002272	3.2	0.002682	-201.0	130.7
	367.85	0.001354	1.9	0.002718	-205.4	131.0

[HEMIm][NTf$_2$]

$$\ln(p^*_{\mathrm{sat}}/p^{\mathrm{o}}) = -\frac{74973}{RT_0} - \frac{122075}{R}\left(\frac{1}{T} - \frac{1}{T_0}\right) - \frac{65}{R}\left(\frac{T_0}{T} - 1 - \ln\left(\frac{T}{T_0}\right)\right),\ T_0 = 382.0\ \mathrm{K}$$

1	403.30	0.1415	42	0.002480	-179.5	120.7
	398.45	0.09086	27	0.002510	-183.3	121.0
	393.57	0.05912	17	0.002541	-186.9	121.3
	388.66	0.03772	10.9	0.002573	-190.7	121.6
	383.74	0.02320	6.7	0.002606	-194.8	122.0
	378.79	0.01437	4.1	0.002640	-198.8	122.3
	373.82	0.008561	2.4	0.002675	-203.2	122.6
	368.79	0.004842	1.4	0.002712	-208.0	122.9
	363.77	0.002859	0.80	0.002749	-212.4	123.3
	358.75	0.001577	0.44	0.002787	-217.4	123.6
2	406.02	0.1809	54	0.002463	-177.5	120.5
	401.29	0.1186	35	0.002492	-181.0	120.8
	396.46	0.07671	22	0.002522	-184.7	121.1
	391.54	0.04891	14	0.002554	-188.5	121.5
	386.56	0.02994	8.7	0.002587	-192.6	121.8
	381.56	0.01932	5.6	0.002621	-196.3	122.1
	376.54	0.01124	3.2	0.002656	-200.9	122.4
	371.49	0.006773	1.9	0.002692	-205.2	122.8
	366.41	0.003915	1.1	0.002729	-209.8	123.1
	361.34	0.002209	0.62	0.002768	-214.6	123.4

[HEMIm][OMs]

$$\ln(p^*_{\mathrm{sat}}/p^{\mathrm{o}}) = -\frac{81032}{RT_0} - \frac{136924}{R}\left(\frac{1}{T} - \frac{1}{T_0}\right) - \frac{71}{R}\left(\frac{T_0}{T} - 1 - \ln\left(\frac{T}{T_0}\right)\right),\ T_0 = 416.1\ \mathrm{K}$$

1	438.48	0.1616	68	0.002281	-175.5	135.4
	433.50	0.1017	43	0.002307	-179.4	135.7
	428.53	0.06544	27	0.002334	-183.1	136.1
	423.54	0.04201	17	0.002361	-186.8	136.4

	418.58	0.02627	11	0.002389	-190.8	136.7
	413.58	0.01670	6.8	0.002418	-194.6	137.1
	408.58	0.01024	4.2	0.002447	-198.7	137.4
	403.58	0.006282	2.5	0.002478	-202.8	137.8
	398.58	0.003742	1.5	0.002509	-207.2	138.1
	393.58	0.002257	0.90	0.002541	-211.4	138.5
2	440.75	0.1873	79	0.002269	-174.2	135.2
	435.71	0.1180	50	0.002295	-178.1	135.6
	430.66	0.07658	32	0.002322	-181.8	135.9
	425.63	0.04945	21	0.002349	-185.5	136.3
	420.46	0.03215	13	0.002378	-189.1	136.6
	415.43	0.02009	8.3	0.002407	-193.0	137.0
	410.44	0.01247	5.1	0.002436	-197.1	137.3
	405.46	0.007623	3.1	0.002466	-201.2	137.7
	400.54	0.004722	1.9	0.002497	-205.2	138.0
	395.65	0.002931	1.17	0.002528	-209.3	138.4
3	438.21	0.1553	66	0.002282	-175.8	135.4
	433.17	0.09861	41	0.002309	-179.6	135.7
	428.14	0.06373	27	0.002336	-183.3	136.1
	423.11	0.04119	17	0.002363	-187.0	136.4
	418.09	0.02538	10.5	0.002392	-191.1	136.8
	413.06	0.01600	6.6	0.002421	-195.0	137.1
	408.05	0.009883	4.0	0.002451	-199.0	137.5
	403.06	0.005984	2.4	0.002481	-203.2	137.8
	398.09	0.003484	1.4	0.002512	-207.8	138.2
	393.16	0.002107	0.84	0.002543	-212.0	138.5

[HEPy][NTf$_2$]

	$\ln(p^*_{\mathrm{sat}}/p^{\circ}) = -\frac{79438}{RT_0} - \frac{134624}{R}\left(\frac{1}{T} - \frac{1}{T_0}\right) - \frac{81}{R}\left(\frac{T_0}{T} - 1 - \ln\left(\frac{T}{T_0}\right)\right)$, T_0 = 403.6 K					
1	423.17	0.1065	33	0.002363	-181.6	133.0
	418.24	0.06977	21	0.002391	-185.2	133.4
	413.41	0.04385	13	0.002419	-189.1	133.8
	408.52	0.02833	8.6	0.002448	-192.7	134.2
	403.59	0.01771	5.3	0.002478	-196.7	134.6
	398.63	0.01045	3.1	0.002509	-201.1	135.0
	393.69	0.006467	1.9	0.002540	-205.2	135.4
	388.76	0.003860	1.1	0.002572	-209.5	135.8
	383.76	0.002246	0.66	0.002606	-214.1	136.2
	378.76	0.001265	0.37	0.002640	-218.9	136.6
2	426.41	0.1472	45	0.002345	-178.9	132.8
	420.81	0.08558	26	0.002376	-183.4	133.2
	415.82	0.05295	16	0.002405	-187.5	133.6
	410.85	0.03363	10	0.002434	-191.3	134.0
	405.87	0.02146	6.5	0.002464	-195.1	134.4
	400.90	0.01419	4.2	0.002494	-198.6	134.8
	395.94	0.008431	2.5	0.002526	-203.0	135.2
	390.99	0.004736	1.4	0.002558	-207.8	135.6
	385.99	0.003009	0.88	0.002591	-211.6	136.0
	381.04	0.001590	0.46	0.002624	-217.0	136.5
3	428.19	0.1713	53	0.002335	-177.6	132.6
	423.15	0.1101	34	0.002363	-181.3	133.0
	418.13	0.06893	21	0.002392	-185.3	133.4
	413.10	0.04401	13	0.002421	-189.0	133.9
	408.08	0.02744	8.3	0.002451	-193.0	134.3

	403.06	0.01623	4.9	0.002481	-197.4	134.7
	403.17	0.01624	4.9	0.002480	-197.4	134.7
	398.25	0.01011	3.0	0.002511	-201.4	135.1
	393.29	0.006135	1.8	0.002543	-205.6	135.5
	388.33	0.003591	1.1	0.002575	-210.1	135.9

[HPPy][NTf$_2$]

$$\ln(p^*_{\mathrm{sat}}/p^{\circ}) = -\frac{79817}{RT_0} - \frac{136787}{R}\left(\frac{1}{T} - \frac{1}{T_0}\right) - \frac{91}{R}\left(\frac{T_0}{T} - 1 - \ln\left(\frac{T}{T_0}\right)\right),\ T_0 = 412.5\ \mathrm{K}$$

1	433.17	0.1663	51	0.002309	-177.9	134.9
	428.21	0.11197	34	0.002335	-181.3	135.4
	423.35	0.07245	22	0.002362	-184.9	135.8
	418.48	0.04455	13	0.002390	-189.0	136.2
	413.62	0.02949	8.8	0.002418	-192.5	136.7
	408.73	0.01857	5.5	0.002447	-196.4	137.1
	403.84	0.01127	3.3	0.002476	-200.6	137.6
	398.94	0.006603	1.9	0.002507	-205.1	138.0
	394.01	0.003912	1.1	0.002538	-209.5	138.5
	389.06	0.002518	0.73	0.002570	-213.2	138.9
2	436.21	0.2259	69	0.002292	-175.4	134.6
	431.23	0.1449	44	0.002319	-179.1	135.1
	426.30	0.09634	29	0.002346	-182.5	135.5
	421.38	0.05913	18	0.002373	-186.6	136.0
	416.45	0.03817	11	0.002401	-190.3	136.4
	411.50	0.02322	6.9	0.002430	-194.5	136.9
	406.55	0.01417	4.2	0.002460	-198.7	137.3
	401.59	0.008873	2.6	0.002490	-202.6	137.8
	396.60	0.005386	1.6	0.002521	-206.8	138.2

	391.61	0.003379	0.98	0.002554	-210.7	138.7
3	436.07	0.2054	63	0.002293	-176.1	134.6
	431.12	0.1403	43	0.002320	-179.4	135.1
	426.21	0.09363	28	0.002346	-182.8	135.5
	421.28	0.06048	18	0.002374	-186.5	136.0
	416.37	0.03847	12	0.002402	-190.3	136.4
	411.45	0.02420	7.2	0.002430	-194.2	136.9
	406.51	0.01468	4.3	0.002460	-198.4	137.3
	401.56	0.008883	2.6	0.002490	-202.6	137.8
	396.60	0.005285	1.5	0.002521	-207.0	138.2
	391.61	0.003010	0.87	0.002554	-211.7	138.7

[a] the combined expanded uncertainties are $U_c(T) = 0.02$ K, $U_r(df \cdot dt^{-1}) = 0.01$ $U_r(p_{sat}) = 0.5$ for confidence level = 0.95, $k \approx 2$.

References:

1 S. P. Verevkin, D. H. Zaitsau, V. N. Emel`yanenko and A. Heintz, A new method for the determination of vaporization enthalpies of ionic liquids at low temperatures, *J. Phys. Chem. B*, 2011, **115**, 12889–12895.

2 G. Sauerbrey, Verwendung von Schwingquarzen zur Wägung dünner Schichten und zur Mikrowägung, *Z. Phys.*, 1959, **155**, 206–222.

3 D. H. Zaitsau, A. V Yermalayeu, V. N. Emel'yanenko, S. Butler, T. Schubert and S. P. Verevkin, Thermodynamics of imidazolium-based ionic liquids containing PF6 anions, *J. Phys. Chem. B*, 2016, **120**, 7949–7957.

4 E. C. W. Clarke and D. N. Glew, Evaluation of thermodynamic functions from equilibrium constants, *Trans. Faraday Soc.*, 1966, **62**, 539–547.

3. FT-IR Spectroscopy of the liquid phase

IR experiments for the condensed phase were performed on a TENSOR II FTIR spectrometer from BRUKER. The spectrometer uses a Globar® source, a KBr beam splitter and a DTGS room temperature detector. The sample cell was a demountable liquid cell with CaF_2-windows and a 12 µm Mylar®-spacer. For data collection analyses the OPUS 7.5 software was used. Every spectrum was accumulated for 128 scans with a resolution of 1 cm^{-1} and a 3 mm aperture. To avoid interference fringes, CCl_4 was used as background. The pure ILs were dried in vacuum to a water contend below 15 ppm. The ILs were prepared under SCHLENK-conditions in a 5 ml SCHLENK-tube in 2 g portions.

4 Molecular Dynamics Simulations

We did NpT molecular dynamics simulation using GROMACS 5.0.6 [1–5] at a temperature of $T = 300\,\mathrm{K}$ and a pressure of $p = 1\,\mathrm{bar}$. The ionic liquid was represented by a cubic simulation box containing 512 ion pairs. The box was first equilibrated for 2 ns at $T = 500\,\mathrm{K}$ employing the BERENDSEN thermostat as well as the BERENDSEN barostat [6] with coupling times of $\tau_\mathrm{T} = \tau_\mathrm{p} = 0.5\,\mathrm{ps}$. After that, another equlibration for 2 ns at the desired temperature of 300 K followed. Production runs of 100 ns length utilizing the NOSÉ-HOOVER thermostat [7, 8] with $\tau_\mathrm{T} = 1\,\mathrm{ps}$ and RAHMAN-PARRINELLO barostat [9, 10] with $\tau_\mathrm{p} = 2\,\mathrm{ps}$ were performed for each temperature.
The gas phase simulations were done on an ion pair of the corresponding ionic liquid. After equilibration over 2 ns at $T = 300\,\mathrm{K}$ production runs of 400 ns length were performed, employing the NOSÉ-HOOVER thermostat with $\tau_\mathrm{T} = 1\,\mathrm{ps}$.
All simulations were done with a 2.0 fs time step employing periodic boundary conditions and the LINCS algorithm [11] for fixed bond lengths. The smooth particle mesh EWALD summation [12] was applied in the liquid with a mesh spacing of 0.12 nm, a real space cutoff of 0.9 nm and 4th order interpolation. The relative accuracy of the EWALD sum was set to 10^{-5} corresponding to a convergence factor $\alpha = 3.38\,\mathrm{nm}^{-1}$.
The forcefield of the $[\mathrm{NTf_2}]^-$ anion is published in reference [13]. The forcefield of the $[\mathrm{PMIm}]^+$ cation is published in reference [14]. The forcefields of the other cations are described below.

4.1 $[\mathrm{HEPy}]^+$ Forcefield

The pyridinium forcefield was derived from the OPLS forcefield for pyridine from Jorgensen [15, 16]. The dihedral potentials of the hydroxyalkyl chain were fitted on ab initio calculations employing second order Møller-Plesset perturbation theory using the cc-pvtz basis set. The point charges were derived from the electostatic potential according to the CHelpG scheme [17]. All forcefield parameters for the $[\mathrm{HEPy}]^+$ cation can be found below.

SI Tab. S2: Lennard-Jones parameters σ and ϵ for all interaction sites of the $[HEPy]^+$ cation.

site	σ / Å	$\epsilon \cdot k_B^{-1}$ / K
N	3.25	85.55
C_a	3.55	35.23
H_a	2.42	15.10
C_c	3.50	33.20
H_c	2.50	15.10
H_m	2.50	15.10
O	3.12	85.60
H_o	0.00	0.00

SI Tab. S3: Bond length $r^0_{\kappa\lambda}$ and angle parameters $\phi^0_{\kappa\lambda\omega}$ und $k^a_{\kappa\lambda\omega}$ for the angle potential $V^a_{\kappa\lambda\omega} = \frac{1}{2}k^a_{\kappa\lambda\omega}(\phi_{\kappa\lambda\omega} - \phi^0_{\kappa\lambda\omega})^2$ in the force field of the $[HEPy]^+$ cation.

bond	$r^0_{\kappa\lambda}$ / Å	angle	$\phi^0_{\kappa\lambda\omega}$ / °	$k^a_{\kappa\lambda\omega}$ / kJ mol^{-1}rad^{-2}
C_a-N	1.339	C_a-C_a-C_a	120.0	527.20
C_a-H_a	1.080	C_a-C_a-N	124.0	585.80
C_a-C_a	1.400	C_a-N-C_a	117.0	585.80
N-C_c	1.339	C_a-C_a-H_a	120.0	292.90
C_c-C_c	1.529	N-C_a-H_a	116.0	292.90
C_c-H_c	1.090	C_a-N-C_c	121.5	585.80
C_c-O	1.410	N-C_c-C_c	112.7	487.43
O-H_o	0.945	H_c-C_c-N	110.7	313.26
C_c-H_m	1.090	H_c-C_c-H_c	107.8	275.70
		H_c-C_c-C_c	110.7	313.26
		H_m-C_c-C_c	110.7	313.26
		H_m-C_c-H_m	107.8	275.70
		C_c-C_c-C_c	112.7	487.43
		H_o-O-C_c	108.5	460.55
		C_c-C_c-O	109.5	418.68
		H_c-C_c-O	109.5	293.08

SI Tab. S4: Parameters m_n, k_m^{dp} and ψ_m^0 for the improper dihedral potential $V_{\kappa\lambda\omega\tau}^{\mathrm{dp}} = \sum_n k_m^{\mathrm{dp}}[1 + \cos(m_n\psi_m - \psi_m^0)]$ in the force field of the $[\mathrm{HEPy}]^+$ cation. The central atom is the first in the list.

	m_n	k_m^{dp} / kJ mol^{-1}	ψ_m^0 / °
N-C_a-C_a-C_c	2	4.6060	180.0
C_a-N-C_a-H_a	2	4.6060	180.0
C_a-C_a-C_a-H_a	2	4.6060	180.0

SI Tab. S5: Parameters m_n, k_m^{dp} and ψ_m^0 for the torsion potential $V_{\kappa\lambda\omega\tau}^{\mathrm{dp}} = \sum_n k_m^{\mathrm{dp}}[1+\cos(m_n\psi_m - \psi_m^0)]$ in the force field of the $[\mathrm{HEPy}]^+$ cation.

	$n(\kappa\lambda\omega\tau)$	m_n	k_m^{dp} / kJ mol^{-1}	ψ_m^0 / °
X-C_a-C_a-X	1	2	15.1780	180.0
X-C_a-N-X	1	2	15.1780	180.0
C_a-N-C_c-C_c	1	2	0.0802	0
	2	4	-0.4693	0
N-C_c-C_c-O	1	1	-0.7375	0.0
	2	2	1.8576	0.0
	3	3	7.2898	0.0
C_c-C_c-O-H_o	1	1	-5.8097	0.0
	2	2	1.8939	0.0
	3	3	2.5150	0.0

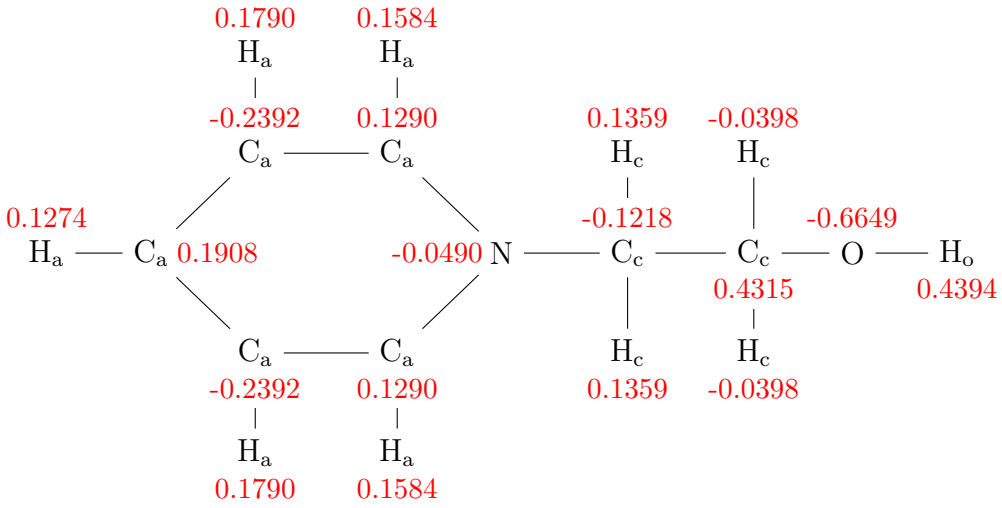

SI Fig. S1: Structure of the $[\mathrm{HEPy}]^+$ cation with atom types and corresponding point charges q/e in red.

4.2 $[PPy]^+$ Forcefield

The forcefield of the $[PPy]^+$ was derived similarly to the $[HEPy]^+$ forcefield. The parameters for the Lennard-Jones, bond, angle as well as the improper dihedral potential are the same and can be found in table 1 to 3 respectively. The dihedral potentials as well as the point charges can be found below.

SI Tab. S6: Parameters m_n, k_m^{dp} and ψ_m^0 for the torsion potential $V_{\kappa\lambda\omega\tau}^{\mathrm{dp}} = \sum_n k_m^{\mathrm{dp}}[1+\cos(m_n\psi_m - \psi_m^0)]$ in the force field of the $[PPy]^+$ cation.

	$n(\kappa\lambda\omega\tau)$	m_n	k_m^{dp} / kJ mol^{-1}	ψ_m^0 / °
X-C_a-C_a-X	1	2	15.1780	180.0
X-C_a-N-X	1	2	15.1780	180.0
C_a-N-C_c-C_c	1	2	-0.4178	0
	2	4	-0.4138	0
N-C_c-C_c-C_c	1	1	-1.4934	0.0
	3	3	6.8503	0.0
C_c-C_c-C_c-H_m	1	3	1.8318	0.0

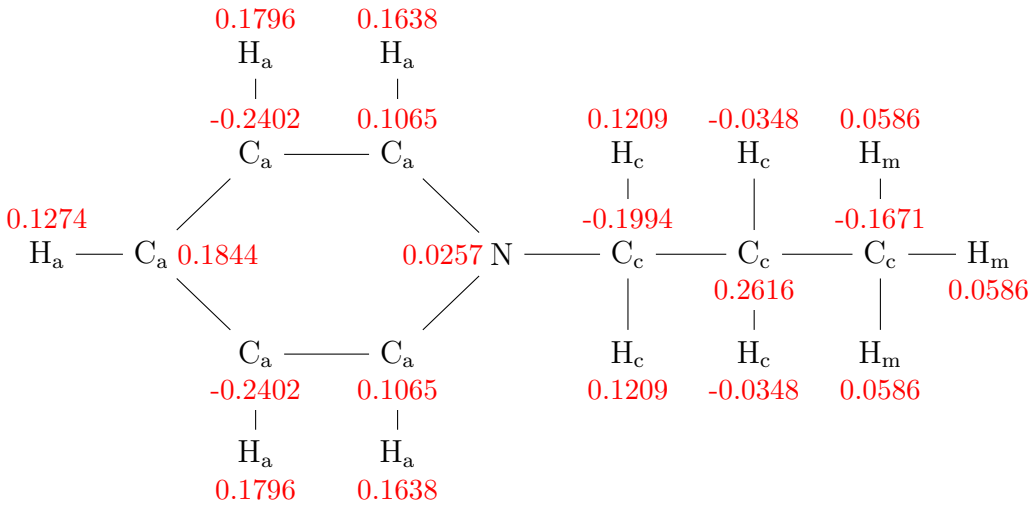

SI Fig. S2: Structure of the $[PPy]^+$ cation with atom types and corresponding point charges q/e in red.

4.3 $[HEMIm]^+$ Forcefield

The imidazolium forcefields are based on the forcefield from Kddermann et al. [14]. The dihedral potentials of the hydroxyalkyl chain were fitted on ab initio calculations employing second order Møller-Plesset perturbation theory using the cc-pvtz basis set. The original point charges on the ring atoms as well as the methyl group

were used. Only the point charges on the hydroxyalkl chain were calculated from the electostatic potential according to the Merz-Singh-Kollman scheme [18, 19] and scaled to give a resulting charge of the whole cation of +1 e. All forcefield parameters for the $[HEPy]^+$ cation can be found below.

SI Tab. S7: Lennard-Jones parameters σ and ϵ for all interaction sites of the $[HEMIm]^+$ cation.

site	σ / Å	$\epsilon \cdot k_B^{-1}$ / K
N	3.25	85.55
C_r	2.13	52.84
C_w	3.0175	24.66
H_a	1.452	22.65
H_b	2.057	10.60
C_1	3.50	33.20
C_c	3.50	33.20
H_1	2.50	15.10
H_c	2.50	15.10
O	3.12	85.60
H_o	0.00	0.00

SI Tab. S8: Bond length $r^0_{\kappa\lambda}$ and angle parameters $\phi^0_{\kappa\lambda\omega}$ und $k^{\mathrm{a}}_{\kappa\lambda\omega}$ for the angle potential $V^{\mathrm{a}}_{\kappa\lambda\omega} = \frac{1}{2}k^{\mathrm{a}}_{\kappa\lambda\omega}(\phi_{\kappa\lambda\omega} - \phi^0_{\kappa\lambda\omega})^2$ in the force field of the $[\mathrm{HEMIm}]^+$ cation.

bond	$r^0_{\kappa\lambda}$ / Å	angle	$\phi^0_{\kappa\lambda\omega}$ / °	$k^{\mathrm{a}}_{\kappa\lambda\omega}$ / kJ mol^{-1}rad^{-2}
C_c-C_c	1.529	C_c-C_c-C_c	112.7	487.43
C_c-H_c	1.090	H_c-C_c-H_c	107.8	275.70
C_1-H_1	1.090	H_c-C_c-C_c	110.7	313.26
C_c-O	1.410	H_1-C_1-C_1	107.8	275.70
O-H_o	0.945	H_1-C_1-N	110.7	313.26
C_w-C_w	1.341	H_C-C_C-N	110.7	313.26
N-C_1	1.466	C_1-N-C_r	126.4	292.60
N-C_c	1.466	C_1-N-C_w	125.6	292.60
C_w-N	1.378	C_c-N-C_r	126.4	292.60
C_r-N	1.315	C_c-N-C_w	125.6	292.60
C_r-H_a	1.080	H_a-C_r-N	125.1	146.30
C_w-H_b	1.080	H_b-C_w-N	122.0	146.30
		H_b-C_w-C_w	130.9	146.30
		H_o-O-C_c	108.5	460.55
		C_c-C_c-O	109.5	418.68
		H_c-C_c-O	109.5	293.08

SI Tab. S9: Parameters m_n, k^{dp}_m and ψ^0_m for the improper dihedral potential $V^{\mathrm{dp}}_{\kappa\lambda\omega\tau} = \sum_n k^{\mathrm{dp}}_m[1 + \cos(m_n\psi_m - \psi^0_m)]$ in the force field of the $[\mathrm{HEMIm}]^+$ cation. The central atom is the first in the list.

	m_n	k^{dp}_m / kJ mol^{-1}	ψ^0_m / °
N-C_w-C_r-C_1	2	9.20	180.0
C_r-N-N-H_a	2	9.20	180.0
C_w-C_w-N-H_b	2	8.37	180.0

SI Tab. S10: Parameters m_n, k_m^{dp} and ψ_m^0 for the torsion potential $V_{\kappa\lambda\omega\tau}^{\mathrm{dp}} = \sum_n k_m^{\mathrm{dp}}[1+\cos(m_n\psi_m - \psi_m^0)]$ in the force field of the $[\mathrm{HEMIm}]^+$ cation.

	$n(\kappa\lambda\omega\tau)$	m_n	k_m^{dp} / kJ mol^{-1}	ψ_m^0 / °
X-N-C_r-X	1	2	19.46	180.0
X-C_w-C_w-X	1	2	44.98	180.0
X-N-C_w-X	1	2	12.55	180.0
C_w-N-C_1-H_1	1	3	0.55	0
C_r-N-C_c-C_c	1	2	1.8560	0
	2	3	-0.6785	0.0
	3	4	-0.5112	0.0
N-C_c-C_c-O	1	1	-1.9592	0.0
	2	2	1.0784	0.0
	3	3	7.08193	0.0
	4	4	0.5216	0.0
C_c-C_c-O-H_o	1	1	-3.3455	0.0
	2	2	1.9342	0.0
	3	3	2.5818	0.0

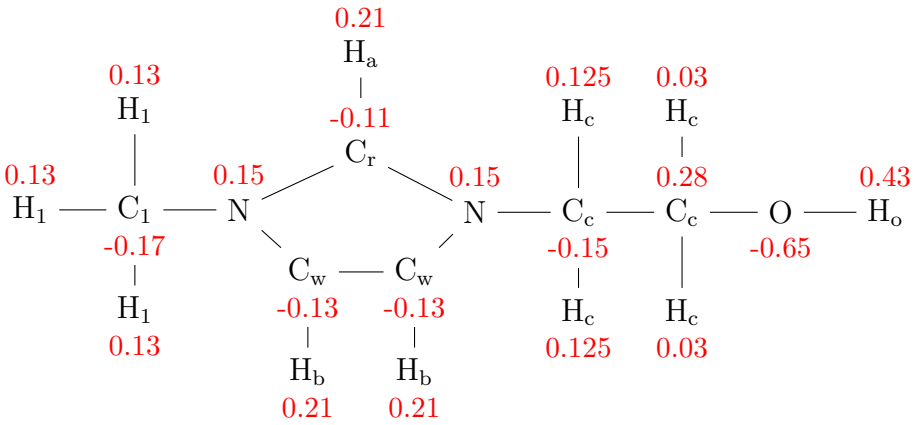

SI Fig. S3: Structure of the $[\mathrm{HEMIm}]^+$ cation with atom types and corresponding point charges q/e in red.

References

[1] E. Lindahl, B. Hess, D. van der Spoel, "Gromacs 3.0: A package for molecular simulation and trajectory analysis", *J. Mol. Mod.* **2001**, *7*, 306–317.

[2] H. J. C. Berendsen, D. van der Spoel, R. van Drunen, "Gromacs: A Message-Passing Parallel Molecular Dynamics Implementation", *Comp. Phys. Comm.* **1995**, *91*, 43–46.

[3] B. Hess, C. Kutzer, D. van der Spoel, E. Lindahl, "Gromacs 4: Algorithms for highly efficient, load-balanced, and scalable molecular simulation", *J. Chem. Theory Comput.* **2008**, *4*, 435–447.

[4] S. Pronk, S. Pall, R. Schulz, P. Larsson, P. Bjelkmar, R. Apostolov, M. R. Shirts, J. C. Smith, P. M. Kasson, D. van der Spoel, B. Hess, E. Lindahl, "Gromacs 4.5: A high-throughput and highly parallel open source molecular simulation toolkit", *Bioinformatics* **2013**, *29*, 845–54.

[5] M. Abraham, B. Hess, D. van der Spoel, E. Lindahl, E. Apol, R. Apostolov, H. J. C. Berendsen, A. van Buuren, P. Bjelkmar, R. van Drunen, A. Feenstra, S. Fritsch, G. Groenhof, C. Jungshans, J. Hub, P. Kasson, C. Kutzner, B. Lambeth, P. Larsson, J. A. Lemkul, E. Marklund, P. Meulenhoff, T. Murtola, S. Pall, S. Pronk, R. Schulz, M. Shirts, A. Sijbers, P. Tieleman, C. Wennberg, M. Wolf, Gromacs 5.0.6, **2015**.

[6] H. J. C. Berendsen, J. P. M. Postma, W. F. van Gunsteren, A. DiNola, J. R. Haak, "Molecular dynamics with coupling to an external bath", *J. Chem. Phys.* **1984**, *81*, 3684–3690.

[7] S. Nosé, "A molecular dynamics method for simulating in the canonical ensemble", *Mol. Phys.* **1984**, *52*, 255–268.

[8] W. G. Hoover, "Canonical Dynamics: Equilibrium Phase space distributions", *Phys. Rev. A* **1985**, *31*, 1695–1697.

[9] M. Parrinello, A. Rahman, "Polymorphic transitions in single crystals: A new molecular dynamics method", *J. Appl. Phys.* **1981**, *52*, 7182–7180.

[10] S. Nosé, M. L. Klein, "Constant pressure molecular dynamics for molecular systems", *Mol. Phys.* **1983**, *50*, 1055–1076.

[11] B. Hess, H. Bekker, H. J. C. Berendsen, J. G. E. M. Fraaije, "LINCS: A linear constraint solver for molecular simulations", *J. Comp. Chem.* **1997**, *18*, 1463–1472.

[12] U. Essmann, L. Perera, M. L. Berkowitz, T. A. Darden, H. Lee, L. G. Pedersen, "A smooth particle mesh Ewald method", *J. Chem. Phys.* **1995**, *103*, 8577–8593.

[13] J. Neumann, B. Golub, L.-M. Odebrecht, R. Ludwig, D. Paschek, "Revisiting imidazolium based ionic liquids: Effect of the conformation bias of the [ntf2] anion studied by molecular dynamics simulations", *The Journal of Chemical Physics* **2018**, *148*, 193828.

[14] T. Köddermann, D. Paschek, R. Ludwig, "Molecular dynamic simulations of ionic liquids: A reliable description of structure, thermodynamics and dynamics", *ChemPhysChem* **2007**, *8*, 2464–2470.

[15] W. L. Jorgensen, D. S. Maxwell, J. Tirado-Rives, "Development and testing of the OPLS all-atom force field on conformational energetics and properties of organic liquids", *Journal of the American Chemical Society* **1996**, *118*, 11225–11236.

[16] W. L. Jorgensen, N. A. McDonald, "Development of an all-atom force field for heterocycles. Properties of liquid pyridine and diazenes", *Journal of Molecular Structure: THEOCHEM* **1998**, *424*, 145–155.

[17] C. M. Breneman, K. B. Wiberg, "Determining atom-centered monopoles from molecular electrostatic potentials. The need for high sampling density in formamide conformational analysis", *Journal of Computational Chemistry* **1990**, *11*, 361–373.

[18] U. C. Singh, P. A. Kollman, "An approach to computing electrostatic charges for molecules", *Journal of Computational Chemistry* **1984**, *5*, 129–145.

[19] B. H. Besler, K. M. Merz Jr, P. A. Kollman, "Atomic charges derived from semiempirical methods", *Journal of Computational Chemistry* **1990**, *11*, 431–439.

V. Kinetics of Hydrogen Bonding between Ions of Opposite and Ions of Like Charge in Hydroxyl-Functionalized Ionic Liquids

J. Neumann, D. Paschek, A. Strate, R. Ludwig, *J. Phys. Chem. B* **2021**, *125*, 281. DOI: 10.1021/acs.jpcb.0c09278.

Contribution:
I developed the force fields of the examined ILs and generated and analyzed their MD trajectories. The calculation of the HB lifetime population correlation functions is based on self-made python scripts using the convolution theorem. I wrote the first draft of the manuscript and took part in its revision. The share of my work sums up to approximately 60 %.

THE JOURNAL OF PHYSICAL CHEMISTRY B

pubs.acs.org/JPCB Article

Kinetics of Hydrogen Bonding between Ions with Opposite and Like Charges in Hydroxyl-Functionalized Ionic Liquids

Jan Neumann, Dietmar Paschek, Anne Strate, and Ralf Ludwig*

Cite This: J. Phys. Chem. B 2021, 125, 281−286 Read Online

ACCESS | Metrics & More | Article Recommendations | Supporting Information

ABSTRACT: Hydrogen-bonded structures and their lifetimes in ionic liquids (ILs) are governed by the subtle balance between Coulomb interactions, hydrogen bonding, and dispersion forces. Despite the dominant Coulomb interaction, local and directional hydrogen bonds (HBs) can play an important role in the behavior of ILs. Compared to water, the archetype of hydrogen-bonded liquids, ILs have larger constituents and higher viscosities but are typically lacking a three-dimensional HB network. Hydroxyl-functionalized ionic liquids are even more special: regular HBs between cations and anions (ca) are accompanied by HBs between pairs of cations (cc). Recently, infrared (IR) measurements have suggested that the (cc) HBs are even stronger than their (ca) counterparts and their strength can be controlled via the hydroxyalkyl chain length. In this paper, we show by means of molecular dynamics (MD) simulations that the presence of HBs has a profound effect on the molecular mobility of the ions. We investigate the kinetic mechanism of hydrogen bonding in ILs and show that the lifetimes and hence the stability of (cc) HBs increase with the chain length, making them more stable than the respective (ca) HBs. The observed HB equilibrium can explain the peculiar chain length dependence of the relative molecular mobilities of the ions by a direct comparison between hydroxyl-functionalized ILs with their nonfunctionalized counterparts.

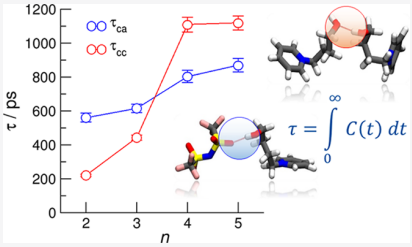

INTRODUCTION

Water is the archetype of hydrogen-bonded liquids.[1] The fundamental dynamical process of liquid water is the making and breaking of hydrogen bonds (HB). It is evident that understanding the dynamics of an HB network provides critical insights into the properties of water. X-ray and neutron diffraction techniques, in addition to X-ray scattering and absorption experiments, as well as IR spectroscopy are often interpreted in terms of hydrogen bonding but probe the HB dynamics only in a qualitative way.[2] Luzar and Chandler demonstrated by molecular dynamics (MD) simulations that HB dynamics are characterized by relaxation processes, which are essentially rather uncorrelated with respect to the specific bonding patterns near the tagged HB.[3] In their model, essentially, diffusion governs whether molecules are near neighbors, and HBs between such pairs form and persist at random with average lifetimes determined by rate constants for bond making and breaking.

In ionic liquids (ILs), the hydrogen-bonding situation is expected to be different from that in molecular liquids such as water. ILs consist solely of cations and anions and their hydrogen-bonding structures and lifetimes are governed by the subtle balance between Coulomb interactions, hydrogen bonding, and dispersion forces.[4] Since ILs attract increasing interest in science and technology with applications in electrochemical charge storage, electrodeposition, lubrication, etc., it is no surprise that attention has also been devoted to the understanding of hydrogen bonding in these liquid salts. Recently, Gehrke et al. studied the dynamics of hydrogen bonding and ion pair formation in imidazolium ILs. They reported HB lifetimes between 10 and 2000 ps depending on the IL viscosity.[5,6] Deriving HB lifetimes in ILs reliably from MD simulations still remains a challenge, which is affected by the quality of the used force fields and have sampling efficiency issues based on the length of the simulation runs. For hydroxyl-functionalized ILs, the situation is even more complicated. In this type of IL, two distinct types of hydrogen bonding coexist: the "conventional" HBs between cations and anions (ca) are enhanced by the attractive Coulomb interaction, whereas the "elusive" HBs between like-charged ions (cc) are supposed to be much weaker due to the repulsive Coulomb forces.[7−11] Despite this expectation, however, structural motifs involving hydrogen-bonded cationic clusters were recently observed in the bulk liquid and the gas phase.[12−19] Vibrational spectroscopy clearly identified two distinct vibrational bands that were assigned to (ca) and (cc) hydrogen-bonded species. The magnitudes of the observed red shifts indicated that (cc) HBs are evidently stronger than (ca) HBs.[17−19] Strongly enhanced (cc) cluster formation was observed for ILs 1-(*n*-hydroxyalkyl)-pyridinium bis(trifluoromethanesulfonyl)imide

Received: October 13, 2020
Revised: November 26, 2020
Published: December 23, 2020

https://dx.doi.org/10.1021/acs.jpcb.0c09278
J. Phys. Chem. B 2021, 125, 281−286

$[HOC_nPy][NTf_2]$ comprising polarizable pyridinium $[HOC_nPy]^+$ cations with n = 2−5, a weakly interacting bis(trifluoromethanesulfonyl)imide anion $[NTf_2]^-$, and hydroxyalkyl chains of various length for keeping the positively charged pyridinium ring away from the hydroxyl group; finally, allowing hydrogen bonding between the hydroxyl groups of the cations. Although (cc) HBs are stronger than (ca) HBs, as indicated by frequency red shifts in IR spectra and HB length shortening in neutron diffraction (ND) experiments, the knowledge of the HB kinetics of these two competing types of HB and their relation to the dynamics of the ILs are still lacking.

In this study, we will address several relevant issues: How do the HB population correlation functions for the (ca) and (cc) species differ? Are the lifetimes of (ca) and (cc) HBs affected by the variation of the alkyl chain length of the hydroxyl-functionalized IL? Are the lifetimes of (cc) HBs longer or shorter than those of the (ca) HBs, given the presence of repulsive Coulomb interactions in the first and the attractive Coulomb interaction in the latter case? And finally, does the microdynamics of HB lifetimes have an effect on the overall mobility of the ions.

METHODS

First, we probe the hydrogen bonding of the hydroxyl-functionalized ILs $[HOC_nPy][NTf_2]$ with n = 2−5 by means of infrared (IR) spectroscopy. ILs were synthesized in our labs following standard protocols.[20] In Figure 1, we show the IR spectra in the OH stretch region recorded at 293 K. The high-frequency vibrational bands around 3550 cm^{-1} are present in all ILs and describe the Coulomb-enhanced $^+OH\cdots O^-$ (ca) HB. From n = 2 to 5, these vibrational bands are shifted to higher wavenumbers because of weaker Coulomb-enhanced HBs with increasing hydroxyalkyl chain length. The significantly red-shifted vibrational band at 3400 cm^{-1} is mainly observed for $[HOC_4Py][NTf_2]$ and $[HOC_5Py][NTf_2]$. In accordance with recent work, we assigned these low-frequency bands to $^+OH\cdots O^+$ (cc) HBs.[12−15] We observe that from n = 2 to 5, the intensity of the (ca) vibrational bands for ILs $[HOC_nPy][NTf_2]$ decreases for the benefit of the (cc) vibrational bands, which are significantly red-shifted by about $\Delta\tilde{\nu}$ = 150 cm^{-1}. We could clearly assign these red shifts to increasing formation of cationic clusters with increasing hydroxyalkyl chain length by reducing the repulsive Coulomb forces. In particular, we could show that (cc) HBs are favored over (ca) HBs with decreasing temperature.[12−15]

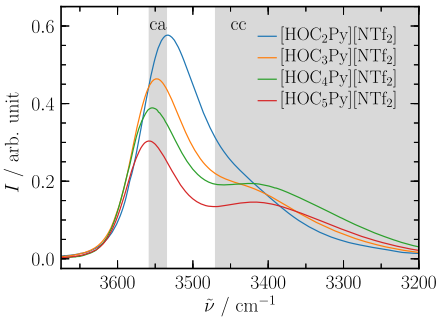

Figure 1. Infrared spectra of the hydroxyl-functionalized ionic liquids $[HOC_nPy][NTf_2]$ with n = 2, 3, 4, and 5 in the OH stretch region at 293 K. We observe two vibrational bands assigned to hydroxyl groups hydrogen-bonded to anions (ca) and to hydroxyl groups of other cations (cc). The (cc) HBs are evidently stronger than the (ca) HBs as indicated by the stronger OH red shifts. The intensities of the (cc) vibrational bands increase with longer hydroxyalkyl chain lengths of the cations due to decreasing repulsive interaction between ions of like charge.

To understand the nature of these two types of hydrogen bonding, in particular their dynamics and lifetimes, we perform MD simulations of hydroxyl-functionalized ILs $[HOC_nPy][NTf_2]$ with n = 2, 3, 4, and 5 as well as their not functionalized counterparts $[C_{n+1}Py][NTf_2]$. All simulations are covering the temperature range between 300 and 400 K. The *NpT* molecular dynamics simulations of $[HOC_nPy][NTf_2]$ and $[C_{n+1}Py][NTf_2]$ ILs with n = 2−5 were done with system sizes of 512 ion pairs using Gromacs 5.0.6.[21−25] The ions were first arranged on an interpenetrating primitive cubic lattice and then equilibrated at 500 K for 2 ns. After another equilibration for 2 ns at the desired temperature of 300 K, production runs of 100 ns were carried out. The force field of the $[NTf_2]^-$ anion has been published in refs 26, 27. The pyridinium force fields were derived from the OPLS force field for pyridine from Jorgensen et al.[28] Further details on the simulation are given in the SI.

RESULTS AND DISCUSSION

As shown in Figure 2, the introduction of a hydroxyl group has a profound effect on the mobility of the cations: All hydroxyl-functionalized ILs possess a consistently reduced molecular mobility. On average, a reduction by a factor of about one-third is observed. In addition, as shown in Figure 2b, this retardation effect is found to be more strongly pronounced at lower temperatures, possibly facilitated by the increasing influence of hydrogen bonding. Quite surprisingly, however, a chain length increase does not lead to a further reduction in relative mobility but instead to the increased diffusivity, as shown in Figure 2b. This effect is quite possibly related to the competition between (ca) and (cc) HBs. To illustrate this, we have plotted the ratio of the self-diffusion coefficients of cations and anions as a function of the chain length at 300 K for both hydroxyl-functionalized ILs and their nonfunctionalized counterparts in Figure 3. In all cases, the cations are more mobile than the anions, hence $D_{cation}/D_{anion} > 1$. With the increasing size of the cations (i.e., chain length), of course, this "mobility-benefit" of cations diminishes and D_{cation}/D_{anion} decreases. However, in all cases, the ratio obtained for the hydroxyl-functionalized IL is significantly smaller than the ratio of their nonfunctionalized counterparts. Apparently, the HB-enhanced anion−cation interaction leads to a more concerted movement of anions and cations, leading to a value of D_{cation}/D_{anion} closer to 1. To untangle the effects of the cation size from hydrogen bonding, we have plotted the ratios for both hydroxyl-functionalized and nonfunctionalized ILs in Figure 3b. The data shown here suggest that there is a stronger effect on the anion−cation correlation observed for short chain lengths than for long chain lengths. This could quite possibly be related to a shifting equilibrium between (ca) and (cc) HBs with increasing chain length: the competition due to the increasing importance of (cc) HBs with increasing chain length would thus have a weakening effect on the enhanced anion−cation interaction due to (ca) HBs. To study these HB-based effects in detail, we study both the equilibrium and kinetics of (cc) and (ca) HBs in the remainder of this paper.

https://dx.doi.org/10.1021/acs.jpcb.0c09278
J. Phys. Chem. B 2021, 125, 281−286

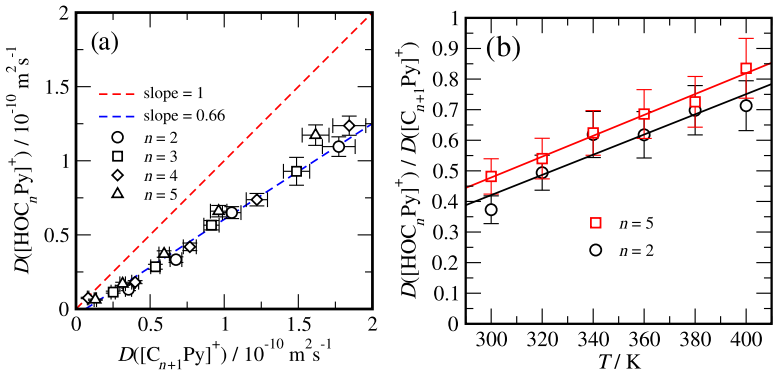

Figure 2. (a) Self-diffusion coefficients of the hydroxyl-functionalized ILs $[HOC_nPy][NTf_2]$ with $n = 2-5$ plotted versus the diffusivities of their nonfunctionalized counterparts $[C_{n+1}Py][NTf_2]$. Diffusion coefficients shown were obtained for temperatures between 300 and 400 K. On average, the diffusivities of the hydroxyl-functionalized ILs are reduced by about one-third. (b) Temperature and chain length dependence of the retardation effect observed for hydroxyl-functionalized ILs: A temperature decrease leads to a more pronounced retardation effect, whereas a chain length increase leads to an apparent reduction of the effect.

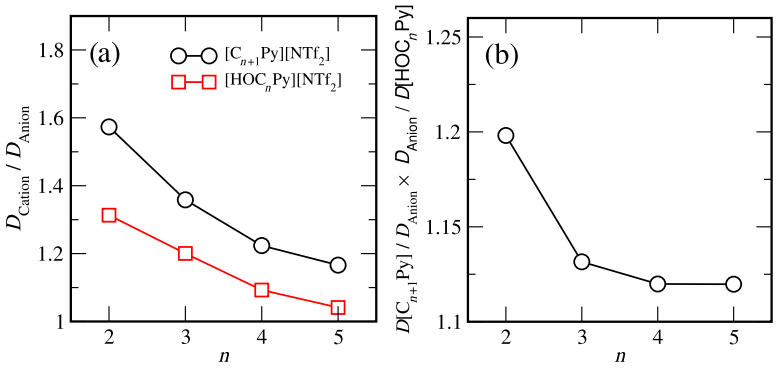

Figure 3. (a) Ratio of the self-diffusion coefficients of cations and anions of the hydroxyl-functionalized ILs $[HOC_nPy][NTf_2]$ and their nonfunctionalized counterparts $[C_{n+1}Py][NTf_2]$ with $n = 2-5$ at a temperature of 300 K. (b) Ratio of $[HOC_nPy][NTf_2]$ and $[C_{n+1}Py][NTf_2]$ data shown in (a).

Whether a pair of ions is hydrogen-bonded or not is decided solely by geometric criteria, extracted from pair correlation functions and probability density plots shown in Figure 4 and in the Supporting Information. Figure 4 shows a maximum in the probability density function at short intermolecular O−H distances r_{oh} and a linear HB angle α at $\cos(\alpha) = -1$ for the (cc) HB. As the intermolecular distance between the hydrogen and oxygen increases, the angle of the HB becomes more bent. To define the HB, we chose an angle cutoff of $\cos(\alpha) \leq -0.5$ ($\alpha \geq 120°$) and a distance cutoff of $r_c = 2.7$ Å for the (cc) HB and $r_c = 2.8$ Å for the (ca) HB.

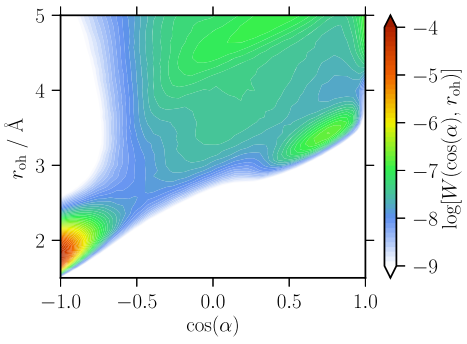

Figure 4. Logarithmic representation of the probability density W of finding an intermolecular O−H distance r_{oh} and the cosine of the angle α between the intermolecular H−O vector and the intramolecular O−H vector for the (cc) HB obtained at 300 K for $[HOC_2Py][NTf_2]$. Note that the probability density is weighted with r^{-2}. The (cc) HB for all considered ionic liquids can be characterized by a distance cutoff of $r_c = 2.7$ Å and an angular cutoff at $\cos(\alpha_c) = -0.5$. For the (ca) HB, the same angular cutoff was used with a distance cutoff of $r_c = 2.8$ Å.

Defining the different HBs in our system enables us to assess the amount of cations forming (cc) and (ca) HBs. Our simulations show that more cations form HBs to anions than to other cations for all of the investigated chain lengths at 300 K. An increase in the chain length leads to an increase in (cc) hydrogen bonding from around 5% for the $[HOC_2Py]^+$ cation to around 22% for the $[HOC_5Py]^+$ cation. Conversely, the amount of (ca) hydrogen-bonded cations decreases from 89% for the $[HOC_2Py]^+$ cation to 68% for the $[HOC_5Py]^+$ cation. Cations that form HBs neither with anions nor with another cation at the time of observation are considered "free", although their hydroxyl group might interact with other parts of the ions such as trifluoromethyl groups. With an increasing hydroxyalkyl chain length, the average distance between the aromatic rings (which bear most of the positive charge) of two hydrogen-bonded cations increases, thus stabilizing (cc) hydrogen-bonded configurations by reducing the Coulombic repulsion between the two cations. This shifts the HB

https://dx.doi.org/10.1021/acs.jpcb.0c09278
J. Phys. Chem. B 2021, 125, 281−286

equilibrium of cations with longer hydroxyalkyl chains toward more (cc) HBs. At the same time, however, the addition of one or multiple CH_2 groups decreases the density of possible HB acceptors, i.e., the oxygen atoms on both cations and anions. This reduces the probability of the hydroxyl group to find a suitable acceptor for an HB and increases the amount of "free" hydroxyl groups. Both effects lead to a decreasing amount of (ca) HBs in the systems with longer alkyl chains. For $[HOC_5Py][NTf_2]$, the amount of (ca) HBs exceeds the amount of (cc) HBs by about a factor of 3. Since each anion could provide up to eight possible HB acceptors (keep in mind that each sulfonyl group could accept up to four HBs) compared to one single hydroxyl group per cation, a ratio of 1:3 clearly suggests that (cc) HBs are significantly stronger than their (ca) counterparts in the case of $[HOC_5Py][NTf_2]$.

To study the detailed HB kinetics, we compute the intermolecular HB population function $h(t)$ for all possible donor−acceptor pairs in our system as a function of time. Here, we consider the hydroxyl group of the cation as the donor in all cases, whereas the acceptor can either be a hydroxyl group of another cation in the case of the (cc) HB or one oxygen atom of the $[NTf_2]^-$ anion for the (ca) HB. If an HB exists according to our criteria at time t between the donor−acceptor pair $h(t) = 1$. Conversely, if there is no HB, $h(t) = 0$. The HB population correlation function $C(t)$ describes the fluctuations in the HB population.

$$C(t) = [\langle h(0)h(t)\rangle - \langle h\rangle^2]/[\langle h\rangle(1 - \langle h\rangle)] \quad (1)$$

where $h(t) = h^2(t)$ and thus $\langle h\rangle = \langle h^2\rangle$. We would like to point out that the often used approximation $1 - \langle h\rangle \approx 1$ leads to a misrepresentation of $C(t)$ at long times here. $C(t)$ is related to the reactive flux correlation function $k(t)$ via $k(t) = -\mathrm{d}C(t)/\mathrm{d}t = -\langle \dot{h}(0)[1 - h(t)]\rangle/[\langle h\rangle(1 - \langle h\rangle)]$. The brackets indicate averaging over all times "0" as well as over all possible HB donor−acceptor pairs of the same HB species. The correlation function $C(t)$ can be regarded as the fraction of HBs that are intact after time t provided an HB existed at $t_0 = 0$. But the HB does not necessarily need to be intact during the entire time interval $t - t_0$.

We calculated these correlation functions for all simulated ionic liquids for times t ranging from 1 ps to 100 ns. As shown in Figure 5, the correlation functions for both (ca) and (cc) HB populations need a relatively long time to decay fully. In Figure 5, clearly, two time domains can be observed. It is likely that these time domains are correlated with the rotational and translational motion of the cation: For sufficiently short times, the solvation shell of anions around a cation stays mostly intact, such that HB breaking and reformation are solely associated with the reorientation of the cation. On a longer timescale, anions in the solvation shell of a cation are being replaced, such that the HB reformation process requires translatoric diffusion. We would like to point out that although the correlation function has dropped to a plateau value of only a few percent, the long-time tail still contributes to the HB lifetime to a roughly equal amount due to its extremely slow decaying nature. We compute the lifetime of a respective HB species as the time integral over the HB population correlation function of this species according to

$$\tau_{hb} = \int_0^\infty C(t)\mathrm{d}t \quad (2)$$

To calculate the HB lifetime, we fitted the HB population correlation function to a sum of two stretched exponential

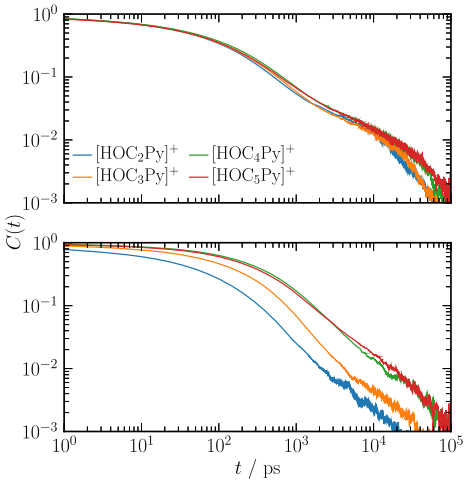

Figure 5. Normalized HB population correlation function $C(t)$ for (ca) (top) and (cc) (bottom) HBs in $[HOC_nPy][NTf_2]$ at $T = 300$ K.

functions, representing the short- and long-time decay (details are given in the SI). It is evident that the (ca) HB population correlation functions show a rather little variation with respect to the changing alkyl chain length. This is particularly true for the short-time part of the correlation function. The computed change of the lifetimes is therefore largely attributed to the long-time behavior and is quite possibly related to the changing diffusion coefficients. In fact, the observed change in the lifetimes roughly corresponds to the relative change in the diffusivities. A quite different scenario, however, is observed for the (cc) HB population correlation functions, which show a strong variation with the chain length, each extending over the entire observed time range. Moreover, the presence of two distinguishable time domains, as determined for the (ca) HBs, seems to be largely absent. While for short chains ($n \leq 3$), the computed (cc) HB lifetimes are found to be significantly shorter than the (ca) HB lifetimes, and the opposite is true for longer chains (see Figure 6). Comparing n

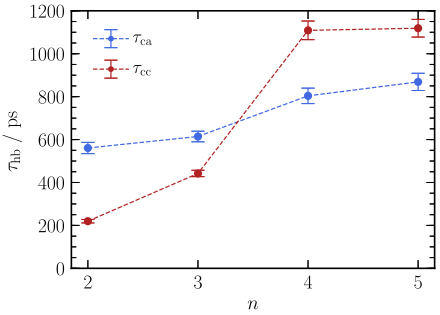

Figure 6. HB lifetimes τ_{hb} for (ca) (blue) and (cc) (red) HBs as a function of the hydroxyalkyl chain length n at 300 K. For short chains ($n = 2, 3$), the (ca) HB lifetime is greater than the (cc) HB lifetime. Conversely, for longer chains ($n = 4, 5$), the (cc) HB is more stable.

= 2 and 5 leads to a change in (cc) HB lifetimes by a factor of about 5, thus suggesting strongly enhanced (cc) HBs. To summarize, we find that not only does the equilibrium shift toward (cc) HBs with increasing chain length. Also, the lifetimes of these HBs increase significantly. Moreover, due to the increasing competition from hydrogen-bonded (cc) interactions, non-hydrogen-bonded anions could be "released",

https://dx.doi.org/10.1021/acs.jpcb.0c09278
J. Phys. Chem. B 2021, 125, 281−286

thus allowing for an enhanced mobility of the ions in the respective IL.

CONCLUSIONS

In summary, IR spectra of hydroxyl-functionalized ILs with varying alkyl chain lengths show two vibrational bands in the OH stretching region that are assigned to hydroxyl groups involved in either (ca) or (cc) hydrogen bonding. The IR experiments suggest that (cc) HBs are even stronger than (ca) HBs as indicated by a significant red shift of their corresponding IR bands. Using MD simulations, we could identify the presence of both types of HBs. In addition, we could also detect their shifting equilibrium as well as their changing lifetimes.

We could show that the lifetime correlation functions are different for (ca) and (cc) HBs. Whereas the (ca) HB lifetimes vary only a little, the (cc) HB lifetimes significantly increase with the alkyl chain length, reflecting enhanced (cc) cluster formation and strengthening of (cc) HBs. The (ca) HBs clearly exhibit two time domains, which are quite possibly related to different types of motion, such as the reorientational and translational dynamics of the cation. The increasing competition of (cc) hydrogen bonding with (ca) HB interactions with increasing chain length is accompanied by decorrelation of the individual anion and cation mobilities and has thus a significant effect on the diffusivities of ILs, which could be experimentally tested.

ASSOCIATED CONTENT

Supporting Information

The Supporting Information is available free of charge at https://pubs.acs.org/doi/10.1021/acs.jpcb.0c09278.

Force fields and computational details (hydrogen-bonding criteria; mean square displacement and diffusion; and hydrogen-bonding lifetime) (PDF)

AUTHOR INFORMATION

Corresponding Author

Ralf Ludwig − *Institut für Chemie, Abteilung Physikalische und Theoretische Chemie and Department Life, Light & Matter, Universität Rostock, D-18059 Rostock, Germany; Leibniz Institut für Katalyse an der Universität Rostock, D-18059 Rostock, Germany;* orcid.org/0000-0002-8549-071X; Email: ralf.ludwig@uni-rostock.de

Authors

Jan Neumann − *Institut für Chemie, Abteilung Physikalische und Theoretische Chemie, Universität Rostock, D-18059 Rostock, Germany*

Dietmar Paschek − *Institut für Chemie, Abteilung Physikalische und Theoretische Chemie, Universität Rostock, D-18059 Rostock, Germany;* orcid.org/0000-0002-0342-324X

Anne Strate − *Institut für Chemie, Abteilung Physikalische und Theoretische Chemie and Department Life, Light & Matter, Universität Rostock, D-18059 Rostock, Germany*

Complete contact information is available at: https://pubs.acs.org/10.1021/acs.jpcb.0c09278

Notes

The authors declare no competing financial interest.

ACKNOWLEDGMENTS

The authors thank the computer center of the University of Rostock (ITMZ) for providing computational resources on their Haumea and Titan HPC clusters. They also thank the Leibniz Association, the State of Mecklenburg-Vorpommern, and the University of Rostock for financial support within the ComBioCat programme. This work has been supported by the DFG Research Grant LU-506/14-2 (No. 286149019).

REFERENCES

(1) Kumar, R.; Schmidt, J.; Skinner, J. Hydrogen bonding definitions and dynamics in liquid water. *J. Chem. Phys.* **2007**, *126*, No. 204107.

(2) Luzar, A.; Chandler, D. Effect of environment on hydrogen bond dynamics in liquid water. *Phys. Rev. Lett.* **1996**, *76*, 928−931.

(3) Luzar, A.; Chandler, D. Hydrogen-bond kinetics in liquid water. *Nature* **1996**, *379*, 55−57.

(4) Strate, A.; Neumann, J.; Overbeck, V.; Bonsa, A.-M.; Michalik, D.; Paschek, D.; Ludwig, R. Rotational and translational dynamics and their relation to hydrogen bond lifetimes in an ionic liquid by means of NMR relaxation time experiments and molecular dynamics simulation. *J. Chem. Phys.* **2018**, *148*, No. 193843.

(5) Gehrke, S.; von Domaros, M.; Clark, R.; Hollóczki, O.; Brehm, M.; Welton, T.; Luzar, A.; Kirchner, B. Structure and lifetimes in ionic liquids and their mixtures. *Faraday Discuss.* **2017**, *206*, 219−245.

(6) Gehrke, S.; Kirchner, B. Robustness of the hydrogen bond and ion pair dynamics in ionic liquids to different parameters from the reactive flux method. *J. Chem. Eng. Data* **2019**, *65*, 1146−1158.

(7) Katsyuba, S. A.; Vener, M. V.; Zvereva, E. E.; Fei, Z.; Scopelliti, R.; Laurenczy, G.; Yan, N.; Paunescu, E.; Dyson, P. J. How strong is hydrogen bonding in ionic liquids? Combined X-ray crystallographic, infrared/Raman spectroscopic, and density functional theory study. *J. Phys. Chem. B* **2013**, *117*, 9094−9105.

(8) Fakhraee, M.; Zandkarimi, B.; Salari, H.; Gholami, M. R. Hydroxyl-functionalized 1-(2-hydroxyethyl)-3-methyl imidazolium ionic liquids: thermodynamic and structural properties using molecular dynamics simulations and ab initio calculations. *J. Phys. Chem. B* **2014**, *118*, 14410−14428.

(9) Panja, S. K.; Haddad, B.; Kiefer, J. Clusters of the Ionic Liquid 1-Hydroxyethyl-3-methylimidazolium Picrate: From Theoretical Prediction in the Gas Phase to Experimental Evidence in the Solid State. *ChemPhysChem* **2018**, *19*, 3061−3068.

(10) Knorr, A.; Ludwig, R. Cation-cation clusters in ionic liquids: Cooperative hydrogen bonding overcomes like-charge repulsion. *Sci. Rep.* **2015**, *5*, 1−7.

(11) Knorr, A.; Fumino, K.; Bonsa, A.-M.; Ludwig, R. Spectroscopic evidence of 'jumping and pecking' of cholinium and H−bond enhanced cation-cation interaction in ionic liquids. *Phys. Chem. Chem. Phys.* **2015**, *17*, 30978−30982.

(12) Knorr, A.; Stange, P.; Fumino, K.; Weinhold, F.; Ludwig, R. Spectroscopic Evidence for Clusters of Like-Charged Ions in Ionic Liquids Stabilized by Cooperative Hydrogen Bonding. *ChemPhysChem* **2016**, *17*, 458−462.

(13) Strate, A.; Niemann, T.; Michalik, D.; Ludwig, R. When like charged ions attract in ionic liquids: Controlling the formation of cationic clusters by the interaction strength of the counterions. *Angew. Chem., Int. Ed.* **2017**, *56*, 496−500.

(14) Strate, A.; Niemann, T.; Ludwig, R. Controlling the kinetic and thermodynamic stability of cationic clusters by the addition of molecules or counterions. *Phys. Chem. Chem. Phys.* **2017**, *19*, 18854−18862.

(15) Niemann, T.; Zaitsau, D.; Strate, A.; Villinger, A.; Ludwig, R. Cationic clustering influences the phase behaviour of ionic liquids. *Sci. Rep.* **2018**, *8*, 1−7.

(16) Menges, F. S.; Zeng, H. J.; Kelleher, P. J.; Gorlova, O.; Johnson, M. A.; Niemann, T.; Strate, A.; Ludwig, R. Structural Motifs in Cold Ternary Ion Complexes of Hydroxyl-Functionalized Ionic Liquids: Isolating the Role of Cation−Cation Interactions. *J. Phys. Chem. Lett.* **2018**, *9*, 2979−2984.

(17) Niemann, T.; Strate, A.; Ludwig, R.; Zeng, H. J.; Menges, F. S.; Johnson, M. A. Spectroscopic Evidence for an Attractive Cation−Cation Interaction in Hydroxy-Functionalized Ionic Liquids: A Hydrogen-Bonded Chain-like Trimer. *Angew. Chem., Int. Ed.* **2018**, *57*, 15364−15368.
(18) Strate, A.; Overbeck, V.; Lehde, V.; Neumann, J.; Bonsa, A.-M.; Niemann, T.; Paschek, D.; Michalik, D.; Ludwig, R. The influence of like-charge attraction on the structure and dynamics of ionic liquids: NMR chemical shifts, quadrupole coupling constants, rotational correlation times and failure of Stokes−Einstein−Debye. *Phys. Chem. Chem. Phys.* **2018**, *20*, 5617−5625.
(19) Niemann, T.; Strate, A.; Ludwig, R.; Zeng, H. J.; Menges, F. S.; Johnson, M. A. Cooperatively enhanced hydrogen bonds in ionic liquids: closing the loop with molecular mimics of hydroxy-functionalized cations. *Phys. Chem. Chem. Phys.* **2019**, *21*, 18092−18098.
(20) Niemann, T.; Zaitsau, D. H.; Strate, A.; Stange, P.; Ludwig, R. Controlling "like−likes−like" charge attraction in hydroxy-functionalized ionic liquids by polarizability of the cations, interaction strength of the anions and varying alkyl chain length. *Phys. Chem. Chem. Phys.* **2020**, *22*, 2763−2774.
(21) Páll, S.; Abraham, M. J.; Kutzner, C.; Hess, B.; Lindahl, E. In *Solving Software Challenges for Exascale*, Proceedings of the International Conference on Exascale Applications and Software, Stockholm, Sweden, April 2−3, 2014; Markidis, S.; Laure, E., Eds.; Springer: Cham, 2015.
(22) Pronk, S.; Páll, S.; Schulz, R.; Larsson, P.; Bjelkmar, P.; Apostolov, R.; Shirts, M. R.; Smith, J. C.; Kasson, P. M.; van der Spoel, D.; et al. GROMACS 4.5: a high-throughput and highly parallel open source molecular simulation toolkit. *Bioinformatics* **2013**, *29*, 845−854.
(23) Hess, B.; Kutzner, C.; Van Der Spoel, D.; Lindahl, E. GROMACS 4: algorithms for highly efficient, load-balanced, and scalable molecular simulation. *J. Chem. Theory Comput.* **2008**, *4*, 435−447.
(24) Van Der Spoel, D.; Lindahl, E.; Hess, B.; Groenhof, G.; Mark, A. E.; Berendsen, H. J. GROMACS: fast, flexible, and free. *J. Comput. Chem.* **2005**, *26*, 1701−1718.
(25) Berendsen, H. J.; van der Spoel, D.; van Drunen, R. GROMACS: a message-passing parallel molecular dynamics implementation. *Comput. Phys. Commun.* **1995**, *91*, 43−56.
(26) Köddermann, T.; Paschek, D.; Ludwig, R. Molecular dynamic simulations of ionic liquids: A reliable description of structure, thermodynamics and dynamics. *ChemPhysChem* **2007**, *8*, 2464−2470.
(27) Neumann, J.; Golub, B.; Odebrecht, L.-M.; Ludwig, R.; Paschek, D. Revisiting imidazolium based ionic liquids: Effect of the conformation bias of the [ntf2] anion studied by molecular dynamics simulations. *J. Chem. Phys.* **2018**, *148*, No. 193828.
(28) Jorgensen, W. L.; McDonald, N. A. Development of an all-atom force field for heterocycles. Properties of liquid pyridine and diazenes. *J. Mol. Struct.: THEOCHEM* **1998**, *424*, 145−155.

https://dx.doi.org/10.1021/acs.jpcb.0c09278
J. Phys. Chem. B 2021, 125, 281−286

Kinetics of Hydrogen Bonding between Ions of Opposite and Ions of Like Charge in Hydroxy-Functionalized Ionic Liquids

Jan Neumann[†], Dietmar Paschek[†], Anne Strate[†,‡], Ralf Ludwig[†,‡,¶]

† *Institut für Chemie, Abteilung Physikalische und Theoretische Chemie, Universität Rostock, Dr.-Lorenz-Weg 2, D-18059 Rostock, Germany*
‡ *Department Life, Light & Matter, Universität Rostock, Albert-Einstein-Straße 25, D-18059 Rostock, Germany*
¶ *Leibniz Institut für Katalyse an der Universität Rostock, Albert-Einstein-Straße 29a, D-18059 Rostock, Germany*

E-mail: ralf.ludwig@uni-rostock.de

1 Forcefields

The force-field of the $[NTf_2]^-$ anion has been published in reference [1]. The force fields for the pyridinium cations were derived from the OPLS firce field for pyridine from Jorgensen et al.[2, 3] The point charges were derived from the electrostatic potential around the all-trans conformation of the respective cation according to the CHelpG scheme.[4] The dihedral potential of the hydroxyalkyl chains were calculated employing second order Møller-Plesset perturbation theory using the cc-pvtz basis set using Gaussian 09.[5] Energy profiles $V^{\mathrm{QM}}_{\kappa\lambda\omega\tau}(\psi)$ of a given dihedral between the atoms κ, λ, ω and τ were obtained by rotating each dihedral individually in steps of 10° to a total of 360° starting from the all-trans conformation. The non-bonded interaction energy of every conformation $V^{\mathrm{nb}}_{\kappa\lambda\omega\tau}(\psi)$ was calculated following the same procedure using MOSCITO.[6] The dihedral potential for a given dihedral was then calculated as $V^{\mathrm{dp}}_{\kappa\lambda\omega\tau}(\psi) = V^{\mathrm{QM}}_{\kappa\lambda\omega\tau}(\psi) - V^{\mathrm{nb}}_{\kappa\lambda\omega\tau}(\psi)$ and fitted to

$$V^{\mathrm{dp}}_{\kappa\lambda\omega\tau}(\psi) = \sum_n k^{\mathrm{dp}}_m [1 + \cos(m_n \psi_m - \psi^0_m)]. \quad (1)$$

Table S1: Lennard-Jones parameters σ and ϵ for all interaction sites of the $[HOC_2Py]^+$, $[HOC_3Py]^+$, $[HOC_4Py]^+$ and $[HOC_5Py]^+$ cation.

site	σ / Å	$\epsilon \cdot k_B^{-1}$ / K
N	3.25	85.55
C_a	3.55	35.23
H_a	2.42	15.10
C_c	3.50	33.20
C_m	3.50	33.20
H_c	2.50	15.10
O	3.12	85.60
H_o	0.00	0.00

Table S2: Bond length $r^0_{\kappa\lambda}$ and angle parameters $\phi^0_{\kappa\lambda\omega}$ und $k^a_{\kappa\lambda\omega}$ for the angle potential $V^a_{\kappa\lambda\omega} = \frac{1}{2}k^a_{\kappa\lambda\omega}(\phi_{\kappa\lambda\omega} - \phi^0_{\kappa\lambda\omega})^2$ in the force field of the $[HOC_2Py]^+$, $[HOC_3Py]^+$, $[HOC_4Py]^+$ and $[HOC_5Py]^+$ cation.

bond	$r^0_{\kappa\lambda}$ / Å	angle	$\phi^0_{\kappa\lambda\omega}$ / °	$k^a_{\kappa\lambda\omega}$ / kJ mol^{-1}rad^{-2}
C_a-N	1.339	C_a-C_a-C_a	120.0	527.20
C_a-H_a	1.080	C_a-C_a-N	124.0	585.80
C_a-C_a	1.400	C_a-N-C_a	117.0	585.80
N-C_c	1.339	C_a-C_a-H_a	120.0	292.90
C_c-C_c	1.529	N-C_a-H_a	116.0	292.90
C_c-H_c	1.090	C_a-N-C_c	121.5	585.80
C_c-O	1.410	N-C_c-C_c	112.7	487.43
O-H_o	0.945	H_c-C_c-N	110.7	313.26
C_c-C_m	1.529	H_c-C_c-H_c	107.8	275.70
		H_c-C_c-C_c	110.7	313.26
		C_c-C_c-C_c	112.7	487.43
		C_c-C_c-C_m	112.7	487.43
		H_c-C_c-C_m	110.7	313.26
		H_c-C_m-C_c	110.7	313.26
		H_c-C_m-H_c	107.8	275.70
		H_o-O-C_m	108.5	460.55
		C_c-C_m-O	109.5	418.68
		H_c-C_m-O	109.5	293.08

Table S3: Parameters m_n, k_m^{dp} and ψ_m^0 for the improper dihedral potential $V_{\kappa\lambda\omega\tau}^{\mathrm{dp}} = \sum_n k_m^{\mathrm{dp}}[1 + \cos(m_n\psi_m - \psi_m^0)]$ in the force field of the $[HOC_2Py]^+$, $[HOC_3Py]^+$, $[HOC_4Py]^+$ and $[HOC_5Py]^+$ cation. The central atom is the first in the list.

	m_n	k_m^{dp} / kJ mol^{-1}	ψ_m^0 / $^\circ$
N-C_a-C_a-C_c	2	4.6060	180.0
C_a-N-C_a-H_a	2	4.6060	180.0
C_a-C_a-C_a-H_a	2	4.6060	180.0

Table S4: Parameters m_n, k_m^{dp} and ψ_m^0 for the torsion potential $V_{\kappa\lambda\omega\tau}^{\mathrm{dp}} = \sum_n k_m^{\mathrm{dp}}[1 + \cos(m_n\psi_m - \psi_m^0)]$ in the force field of the $[HOC_2Py]^+$ cation.

	$n(\kappa\lambda\omega\tau)$	m_n	k_m^{dp} / kJ mol^{-1}	ψ_m^0 / $^\circ$
X-C_a-C_a-X	1	2	15.1780	180.0
X-C_a-N-X	1	2	15.1780	180.0
C_a-N-C_c-C_c	1	2	0.0802	0
	2	4	-0.4693	0
N-C_c-C_c-O	1	1	-0.7375	0.0
	2	2	1.8576	0.0
	3	3	7.2898	0.0
C_c-C_c-O-H_o	1	1	-5.8097	0.0
	2	2	1.8939	0.0
	3	3	2.5150	0.0

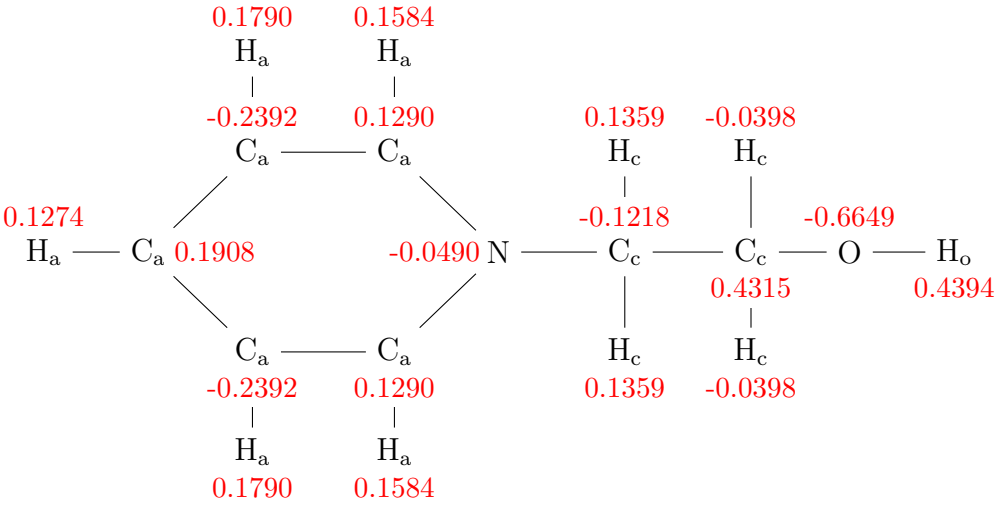

Figure S1: Structure of the $[HOC_2Py]^+$ cation with atom types and corresponding point charges q/e in red.

Table S5: Parameters m_n, k_m^{dp} and ψ_m^0 for the torsion potential $V_{\kappa\lambda\omega\tau}^{\mathrm{dp}} = \sum_n k_m^{\mathrm{dp}}[1 + \cos(m_n\psi_m - \psi_m^0)]$ in the force field of the $[HOC_3Py]^+$ cation.

	$n(\kappa\lambda\omega\tau)$	m_n	k_m^{dp} / kJ mol^{-1}	ψ_m^0 / $^\circ$
X-C_a-C_a-X	1	2	15.1780	180.0
X-C_a-N-X	1	2	15.1780	180.0
C_a-N-C_c-C_c	1	2	-0.7379	0
	2	4	-0.2237	0
N-C_c-C_c-C_c	1	1	-3.0206	0.0
	2	2	0.6685	0.0
	3	3	5.1206	0.0
	4	4	0.4708	0.0
C_c-C_c-C_c-O	1	1	4.1980	0.0
	2	3	5.2448	0.0
	3	4	1.0859	0.0
C_c-C_c-O-H_o	1	1	-1.8926	0.0
	2	2	1.0349	0.0
	3	3	2.5840	0.0
	4	4	0.0316	0.0

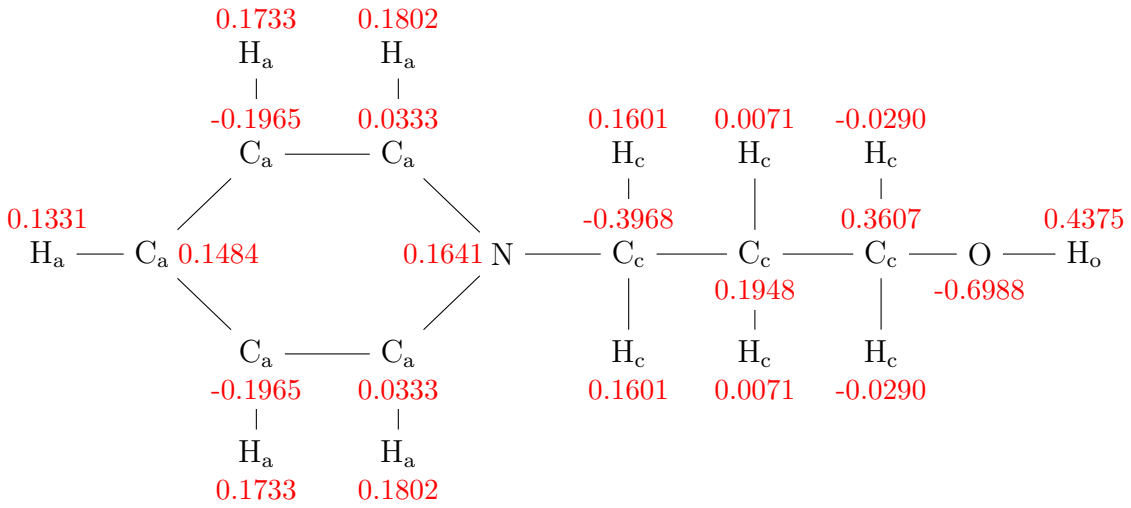

Figure S2: Structure of the $[HOC_3Py]^+$ cation with atom types and corresponding point charges q/e in red.

Table S6: Parameters m_n, k_m^{dp} and ψ_m^0 for the torsion potential $V_{\kappa\lambda\omega\tau}^{\mathrm{dp}} = \sum_n k_m^{\mathrm{dp}}[1 + \cos(m_n\psi_m - \psi_m^0)]$ in the force field of the $[HOC_4Py]^+$ cation.

	$n(\kappa\lambda\omega\tau)$	m_n	k_m^{dp} / kJ mol^{-1}	ψ_m^0 / $^\circ$
X-C_a-C_a-X	1	2	15.1780	180.0
X-C_a-N-X	1	2	15.1780	180.0
C_a-N-C_c-C_c	1	2	-0.3579	0
C_a-N-C_c-C_c	2	4	-0.4037	0
C_c-C_c-C_c-C_c	1	1	-0.2825	0.0
	2	2	0.6065	0.0
	3	3	4.6858	0.0
	4	4	0.7018	0.0
	5	5	0.4468	0.0
	6	6	0.4564	0.0
C_c-C_c-C_c-O	1	1	-2.3748	0.0
	2	3	6.8089	0.0
	3	4	0.9531	0.0
C_c-C_c-O-H_o	1	1	-3.5552	0.0
	2	2	0.5886	0.0
	3	3	2.5272	0.0
	4	4	0.1504	0.0

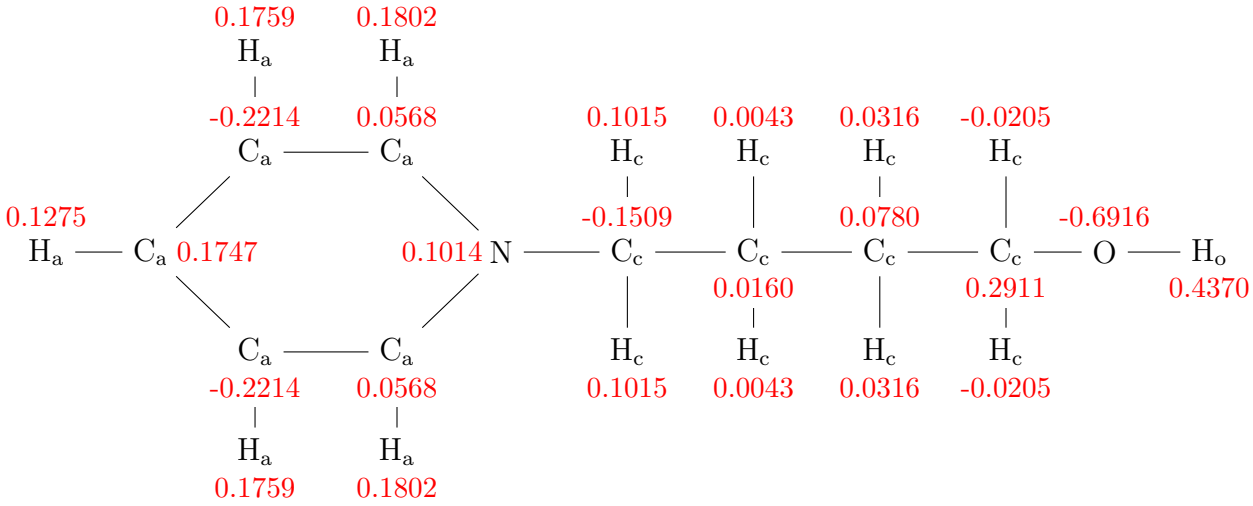

Figure S3: Structure of the $[HOC_4Py]^+$ cation with atom types and corresponding point charges in red.

Table S7: Parameters m_n, k_m^{dp} and ψ_m^0 for the torsion potential $V_{\kappa\lambda\omega\tau}^{\mathrm{dp}} = \sum_n k_m^{\mathrm{dp}}[1 + \cos(m_n\psi_m - \psi_m^0)]$ in the force field of the $[\mathrm{HOC_5Py}]^+$ cation.

	$n(\kappa\lambda\omega\tau)$	m_n	k_m^{dp} / kJ mol^{-1}	ψ_m^0 / $^\circ$
X-C_a-C_a-X	1	2	15.1780	180.0
X-C_a-N-X	1	2	15.1780	180.0
C_a-N-C_c-C_c	1	2	-0.4663	0
C_a-N-C_c-C_c	2	4	-0.3648	0
C_c-C_c-C_c-C_c	1	1	-0.9736	0.0
	2	2	0.1905	0.0
	3	3	5.6022	0.0
	4	4	0.6932	0.0
	5	5	0.3076	0.0
	6	6	0.3493	0.0
C_c-C_c-C_c-C_m	1	1	2.2559	0.0
	2	2	0.5340	0.0
	3	3	4.9032	0.0
	4	4	0.6508	0.0
	5	5	0.3897	0.0
	6	6	0.4302	0.0
C_c-C_c-C_m-O	1	1	0.2341	0.0
	2	2	0.4898	0.0
	3	3	6.6545	0.0
	4	4	0.9830	0.0
C_c-C_c-O-H_o	1	1	-3.4972	0.0
	2	2	0.3471	0.0
	3	3	2.5003	0.0
	4	4	0.0941	0.0

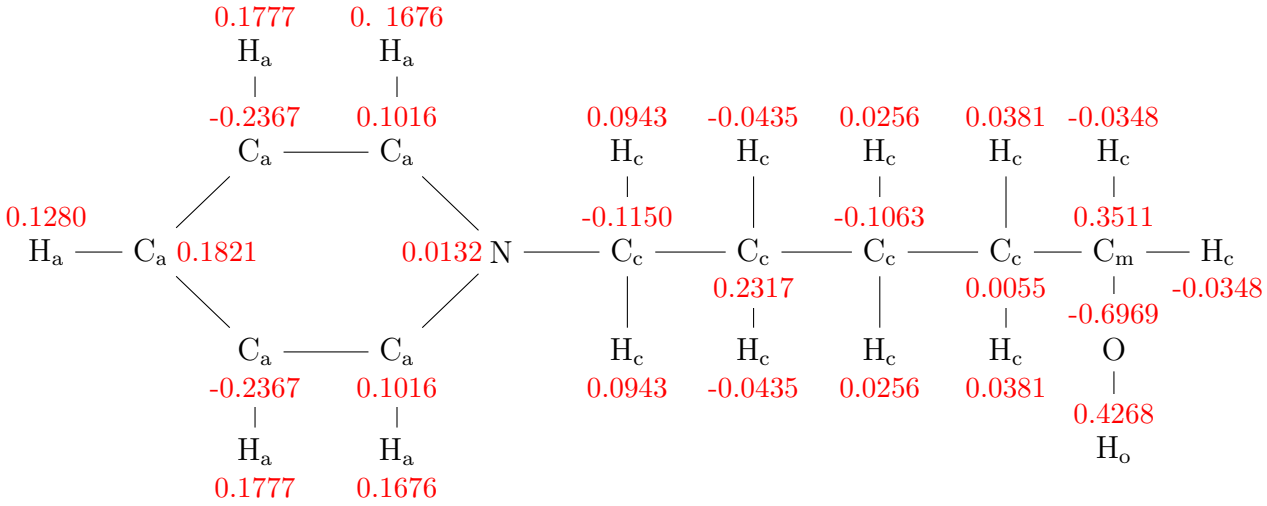

Figure S4: Structure of the $[HOC_5Py]^+$ cation with atom types and corresponding point charges in red.

Table S8: Parameters m_n, k_m^{dp} and ψ_m^0 for the torsion potential $V_{\kappa\lambda\omega\tau}^{\mathrm{dp}} = \sum_n k_m^{\mathrm{dp}}[1 + \cos(m_n\psi_m - \psi_m^0)]$ in the force field of the $[C_3Py]^+$ cation.

	$n(\kappa\lambda\omega\tau)$	m_n	k_m^{dp} / kJ mol^{-1}	ψ_m^0 / °
X-C_a-C_a-X	1	2	15.1780	180.0
X-C_a-N-X	1	2	15.1780	180.0
C_a-N-C_c-C_c	1	2	-0.4178	0
	2	4	-0.4138	0
N-C_c-C_c-C_m	1	1	-1.4934	0.0
	2	3	6.8503	0.0
C_c-C_c-C_m-H_m	1	3	1.8318	0.0

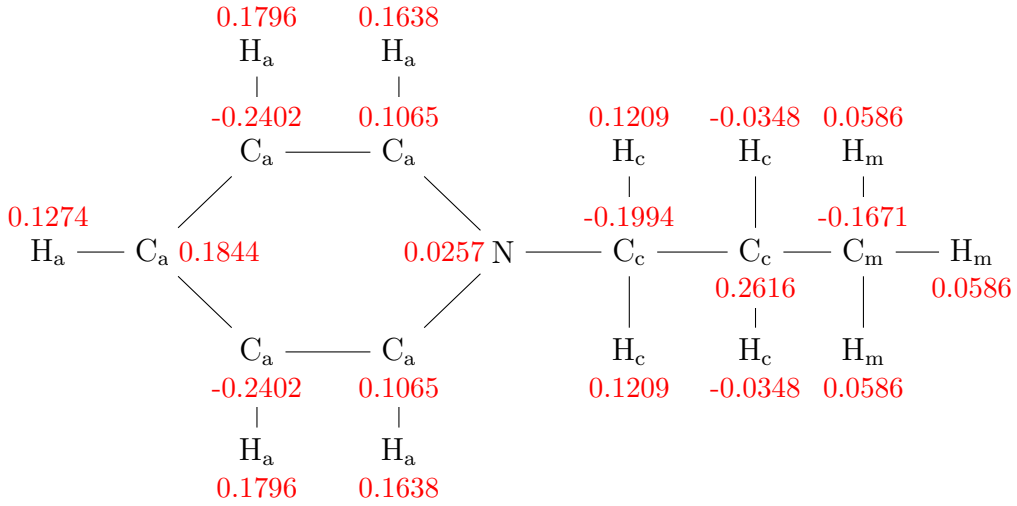

Figure S5: Structure of the $[C_3Py]^+$ cation with atom types and corresponding point charges q/e in red.

Table S9: Parameters m_n, k_m^{dp} and ψ_m^0 for the torsion potential $V_{\kappa\lambda\omega\tau}^{\mathrm{dp}} = \sum_n k_m^{\mathrm{dp}}[1 + \cos(m_n\psi_m - \psi_m^0)]$ in the force field of the $[C_4Py]^+$ cation.

	$n(\kappa\lambda\omega\tau)$	m_n	k_m^{dp} / kJ mol^{-1}	ψ_m^0 / °
X-C_a-C_a-X	1	2	15.1780	180.0
X-C_a-N-X	1	2	15.1780	180.0
C_a-N-C_c-C_c	1	2	-0.4052	0
	2	4	-0.4532	0
N-C_c-C_c-C_c	1	1	-2.9345	0.0
	2	3	6.6723	0.0
	3	4	0.3431	0.0
C_c-C_c-C_c-C_m	1	1	2.4114	0.0
	2	2	0.3899	0.0
	3	3	5.6540	0.0
	4	4	0.5565	0.0
	5	5	0.3099	0.0
C_c-C_c-C_m-H_m	1	3	1.8976	0.0

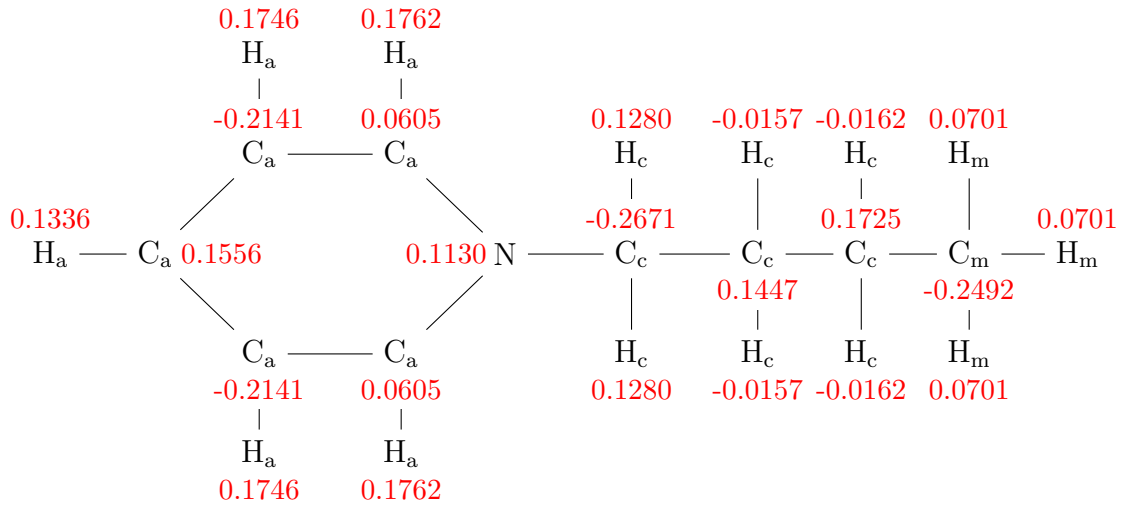

Figure S6: Structure of the $[C_4Py]^+$ cation with atom types and corresponding point charges q/e in red.

Table S10: Parameters m_n, k_m^{dp} and ψ_m^0 for the torsion potential $V_{\kappa\lambda\omega\tau}^{\mathrm{dp}} = \sum_n k_m^{\mathrm{dp}}[1 + \cos(m_n\psi_m - \psi_m^0)]$ in the force field of the $[C_5Py]^+$ cation.

	$n(\kappa\lambda\omega\tau)$	m_n	k_m^{dp} / kJ mol^{-1}	ψ_m^0 / °
X-C_a-C_a-X	1	2	15.1780	180.0
X-C_a-N-X	1	2	15.1780	180.0
C_a-N-C_c-C_c	1	2	-0.4172	0
	2	4	-0.4759	0
N-C_c-C_c-C_c	1	1	-2.9885	0.0
	2	3	6.7221	0.0
	3	4	0.3547	0.0
C_c-C_c-C_c-C_c	1	1	-0.4882	0.0
	2	2	0.2620	0.0
	3	3	5.3908	0.0
	4	4	0.6635	0.0
	5	5	0.3339	0.0
C_c-C_c-C_c-C_m	1	3	6.0396	0.0
	2	4	0.5463	0.0
C_c-C_c-C_m-H_m	1	3	1.8773	0.0

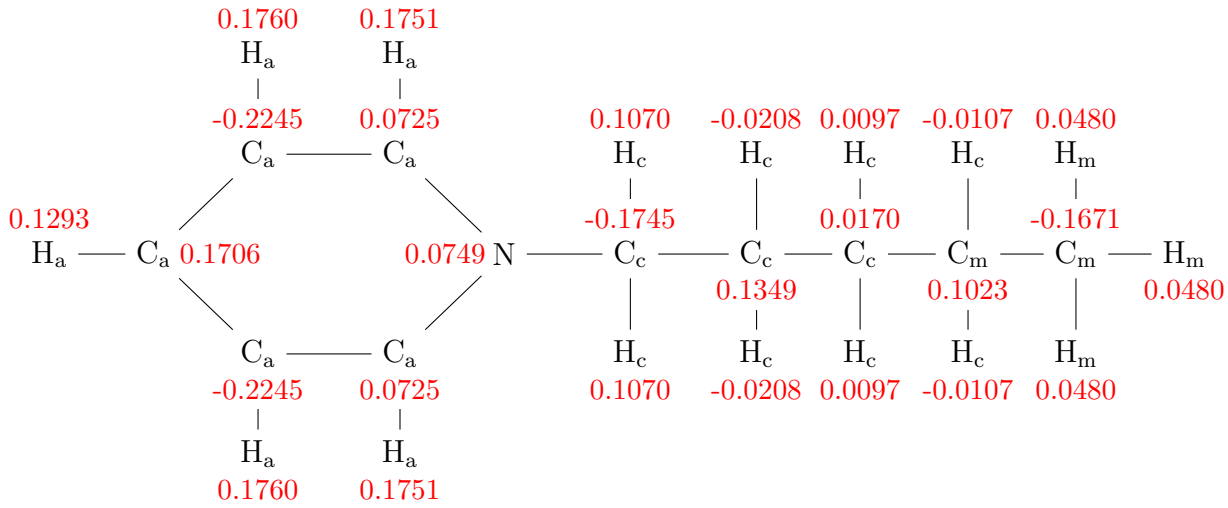

Figure S7: Structure of the $[C_5Py]^+$ cation with atom types and corresponding point charges q/e in red.

Table S11: Parameters m_n, k_m^{dp} and ψ_m^0 for the torsion potential $V_{\kappa\lambda\omega\tau}^{\mathrm{dp}} = \sum_n k_m^{\mathrm{dp}}[1 + \cos(m_n\psi_m - \psi_m^0)]$ in the force field of the $[C_6Py]^+$ cation.

	$n(\kappa\lambda\omega\tau)$	m_n	k_m^{dp} / kJ mol^{-1}	ψ_m^0 / °
X-C_a-C_a-X	1	2	15.1780	180.0
X-C_a-N-X	1	2	15.1780	180.0
C_a-N-C_c-C_c	1	2	-0.4571	0
	2	4	-0.4824	0
N-C_c-C_c-C_c	1	1	-2.6581	0.0
	2	3	6.6966	0.0
	3	4	0.3447	0.0
C_c-C_c-C_c-C_c	1	1	0.5700	0.0
	2	2	0.2527	0.0
	3	3	5.5338	0.0
	4	4	0.6355	0.0
	5	5	0.3093	0.0
C_c-C_c-C_c-C_m	1	1	0.7379	0.0
	2	2	0.2352	0.0
	3	3	5.9593	0.0
	4	4	0.5423	0.0
	5	5	0.2850	0.0
C_c-C_c-C_m-H_m	1	3	1.8773	0.0

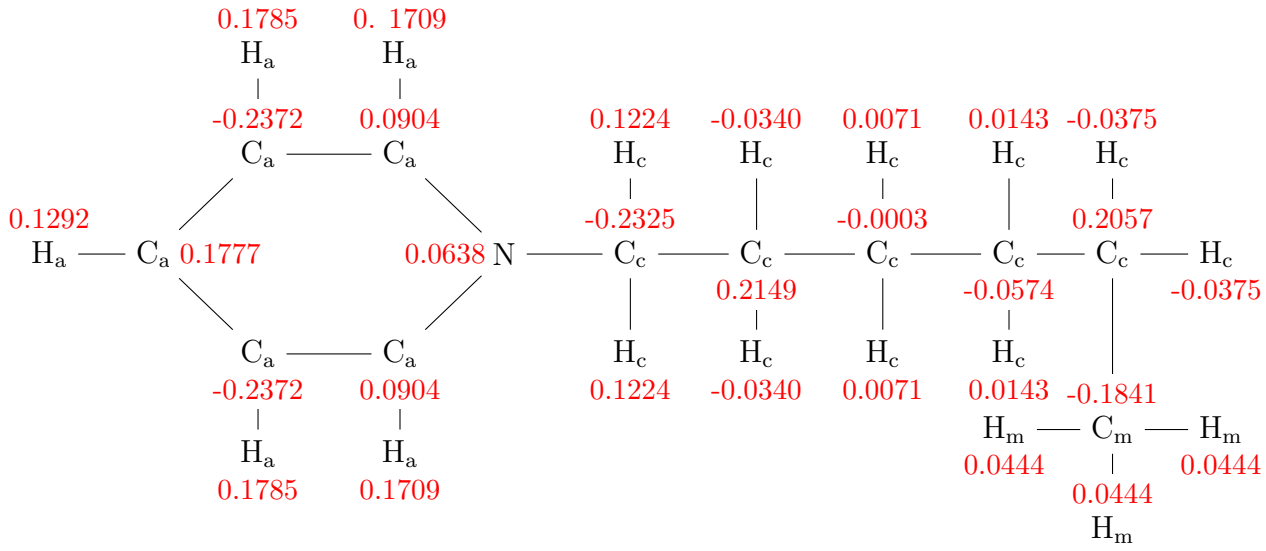

Figure S8: Structure of the $[C_6Py]^+$ cation with atom types and corresponding point charges in red.

2 Molecular Dynamics Simulation

The *NpT* molecular dynamics simulations on the $[HOC_nPy][NTf_2]$ ILs with n =2–5 were done using GROMACS 5.0.6 [7–11]. To build our simulation boxes of 512 ion pairs we arranged the ions on an interpenetrating primitiv cubic lattice and equilibrated the systems at 500 K for 2 ns employing the BERENDSEN thermostat and barostat [12] with coupling times of $\tau_T = \tau_p = 0.5$ ps. The systems were the equilibrated again for 2 ns at the desired temperature of 300 K.
After the equilibration, production runs of 100 ns were carried out, employing the NOSÉ-HOOVER thermostat [13, 14] and the PARRINELLO-RAHMAN barostat [15, 16] with coupling times of $\tau_T = 1$ ps and $\tau_p = 2$ ps respectively. All simulations were done with a 2.0 fs time step employing periodic boundary conditions and the LINCS algorithm [17] for fixed bond lengths. The smooth particle mesh EWALD summation [18] was applied in the liquid with a mesh spacing of 0.12 nm, a real space cutoff of 0.9 nm and 4th order interpolation. The relative accuracy of the EWALD sum was set to 10^{-5} corresponding to a convergence factor $\alpha = 3.38\,\mathrm{nm}^{-1}$.

3 Hydrogen Bond Criteria

Whether a pair of ions is hydrogen-bonded or not is decided by geometric criteria, extracted from pair correlation functions and probability density plots (Figure S9 and S10). Figure S10 shows a maximum in the probability density function at short intermolecular O-H distances and a linear HB angle α at $\cos(\alpha) = -1$ for the (cc) as well as the (ca)

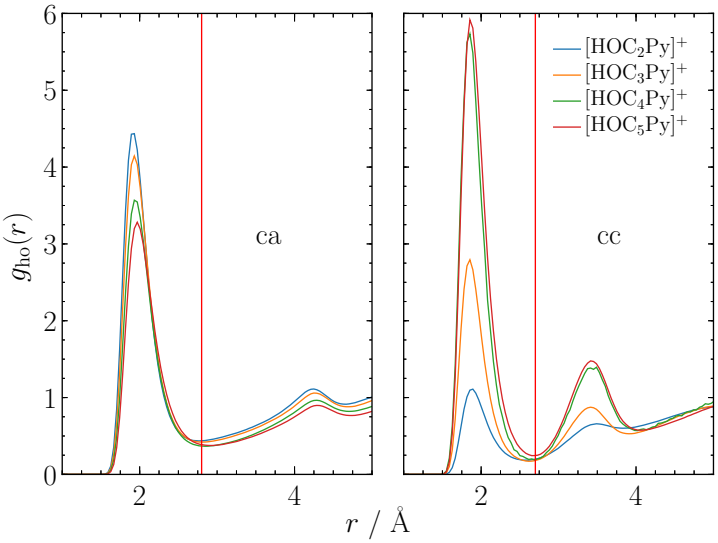

Figure S9: Pair correlation functions between the hydroxyl hydrogen of the cation and oxygen atoms on the anion (ca, left) and the cation (cc, right) for the different chain lengths obtained at 300 K. The distance cutoff used to define the HB is shown as a red horizontal line at 2.8 Å for the (ca) HB (left) and 2.7 Å for the (cc) HB (right) respectively.

HB. As the intermolecular distance between hydrogen and oxygen increases the angle of the HB becomes more bent. To define the HB we chose an angle cutoff of $\cos(\alpha) \leq -0.5$ ($\alpha \geq 120°$) and a distance cutoff of $r_c = 2.7$ Å for the (cc) HB and $r_c = 2.8$ Å for the (ca) HB respectively.
Figure S11 shows the average percentage of cations per timestep involved in hydrogen bonding with anions and other cations respectively. Cations not forming a HB are considered "free" and mostly interact with the flourine atoms on the anion or are transitioning between different kinds of interactions.

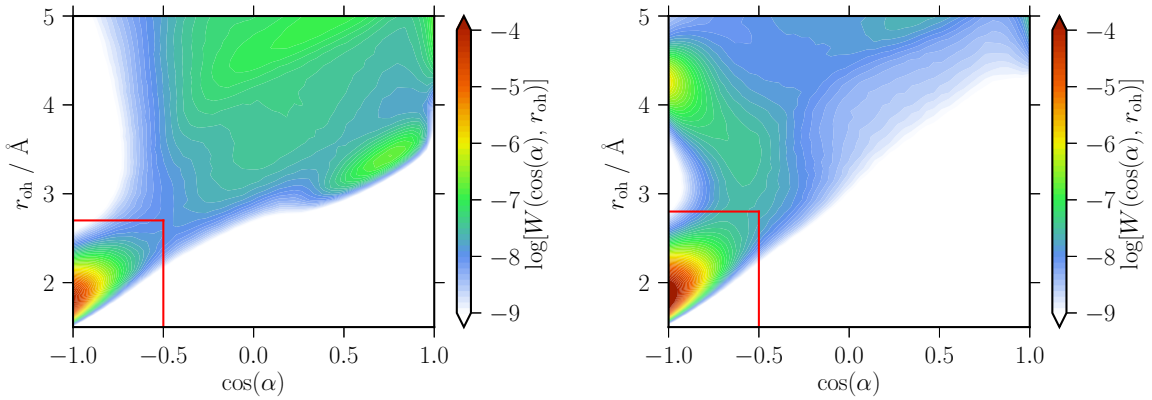

(a) $[HOC_2Py][NTf_2]$

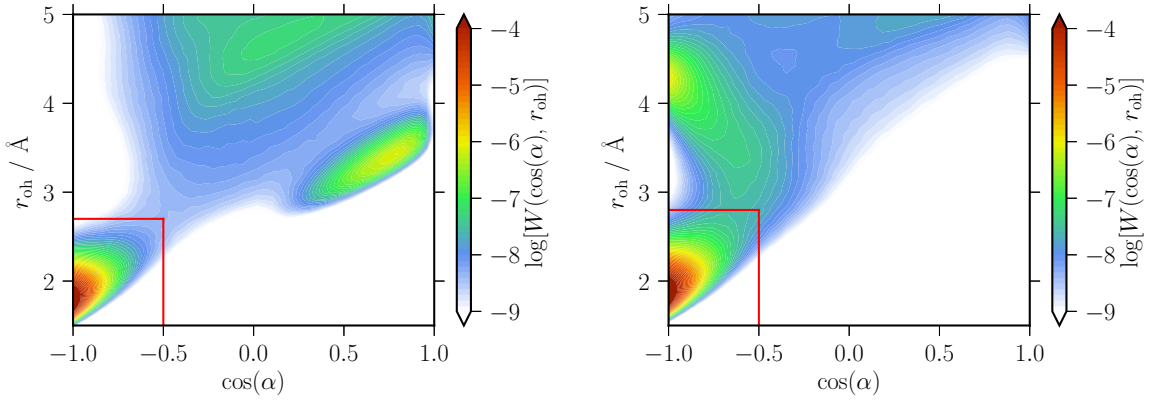

(b) $[HOC_3Py][NTf_2]$

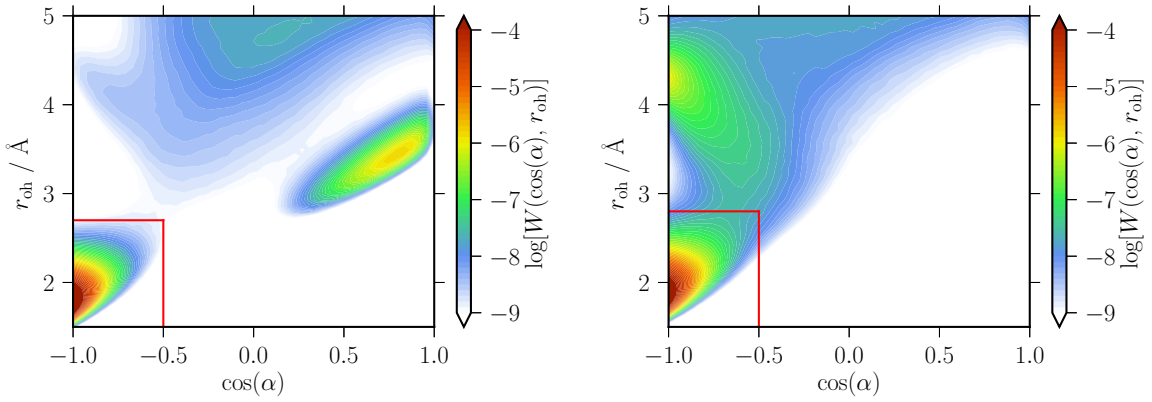

(c) $[HOC_4Py][NTf_2]$

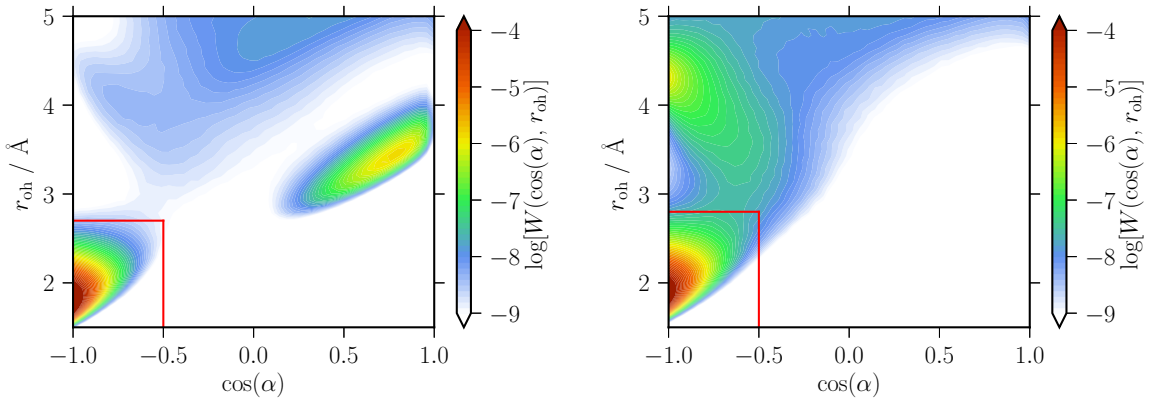

(d) $[HOC_5Py][NTf_2]$

Figure S10: Logarithmic representation of the probability density of finding an intermolecular O-H distance r_{oh} and the cosine of the angle α between the intermolecular H-O vector and the intramolecular O-H vector for the (cc) (left) and the (ca) (right) HB obtained at 300 K for the specified ionic liquid. The probability density is weighted with r^{-2}. The (cc) HB for all considered ionic liquids can be characterised by a distance cutoff of $r_c = 2.7$ Å and an angular cutoff at $\cos(\alpha_c) = -0.5$. For the (ca) HB the same angular cutoff was used with a distance cutoff of $r_c = 2.8$ Å.

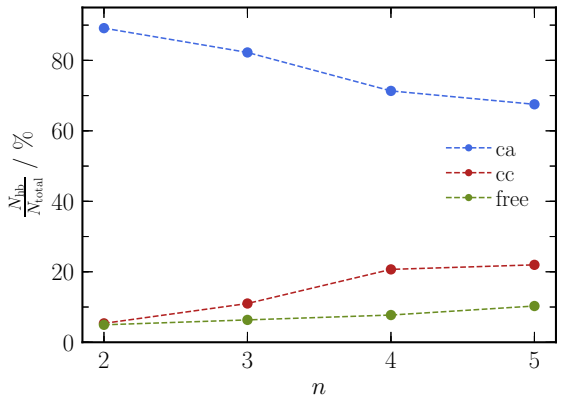

Figure S11: Percentage of cations donating a (ca) (blue) or (cc) (red) HB respectively. With increasing alkyl chain length the amount of (cc) hydrogen bonding increases, whereas the amount of (ca) hydrogen bonding decreases. Cations that do not form HB as defined in Figure S10 interact with different parts of the two ions and are considered "free" (green).

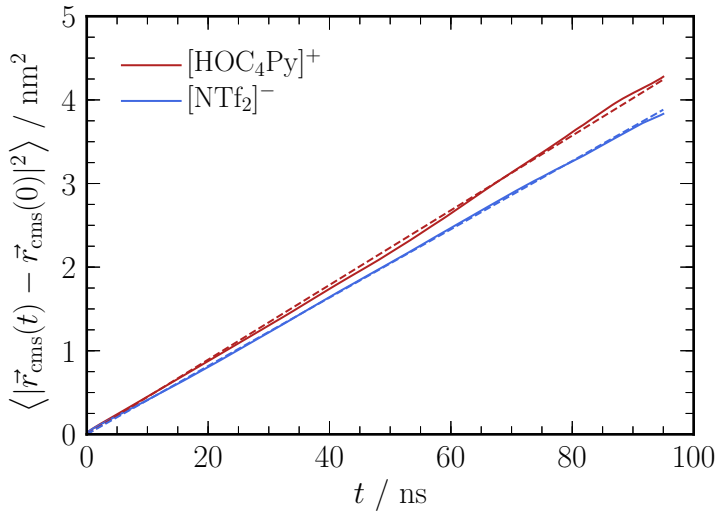

Figure S12: Mean square displacement of the cation (red) and anion (blue) in $[HOC_4Py][NTf_2]$ at 300 K (solid lines) and the corresponding fitted functions according to Eq. 2 (dashed lines).

4 Mean Square Displacement and Diffusion

To obtain the self-diffusion coefficients of the ions in our ionic liquid we used the Einstein relation

$$D = \frac{1}{6}\frac{\partial}{\partial t}\lim_{t\to\infty}\left\langle|\vec{r}_{\mathrm{cms}}(t) - \vec{r}_{\mathrm{cms}}(0)|^2\right\rangle, \tag{2}$$

where $\vec{r}_{\mathrm{cms}}$ denotes the position vector of the center of mass of the respective ion. The brackets indicate averaging over all $t = 0$ and ions of the desired type. The mean square displacement $\langle|\vec{r}_{\mathrm{cms}}(t) - \vec{r}_{\mathrm{cms}}(0)|^2\rangle$ was fitted over a range from 10 ns to 95 ns to obtain the self-diffusion coefficient D according to Eq. 2. The self-diffusion coefficients of the cations D_{Cation} and anions D_{Anion} in the functionalized and unfunctionalized IL for the different temperatures can be found in Table S12 and S13, respectively. The errors given in the tables represent two times the standard error of the mean ($2 \cdot s_{\overline{D}}$) and were determined by calculating the diffusion coefficient for every ion separatly and then averaging over ions of the same kind.

5 Hydrogen Bond Lifetime

To calculate the HB lifetime τ_{hb}, we fitted the average HB population-correlation function to a sum of two streched exponential functions:

$$C(t) = A_1 \cdot \exp\left(-\left(\frac{t}{\tau_1}\right)^{\beta_1}\right) + A_2 \cdot \exp\left(-\left(\frac{t}{\tau_2}\right)^{\beta_2}\right). \tag{3}$$

Table S12: Temperature dependence of the self-diffusion coefficient of the cation D_{Cation} and the anion D_{Anion} in the respective functionalized ionic liquid.

T / K	D_{Cation} / $10^{-11}\,\mathrm{m^2 s^{-1}}$	D_{Anion} / $10^{-11}\,\mathrm{m^2 s^{-1}}$
	$[HOC_2Py][NTf_2]$	
300	1.32 ± 0.08	1.01 ± 0.06
320	3.33 ± 0.20	2.70 ± 0.17
340	6.5 ± 0.5	5.5 ± 0.4
360	11.0 ± 0.7	9.0 ± 0.6
380	17.3 ± 1.1	13.9 ± 0.0
400	23.8 ± 1.4	20.3 ± 1.2
	$[HOC_3Py][NTf_2]$	
300	1.14 ± 0.07	0.95 ± 0.06
320	2.85 ± 0.17	2.25 ± 0.14
340	5.7 ± 0.4	4.7 ± 0.3
360	9.3 ± 0.7	8.2 ± 0.6
380	15.7 ± 1.0	13.3 ± 0.9
400	23.1 ± 1.3	18.2 ± 1.2
	$[HOC_4Py][NTf_2]$	
300	0.74 ± 0.05	0.68 ± 0.05
320	1.81 ± 0.11	1.66 ± 0.10
340	4.21 ± 0.26	3.76 ± 0.22
360	7.4 ± 0.5	6.7 ± 0.4
380	12.4 ± 0.7	11.0 ± 0.6
400	19.5 ± 1.3	17.1 ± 1.0
	$[HOC_5Py][NTf_2]$	
300	0.63 ± 0.04	0.60 ± 0.04
320	1.70 ± 0.11	1.60 ± 0.10
340	3.71 ± 0.22	3.16 ± 0.18
360	6.6 ± 0.4	6.5 ± 0.5
380	11.7 ± 0.7	10.2 ± 0.7
400	17.8 ± 1.1	17.7 ± 1.1

Table S13: Temperature dependence of the self-diffusion coefficient of the cation D_{Cation} and the anion D_{Anion} in the respective unfunctionalized ionic liquid.

T / K	D_{Cation} / $10^{-11}\,\mathrm{m^2 s^{-1}}$	D_{Anion} / $10^{-11}\,\mathrm{m^2 s^{-1}}$
	$[C_3Py][NTf_2]$	
300	3.54 ± 0.21	2.25 ± 0.14
320	6.7 ± 0.4	4.36 ± 0.26
340	10.5 ± 0.7	7.6 ± 0.5
360	17.7 ± 1.2	11.8 ± 0.7
380	24.8 ± 1.4	17.9 ± 1.1
400	33.4 ± 2.0	25.6 ± 1.7
	$[C_4Py][NTf_2]$	
300	2.51 ± 0.15	1.85 ± 0.12
320	5.4 ± 0.4	3.81 ± 0.25
340	9.1 ± 0.6	6.6 ± 0.4
360	14.9 ± 0.9	11.5 ± 0.7
380	21.8 ± 1.3	17.0 ± 1.0
400	30.9 ± 1.9	24.5 ± 1.6
	$[C_5Py][NTf_2]$	
300	0.82 ± 0.06	0.67 ± 0.04
320	3.98 ± 0.24	3.17 ± 0.21
340	7.7 ± 0.5	6.1 ± 0.4
360	12.2 ± 0.8	10.0 ± 0.7
380	18.4 ± 1.2	16.0 ± 1.0
400	26.1 ± 1.5	19.5 ± 1.2
	$[C_6Py][NTf_2]$	
300	1.30 ± 0.08	1.12 ± 0.07
320	3.15 ± 0.19	2.67 ± 0.17
340	5.9 ± 0.4	5.1 ± 0.4
360	9.6 ± 0.6	8.6 ± 0.5
380	16.2 ± 1.0	13.6 ± 0.8
400	21.3 ± 1.3	21.0 ± 136

Table S14: HB lifetime of the (ca) HB τ_{ca} and of the (cc) HB τ_{cc} as a function of the alkyl chain length n in $[HOC_nPy][NTf_2]$ at 300 K.

n	τ_{ca} / ps	τ_{cc} / ps
2	561 ± 27	220 ± 9
3	614 ± 25	442 ± 15
4	800 ± 40	1110 ± 50
5	870 ± 50	1120 ± 50

To get a consistent fitting behavior the parameter A_2 was fixed for all ILs at 0.048 for the (ca) correlation functions and 0.25 for the (cc) correlation functions. Eq. 3 can be integrated analytically to obtain the HB lifetime τ_{hb} (Table S14) using

$$\tau_{hb} = A_1 \cdot \frac{\tau_1}{\beta_1}\Gamma(\beta_1^{-1}) + A_2 \cdot \frac{\tau_2}{\beta_2}\Gamma(\beta_2^{-1}). \tag{4}$$

To obtain the error bars of the HB lifetimes, we calculated the corresponding HB population-correlation function for every hydroxyl group separatly and integrated them numerically using Simpson's rule. The error given in Table S14 corresponds to $2.5 \cdot s_{\overline{\tau}_{hb}}$ where $s_{\overline{\tau}_{hb}}$ denotes the standard error of the mean of the obtained HB lifetimes.

References

[1] J. Neumann, B. Golub, L.-M. Odebrecht, R. Ludwig, D. Paschek, *J. Chem. Phys.* **2018**, *148*, 193828.

[2] W. L. Jorgensen, D. S. Maxwell, J. Tirado-Rives, *J. Am. Chem. Soc.* **1996**, *118*, 11225–11236.

[3] W. L. Jorgensen, N. A. McDonald, *J. Mol. Struct.: THEOCHEM* **1998**, *424*, 145–155.

[4] C. M. Breneman, K. B. Wiberg, *J. Comput. Chem.* **1990**, *11*, 361–373.

[5] M. Frisch, G. Trucks, H. Schlegel, G. Scuseria, M. Robb, J. Cheeseman, G Scalmani, V Barone, B Mennucci, G. Petersson, et al., *Wallingford CT* **2013**.

[6] D. Paschek, A. Geiger, *Department of Physical Chemistry University of Dortmund* **2002**.

[7] S. Páll, M. J. Abraham, C. Kutzner, B. Hess, E. Lindahl in International Conference on Exascale Applications and Software, Springer, **2014**, pp. 3–27.

[8] S. Pronk, S. Páll, R. Schulz, P. Larsson, P. Bjelkmar, R. Apostolov, M. R. Shirts, J. C. Smith, P. M. Kasson, D. van der Spoel, et al., *Bioinformatics* **2013**, *29*, 845–854.

[9] B. Hess, C. Kutzner, D. Van Der Spoel, E. Lindahl, *J. Chem. Theory Comput.* **2008**, *4*, 435–447.

[10] D. Van Der Spoel, E. Lindahl, B. Hess, G. Groenhof, A. E. Mark, H. J. Berendsen, *J. Comput. Chem.* **2005**, *26*, 1701–1718.

[11] H. J. Berendsen, D. van der Spoel, R. van Drunen, *Comput. Phys. Commun.* **1995**, *91*, 43–56.

[12] H. J. C. Berendsen, J. P. M. Postma, W. F. van Gunsteren, A. DiNola, J. R. Haak, *J. Chem. Phys.* **1984**, *81*, 3684–3690.

[13] S. Nosé, *Mol. Phys.* **1984**, *52*, 255–268.

[14] W. G. Hoover, *Phys. Rev. A* **1985**, *31*, 1695–1697.

[15] M. Parrinello, A. Rahman, *J. Appl. Phys.* **1981**, *52*, 7182–7180.

[16] S. Nosé, M. L. Klein, *Mol. Phys.* **1983**, *50*, 1055–1076.

[17] B. Hess, H. Bekker, H. J. C. Berendsen, J. G. E. M. Fraaije, *J. Comp. Chem.* **1997**, *18*, 1463–1472.

[18] U. Essmann, L. Perera, M. L. Berkowitz, T. A. Darden, H. Lee, L. G. Pedersen, *J. Chem. Phys.* **1995**, *103*, 8577–8593.

VI. Hydrogen Bonds between Ions of Opposite and Like Charge in Hydroxyl-functionalized Ionic Liquids: an Exhaustive Examination of the Interlay Between Global and Local Motions and Intermolecular Hydrogen Bond Lifetimes and Kinetics

J. Neumann, R. Ludwig, D. Paschek, *J. Phys. Chem. B* **2021**, *125*, 5132.
DOI: 10.1021/acs.jpcb.1c02756

Contribution:
I performed the simulation as well as most of the analyses concerning the MD trajectories for this manuscript. The random-walker model was developed and analyzed by D. Paschek. I wrote the first draft of the manuscript and took part in its revision. My contribution sums up to about 60 %.

THE JOURNAL OF PHYSICAL CHEMISTRY B
A JOURNAL OF THE AMERICAN CHEMICAL SOCIETY

pubs.acs.org/JPCB

Article

Hydrogen Bonds between Ions of Opposite and Like Charge in Hydroxyl-Functionalized Ionic Liquids: an Exhaustive Examination of the Interplay between Global and Local Motions and Intermolecular Hydrogen Bond Lifetimes and Kinetics

Jan Neumann, Ralf Ludwig,* and Dietmar Paschek*

Cite This: *J. Phys. Chem. B* 2021, 125, 5132–5144

Read Online

ACCESS | Metrics & More | Article Recommendations | Supporting Information

ABSTRACT: Hydroxyl-functionalized ionic liquids (ILs) represent a new interesting class of ILs where hydrogen bonds (HBs) play an important role: here, "typical" HBs between cations and anions (ca) are competing with "atypical" HBs connecting pairs of cations (cc). We study the equilibrium and kinetics of (cc) and (ca) HBs in 1-(*n*-hydroxyalkyl)-pyridinium bis-(trifluoromethlysulfonyl)imide [HOC_nPy][NTf_2] ILs by means of molecular dynamics simulations. (cc) HBs are found to be between 0.96 and 3.76 kJ mol^{-1} stronger than their (ca) counterparts, depending on the alkyl chain length. HB lifetimes and kinetics are analyzed by means of HB population and reactive flux correlation functions. Essentially, four different HB lifetimes have to be considered, spanning about 3 orders of magnitude, each valid in its own right and each associated with different aspects of HB breaking and HB reformation. The long-time limiting behavior of the HB population correlation function is controlled by diffusion of the ions and can be quantitatively described by analytical expressions. The short-time HB behavior is tied to the localized dynamics of the hydroxyl group exploring its local solvation environment. A minimalist kinetic two-domain model is introduced to realistically describe the time evolution of the HB population correlation function for both (ca) and (cc) HBs over 5 orders of magnitude. By employing the reactive flux method, we determine the kinetics of HB breaking, unaffected by diffusion processes. We determine both, the ultrafast upper boundary and the average rate of HB breaking, allowing recrossing-events during the transient relaxation time period. For sufficiently long alkyl chains, all those computed HB lifetimes indicate a higher kinetic stability of (cc) HBs over (ca) HBs; for short chains, it is vice-versa.

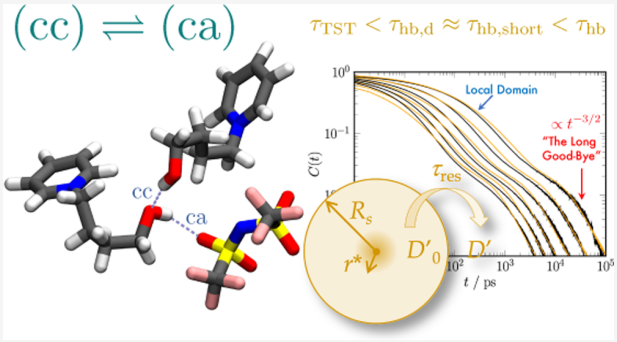

INTRODUCTION

The prototypical hydrogen-bonded liquid is, of course, water.[1] As Stillinger has stated: The key to understanding liquid water and its solutions lies in the concept of the hydrogen bond.[2] Hence, the understanding of the hydrogen bond (HB) formation processes provides a crucial insight into the dynamical properties of the liquid. In 1996, Luzar and Chandler[3] argued that the HB dynamics are characterized by local relaxation processes, which are mostly uncorrelated with respect to the specific bonding patterns near a tagged bond.[4,5] They could show that diffusion processes govern whether a specific pair of water molecules are close neighbors, and HBs between such pairs form and persist randomly with mean lifetimes determined by rate constants for bond making and breaking.

For ionic liquids (ILs), hydrogen bonding has been shown to play an important role as well, for example, in controlling chemical reactions.[6−9] Moreover, HBs have been identified as one key factor that dictates self-assembly in ILs.[10] However, analyzing the role of HBs in ILs is far from trivial.[11] Moreover, HBs in ILs have been thought of to be distinct from their counterparts in molecular liquids: as ILs consist solely of ions, their hydrogen bonding structures and lifetimes are affected by the presence of strong Coulomb interactions.[12] Paschek et al. have studied HB equilibria in mixtures of protic ILs and observed strong nonideal mixing behavior based on HB redistribution effects, caused by the different HB accepting capabilities of the respective anions.[13] Skarmoutsos et al. have examined hydrogen bonding in imidazolium chloride ILs[14,15] and detected a profound temperature effect on HB lifetimes. Recently, Gehrke et al. have investigated the hydrogen bonding

Received: March 27, 2021
Revised: April 24, 2021
Published: May 11, 2021

https://doi.org/10.1021/acs.jpcb.1c02756
J. Phys. Chem. B 2021, 125, 5132−5144

and ion pair formation in imidazolium-based ILs: they observed a wide variation of HB lifetimes, spanning from 10 ps up to 2000 ps depending on the viscosity of the IL.[16,17] Due to their possible longevity, deriving HB lifetimes in ILs from molecular dynamics (MD) simulations is posing a challenge. The situation is perhaps even more complicated for hydroxyl-functionalized ILs[18] since two types of HBs can exist: the "typical" HBs between a cation and anion (ca), strengthened by attractive Coulomb interactions, and "atypical" HBs between like-charged ions (cc), which were suspected to be significantly debilitated due to the repulsive Coulomb forces.[19−23] Quite surprisingly, however, evidence for the existence of hydrogen-bonded cationic clusters has recently been observed for both, the bulk liquid and the gas phase.[24−34] Infrared spectroscopy could clearly identify two distinct vibrational bands that were assigned to (ca) and (cc) hydrogen-bonded species. Moreover, the magnitudes of the observed redshifts indicated that (cc) HBs are even stronger than (ca) HBs.[29−31] A class of ILs exhibiting pronounced (cc) HB formation are 1-(*n*-hydroxyalkyl)-pyridinium bis-(trifluoromethlysulfonyl)imides $[HOC_nPy][NTf_2]$ (see Scheme 1).[35] They are consisting of polarizable pyridinium

Scheme 1. Molecular Constituents of the Studied Ionic Liquids: 1-(*n*-Hydroxyalkyl)-pyridinium Cations (with *n* = 2, 3, 4, 5) Combined with Bis(trifluoromethlysulfonyl)imide Anions

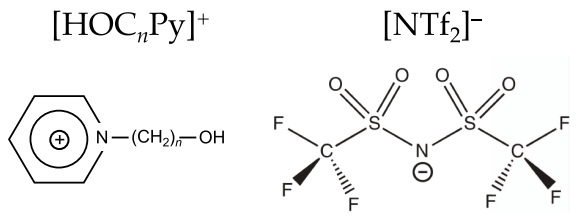

$[HOC_nPy]^+$ cations with chain lengths n = 2, 3, 4, 5 in combination with weakly interacting bis-(trifluoromethlysulfonyl)imide anions $[NTf_2]^-$ with the ability to accept HBs via the oxygen atoms of their sulfonyl groups. Hydroxyalkyl chains of specifically tailored length allow for keeping the positively charged pyridinium ring at a sufficiently large distance from the hydroxyl group.[31,34] This separation between charge-center and hydroxyl group allows for tethering two individual cations together via hydrogen bonding.

Recently, we have demonstrated by use of MD simulations that the lifetimes of (cc) HBs can even exceed those of (ca) HBs despite the presence of repulsive Coulombic interactions.[34] Moreover, this HB microdynamics has been shown to have an effect on the overall mobility of the ions. However, one key observation was that the HB dynamics in those ILs is characterized by a separation into two time domains, which are divided by about two orders of magnitude. In this contribution, we will show that the long-time limiting behavior, which is well extending into the 100 ns regime, is entirely controlled by translatoric diffusion of the ions and is approaching the theoretically predicted $t^{-3/2}$ scaling law, which we coin "the long goodbye".[36] The short-time decay, on the other hand, is related to the local dynamics of the hydroxyl group attached to the cation, exploring its local solvation environment formed by anions and hydroxy-alkyl-group of adjacent cations. Finally, by employing the reactive flux methodology, we determine the rate of HB breaking, unaffected by diffusion processes. We will show that for the case of hydroxyl-functionalized ILs, essentially four different HB lifetimes have to be considered, each valid in its own right, and each associated with different aspects of HB breaking and HB reformation. Short-time kinetics can be probed by ultrashort laser spectroscopy,[37−45] whereas the long-time behavior falls in the realm of NMR relaxation techniques.[46−50]

(CA)/(CC) HB EQUILIBRIUM

All the detailed information of the layout and technical aspects of the performed MD simulations can be found in the Supporting Information in Sections S12 and S13. A rigorous definition of a hydrogen-bonded state would need to involve electronic structure calculations.[12,51,52] Since quantum mechanical calculations of the relevant properties are still exorbitantly expensive, the most rational approach is to rely on geometrical criteria.[17,53] However, those definitions might be delicate and the computed properties could turn out to be sensitive to the chosen criteria.[15] Here, we follow the procedure of Kumar et al.[53] to identify the hydrogen-bonded state as a basin on a free energy landscape, being separated from non-bonded states via barriers. As criteria, we used the intermolecular H−O-distance r_{oh} and the HB angle $\alpha\angle$O−H···O to define a HB: two cations are considered hydrogen-bonded if $r_{oh} < 2.7$ Å and $\cos(\alpha) < -0.5$ ($\alpha > 120°$). For the (ca) HB, the distance criterion is set at $r_{oh} < 2.8$ Å, with the same angle-cutoff. These criteria match the two-dimensional probability density functions shown in Figure S3 in the Supporting Information.

In the large majority of cases, a cation donates one single HB at a given time. "Bifurcated" HBs, according to our definition, are detected rarely, mostly as a transitional configuration, when a hydroxyl group switches from donating a (cc) HB to donating a HB to an adjacent anion (or vice versa) to which the former acceptor cation is itself hydrogen-bonded. For the exact share of those configurations, see Table S6 in the Supporting Information.

In ref 34, we were able to show that the equilibrium between (ca) and (cc) hydrogen-bonded states is influenced by the alkyl chain length of the cations. While the majority of the cations in our simulation form (ca) HBs, the fraction of (cc) HBs increases with increasing alkyl chain length. At 300 K, the percentage p of (ca) HBs decreases from p = 89% for $[HOC_2Py][NTf_2]$ to 68% for $[HOC_5Py][NT_2]$ while the fraction of (cc) HBs increases from p = 5 to 22%. Percentages for all temperatures and alkyl chain lengths are summarized in Table S6 in the Supporting Information. Due to the longer alkyl chain, the charge centers of the cations are kept at a larger distance, thus stabilizing (cc) HB configurations.

Figure 1 shows the average fraction of cations involved in a certain type of HB at temperatures of 300 and 400 K. With decreasing temperature, the equilibrium shifts toward (cc) HBs, indicating that (cc) HBs are enthalpically favored. The dominatingly large amount of (ca) HBs is due to the fact that there are four times more possible accepting oxygen sites located on the anions than on the cations. In addition, each cation is surrounded by a shell of anions, leading to a vastly higher local concentration of anionic HB acceptor sites (for an illustration see Figure 3). Consequently, (cc) HBs are also strongly entropically disfavored. The exact temperature dependence of the equilibrium (ca) ⇌ (cc) for $[HOC_nPy][NTf_2]$ as a function of n is quantified via the van 't Hoff plots shown in Figure 2 with the corresponding standard enthalpies

https://doi.org/10.1021/acs.jpcb.1c02756
J. Phys. Chem. B 2021, 125, 5132−5144

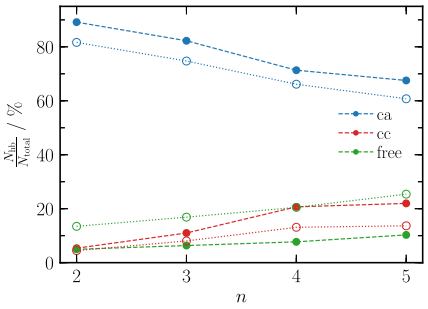

Figure 1. Percentage of cations donating (ca) HB (blue), (cc) HB (red), or no HB at all (green) as a function of alkyl chain length n at 300 K (closed symbols) and 400 K (open symbols), respectively.

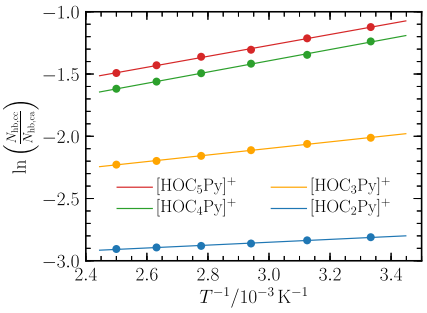

Figure 2. Van' t Hoff plot of $\ln[N_{hb,\,cc}/N_{hb,\,ca}]$ for $[HOC_nPy][NTf_2]$ with n = 2, 3, 4, 5 as a function of inverse temperature. The solid line represents linear fits according to $\ln(K) = -\Delta H^\circ/(RT) + \Delta S^\circ/R$. Fitted thermodynamic parameters are given in Table 1.

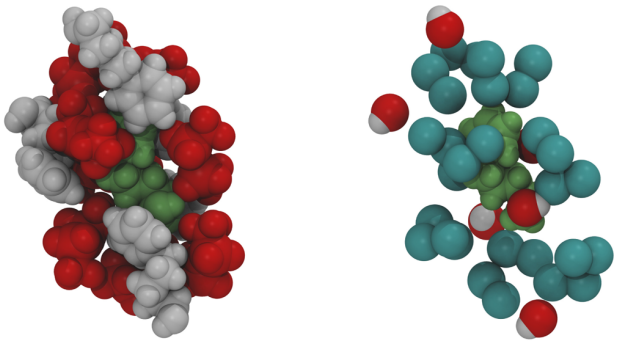

Figure 3. Typical coordination of a central $[HOC_5Py]^+$ cation (colored in lime) taken from a simulation at 300 K. The central cation is involved in a (ca) HB. Left: surrounding $[NTf_2]^-$ anions are shown in red and $[HOC_5Py]^+$ cations are depicted in white. Right: shown are only oxygen atoms located on the surrounding $[NTf_2]^-$ anions (cyan) and the hydroxyl groups of the surrounding $[HOC_5Py]^+$ cations. Images were created using VMD.[54]

and entropies shown in Table 1. Note that with increasing chain length for $n \leq 4$ the (cc) HBs also become increasingly enthalpically stabilized. The most stable (cc) HBs with ΔH° = −3.75 kJ mol^{-1} are observed for n = 4. Negative entropy differences ΔS° shown in Table 1 indicate an entropic destabilization of (cc) HBs versus (ca) HBs. An increasing chain length also leads to less disfavorable entropy differences. This might be attributed to the fact that for longer alkyl chains, simply more hydroxyl groups are within reach and therefore available to attach to.

Table 1. Thermodynamic Parameters Describing the Temperature Dependence of the Equilibrium (ca) ⇌ (cc) for $[HOC_nPy][NTf_2]$ according to the Van' t Hoff Plot Shown in Figure 2

n	ΔH°/kJ mol^{-1}	ΔS°/J K^{-1}mol^{-1}
2	−0.96	−26.6
3	−2.19	−24.0
4	−3.76	−22.9
5	−3.65	−21.5

Hydroxyl groups not involved in donating a HB at a specific time step are counted as "free" (see also Figure 1). These "free" cations might interact locally with unspecified parts of the surrounding ions, for example, in the form of close contacts with the fluorine atoms. However, a formation of an O−H···F contact occurs rather rarely with p between 1 and 3% of all cations. Of course, due to the large possible number of those configurations, the amount of "free" cations increases as well with temperature.

Finally, we would like to point out that aggregates consisting of more than two hydrogen-bonded cations are also observed. These aggregates are able to form one- and two-dimensional clusters like chains, rings, and lassos. However, the majority of observed cationic clusters is composed of chains of dimers and trimers, with $p(n = 3) \ll p(n = 2)$ due to the rather low overall (cc) HB percentage and their competition with the (ca) HBs. The formation of larger than n = 3 cationic clusters and ring-like structures occurs very rarely and is observed only at low temperatures for longer chain lengths.

"INTERMITTENT" HB LIFETIMES AND DYNAMICS

The theory describing the rate of chemical reactions is a wide ranging subject.[55,56] To study HB dynamics, we will start with the concept of "intermittent" HB lifetimes introduced by Stillinger and others.[57−64] In particular, we adopted the pairwise donor−acceptor definition according to Luzar and Chandler,[4] based on the Bennett−Chandler procedure;[65,66] therefore, we calculate intermolecular HB population functions $h(t)$ for all possible donor−acceptor pairs in our system. For the (ca) HB, a donor−acceptor pair consists of the hydroxyl group of a cation and a single oxygen atom of the anion so that switching to a different oxygen atom of the same $[NTf_2]^-$ anion means breaking the HB of the specific donor−acceptor pair. The same applies to the (cc) HB, where the donor remains the same while the acceptor is the hydroxyl group of a neighboring cation. A "flipping" of an existing (cc) HB, where the former donor cation becomes the acceptor of a HB from the former acceptor cation, is considered a different donor−acceptor pair.

The fluctuations of the HB population are described by the HB population correlation function

$$C(t) = \frac{\langle h(0)h(t)\rangle - \langle h\rangle^2}{\langle h^2\rangle - \langle h\rangle^2} \quad (1)$$

with the HB population function

$$h(t) = \begin{cases} 1, & \text{if HB exists} \\ 0, & \text{if no HB exists} \end{cases} \quad (2)$$

which is calculated for every donor−acceptor pair separately. The brackets denote averaging over all donor−acceptor pairs of a specific HB species and all times t = 0. Due to the property

https://doi.org/10.1021/acs.jpcb.1c02756
J. Phys. Chem. B 2021, 125, 5132−5144

of $h(t)$ with $h(t) = h^2(t)$ and thus $\langle h\rangle = \langle h^2\rangle$, the denominator in eq 1 can be expressed as $[\langle h^2\rangle - \langle h\rangle^2] = \langle h\rangle[1 - \langle h\rangle]$ with $\langle h\rangle[1 - \langle h\rangle] \approx \langle h\rangle$ for $\langle h\rangle \ll 1$. As pointed out by Starr et al.,[63] the approximation $\langle h\rangle^2 \approx 0$ in the numerator of eq 1 could lead to a misrepresentation of $C(t)$ at long time intervals t; therefore,

$$C(t) \approx \frac{\langle h(0)h(t)\rangle}{\langle h\rangle} - \langle h\rangle \tag{3}$$

is a more appropriate representation for the long-time behavior of finite systems. For macroscopic systems, of course, the "$-\langle h\rangle$" can be omitted. The "intermittent" correlation function $C(t)$ describes the fraction of HBs still intact at time t, provided it was intact at $t_0 = 0$, without the need for it to be intact over the whole time interval $t - t_0$.

Figure 4 shows the time evolution of the HB population correlation functions $C(t)$ for (ca) as well as (cc) HBs as a

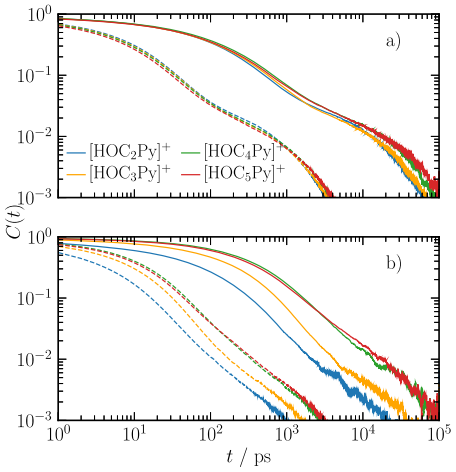

Figure 4. HB population correlation functions $C(t)$ for the (ca) HBs (a) and the (cc) HBs (b) of the $[HOC_nPy][NTf_2]$ ILs for n = 2, 3, 4, 5. Solid lines represent data for T = 300 K; dashed lines indicate T = 400 K.

function of chain length n obtained at the highest and lowest temperatures, respectively. All correlation functions exhibit two distinct time domains: this feature is more strongly pronounced for the (ca) HBs, which show an initial decay, which reaches a plateau after a few nanoseconds, followed by a slow decay over up to a hundred nanoseconds at T = 300 K. This feature is more strongly pronounced for the (ca) HBs than for the (cc) HBs. Another strikingly different behavior of the (cc) and (ca) HB correlation functions becomes evident by comparing the chain length dependence shown in panel (a) and (b) in Figure 4. Irrespective of the temperature, the decay curves for (ca) HBs for different n lie practically on top of each other, whereas the decay rates of (cc) HBs vary strongly for different n, at least for $n \leq 4$.

To quantify the separation into two time domains, we fitted $C(t)$ to an empirical function composed of two Kohlrausch Williams Watts (KWW)[67] terms with

$$C(t) = A_1\exp[-(t/\tau_1)^{\beta_1}] + A_2\exp[-(t/\tau_2)^{\beta_2}] \tag{4}$$

representing short-time and long-time behavior, respectively

$$C(t) = C_{short}(t) + C_{long}(t) \tag{5}$$

Figure 5 Depicts the fitted $C_{short}(t)$ and $C_{long}(t)$ for $[HOC_5Py][NTf_2]$ at 300 K as well as the sum of both terms

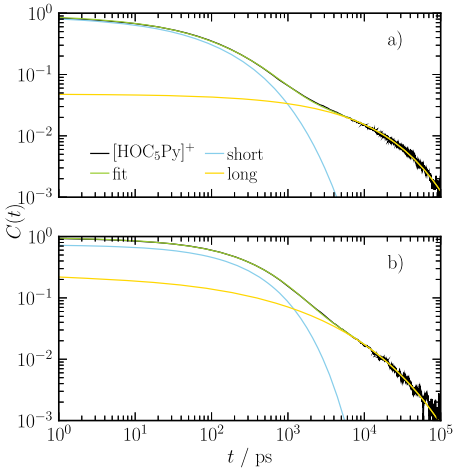

Figure 5. Fit of the HB population correlation functions according to eq 4 for the (ca) HBs (a) and the (cc) HBs (b) for $[HOC_5Py][NTf_2]$ at 300 K (black). The correlation functions for the (ca) as well as the (cc) HB is represented by the sum of two stretched exponential functions (green), composed of the short-time behavior (blue) and the long-time behavior (yellow).

in comparison with the original $C(t)$ as obtained from MD simulation. To achieve a slightly improved consistency of the fit with varying temperature T and chain length n, the parameter A_2 was kept fixed during fitting. For the (ca) functions, a value of A_2 = 0.048 and for the (cc) functions, a value of A_2 = 0.25 was used, leading to the overall best representation of the entire data set. The fitted parameters describing all HB population correlation functions are summarized in Table S7 in the Supporting Information.

KWW functions can be thought of representing a distribution of monoexponential relaxation functions:[68] the fitted KWW exponents β are close to 1/2 (see Table S7 in the Supporting Information) except for the short-time (cc) contribution. One possible interpretation thus would be the existence of a broad distribution of relaxation times, extending (for $\beta \approx 1/2$) to about ten times the average lifetime.[69] For the short-time (cc) correlation function, values for β between 0.2 and 0.3 are obtained, pointing at an even broader distribution, possibly catering to the fact that the separation between short-time and long-time behavior is less well pronounced for (cc) HBs.

The integral of the HB population correlation functions determines the average lifetime τ_{hb} of a HB, which can be considered as a quantitative measure for the kinetic stability of the respective HB species

$$\tau_{hb} = \int_0^\infty C(t)\mathrm{d}t \tag{6}$$

Using the empirical representation of $C(t)$ according to eq 4, τ_{hb} is calculated analytically via[68]

$$\tau_{hb} = A_1\frac{\tau_1}{\beta_1}\Gamma(\beta_1^{-1}) + A_2\frac{\tau_2}{\beta_2}\Gamma(\beta_2^{-1}) \tag{7}$$

where $\Gamma(x)$ denotes the gamma function. The computed average HB lifetimes τ_{hb} for the (ca) and the (cc) HBs as a function of alkyl chain length n for 300, 360, and 400 K are

https://doi.org/10.1021/acs.jpcb.1c02756
J. Phys. Chem. B 2021, 125, 5132−5144

shown in Figure 6. For a better quantitative examination of the relative changes, Figure 7 shows the ratio of the (cc) and (ca)

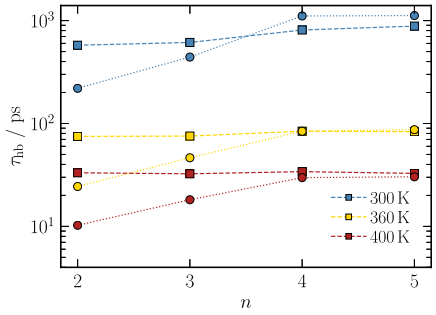

Figure 6. Average HB lifetimes τ_{hb} as a function of the alkyl chain length n in $[HOC_nPy][NTf_2]$ at T = 300, 360, and 400 K. Lifetimes for (cc) HBs are indicated as circles, whereas the lifetimes for (ca) HBs are given as squares.

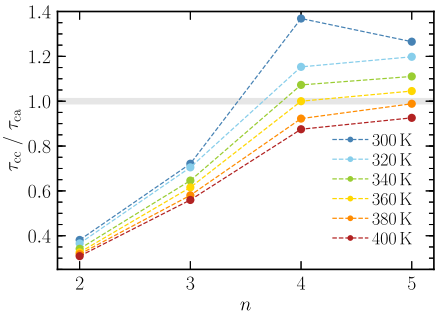

Figure 7. Ratio of the (cc) and (ca) HB lifetimes τ_{hb} as a function of the alkyl chain length n in $[HOC_nPy][NTf_2]$. With increasing temperatures, the ratio decreases for all chain lengths but the ratio increases with increasing chain length. Only for n = 4, 5 and up to 360 K, τ_{cc} is bigger than τ_{ca} meaning that the (cc) HB is more stable than the (ca) HB in those systems.

HB lifetimes. The pattern that was previously revealed by visual inspection of Figure 5 is also apparent here: the lifetimes for (ca) HBs show little variation with respect to n, whereas the lifetimes for (cc) HBs increase strongly up to n = 4 and then level off. In particular, we would like to point at two features shown in Figure 6: (1) with decreasing temperature, the lifetimes for (ca) HBs start to develop a slight tendency to increase with larger n. (2) for n = 2 the lifetimes for (cc) HBs are consistently shorter than their (ca) counterparts, whereas this behavior reverses for $n \geq 4$ at lower temperatures. As shown in Figure 7, the threshold temperature with $\tau_{ca} \approx \tau_{cc}$ for $n \geq 4$ is located between 360 and 380 K.

The factorization in short-time and long-time behavior is shown in Figure 8, depicting the ratio τ_{long}/τ_{short} as a function of temperature. The shown ratios indicate that τ_{long} is always longer than the respective τ_{short}, although the prefactor of the corresponding $C_{long}(t)$ is between 4 and 20 times smaller than that of $C_{short}(t)$. Thus, the ultraslow decay of $C_{long}(t)$ even overcompensates for its small amplitude. For the (ca) HBs, the computed ratios are found to lie between 2.5 and 4, while showing a strong temperature dependence, leading to an increasing ratio for decreasing temperatures. For the (cc) HBs, the ratios are found to be rather constant, closer to one for $n \leq 4$. Only with $n \geq 4$, a temperature dependence develops, also

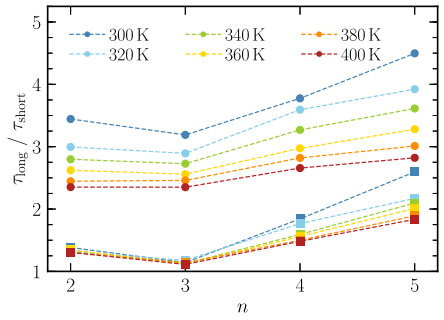

Figure 8. Ratio of the τ_{long} and τ_{short} parts of the HB lifetime for (ca) HBs (circles) and (cc) HBs (squares) as a function of the alkyl chain length n in $[HOC_nPy][NTf_2]$ at different temperatures. For both types of HBs, τ_{long} is greater than τ_{short}, but especially for the (ca) HBs, the ratio indicates a considerable difference between the two time domains.

leading to an increasing ratio with decreasing temperatures. Here, we would like to point out that the fixing parameter A_2 during fitting has only a small effect on the computed τ_{long}, τ_{short}, and τ_{hb}. Lifetimes computed with and without fixing A_2 agree within a few percent for both (cc) and (ca) lifetimes.

Further insights on how the different contributions to the HB lifetimes are interrelated with the overall fluidity of the ILs can be gained from Figure 9: both, τ_{short} and τ_{long} scale linearly

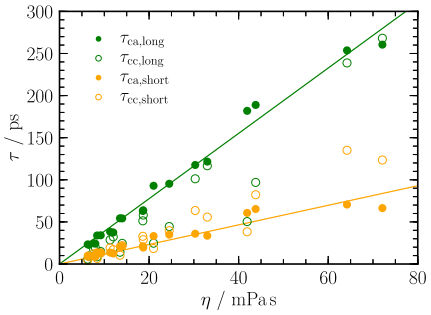

Figure 9. Contributions τ_{short} and τ_{long} to the average (ca) and (cc) HB lifetimes of $[HOC_nPy][NTf_2]$ for temperatures with T > 300 K and all chain lengths n as a function of the viscosity η. The green line indicates a slope of 3.88 ps/(mPa·s), whereas the orange line corresponds to a slope of 1.16 ps/(mPa·s).

with the computed viscosity of the ILs. The data for the (ca) HBs scale very well with the viscosity, whereas significantly more scattering for the (cc) HBs is denoted. A large portion of the enhanced scattering of the (cc) HB data, particularly for their short-time behavior, has to be attributed to the fact that the observed chain-length-dependent variation of the (cc) HB lifetimes is not fully reflected by the chain-length dependence of the viscosity. Overall, there is a factor of about 3.3 between the scaling of τ_{short} and τ_{long}, pointing at a higher mobility of the involved species at short times.

Finally, Figure 10 compares the short-time contribution of the (cc) and (ca) HB lifetimes with the reorientational dynamics of the OH-bond vector and the intramolecular N···O vector on the cation in $[HOC_4Py][NTf_2]$. Reorientational correlation times are computed as integral over time correlation functions

$$R_2(t) = \langle P_2[\vec{e}(0)\cdot\vec{e}(t)]\rangle \quad (8)$$

https://doi.org/10.1021/acs.jpcb.1c02756
J. Phys. Chem. B 2021, 125, 5132−5144

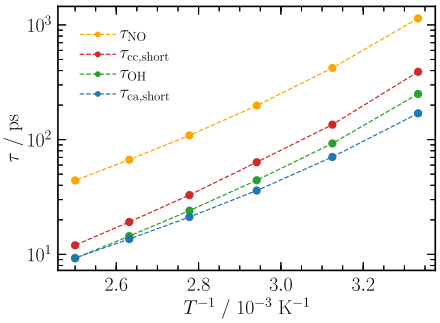

Figure 10. Reorientational correlation times for the OH-bond vector (τ_{OH}) and for the cationic intramolecular N···O vector (τ_{NO}) in comparison with the short time part of the HB lifetime for the (ca) HB ($\tau_{ca,\,short}$) and the (cc) HB ($\tau_{cc,\,short}$) as a function of the inverse temperature T for $[HOC_4Py][NTf_2]$.

where $\vec{e}$ is the unit vector along a particular molecular axis, P_2 is the 2nd Legendre polynomial, and $\langle\cdots\rangle$ indicates a thermal average. Respective reorientational correlation times obtained for all studied ILs and temperatures are available in Table S5 in the Supporting Information. Note that the reorientational correlation times of the hydroxyl group match the short-time (ca) HB lifetimes. This might not be surprising, if after HB breaking, or associated with HB switching, the OH-bond vector performs large angular jumps, similar to what has been observed for short chain alcohols[70] and water.[71,72] A further detailed analysis, following Laage's factorization into a "frame reorientation time" of OH-bonds rotating while staying within intact HBs, and "jump times"[70,72] will be the subject of a separate publication. The reorientation of the alkyl chain, as represented by the "end-to-end" N···O vector, is found to be about a factor of 5 slower than the OH-bond vector reorientation, suggesting that the shape of the $C_{short}(t)$ correlation functions is only partly associated with the reorientation of the entire cation and dominated by the exchange of hydrogen-bonded partners in the more confined, localized environment of the hydroxyl group.

LONG-TIME LIMITING BEHAVIOR: "THE LONG GOOD-BYE"

The HB population correlation functions of hydroxyl-functionalized ILs exhibit two time domains. The long-time behavior is associated with the diffusion process of the individual ions, finally pulling the formerly hydrogen-bonded partners apart. To demonstrate this effect, we have eliminated the global diffusion of the ions by using position restraints. For the case of $[HOC_4Py][NTf_2]$ at 400 K, we have performed MD simulations with position restraints applied to the nitrogen atoms of the anions and cations, respectively. Those atoms were selected since they are located close to the center-of-mass of their respective ions. A harmonic potential

$$V = \frac{k'}{2}\,|\vec{r}_N(t) - \vec{r}_N(0)|^2 \tag{9}$$

with the force constant

$$k' = l{\cdot}k = l{\cdot}[RT/r_{peak}{}^2] \tag{10}$$

was used for this purpose. Here, R is the universal gas constant, T the temperature, and r_{peak} = 0.57 nm the distance of the first peak of the center-of-mass anion−cation pair correlation function at 400 K. The factor l is introduced for controlling the size of the confinement of the ions, with k' being multiples of the force constant k = 10.236 kJ mol^{-1} nm^{-2}. The final configuration of the 100 ns production run of the undisturbed simulation of $[HOC_4Py][NTf_2]$ at 400 K was chosen as the starting point for all simulations with position restraints. *NVT* MD simulations with identical parameters of 100 ns length were conducted, where the value of l was varied between l = 1, 1.5, 2, 4, and 10. For weak restraints with $l \leq 4$, as shown in the Supporting Information, the structure and reorientational correlation functions are only mildly affected. In addition, Figure S3 in the Supporting Information illustrates the effect of the position restraints on the time evolution of the mean square displacement

$$\mathrm{msd}_x(t) = \langle|\vec{r}_x(t) - \vec{r}_x(0)|^2\rangle \tag{11}$$

of the center-of-mass of the ions (x = cms), approaching plateau values after about 10 ns.

Figure 11 shows the effect of position restraints on the (ca) HB population correlation function of $[HOC_4Py][NTf_2]$ at

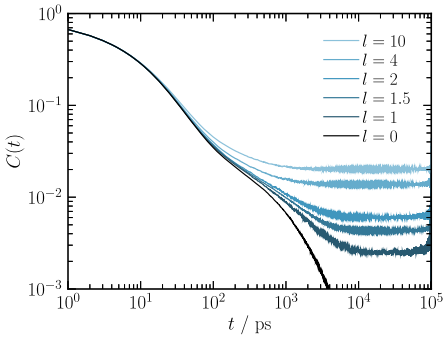

Figure 11. HB population correlation function $C(t)$ for the (ca) HB of the undisturbed $[HOC_4Py][NTf_2]$ at 400 K shown in black, and with position restraints of different strengths $k' = l{\cdot}k$ shown in different shades of blue.

400 K. Without position restraints (k' = 0), the correlation function exhibits two time domains. Applying restraints leads to the emergence of a plateau for long times t without majorly influencing the short-time behavior. Here, the plateau value C_∞ describes the fraction of the time and the initial HB partners spend with each other in equilibrium.[5] Assuming that a selected HB donor switches constantly from one hydrogen-bonded state to another and that the average "residence times" for each hydrogen-bonded configuration are equal, the inverse of the plateau values $C_\infty{}^{-1}$ describes the number of HB acceptors $\langle N_{acc,\,short}\rangle$, accessible to this HB donor

$$C_\infty{}^{-1} = \langle N_{acc,short}\rangle = \rho_{acc} V_{short} \tag{12}$$

Here, ρ_{acc} is the average acceptor site density and V_{short} represents the explored volume, taking into account the interdiffusing behavior of hydroxyl groups and oxygen acceptor sites. In Figure 12a, $C_\infty{}^{-1}$ is plotted versus $[\mathrm{msd}_{OH}(\infty)]^{3/2} \propto V_{short}$, with $\mathrm{msd}_{OH}(\infty)$ being the plateau value of the mean square displacement of the hydroxyl group. The plot indicates a linear relationship, which passes through the origin with a slope of 106.4 nm^3. Figure 12b shows the $\mathrm{msd}_{OH}(\infty)$ as a function of the inverse force constant k'^{-1}. The axis-intersection of 0.316 nm^2 for k'^{-1} = 0 describes the mean square displacement of the OH group in case the global translational dynamics of the ions has been completely

https://doi.org/10.1021/acs.jpcb.1c02756
J. Phys. Chem. B 2021, 125, 5132−5144

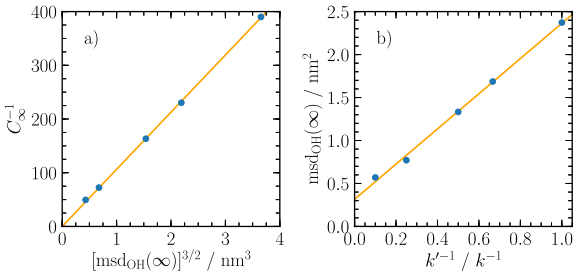

Figure 12. (a) Inverse of the plateau value of the HB population correlation function $C_\infty{}^{-1}$ as a function of mean-square displacement of the hydroxyl group $[msd_{OH}(\infty)]^{3/2}$ for l = 1, 1.5, 2, 4, and 10. The orange line describes a fit, with a slope of 106.4 nm^{-3} indicating the linear relation between the number of accessible HB acceptors and the volume explored by the HB donor, starting in the origin. (b) Mean-square displacement of the hydroxyl group $msd_{OH}(\infty)$ as a function of the inverse force constant used for position restraints $k'^{-1}/k^{-1} = l^{-1}$, extrapolating to a value of $msd_{OH}(\infty)$ = 0.316 nm^2 for k'^{-1} = 0.

eradicated. Note that the corresponding value of $C_\infty(k^{-1} \to 0) = 1/[106.4 \times 0.316^{3/2}] = 0.053$ is close to the plateau value of the fitted $C_{short}(t)$ with 0.048. Given that the transition between short-time behavior and long-time behavior of $C(t)$ for $[HOC_4Py][NTf_2]$ at 400 K is located between 100 and 200 ps and that the plateau value is ≈0.05, an average "residence time" for each hydrogen-bonded state between 5 and 10 ps can be estimated, which is, admittedly, a rather crude approach.

It has been demonstrated that the long-time behavior of the HB population correlation function in an unrestricted three-dimensional environment follows a $t^{-3/2}$ scaling law,[73,74] which also follows directly from solving Fick's equation for an instantaneous point source assuming an isotropic and homogeneous diffusion coefficient.[75] In addition, for particles hopping between discrete bonded states, we find that the long-time behavior can be quantitatively expressed by

$$\lim_{t\to\infty} C(t) = \frac{1}{s\rho_{acc}(4\pi D' t)^{3/2}} \tag{13}$$

where D' is the interdiffusion coefficient $D' = D_{donor} + D_{acceptor}$ (available from the Supporting Information of ref 34), $\rho_{acc} \approx 10.15$ nm^{-3} is the acceptor-site density (here $5 \times 512/\langle V_{box}\rangle$). s is a scaling parameter, depending on the topology of the "network" of HB accepting sites, formed by the HB switching pathways interconnecting adjacent sites. For instance, a random walker on a primitive cubic lattice with six next neighbors is described by s = 1/2 (see Figure S11 in the Supporting Information). Here, we use s = 1.2, as demonstrated by the matched $t^{-3/2}$ behavior of the straight orange lines shown in Figure 13. Keep in mind that the parameter $(s\rho_{acc})^{-1}$ is essentially assigning a volume to the initial hydrogen-bonded state $h(0)$. Note also, however, that for short times, eq 13 leads to unphysical results with $C(t) > 1$.

A more appropriate description of the long-time behavior follows from a division of the volume surrounding a hydrogen-bonded pair into a "local domain", characterized by a radius R_s and the volume outside this sphere. Assuming that the particles move (infinitely) fast within the local domain and that the flux from inside the local domain toward the outside happens at a rate that corresponds exactly to the rate at which a normally diffusing particle would leave the sphere, we obtain the

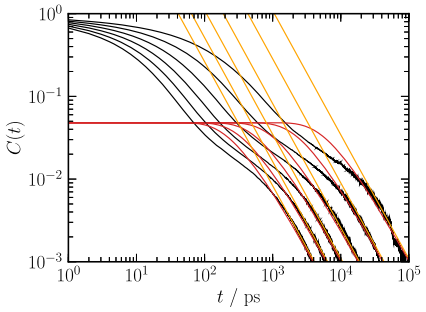

Figure 13. Solid black lines: HB population correlation function $C(t)$ for the (ca) HB of $[HOC_4Py][NTf_2]$ at 400, 380, 360, 340, 320, and 300 K, respectively. Solid orange lines: Long-time limiting behavior $\lim_{t\to\infty} C(t)$ according to eq 13. Solid red lines: long-time behavior according to eq 14.

following analytical expression describing the long-time behavior

$$C_{long}(t) = A_1 \mathrm{erf}\left[\frac{R_s}{\sqrt{4D't}}\right] - \frac{A_1 R_s}{\sqrt{\pi D' t}} \exp\left[-\frac{R_s{}^2}{4D't}\right] \tag{14}$$

Here, A_1 accounts for the particle being equally shared among all the sites within the "local domain" with $A_1 = 3/(s\rho_{acc}4\pi R_s{}^3)$. Of course, with $A_1 = 1$ and $D' = D_{self}$, eq 14 just represents the analytical solution for the probability of a diffusing particle, with a self-diffusion coefficient D_{self}, to be found within a sphere of radius R_s around the position of the particle at time t = 0. Note that the parameter s has exactly the same meaning and size as in eq 13. Plots according to eq 14 with R_s = 0.741 nm (corresponding to a prefactor of 0.048) are shown in Figure 13. For $t \to \infty$, eq 14 approaches asymptotically $t^{-3/2}$ behavior. As shown in the Supporting Information, eq 14 also correctly represents the chain length dependence of $C(t)$ for the (ca) HBs, based on the changing diffusion coefficients and densities and indicated by Figure S6. The correct representation of the behavior (cc) HBs for $n < 4$, however, requires an adjustment of the factor s (see Figure S7), to account for the significantly diminished return-probability, once the strained (cc) HBs have been broken. As it will be demonstrated in the following section, short-time diffusion within the local domain is faster than on the outside but certainly not infinitely fast. Thus, by describing the local diffusion process more realistically, we will also need to find an appropriate description of the entire $C(t)$, including $C_{short}(t)$.

Finally, we want to comment on the procedure how we have determined the HB lifetimes. As we have demonstrated here, the empirical KWW functions used in section, although being able of quantitatively describing the function $C(t)$ for $C(t) \geq 10^{-3}$, lead to an inappropriate description of the long-time limiting behavior. However, replacing the KWW functions by $C_{long}(t)$ for $C(t) \leq 10^{-3}$ affects the computed lifetimes given in Table S8 by less than 1%. Therefore, we did not see the need to recompute those lifetimes.

DESCRIBING BOTH SHORT- AND LONG-TIME BEHAVIOR BY RANDOM WALKS

To represent the entire function $C(t)$, Chen et al.[73] have suggested a method based on a distance-dependent-diffusion coefficient. Their approach is catering to an enhanced short-time mobility of the involved particles. Here, we observe a similar behavior: as shown in Figure 14a, at short times, the

https://doi.org/10.1021/acs.jpcb.1c02756
J. Phys. Chem. B 2021, 125, 5132−5144

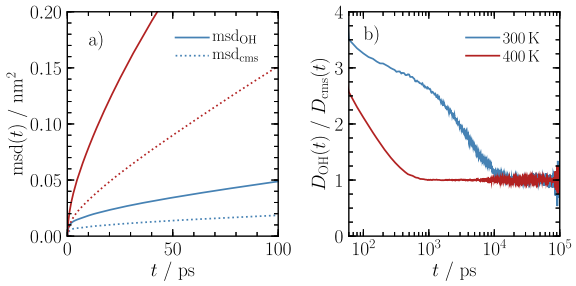

Figure 14. (a) Short-time mean-square displacement of the hydroxyl group $\mathrm{msd}_{OH}(t)$ (full line) and the center-of-mass $\mathrm{msd}_{cms}(t)$ (dotted line) of the $[HOC_4Py]^+$ cation for 300 K (blue) and 400 K (red). (b) Relative, time-dependent self-diffusion coefficient of the hydroxyl group, quantifying the enhanced mobility of the hydroxyl group with respect to the mobility of the cation. Here, $D_x(t) = (1/6)(\partial/\partial t)\mathrm{msd}_x(t)$ with x = OH, cms.

depicted mean square displacements of the entire cation and the hydroxyl group are characterized by steeper slopes, suggesting a higher mobility. In addition, the mean square displacement of the hydroxyl group significantly outpaces the center-of-mass motion of the cation. This is likely due to the flexibility of the alkyl chain and assisted by reorientational motions of the cation. The enhanced mobility is quantified by the ratio of time-dependent self-diffusion coefficients $D_{OH}(t)/D_{cms}(t)$ of the $[HOC_4Py]^+$ cation shown in Figure 14b. A roughly threefold enhanced diffusivity of the hydroxyl group at short times is observed. The period of enhanced diffusivity lasts to about 10^4 ps at 300 K and to about 500 ps at 400 K, coinciding with the times after which the (ca) HB population correlation function has switched over to the long-time behavior (see Figure 4a for comparison). Unfortunately, we find that the computed HB population correlation functions $C(t)$ using the approach of Chen et al.[73] (not shown) are lacking a well-defined separation into two-time domains.

Therefore, by distilling what we have learned about the motions of the HB partners so far, we introduce a minimalist model capable of realistically describing the HB population correlation functions. The model is illustrated in Figure 15 and

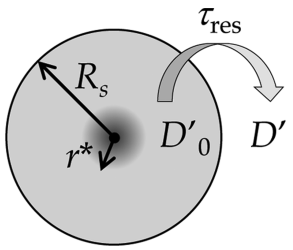

Figure 15. Schematic representation of the minimalist model used to describe the time evolution of the HB population correlation functions.

consists of two domains. At short times, the particle is confined to a "local domain" and possesses an enhanced diffusivity D_0'. After an average residence time τ_{res}, the particle can leave the local domain. The model is "solved" by sampling over many trajectories produced by random walkers. Each walker starts at the origin at $t = 0$ in a hydrogen-bonded state ($h(0) = 1$). New coordinates are computed for discrete time intervals δt from $\vec{r}(t + \delta t) = \vec{r}(t) + \vec{d}$, where $\vec{d}$ is vector with random orientation and $|\vec{d}| = (6D_{jump}\delta t)^{1/2}$. A "hydrogen-bonded" state $h(t)$ is detected applying a distance-dependent HB criterion, which is fulfilled if $u \le A^* \times \exp[-|\vec{r}(t) - \vec{r}(0)|/r^*]$, where $u \in [0, 1]$ is a uniform random deviate. For times shorter than the residence time $t \le t_{res}$, the local domain is preserved by confining the walker to a spherical volume with radius R_s by means of a reflective wall. Within the local domain, the walker moves with an enhanced mobility $D_{jump} = D_0'$. For times $t > t_{res}$, the reflective wall disappears, and the particles progress with $D_{jump} = D' = (D_{cat} +$ Dani). For each trajectory, the residence times are sampled from a Poisson distribution $t_{res} = -\tau_{res} \times \ln(u)$, where $u \in [0, 1]$ is another uniform random deviate, thus mimicking a first order kinetic for leaving the local domain. The average residence time τ_{res} was designed to be related to the diffusion coefficient via $\tau_{res} = d_{res}^2/D'$ with $d_{res} = 0.3$ nm. A Fortran implementation of the algorithm can be found in section S10 of the Supporting Information. We sample over 5×10^6 trajectories to obtain the data shown in Figures 16 and 17.

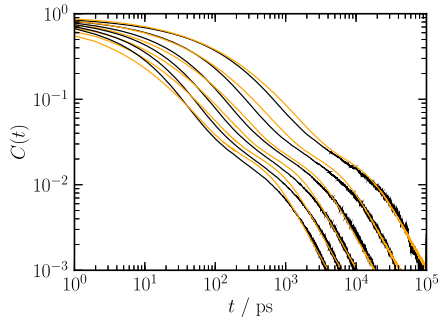

Figure 16. HB population correlation functions $C(t)$ for (ca) HBs obtained for $[HOC_4Py][NTf_2]$ at 300, 320, 340, 360, 380, and 400 K, respectively. Orange lines: minimalist model predictions with R_s = 1.05 nm, A^* = 0.97, r^* = 0.15 nm, $D_0' = 3.3 \times D'$, and $\tau_{res} = d_{res}^2/D'$ with d_{res} = 0.3 nm.

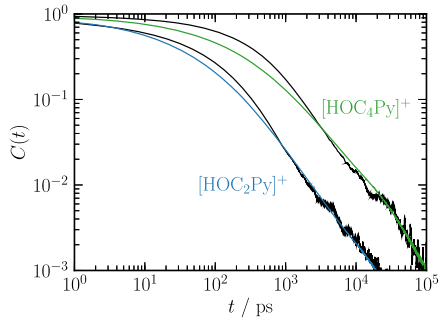

Figure 17. HB population correlation functions $C(t)$ for (cc) HBs obtained for $[HOC_2Py][NTf_2]$ and $[HOC_4Py][NTf_2]$ at 300 K. Green and blue: minimalist model predictions with R_s = 1.3 nm, A^* = 0.97, $D_0' = 2.0 \times D'$, and $\tau_{res} = d_{res}^2/D'$ with d_{res} = 0.3 nm. Green: r^* = 0.15 nm. Blue: r^* = 0.085 nm.

We would like to point out that the parameters cannot be chosen randomly. The parameters A^* and r^*, for example, play the same role here as the factor $s \cdot \rho_{acc}$ in eqs 13 and 14 by essentially assigning a volume to each hydrogen-bonded state and thus being responsible for the correct description of $\lim_{t\to\infty} C(t)$. Moreover, the ratio of r^* and R_s determines the location of the plateau value of $C(t)$. To describe the temperature dependence of $C(t)$ for $[HOC_4Py][NTf_2]$

https://doi.org/10.1021/acs.jpcb.1c02756
J. Phys. Chem. B 2021, 125, 5132−5144

shown in Figure 16, the scaling of the enhanced local diffusivity $D_0' = 3.3D'$ was chosen to exactly match the different response of short- and long-time HB lifetimes to the viscosity, as shown in Figure 9. Judging the domain size parameter R_s, we have to keep in mind that it has to account for both, the movement of the hydroxyl group as well as the movement of the HB acceptors.

Note that the temperature dependence for $C(t)$ for (ca) HBs, as shown in Figure 16, is reproduced very satisfactorily, considering that all parameters except $D' = (D_{donor} + D_{acceptor})$ (taken from the Supporting Information of ref 34) are kept unchanged. The same is true for the chain length dependence shown in Figure 17. To represent (cc) HBs, however, the size of the local domain needs to be enlarged, catering to the effect that both hydroxyl groups (donor and acceptor) explore large volumes each, with the ratio $(1.3/1.05)^3 \approx 2$. In addition, the intradomain diffusion needs to be reduced to $D_0' = 2D'$. For properly describing, the chain length dependence for $[HOC_2Py][NTf_2]$, shown in Figure 17, also r^* has to be adjusted as discussed earlier. We would like to mention that the accuracy of representing the MD data via our model could be improved by introducing a distribution of domain sizes instead of a fixed radius R_s, and by finetuning the functional form of the distance-dependent HB acceptance criterion. We did not do this here in favor of a simpler model, better serving its educational purpose.

"ALL HB LIFETIMES, GREAT AND SMALL": COMPARING WITH THE REACTIVE FLUX APPROACH

In the previous sections, we have discussed the HB dynamics and lifetimes based on the "intermittent" picture, considering the possibility of a meanwhile disconnected state between hydrogen-bonded partners. Hence, the shape of the computed HB population correlation function is affected by the detailed nature of the "random walk" of the hydroxyl groups, exploring their local environment, constantly switching between adjacent HB acceptors. In this section, we have made an estimate about the lifetimes of those individual short-lived hydrogen-bonded states, based on the observation that $C_{short}(t)$ is decaying to a plateau value, and providing us with a number of hydrogen-bonded states visited on the τ_{short} time scale. This showed that the individual "residence times" are in the order of about 10 ps for $[HOC_4Py][NTf_2]$ at 400 K.

A more rigorous approach to determine the short-term HB kinetics is the reactive flux method.[3−5] Starting from the definition of the HB population correlation function $C(t)$ given in eq 1 and applying the time inversion symmetry $dC(t)/dt = -dC(-t)/dt$ and the stationary condition,[4] $\langle \dot{h}(0) \rangle = 0$, $C(t)$ is related to the reactive flux correlation function via

$$k(t) = -\frac{dC(t)}{dt} = -\frac{\langle \dot{h}(0)[1 - h(t)] \rangle}{\langle h \rangle (1 - \langle h \rangle)} \tag{15}$$

where $\dot{h}(0)$ is the integrated flux departing the HB configuration space at time zero.[3] The function $k(t)$ is the average of this integrated flux for those trajectories where the bond is broken at a later time t. The time-dependent rate constant $k(t)$ measures the reactive flux for trajectories, where the bond between a tagged pair of molecules is broken at a time t later. For all trajectories that are passing the transition interface in the reactive direction (HB breaking) and end up in the dissociated state for a long time and never recross, the transition state for bond reforming is the zero time value of the rate of relaxation.[5,76] $\lim_{t \to 0^+} k(t) = k_{TST} = \tau_{TST}^{-1}$. Within the TST approximation, recrossings are not allowed; therefore, k_{TST} represents an upper boundary for the rate of HB breaking. Since some fraction of trajectories may cross the dividing surface more than once during the transition between reactant and product states, this recrossing dynamics reduces $k(t)$ from k_{TST}. The reduction can be expressed in terms of a time-dependent transmission coefficient $\kappa(t) = k(t)/k_{TST}$. Of course, for times much longer than the transient relaxation dynamics of HB breaking, $k(t)$ and, hence $\kappa(t)$ are also affected by diffusion processes.

The influence of diffusion can be eliminated with the help of a second state in which a tagged pair is not connected via a HB but is still within a distance that it could be reformed. This is achieved by a vicinity operator $H(t)$, with $H(t) = 1$ if the distance between the acceptor and donor atom is smaller than a certain cutoff, and $H(t) = 0$ otherwise. On the basis of the time invariance of the autocorrelation function, one can define a function of bond reformation[4]

$$k_{in}(t) = -\frac{\langle \dot{h}(0)[1 - h(t)]H(t) \rangle}{\langle h \rangle (1 - \langle h \rangle)} \tag{16}$$

The integral

$$N(t) = \int_0^t k_{in}(t')dt' \tag{17}$$

gives the probability of finding a certain pair of atoms initially connected by a HB at time $t = 0$, not being bonded anymore, but still in the vicinity at time t. From this, one obtains the rate of decay k_d and the rate of reformation k_f by fitting the coefficients of a linear combination of functions $C(t)$ and $N(t)$ to the kinetic equation[4]

$$k(t) = k_d C(t) - k_f N(t) \tag{18}$$

Following Gehrke and Kirchner,[17] we have modified the two parameters k_d and k_f stepwise in a way that the root-mean-square deviation according to eq 18 is minimized. As it has been pointed out earlier,[5,16] the ultrashort time scale is also ignored here, to avoid disturbances according to bond vibration and libration effects. Final values were accepted with a tolerance of 10^{-14}. The inverse of the rate constant k_d denotes the average lifetime of a HB $\tau_{hb,d} = k_d^{-1}$.

In order to be able to numerically solve eq 18, the state defined by the vicinity operator $H(t)$ has to be designed properly. Following Luzar and Chandler, we used the oxygen−oxygen distance as a criterion for both, (ca) and (cc) HBs. The cutoff-distance r_{OO} was chosen such that the h-states are a subset of H and that the average fraction of hydrogen-bonded states $\langle h \cdot H \rangle / \langle H \rangle \approx 30\%$. These values were obtained by re-examining SPC water simulations using the same conditions as reported by Luzar and Chandler.[3] These conditions are matched by values of $r_{OO} \leq 0.48$ nm for (ca) HBs and $r_{OO} \leq 0.41$ nm for (cc) HBs. Only modest variations of the percentages for different chain length n are observed. In addition, the deduced lifetimes $\tau_{hb,d} = k_d^{-1}$ are found to be largely unaffected by variations of the cutoff criteria for H, whereas k_f, of course, is found to depend on the "size" of the H-state.

We have analyzed the reactive flux correlation functions for two ILs, $[HOC_2Py][NTf_2]$ and $[HOC_4Py][NTf_2]$ and for

https://doi.org/10.1021/acs.jpcb.1c02756
J. Phys. Chem. B 2021, 125, 5132−5144

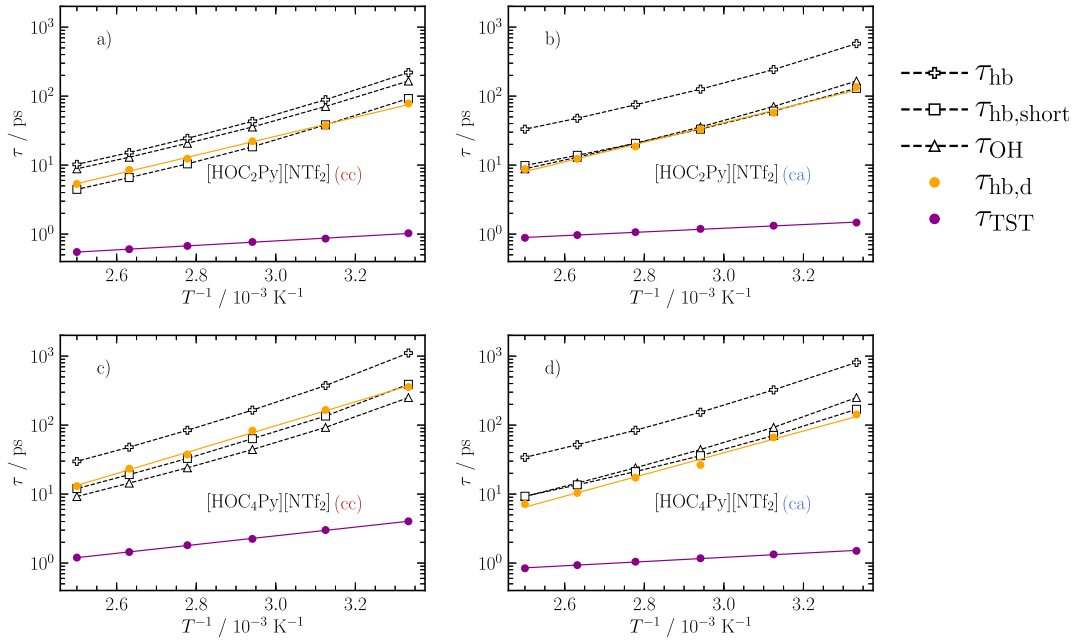

Figure 18. (cc) and (ca) HB lifetimes for HB breaking $\tau_{hb,d} = k_d^{-1}$, and τ_{TST} determined via the Luzar−Chandler approach compared with HB lifetimes τ_{hb} and $\tau_{hb,\,short}$ obtained via integrating $C(t)$ and C_{short}, respectively, and the OH-bond vector reorientation correlation time τ_{OH}. Top panels: $[HOC_2Py][NTf_2]$. Bottom panels: $[HOC_4Py][NTf_2]$. Left panels: (cc). Right panels: (ca). Dashed lines linearly connect adjacent data points. Solid lines represent Arrhenius fits.

both, (ca) and (cc) HBs. The corresponding lifetimes $\tau_{hb,\,d}$ and τ_{TST} are shown in Figure 18 and are given in Table S9 in the Supporting Information. An exemplary analysis of the kinetics of (cc) and (ca) HBs for $[HOC_4Py][NTf_2]$ at 400 K including $k(t)$, $k_{in}(t)$, and a correlation plot of $k(t)$ versus $k_d\ C(t) - k_f\ N(t)$ is given in Figures S9 and S10 in the Supporting Information. From the data shown in Figure 18, it is obvious that recrossing events during the transient relaxation period strongly affect the HB lifetimes. Here, τ_{TST} is found to be between one and two orders of magnitude smaller than $\tau_{hb,\,d}$, which is in accordance with earlier observations made for HBs in non-hydroxyl-functionalized imidazolium-based ILs.[16,17] Note also that both $\tau_{hb,\,d}$ and τ_{TST} follow an Arrhenius behavior. Such a behavior has also been reported numerous times for water[5] and imidazolium-based ILs.[17] Hence, the kinetics of HB breaking is apparently rather unaffected by collective motions associated with rearrangements in its environment. The temperature dependence of the transmission coefficient $\kappa(t)$ plays an important role for the kinetics of HB breaking since the activation energy of $\tau_{hb,\,d}$ is found to be between three and six times larger than the activation energy τ_{TST} (see Table S10 for details). For (ca) HBs in $[HOC_4Py][NTf_2]$, we obtain a lifetime for HB breaking of 7.2 ps, which matches well the crude estimate made in section.

Figure 18 shows that that τ_{short} according to the "intermittent picture" roughly match the same time range and temperature dependence as the $\tau_{hb,\,d}$ determined via the reactive flux formalism. We find this coincidence remarkable since it seems to hold for both (ca) and (cc) HBs, as well as for varying chain lengths. However, the coincidence is not perfect: for (cc) HBs, the τ_{short} appear to be systematically slightly shorter, whereas for (ca) HBs, larger or equally sized. It cannot be ruled out that this coincidence is merely accidental since the strongly non-monoexponential $C_{short}(t)$ are subject to a fast quenching and slow decay toward equilibrium due to diffusion processes in the local domain, whereas contributions from diffusion have been ruled out for $\tau_{hb,\,d}$.

For both, $[HOC_2Py][NTf_2]$ and $[HOC_4Py][NTf_2]$ the reorientational correlation times τ_{OH} are located in the vicinity of $\tau_{hb,\,d}$ for (ca) HBs. We would like to point out that the τ_{OH} represent an average over all different hydrogen-bonded states as well as non-bonded states. It is likely to assume that τ_{OH} recorded solely for (cc) hydrogen-bonded configurations would be larger than the average values shown here. Therefore, we believe that the fact that the τ_{OH} being smaller than the respective $\tau_{hb,\,d}$ in Figure 18a,c has no deeper meaning. A detailed analysis of the variation of the OH-bond vector reorientational dynamics in relation hydrogen bonding will be the subject of a separate publication.

CONCLUSIONS

Hydroxyl-functionalized ILs represent an interesting new class of ILs where hydrogen bonding plays a significant role. In these ILs, two types of HBs can be identified: "typical" (ca) HBs between anions and cations and "atypical" (cc) HBs connecting two cations. Here, we have investigated 1-(*n*-hydroxyalkyl)-pyridinium bis(trifluoromethylsulfonyl)imide $[HOC_nPy][NTf_2]$ ILs which show a pronounced (cc) HB formation. Recent IR experiments have been suggesting that the (cc) HBs in those ILs are stronger than the (ca) HBs, indicated by a significant redshift of their corresponding IR bands.[29−31] Our MD simulations confirm the presence of both types of HBs. In addition, we can also confirm an enthalpic stabilization of (cc) HBs over (ca) HBs. This stabilization is found to increase for longer alkyl chains and maxes out for $[HOC_4Py][NTf_2]$ at $\Delta H^\circ = -3.75$ kJ mol^{-1}. This is, however, counterbalanced by an entropy penalty of $\Delta S^\circ = -22.9$ J K^{-1} mol^{-1}.

We have studied the HB kinetics of each of these HBs via HB population and reactive flux correlation functions.

https://doi.org/10.1021/acs.jpcb.1c02756
J. Phys. Chem. B 2021, 125, 5132−5144

Respective HB lifetimes are available either as integrals over HB population correlation functions or as inverse rates of HB breaking, deduced from a kinetic equation outlined in eq 18.

For the case of hydroxyl-functionalized ILs, we have to deal with four different HB lifetimes, each valid in its own right, and each associated with different aspects of HB breaking and HB reformation: the TST approximation τ_{TST} represents the "speed-limit" for HB kinetics in the sense that they characterize the fastest possible way to break a HB. Here, the τ_{TST} ranges from the subpicosecond time scale to a few picoseconds and shows a relatively weak temperature dependence. The lifetimes $\tau_{hb,d}$ essentially represent the kinetics of HB breaking while allowing for (many) recrossing-events during the transient relaxation time period associated with HB breaking, albeit still unaffected by diffusion processes. The $\tau_{hb,d}$ ranges from below 10 ps to a few hundred picoseconds and exhibits a much stronger temperature dependence than the τ_{TST}. The τ_{short} represent the lifetimes including contributions due the exchange of hydrogen-bonded partners within the close neighborhood. Their size matches the time range and temperature dependence of $\tau_{hb,d}$ rather well. However, it cannot be ruled out that this coincidence is merely accidental. The largest available HB lifetime τ_{hb} ultimately encompasses all previously discussed phenomena: transient kinetics, local, and global diffusion events. Those τ_{hb} extend into the nanosecond time domain. As elaborated in great detail in this paper, the latter two lifetimes represent integrals over complicated non-mono-exponential functions and are prone to details of the local and global dynamics of the respective hydrogen-bonded partners, which can be realistically described via a kinetic two domain model outlined in this paper. Almost three orders of magnitude lie between the shortest and the largest of those lifetimes, associated with different aspects of HB breaking and HB reformation and also being connected to different realms of experimental techniques or methodologies. Finally, for sufficiently long alkyl chains, all those computed HB lifetimes indicate a higher kinetic stability of (cc) HBs compared to (ca) HBs, whereas for short alkyl chains the opposite is true.

■ ASSOCIATED CONTENT

Supporting Information

The Supporting Information is available free of charge at https://pubs.acs.org/doi/10.1021/acs.jpcb.1c02756.

MD simulations; simulated and experimental density and viscosity data; reorientational correlation times; fits of the computed HB population correlation functions; computed HB lifetimes; and FORTRAN program of the employed random walker model (PDF)

■ AUTHOR INFORMATION

Corresponding Authors

Ralf Ludwig − *Institut für Chemie, Abteilung Physikalische und Theoretische Chemie, Universität Rostock, D-18059 Rostock, Germany; Department Life, Light & Matter, Universität Rostock, D-18059 Rostock, Germany; Leibniz Institut für Katalyse an der Universität Rostock, D-18059 Rostock, Germany;* orcid.org/0000-0002-8549-071X; Email: ralf.ludwig@uni-rostock.de

Dietmar Paschek − *Institut für Chemie, Abteilung Physikalische und Theoretische Chemie, Universität Rostock, D-18059 Rostock, Germany;* orcid.org/0000-0002-0342-324X; Email: dietmar.paschek@uni-rostock.de

Author

Jan Neumann − *Institut für Chemie, Abteilung Physikalische und Theoretische Chemie, Universität Rostock, D-18059 Rostock, Germany*

Complete contact information is available at: https://pubs.acs.org/10.1021/acs.jpcb.1c02756

Notes

The authors declare no competing financial interest.

■ ACKNOWLEDGMENTS

The authors thank Anika Wilhelms for performing the density and viscosity measurements and Johanna Busch for her contribution to the TOC entry. The authors thank the computer center at the University of Rostock (ITMZ) for providing and administrating computational resources. The authors also thank the Leibniz Association, the State of Mecklenburg-Vorpommern, and the University of Rostock for financial support within the ComBioCat programme. This work was supported by the DFG Research grant LU-506/14-2 (no. 286149019).

■ REFERENCES

(1) Ludwig, R. Water: From clusters to the bulk. *Angew. Chem., Int. Ed.* **2001**, *40*, 1808−1827.
(2) Stillinger, F. H. Water Revisited. *Science* **1980**, *209*, 451−457.
(3) Luzar, A.; Chandler, D. Effect of environment on hydrogen bond dynamics in liquid water. *Phys. Rev. Lett.* **1996**, *76*, 928−931.
(4) Luzar, A.; Chandler, D. Hydrogen-bond kinetics in liquid water. *Nature* **1996**, *379*, 55−57.
(5) Luzar, A. Resolving the hydrogen bond dynamics conundrum. *J. Chem. Phys.* **2000**, *113*, 10663−10675.
(6) Aggarwal, A.; Lancaster, N. L.; Sethi, A. R.; Welton, T. The role of hydrogen bonding in controlling the selectivity of Diels-Alder reactions in room-temperature ionic liquids. *Green Chem.* **2002**, *4*, 517−520.
(7) Crowhurst, L.; Lancaster, N. L.; Pérez Arlandis, J. M.; Welton, T. Manipulating Solute Nucleophilicity with Room Temperature Ionic Liquids. *J. Am. Chem. Soc.* **2004**, *126*, 11549−11555.
(8) Bini, R.; Chiappe, C.; Mestre, V. L.; Pomelli, C. S.; Welton, T. A rationalization of the solvent effect on the Diels-Alder reaction in ionic liquids using multiparameter linear solvation energy relationships. *Org. Biomol. Chem.* **2008**, *6*, 2522−2529.
(9) Dong, K.; Zhang, S.; Wang, J. Understanding the hydrogen bonds in ionic liquids and their roles in properties and reactions. *Chem. Commun.* **2016**, *52*, 6744−6764.
(10) Hayes, R.; Warr, G. G.; Atkin, R. Structure and Nanostructure in Ionic Liquids. *Chem. Rev.* **2015**, *115*, 6357−6426.
(11) Kempter, V.; Kirchner, B. The role of hydrogen atoms in interactions involving imidazolium-based ionic liquids. *J. Mol. Struct.* **2010**, *972*, 22−34.
(12) Hunt, P. A.; Ashworth, C. R.; Matthews, R. P. Hydrogen bonding in ionic liquids. *Chem. Soc. Rev.* **2015**, *44*, 1257−1288.
(13) Paschek, D.; Golub, B.; Ludwig, R. Hydrogen bonding in a mixture of protic ionic liquids: a molecular dynamics simulation study. *Phys. Chem. Chem. Phys.* **2015**, *17*, 8431−8440.
(14) Skarmoutsos, I.; Dellis, D.; Matthews, R. P.; Welton, T.; Hunt, P. A. Hydrogen Bonding in 1-Butyl- and 1-Ethyl-3-methylimidazolium Chloride Ionic Liquids. *J. Phys. Chem. B* **2012**, *116*, 4921−4933.
(15) Skarmoutsos, I.; Welton, T.; Hunt, P. A. The importance of timescale for hydrogen bonding in imidazolium chloride ionic liquids. *Phys. Chem. Chem. Phys.* **2014**, *16*, 3675−3685.
(16) Gehrke, S.; von Domaros, M.; Clark, R.; Hollóczki, O.; Brehm, M.; Welton, T.; Luzar, A.; Kirchner, B. Structure and lifetimes in ionic liquids and their mixtures. *Faraday Discuss.* **2018**, *206*, 219−245.

(17) Gehrke, S.; Kirchner, B. Robustness of the hydrogen bond and ion pair dynamics in ionic liquids to different parameters from the reactive flux method. *J. Chem. Eng. Data* **2020**, *65*, 1146−1158.
(18) Strate, A.; Neumann, J.; Overbeck, V.; Bonsa, A.-M.; Michalik, D.; Paschek, D.; Ludwig, R. Rotational and translational dynamics and their relation to hydrogen bond lifetimes in an ionic liquid by means of NMR relaxation time experiments and molecular dynamics simulation. *J. Chem. Phys.* **2018**, *148*, 193843.
(19) Katsyuba, S. A.; Vener, M. V.; Zvereva, E. E.; Fei, Z.; Scopelliti, R.; Laurenczy, G.; Yan, N.; Paunescu, E.; Dyson, P. J. How strong is hydrogen bonding in ionic liquids? Combined X-ray crystallographic, infrared/Raman spectroscopic, and density functional theory study. *J. Phys. Chem. B* **2013**, *117*, 9094−9105.
(20) Fakhraee, M.; Zandkarimi, B.; Salari, H.; Gholami, M. R. Hydroxyl-functionalized 1-(2-hydroxyethyl)-3-methyl imidazolium ionic liquids: thermodynamic and structural properties using molecular dynamics simulations and ab initio calculations. *J. Phys. Chem. B* **2014**, *118*, 14410−14428.
(21) Panja, S. K.; Haddad, B.; Kiefer, J. Clusters of the Ionic Liquid 1-Hydroxyethyl-3-methylimidazolium Picrate: From Theoretical Prediction in the Gas Phase to Experimental Evidence in the Solid State. *ChemPhysChem* **2018**, *19*, 3061−3068.
(22) Knorr, A.; Ludwig, R. Cation-cation clusters in ionic liquids: Cooperative hydrogen bonding overcomes like-charge repulsion. *Sci. Rep.* **2015**, *5*, 17505.
(23) Knorr, A.; Fumino, K.; Bonsa, A.-M.; Ludwig, R. Spectroscopic evidence of 'jumping and pecking' of cholinium and H-bond enhanced cation−cation interaction in ionic liquids. *Phys. Chem. Chem. Phys.* **2015**, *17*, 30978−30982.
(24) Knorr, A.; Stange, P.; Fumino, K.; Weinhold, F.; Ludwig, R. Spectroscopic Evidence for Clusters of Like-Charged Ions in Ionic Liquids Stabilized by Cooperative Hydrogen Bonding. *ChemPhysChem* **2016**, *17*, 458−462.
(25) Strate, A.; Niemann, T.; Michalik, D.; Ludwig, R. When like charged ions attract in ionic liquids: Controlling the formation of cationic clusters by the interaction strength of the counterions. *Angew. Chem., Int. Ed.* **2017**, *56*, 496−500.
(26) Strate, A.; Niemann, T.; Ludwig, R. Controlling the kinetic and thermodynamic stability of cationic clusters by the addition of molecules or counterions. *Phys. Chem. Chem. Phys.* **2017**, *19*, 18854−18862.
(27) Niemann, T.; Zaitsau, D.; Strate, A.; Villinger, A.; Ludwig, R. Cationic clustering influences the phase behaviour of ionic liquids. *Sci. Rep.* **2018**, *8*, 14753.
(28) Menges, F. S.; Zeng, H. J.; Kelleher, P. J.; Gorlova, O.; Johnson, M. A.; Niemann, T.; Strate, A.; Ludwig, R. Structural Motifs in Cold Ternary Ion Complexes of Hydroxyl-Functionalized Ionic Liquids: Isolating the Role of Cation−Cation Interactions. *J. Phys. Chem. Lett.* **2018**, *9*, 2979−2984.
(29) Niemann, T.; Strate, A.; Ludwig, R.; Zeng, H. J.; Menges, F. S.; Johnson, M. A. Spectroscopic Evidence for an Attractive Cation−Cation Interaction in Hydroxy-Functionalized Ionic Liquids: A Hydrogen-Bonded Chain-like Trimer. *Angew. Chem., Int. Ed.* **2018**, *57*, 15364−15368.
(30) Strate, A.; Overbeck, V.; Lehde, V.; Neumann, J.; Bonsa, A.-M.; Niemann, T.; Paschek, D.; Michalik, D.; Ludwig, R. The influence of like-charge attraction on the structure and dynamics of ionic liquids: NMR chemical shifts, quadrupole coupling constants, rotational correlation times and failure of Stokes−Einstein−Debye. *Phys. Chem. Chem. Phys.* **2018**, *20*, 5617−5625.
(31) Niemann, T.; Strate, A.; Ludwig, R.; Zeng, H. J.; Menges, F. S.; Johnson, M. A. Cooperatively enhanced hydrogen bonds in ionic liquids: closing the loop with molecular mimics of hydroxy-functionalized cations. *Phys. Chem. Chem. Phys.* **2019**, *21*, 18092−18098.
(32) Niemann, T.; Neumann, J.; Stange, P.; Gärtner, S.; Youngs, T. G. A.; Paschek, D.; Warr, G. G.; Atkin, R.; Ludwig, R. The double-faced nature of hydrogen bonding in hydroxyl-functionalized ionic liquids shown by neutron diffraction and molecular dynamics simulations. *Angew. Chem., Int. Ed.* **2019**, *58*, 12887−12892.
(33) Zeng, H. J.; Menges, F. S.; Niemann, T.; Strate, A.; Ludwig, R.; Johnson, M. A. Chain Length Dependence of Hydrogen Bond Linkages between Cationic Constituents in Hydroxy-Functionalized Ionic Liquids: Tracking Bulk Behavior to the Molecular Level with Cold Cluster Ion Spectroscopy. *J. Phys. Chem. Lett.* **2020**, *11*, 683−688.
(34) Neumann, J.; Paschek, D.; Strate, A.; Ludwig, R. Kinetics of Hydrogen Bonding between Ions with Opposite and Like Charges in Hydroxyl-Functionalized Ionic Liquids. *J. Phys. Chem. B* **2021**, *125*, 281−286.
(35) Strate, A.; Neumann, J.; Niemann, T.; Stange, P.; Khudozhitkov, A. E.; Stepanov, A. G.; Paschek, D.; Kolokolov, D. I.; Ludwig, R. Counting cations involved in cationic clusters of hydroxy-functionalized ionic liquids by means of infrared and solid-state NMR spectroscopy. *Phys. Chem. Chem. Phys.* **2020**, *22*, 6861−6867.
(36) Chandler, R. T. *The Long Goodbye*; Hamish Hamilton: London, U.K., 1953.
(37) Castner, E. W., Jr.; Chang, Y. J.; Chu, Y. C.; Walrafen, G. E. The intermolecular dynamics of liquid water. *J. Chem. Phys.* **1995**, *102*, 653−659.
(38) Rey, R.; Møller, K. B.; Hynes, J. T. Hydrogen Bond Dynamics in Water and Ultrafast Infrared Spectroscopy. *J. Phys. Chem. A* **2002**, *106*, 11993−11996.
(39) Lawrence, C. P.; Skinner, J. L. Ultrafast infrared spectroscopy probes hydrogen-bonding dynamics in liquid water. *Chem. Phys. Lett.* **2003**, *369*, 472−477.
(40) Fecko, C. J.; Eaves, J. D.; Loparo, J. J.; Tokmakoff, A.; Geissler, P. L. Ultrafast hydrogen-bond dynamics in the infrared spectroscopy of water. *Science* **2003**, *301*, 1698−1702.
(41) Eaves, J. D.; Loparo, J. J.; Fecko, C. J.; Roberts, S. T.; Tokmakoff, A.; Geissler, P. L. Hydrogen bonds in liquid water are broken only fleetingly. *Proc. Natl. Acad. Sci. U.S.A.* **2005**, *102*, 13019−13022.
(42) Lindner, J.; Vöhringer, P.; Pshenichnikov, M. S.; Cringus, D.; Wiersma, D. A.; Mostovoy, M. Vibrational relaxation of pure liquid water. *Chem. Phys. Lett.* **2006**, *421*, 329−333.
(43) Shinokita, K.; Cunha, A. V.; Jansen, T. L. C.; Pshenichnikov, M. S. Hydrogen bond dynamics in bulk alcohols. *J. Chem. Phys.* **2015**, *142*, 212450.
(44) Bonn, M.; Hunger, J. Between a hydrogen and a covalent bond. *Science* **2021**, *371*, 123−124.
(45) Dereka, B.; Yu, Q.; Lewis, N. H. C.; Carpenter, W. B.; Bowman, J. M.; Tokmakoff, A. Crossover from hydrogen to chemical bonding. *Science* **2021**, *371*, 160−164.
(46) Kowalewski, J. Nuclear spin relaxation in liquids and gases. *Nuclear Magnetic Resonance*; Royal Society of Chemistry, 2013; Vol. *42*, pp 230−275.
(47) Ludwig, R.; Gill, D. S.; Zeidler, M. D. Molecular-reorientation in liquid methanol. *Z. Naturforsch., A: Phys. Sci.* **1991**, *46*, 89−94.
(48) Ludwig, R.; Weinhold, F.; Farrar, T. C. Experimental and theoretical studies of hydrogen bonding in neat, liquid formamide. *J. Chem. Phys.* **1995**, *102*, 5118−5125.
(49) Overbeck, V.; Golub, B.; Schröder, H.; Appelhagen, A.; Paschek, D.; Neymeyr, K.; Ludwig, R. Probing Relaxation Models by Means of Fast Field-Cycling Relaxometry, NMR Spectroscopy and Molecular Dynamics Simulations: Detailed Insight Into the Translational and Rotational Dynamics of a Protic Ionic Liquid. *J. Mol. Liq.* **2020**, *319*, 114207.
(50) Overbeck, V.; Appelhagen, A.; Rößler, R.; Niemann, T.; Ludwig, R. Rotational Correlation Times, Diffusion Coefficients and Quadrupolar Peaks of the Protic Ionic Liquid Ethylammonium Nitrate by Means of 1H Fast Field Cycling NMR Relaxometry. *J. Mol. Liq.* **2021**, *322*, 114983.
(51) Grabowski, S. J. What is the Covalency of Hydrogen Bonding? *Chem. Rev.* **2011**, *111*, 2597−2625.

https://doi.org/10.1021/acs.jpcb.1c02756
J. Phys. Chem. B 2021, 125, 5132−5144

(52) Weinhold, F.; Landis, C. R. *Valency and Bonding: A Natural Bond Orbital Donor-Acceptor Perspective*; Cambridge University Press, 2005.
(53) Kumar, R.; Schmidt, J. R.; Skinner, J. L. Hydrogen bonding definitions and dynamics in liquid water. *J. Chem. Phys.* **2007**, *126*, 204107.
(54) Humphrey, W.; Dalke, A.; Schulten, K. VMD − Visual Molecular Dynamics. *J. Mol. Graph.* **1996**, *14*, 33−38.
(55) Hänggi, P.; Talkner, P.; Borkovec, M. Reaction Rate Theory: fifty years after Kramers. *Rev. Mod. Phys.* **1990**, *62*, 251−341.
(56) Makarov, D. E. M. Barrier Crossing Dynamics from Single-Molecule Measurements. *J. Phys. Chem. B* **2021**, *125*, 2467−2476.
(57) Stillinger, F. H. Theory and molecular models for water. *Adv. Chem. Phys.* **1975**, *31*, 1−101.
(58) Rapaport, D. C. Hydrogen bonds in water: Network organization and lifetimes. *Mol. Phys.* **1983**, *50*, 1151−1162.
(59) Geiger, A.; Mausbach, P.; Schnitker, J.; Blumberg, R. L.; Stanley, H. E. Structure and dynamics of the hydrogen-bond network in water by computer-simulations. *J. Phys.* **1984**, *45*, C7-13−C7-30.
(60) Zichi, D. A.; Rossky, P. J. Solvent molecular-dynamics in regions of hydrophobic hydration. *J. Chem. Phys.* **1986**, *84*, 2814−2822.
(61) Sciortino, F.; Fornili, S. L. Hydrogen-bond cooperativity in simulated water - time-dependence analysis of pair interactions. *J. Chem. Phys.* **1989**, *90*, 2786−2792.
(62) Sciortino, F.; Poole, P. H.; Stanley, H. E.; Havlin, S. Lifetime of the bond network and gel-like anomalies in supercooled water. *Phys. Rev. Lett.* **1990**, *64*, 1686−1689.
(63) Starr, F. W.; Nielsen, J. K.; Stanley, H. E. Hydrogen-bond dynamics for the extended simple point-charge model of water. *Phys. Rev. E: Stat. Phys., Plasmas, Fluids, Relat. Interdiscip. Top.* **2000**, *62*, 579−587.
(64) van der Spoel, D.; van Maaren, P. J.; Larsson, P.; Tîmneanu, N. Thermodynamics of Hydrogen Bonding in Hydrophilic and Hydrophobic Media. *J. Phys. Chem. B* **2006**, *110*, 4393−4398.
(65) Bennett, C. H. *Algorithms for Chemical Computations*; *ACS Symposium Series*; American Chemical Society, 1977; Vol. *46*; Chapter 4, pp 63−97.
(66) Chandler, D. Statistical mechanics of isomerization dynamics in liquids and the transition state approximation. *J. Chem. Phys.* **1978**, *68*, 2959−2970.
(67) Williams, G.; Watts, D. C. Non-symmetrical dielectric relaxation behaviour arising from a simple empirical decay function. *Trans. Faraday Soc.* **1970**, *66*, 80−85.
(68) Lindsey, C. P.; Patterson, G. D. Detailed comparison of the Williams-Watts and Cole-Davidson functions. *J. Chem. Phys.* **1980**, *73*, 3348−3357.
(69) Berberan-Santos, M. N.; Bodunov, E. N.; Valeur, B. Mathematical functions for the analysis of luminescence decays with underlying distributions 1. Kohlrausch decay function (stretched exponential). *Chem. Phys.* **2005**, *315*, 171−182.
(70) Vartia, A. A.; Mitchell-Koch, K. R.; Stirnemann, G.; Laage, D.; Thompson, W. H. On the Reorientation and Hydrogen-Bond Dynamics of Alcohols. *J. Phys. Chem. B* **2011**, *115*, 12173−12178.
(71) Laage, D.; Hynes, J. T. A Molecular Jump Mechanism of Water Reorientation. *Science* **2006**, *311*, 832−835.
(72) Laage, D.; Hynes, J. T. On the Molecular Mechanism of Water Reorientation. *J. Phys. Chem. B* **2008**, *112*, 14230−14242.
(73) Chen, H.; Voth, G. A.; Agmon, N. Kinetics of Proton Migration in Liquid Water. *J. Phys. Chem. B* **2010**, *114*, 333−339.
(74) Tuckerman, M. E.; Chandra, A.; Marx, D. A statistical mechanical theory of proton transport kinetics in hydrogen-bonded networks based on population correlation functions with applications to acids and bases. *J. Chem. Phys.* **2010**, *133*, 124108.
(75) Atkins, P. W.; de Paula, J. *Physical Chemistry*, 9th ed.; F. H. Freeman and Company: New York, 2010.
(76) Borgis, D.; Moreau, M. On the equilibrium approach to isomerization dynamics in liquids. *Mol. Phys.* **1986**, *57*, 33−53.

https://doi.org/10.1021/acs.jpcb.1c02756
J. Phys. Chem. B 2021, 125, 5132−5144

Supporting Information:

Hydrogen Bonds between Ions of Opposite and Like Charge in Hydroxyl-functionalised Ionic Liquids: An Exhaustive Examination of the Interplay Between Global and Local Motions and Intermolecular Hydrogen Bond Lifetimes and Kinetics

Jan Neumann[†], Ralf Ludwig[‡,#,§,⋆], Dietmar Paschek[†,⋆]

† *Institut für Chemie, Abteilung Physikalische und Theoretische Chemie, Univesität Rostock, Albert-Einstein-Str. 21, D-18059 Rostock, Germany*
‡ *Institut für Chemie, Abteilung Physikalische und Theoretische Chemie, Universität Rostock, Dr.-Lorenz-Weg 2, D-18059 Rostock, Germany*
\# *Department Life, Light & Matter, Universität Rostock, Albert-Einstein-Str. 25, D-18059 Rostock, Germany*
§ *Leibniz Institut für Katalyse an der Universität Rostock, Albert-Einstein-Str. 29a, D-18059 Rostock, Germany*

⋆**E-mail:** dietmar.paschek@uni-rostock.de, ralf.ludwig@uni-rostock.de

Contents

S1 Density Data

The ionic liquids 1-(n-hydroxybutyl)pyridinium bis(trifluoromethylsulfonyl)imide $[HOC_nPy][NTf_2]$ with $n = 2, 3, 4, 5$ were synthesized using well-established protocols outlined in Refs. [1, 2].

The experimental densities were obtained using an Anton Paar DMA 5000 M density meter (see Table S1) with an accuracy of $\delta\rho = \pm 0.007\,\mathrm{kg\,m^{-3}}$ and $\delta T = \pm 0.01\,\mathrm{K}$ (according to Anton Paar Technical Manual). The deviation of the linear fit of the simulated densities from the experimental data is below 4.2 % at 343.15 K for all ILs. The small difference in the slope leads to smaller deviations below 343.15 K and conversely larger deviations above that temperature. The simulated densities are presented in Table S2.

Table S1: Densities ρ of the respective $[HOC_nPy][NTf_2]$ IL at various temperatures obtained using an Anton Paar DMA 5000 M density meter.

T / K	ρ / kg m^{-3}			
	$[HOC_2Py][NTf_2]$	$[HOC_3Py][NTf_2]$	$[HOC_4Py][NTf_2]$	$[HOC_5Py][NTf_2]$
288.15	–	1560.764	–	1496.187
293.15	1595.479	1555.962	1520.068	1491.722
298.15	–	1551.168	–	1487.252
303.15	1585.595	1546.402	1510.862	1482.770
308.15	–	1541.659	–	1478.283
313.15	1575.821	1536.948	1501.721	1473.831
318.15	–	1532.260	–	1469.396
323.15	1566.148	1527.597	1492.661	1464.987
328.15	–	1522.944	–	1460.597
333.15	1556.571	1518.330	1483.684	1456.231
338.15	–	1513.729	–	1451.878
343.15	1547.079	1509.150	1474.776	1447.543

Table S2: Simulated densities ρ of the respective $[HOC_nPy][NTf_2]$ IL at various temperatures.

T / K	ρ / kg m^{-3}			
	$[HOC_2Py][NTf_2]$	$[HOC_3Py][NTf_2]$	$[HOC_4Py][NTf_2]$	$[HOC_5Py][NTf_2]$
300	1534.6	1492.1	1465.8	1433.1
320	1512.0	1470.5	1444.0	1411.7
340	1489.7	1448.9	1422.8	1391.1
360	1467.7	1427.7	1402.0	1370.3
380	1445.8	1406.9	1381.6	1350.2
400	1425.0	1386.1	1361.2	1330.3

S2 Viscosity Data

Viscosities were calculated following the procedure outlined by Zhang et al. [3], using the Green-Kubo approach [4]

$$\eta = \frac{V}{k_\mathrm{B}T} \int_0^\infty \langle P_{\alpha\beta}(0) \cdot P_{\alpha\beta}(t) \rangle \, dt, \tag{1}$$

with the volume of the system V, the Boltzmann constant k_B, the temperature T, and the $\alpha\beta$ element of the pressure tensor $P_{\alpha\beta}$. To compute the viscosities, 100 additional independent NVT simulations were performed for each temperature and IL, using starting configuration sampled from the initial NPT run. The simulation lengths of the individual trajectories were ranging from 16 ns at high temperatures up to 40 ns length at 300 K. Pressure tensor data for every time step were recorded for this purpose. The resulting viscosities are presented in Table S3. The value of $[HOC_5Py][NTf_2]$ was not calculated here, due to the higher viscosity needing exceedingly more computational resources.

The experimental viscosities reported in the main manuscript were obtained using a rolling-ball viscometer Lovis 2000 M/ME from Anton Paar and are presented in Table S4 with accuracy of $\delta\eta/\eta = \pm 0.5\%$ and $\delta T = \pm 0.02$ K (according to Anton Paar Technical Manual).

Table S3: Simulated viscosities η of the respective $[HOC_nPy][NTf_2]$ IL at various temperatures obtained using the Green-Kubo approach of Zhang et al.[3]

T / K	η / mPa s			
	$[HOC_2Py][NTf_2]$	$[HOC_3Py][NTf_2]$	$[HOC_4Py][NTf_2]$	$[HOC_5Py][NTf_2]$
300	88.1	96.9	145.7	–
320	41.9	43.8	64.2	72.1
340	21.0	24.5	30.3	33.0
360	13.5	14.0	18.6	18.7
380	8.4	9.2	11.3	12.0
400	6.3	6.6	7.6	8.0

Table S4: Viscosities η of the respective $[HOC_nPy][NTf_2]$ IL at various temperatures obtained using an Anton Paar rolling-ball viscometer Lovis 2000 M/ME.

T / K	η / mPa s			
	$[HOC_2Py][NTf_2]$	$[HOC_3Py][NTf_2]$	$[HOC_4Py][NTf_2]$	$[HOC_5Py][NTf_2]$
288.15	–	228.8	–	491.9
293.15	146.9	167.3	241.8	342.0
298.15	–	124.4	–	245.4
303.15	83.8	95.1	131.1	180.6
308.15	–	74.8	–	136.7
313.15	53.0	59.4	78.5	105.5
318.15	–	48.0	–	83.0
323.15	35.6	39.5	51.5	66.7
328.15	–	33.2	–	54.1
333.15	25.4	28.1	35.1	44.7
338.15	–	24.0	–	37.5
343.15	18.9	20.7	25.2	31.8

S3 Reorientational Correlation Times

To examine the rotational dynamic of the OH bond-vector and the intramolecular N$\cdots$O vector, reorientational correlation times τ_{OH} and τ_{NO} are computed as integral over time correlation functions

$$R_2(t) = \langle P_2\left[\vec{e}(0)\cdot\vec{e}(t)\right]\rangle \ , \tag{2}$$

where $\vec{e}$ is the unit vector along the chosen molecular axis, P_2 is the 2nd Legendre polynomial, and $\langle\ldots\rangle$ indicates a thermal average. Reorientational correlation times are computed by fitting a sum of two KWW functions to $R_2(t)$ and integrating them analytically.

Table S5: The reorientational correlation times of the hydroxyl O–H bond vector τ_{OH} and the intramolecular N–O vector of the cation τ_{NO} obtained by integrating the reorientational correlation functions of respective [HOC$_n$Py][NTf$_2$] ILs.

T / K	[HOC$_2$Py][NTf$_2$]		[HOC$_3$Py][NTf$_2$]		[HOC$_4$Py][NTf$_2$]		[HOC$_5$Py][NTf$_2$]	
	τ_{NO}/ps	τ_{OH}/ps	τ_{NO}/ps	τ_{OH}/ps	τ_{NO}/ps	τ_{OH}/ps	τ_{NO}/ps	τ_{OH}/ps
300	339.2	165.3	429.4	207.2	1140.3	250.3	1559.9	223.1
320	148.9	70.8	180.7	85.1	421.7	92.7	572.6	81.6
340	76.6	35.7	93.6	42.4	198.1	44.2	269.0	39.3
360	45.5	20.7	54.6	23.7	108.9	24.0	146.2	21.2
380	29.4	13.0	34.8	14.6	66.8	14.4	89.1	12.7
400	20.0	8.8	24.1	9.7	44.1	9.2	59.1	8.1

S4 Hydrogen Bond Definition and Cutoff Dependence

The first maximum in the H−O pair correlation functions in Figure S1 at around 2 Å represents hydrogen-bonded (ca) and (cc) species respectively. However, the hydrogen-bonded species can not be easily separated from non-hydrogen-bonded configurations by a distance criterium alone, due to the first minimum not reaching $g(r) = 0$. Thus, we used the weighted logarithmic probability density functions $W(\cos(\alpha), r_{\mathrm{oh}})$ shown in Figure S2 to determine the geometric criteria defining the HBs in our system. They show the probability of finding an intermolecular hydrogen-oxygen pair separated by the distance r_{oh} and with a HB angle $\alpha\angle$O–H$\cdots$O weighted with r^{-2}. The maximum at around $r_{\mathrm{oh}} = 2\,\text{Å}$ and at almost linear angle α ($\cos(\alpha) = -1$) describes the hydrogen-bonded species, which can be separated from other configurations by introducing the geometric criteria stated in the caption of the figure.
Especially for the (ca) HB, there still is a significant population density in the crossover region between hydrogen-bonded species and those which are not, which leads to ambiguity in the geometric criteria. We changed the distance cutoff criterium by 0.2 Å in both directions for both HB species at a constant angle criterium and recalculated the HB statistic and HB lifetime τ_{hb}, to assess the cutoff dependence of our results. For the HB statistic the biggest deviation can generally be seen for tightening the cutoff distance of the (ca) HB at the highest temperature of 400 K. Depending on the IL, the number of cations involved in (ca) HBs changes by 5.5 to 9.2 % of its "original" value, the highest change being observed for $[\mathrm{HOC_5Py}][\mathrm{NTf_2}]$, where the percentage decreases from 60.7 % ($r_{\mathrm{c}} = 2.8\,\text{Å}$) to 55.1 % ($r_{\mathrm{c}} = 2.6\,\text{Å}$). Increasing the distance criterium leads to smaller effect as does probing the (cc) HB species, due to the lower population density in the crossover region.
The cutoff dependence of the HB lifetime τ_{hb} was analysed by recalculating the HB population correlation functions of a subset of around 10 % of all donor-acceptor pairs for the IL with the highest change in HB statistics ($[\mathrm{HOC_5Py}][\mathrm{NTf_2}]$). To adjust for the inferior statistics of the donor-acceptor pair subset, the correlation functions at the "original" cutoff was also recalculated. The correlation functions were then integrated numerically to yield τ_{hb}. Similarly, the highest effect is observed by tightening the distance criterium for the (ca) HB, where, depending on the temperature, the lifetime deviates from the "original" value by between 6.4 and 9.8 %. At 400 K the smaller r_{c} of 2.6 Å leads to a decrease in τ_{hb} from 32.5 to 29.3 ps. The lifetime of the (cc) HB only changes by up to 6.1 % at 400 K, where it decreases 29.5 to 27.7 ps. Overall, decreasing the cutoff distance leads to a lower lifetime, while increasing it also increases the lifetime. A change of ±0.2 Å in the cutoff distance can be considered a rather large variation that is not in the realm of the actual error in the determination of the geometric criteria. Nonetheless, it should be kept in mind that these deviations exceed the pure statistical error given in Table S8.

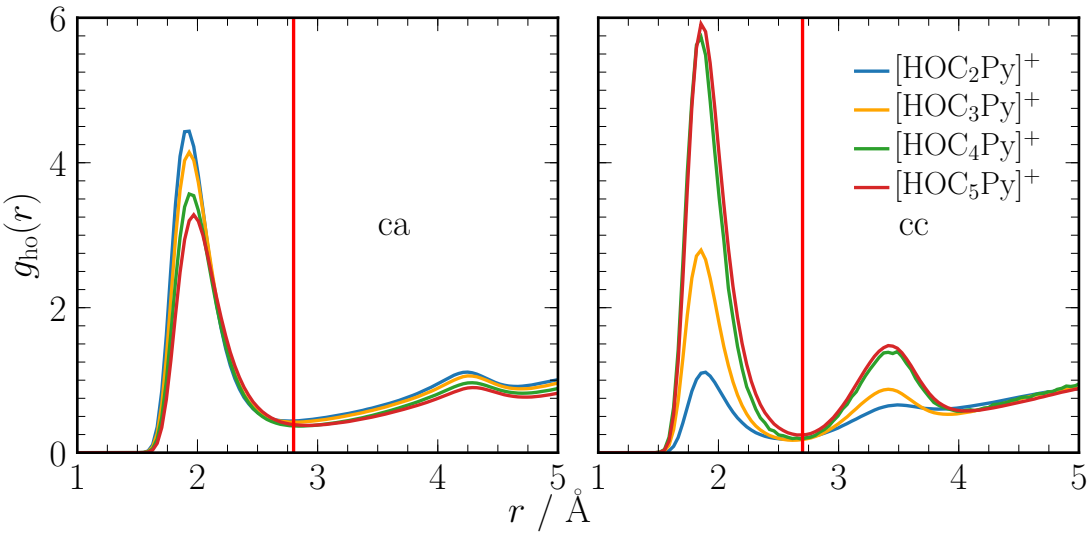

Figure S1: Pair correlation functions between the hydroxyl hydrogen of the cation and oxygen atoms on the anion (ca, left) and the cation (cc, right) for the different chain lengths obtained at 300 K. The distance cutoff used to define the HB is shown as a red horizontal line at 2.8 Å for the (ca) HB (left) and 2.7 Å for the (cc) HB (right) respectively.

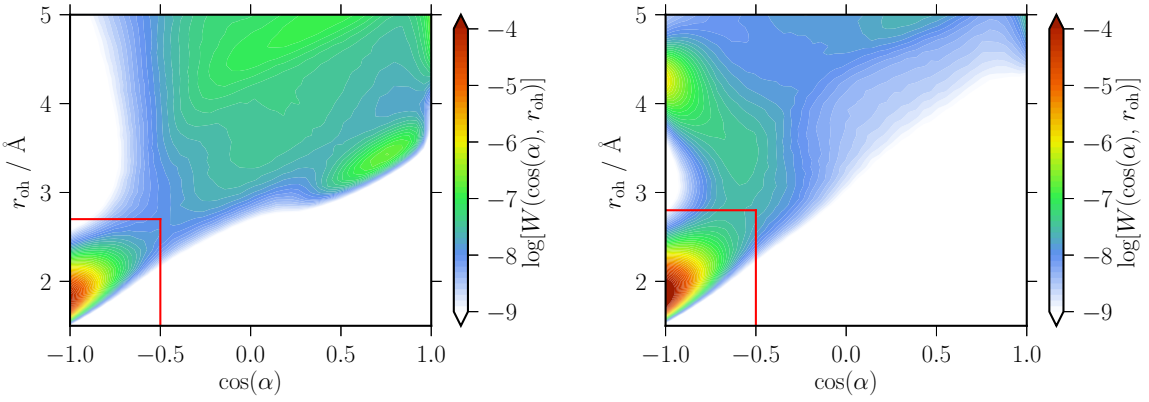

(a) $[HOC_2Py][NTf_2]$

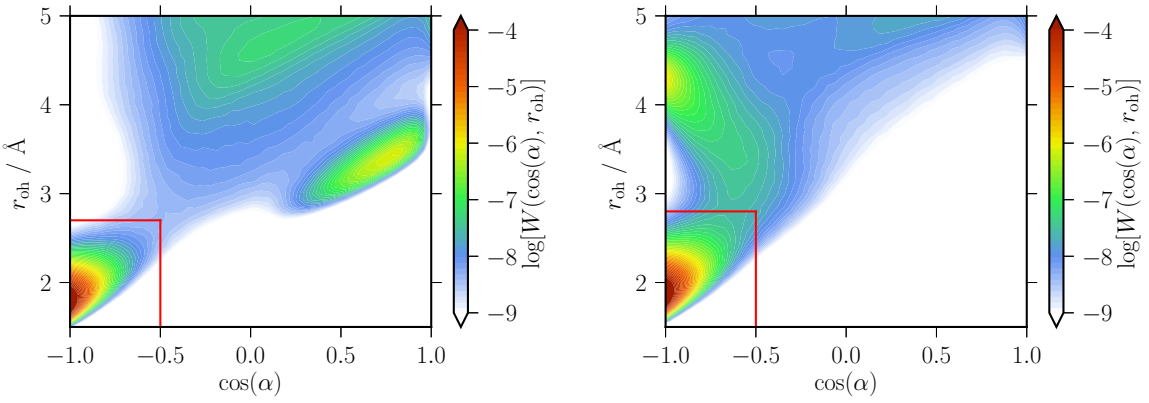

(b) $[HOC_3Py][NTf_2]$

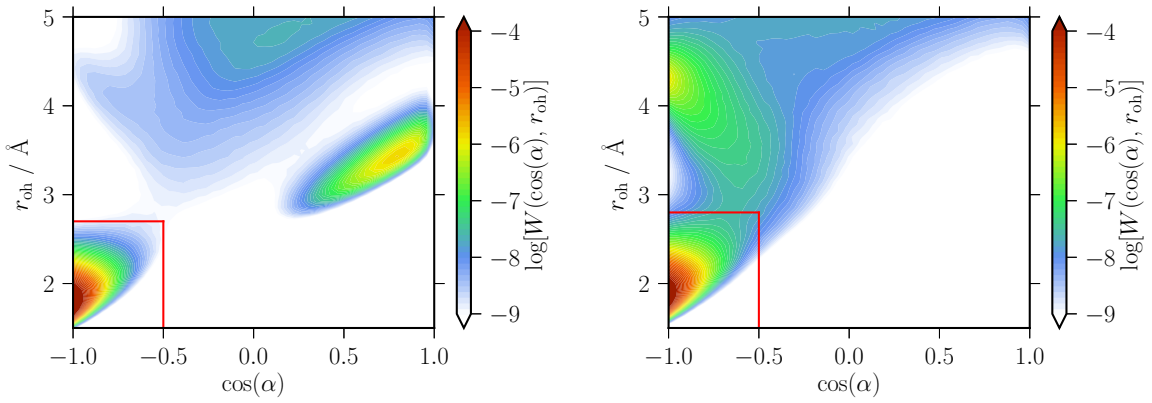

(c) $[HOC_4Py][NTf_2]$

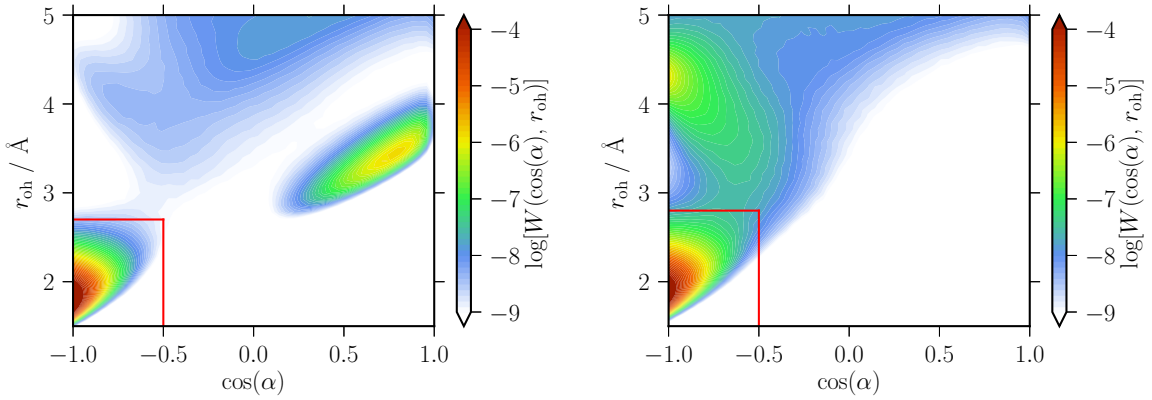

(d) $[HOC_5Py][NTf_2]$

Figure S2: Logarithmic representation of the probability density of finding an intermolecular O-H distance r_{oh} and the cosine of the angle α between the intermolecular H-O vector and the intramolecular O-H vector for the (cc) (left) and the (ca) (right) HB obtained at 300 K for the specified ionic liquid. The probability density is weighted with r^{-2}. The (cc) HB for all considered ionic liquids can be characterised by a distance cutoff of $r_c = 2.7$ Å and an angular cutoff at $\cos(\alpha_c) = -0.5$. For the (ca) HB the same angular cutoff was used with a distance cutoff of $r_c = 2.8$ Å.

S5 Hydrogen Bond Populations

Table S6: Percentage of cations donating no HB $N_{\mathrm{hb,free}}$, a (cc) HB $N_{\mathrm{hb,cc}}$, a (ca) HB $N_{\mathrm{hb,ca}}$, or both HBs at the same time $N_{\mathrm{hb,cc+ca}}$ (as bifurcated HBs) in the respective IL. Differences of the sum of these numbers from 100 % are due to rounding.

T / K	$N_{\mathrm{hb,free}}$ / %	$N_{\mathrm{hb,cc}}$ / %	$N_{\mathrm{hb,ca}}$ / %	$N_{\mathrm{hb,cc+ca}}$ / %
		$[HOC_2Py][NTf_2]$		
300	4.95	5.36	89.14	0.54
320	6.29	5.16	88.03	0.52
340	7.85	4.96	86.69	0.50
360	9.55	4.78	85.20	0.47
380	11.46	4.62	83.47	0.45
400	13.47	4.47	81.65	0.42
		$[HOC_3Py][NTf_2]$		
300	6.34	11.00	82.25	0.41
320	8.08	10.33	81.19	0.40
340	10.00	9.67	79.93	0.39
360	12.13	9.07	78.42	0.38
380	14.46	8.51	76.67	0.36
400	16.87	8.05	74.73	0.34
		$[HOC_4Py][NTf_2]$		
300	7.72	20.68	71.33	0.27
320	9.94	18.54	71.24	0.27
340	12.34	17.05	70.33	0.27
360	14.91	15.55	69.27	0.27
380	17.64	14.24	67.85	0.26
400	20.49	13.11	66.14	0.26
		$[HOC_5Py][NTf_2]$		
300	10.28	21.97	67.53	0.22
320	12.96	19.89	66.93	0.22
340	15.95	17.88	65.95	0.22
360	18.99	16.48	64.31	0.22
380	22.15	14.99	62.65	0.21
400	25.40	13.66	60.74	0.20

S6 Hydrogen Bond Lifetimes

To obtain HB lifetimes τ_{hb}, we first calculated the HB population correlation functions $C(t)$ for every donor-acceptor pair of the respective HB species (cc) or (ca) separately. The averaged $C(t)$ of the corresponding HB species was then fitted with two stretched exponential functions of the form

$$C(t) = A_1 \exp\left[-\left(t/\tau_1\right)^{\beta_1}\right] + A_2 \exp\left[-\left(t/\tau_2\right)^{\beta_2}\right], \tag{3}$$

using a least-squares fit. The two exponential term describe the decay of $C(t)$ on different timescales, namely the short- and long-time behaviour

$$C(t) = C_{\mathrm{short}}(t) + C_{\mathrm{long}}(t). \tag{4}$$

The fitted parameters of equation 3 can be found in Table S7. The parameter A_2 was fixed at 0.048 for the (ca) HB and 0.25 for the (cc) HB to obtain a consistent fitting behaviour and ensure that the second term always refers to the long-time behaviour of $C(t)$. Equation 3 can be analytically integrated yielding the HB lifetime τ_{hb}

$$\tau_{\mathrm{hb}} = \int_0^\infty C(t)\, dt \tag{5}$$

by

$$\tau_{\mathrm{hb}} = A_1 \frac{\tau_1}{\beta_1} \Gamma\left(\beta_1^{-1}\right) + A_2 \frac{\tau_2}{\beta_2} \Gamma\left(\beta_2^{-1}\right), \tag{6}$$

The two terms in equation 6 directly refer to the integral of the corresponding part of $C(t)$ (Eq. 7) giving us the long part τ_{long} as well as the short part τ_{short} of the overall HB lifetime τ_{hb}

$$\tau_{\mathrm{hb}} = \tau_{\mathrm{short}} + \tau_{\mathrm{long}}. \tag{7}$$

Since we can calculate $C(t)$ separately for the HB species (ca) and (cc), we are able to compute distinct average HB lifetimes as well as short- and long-time behaviour for the (cc) and (ca) HB. The overall HB lifetime τ_{hb} and its components τ_{short} and τ_{long} are presented in Table S8 for all ILs and HB species.

To estimate a statistical uncertainty of the calculated HB lifetimes we computed a separate $C(t)$ for every donor (cation) by averaging all the correlation functions related to that donor. This produces 512 (number of donors in our system) distinct correlation functions for every IL and HB species. By numerically integrating these correlation functions we obtain the average HB lifetime for each cation separately and are able to subsequently compute the standard error of the mean HB lifetime $s_{\overline{\tau}_{\mathrm{hb}}}$ given in Table S8. The numerical integration of $C(t)$ is generally in good agreement with the analytical approach used to calculate τ_{hb}, however we forfeit information about the time domains. Separately fitting the donor-specific correlation functions and integrating them analytically would require much longer simulations due to the noise at $C(t) \to 0$.

Table S7: Fitting parameters to describe the HB population correlation function $C(t)$ according to equation 3. The parameter A_2 was fixed at the respective value for the (ca) and (cc) HB to ensure a consistent fitting behavior.

T / K	A_1	τ_1/ps	β_1	A_2	τ_2/ps	β_2
			[HOC_2Py][NTf_2] (ca) HB			
300	0.8775	84.9838	0.5427	0.0480	6172.6619	0.5993
320	0.9007	39.2126	0.5465	0.0480	2506.6475	0.5978
340	0.9184	21.3884	0.5526	0.0480	1277.6366	0.5968
360	0.9309	13.2713	0.5561	0.0480	731.0897	0.5878
380	0.9391	8.9062	0.5600	0.0480	449.9533	0.5814
400	0.9441	6.3993	0.5643	0.0480	301.6465	0.5717
			[HOC_2Py][NTf_2] (cc) HB			
300	0.7176	75.8705	0.5520	0.2500	6.5960	0.2110
320	0.7344	30.3659	0.5466	0.2500	3.5953	0.2201
340	0.7434	14.7316	0.5546	0.2500	1.9764	0.2237
360	0.7476	8.4348	0.5610	0.2500	1.4340	0.2317
380	0.7496	5.4043	0.5672	0.2500	1.0207	0.2369
400	0.7500	3.7516	0.5785	0.2500	0.7023	0.2376
			[HOC_3Py][NTf_2] (ca) HB			
300	0.8857	86.8179	0.5140	0.0480	5343.3495	0.5276
320	0.9092	38.6288	0.5210	0.0480	2168.3578	0.5285
340	0.9266	20.7023	0.5274	0.0480	1081.8495	0.5251
360	0.9373	12.6377	0.5329	0.0480	612.4640	0.5233
380	0.9430	8.4024	0.5409	0.0480	379.4944	0.5193
400	0.9468	5.9611	0.5473	0.0480	252.0729	0.5174
			[HOC_3Py][NTf_2] (cc) HB			
300	0.7499	202.6414	0.6533	0.2500	29.8126	0.2392
320	0.7494	82.0650	0.6626	0.2500	13.0408	0.2415
340	0.7496	39.2683	0.6597	0.2500	7.7057	0.2516
360	0.7522	21.7753	0.6626	0.2500	4.0411	0.2495
380	0.7516	13.0430	0.6689	0.2500	2.6461	0.2529
400	0.7517	8.6362	0.6690	0.2500	1.7188	0.2532
			[HOC_4Py][NTf_2] (ca) HB			
300	0.8858	98.7592	0.5085	0.0480	7836.5566	0.5499
320	0.9120	40.6712	0.5140	0.0480	2883.2371	0.5254
340	0.9273	20.9327	0.5218	0.0480	1324.0435	0.5223
360	0.9382	12.4042	0.5277	0.0480	693.6306	0.5159

T / K	A_1	τ_1/ps	β_1	A_2	τ_2/ps	β_2
380	0.9438	8.0933	0.5347	0.0480	411.8973	0.5086
400	0.9474	5.6339	0.5416	0.0480	262.8168	0.5056
			$[HOC_4Py][NTf_2]$ (cc) HB			
300	0.7629	381.2592	0.6610	0.2500	273.8460	0.2919
320	0.7517	138.7997	0.6839	0.2500	99.6488	0.2977
340	0.7541	64.6464	0.6794	0.2500	41.0859	0.2959
360	0.7532	33.8953	0.6880	0.2500	19.4775	0.2917
380	0.7519	19.9628	0.6939	0.2500	10.3870	0.2887
400	0.7508	12.5150	0.6939	0.2500	6.5047	0.2894
			$[HOC_5Py][NTf_2]$ (ca) HB			
300	0.9022	84.9678	0.4875	0.0480	7583.1360	0.5018
320	0.9171	36.1138	0.4993	0.0480	2719.9975	0.5007
340	0.9298	18.6265	0.5080	0.0480	1229.4144	0.4922
360	0.9385	10.9799	0.5164	0.0480	634.1103	0.4877
380	0.9446	7.1196	0.5218	0.0480	365.3749	0.4825
400	0.9479	4.9623	0.5272	0.0480	226.2624	0.4731
			$[HOC_5Py][NTf_2]$ (cc) HB			
300	0.7356	313.6583	0.6579	0.2500	496.6860	0.3264
320	0.7558	119.1352	0.6477	0.2500	120.1473	0.3025
340	0.7479	55.8183	0.6647	0.2500	51.1103	0.3009
360	0.7468	29.5855	0.6768	0.2500	24.0264	0.2971
380	0.7490	17.4228	0.6760	0.2500	12.2393	0.2915
400	0.7494	10.9746	0.6809	0.2500	6.7256	0.2855

Table S8: Short (τ_{short}) and long (τ_{long}) part of the HB lifetime τ_{hb} of the (ca) as well as the (cc) HB in the respective $[HOC_nPy][NTf_2]$ IL. For details on the standard error of the mean HB lifetime $s_{\overline{\tau}_{\text{hb}}}$ see section S6.

T / K	τ_{short} / ps	τ_{long} / ps	τ_{hb} / ps	$s_{\overline{\tau}_{\text{hb}}}$ / ps
		$[HOC_2Py][NTf_2]$ (ca) HB		
300	129.7	446.5	576.1	5.725
320	60.7	181.9	242.6	1.953
340	33.2	92.9	126.1	0.901
360	20.7	54.3	74.9	0.548
380	13.9	33.9	47.8	0.330
400	9.9	23.3	33.2	0.248
		$[HOC_2Py][NTf_2]$ (cc) HB		

T / K	τ_{short} / ps	τ_{long} / ps	τ_{hb} / ps	$s_{\overline{\tau}_{\mathrm{hb}}}$ / ps
300	92.2	127.5	219.7	3.245
320	38.3	50.4	88.7	0.936
340	18.4	24.7	43.1	0.370
360	10.4	14.0	24.4	0.206
380	6.6	8.6	15.2	0.131
400	4.4	5.8	10.2	0.096
		$[HOC_3Py][NTf_2]$ (ca) HB		
300	146.3	466.7	613.1	5.918
320	65.3	188.9	254.2	2.008
340	34.9	95.3	130.2	0.928
360	21.2	54.2	75.4	0.588
380	13.8	34.1	47.9	0.363
400	9.7	22.8	32.4	0.240
		$[HOC_3Py][NTf_2]$ (cc) HB		
300	206.5	235.7	442.1	5.977
320	82.3	96.9	179.2	2.096
340	39.6	44.5	84.1	0.710
360	21.9	24.5	46.4	0.374
380	13.0	14.8	27.8	0.336
400	8.6	9.6	18.2	0.203
		$[HOC_4Py][NTf_2]$ (ca) HB		
300	169.7	640.5	810.2	8.260
320	70.6	253.7	324.2	2.829
340	36.0	117.6	153.6	1.272
360	21.2	63.0	84.1	0.563
380	13.6	38.3	51.9	0.410
400	9.3	24.7	34.0	0.255
		$[HOC_4Py][NTf_2]$ (cc) HB		
300	390.2	718.8	1108.9	17.392
320	135.1	238.8	373.9	4.190
340	63.5	101.2	164.8	1.780
360	32.9	51.3	84.1	0.776
380	19.2	28.7	47.9	0.426
400	12.0	17.8	29.8	0.302
		$[HOC_5Py][NTf_2]$ (ca) HB		
300	160.9	723.3	884.1	9.831

T / K	τ_{short} / ps	τ_{long} / ps	τ_{hb} / ps	$s_{\overline{\tau}_{\mathrm{hb}}}$ / ps
320	66.4	260.5	326.9	3.227
340	33.6	121.6	155.2	1.184
360	19.5	63.8	83.3	0.559
380	12.5	37.5	50.0	0.367
400	8.6	24.2	32.8	0.245
		$[HOC_5Py][NTf_2]$ (cc) HB		
300	311.1	807.7	1118.8	16.470
320	123.5	268.1	391.6	4.646
340	55.7	116.7	172.3	2.132
360	28.9	58.1	87.0	0.732
380	17.1	32.3	49.4	0.775
400	10.7	19.6	30.3	0.237

S7 Position Restraints

Figure S3 and Figure S4 shows the mean square displacement $\left\langle |\vec{r}(t) - \vec{r}(0)|^2 \right\rangle$ of the center of mass of the $[HOC_4Py]^+$ cations and the $[NTf_2]^-$ anions as well as the the oxygen centers of the hydroxyl groups for simulations with position restraints at various force constants k. Figure S5 shows the cation-anion center of mass pair correlation function $g(r)$ for simulations with position restraints at various force constants k. The position restraints do not influence $g(r)$, because we effectively "freeze" an average configuration maintaining the average $g(r)$. As shown in Figure S6 the reorientational dynamic of the OH bond-vector and intramolecular $N\cdots O$ vector are described by time correlation functions $R_2(t) = \langle P_2 [\vec{e}(0) \cdot \vec{e}(t)] \rangle$ where $\vec{e}$ is the unit vector along a particular molecular axis, P_2 is the 2nd Legendre polynomial, and $\langle \ldots \rangle$ indicates a thermal average. The computed reorientational correlation functions are only majorly influenced by the positional restraints for large force constants k'. At these high force constants we also see a change in the short-time behaviour of the HB population correlation function $C(t)$.

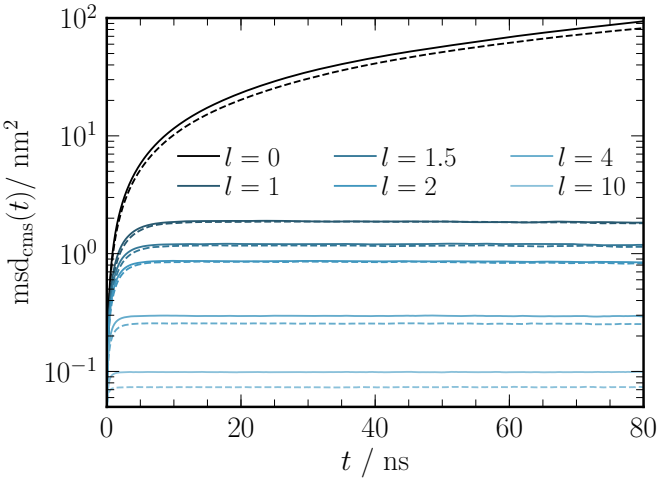

Figure S3: Mean square displacement $\mathrm{msd_{cms}}(t) = \left\langle |\vec{r}_\mathrm{c}(t) - \vec{r}_\mathrm{c}(0)|^2 \right\rangle$ of the center of mass $\vec{r}_\mathrm{c}$ of the $[\mathrm{HOC_4Py}]^+$ cation (solid lines) and the $[\mathrm{NTf_2}]^-$ anion (dashed lines) at 400 K, respectively. Position restraints lead to a constant mean square displacement. Increasing the force constants $k' = l \cdot k$ reduces the distance the ions are able to travel.

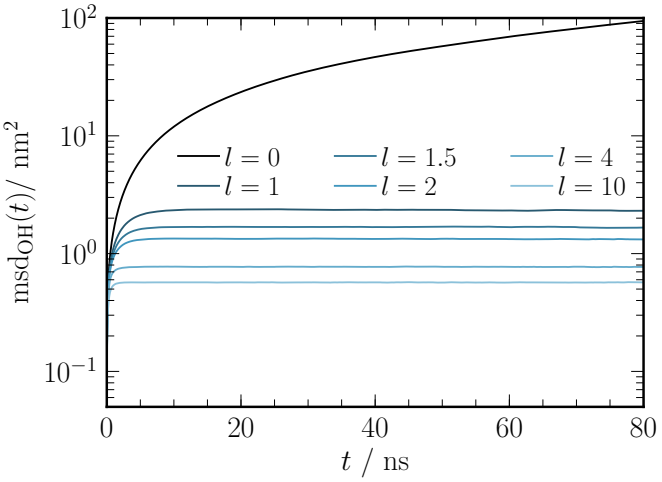

Figure S4: Mean square displacement $\mathrm{msd_{OH}}(t) = \left\langle |\vec{r}_\mathrm{O}(t) - \vec{r}_\mathrm{O}(0)|^2 \right\rangle$ of the hydroxyl group (represented by the position of its oxygen-center $\vec{r}_\mathrm{O}$) of the $[\mathrm{HOC_4Py}]^+$ cation at 400 K, respectively. Increasing the force constants $k' = l \cdot k$ reduces the distance the ions are able to travel.

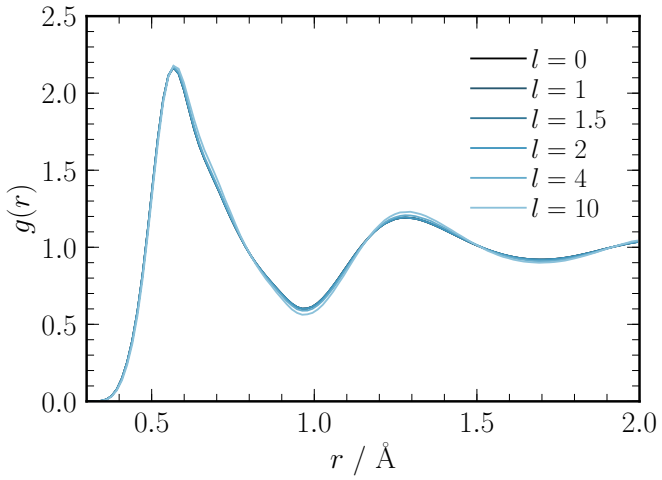

Figure S5: Anion-cation center of mass pair correlation functions $g(r)$ obtained for $[HOC_4Py][NTf_2]$ at 400 K for varying confinement due to position restraints. The structure of ionic liquid is only weakly perturbed by the introduction of position restraints with $k' = l \cdot k$ for $l \leq 4$.

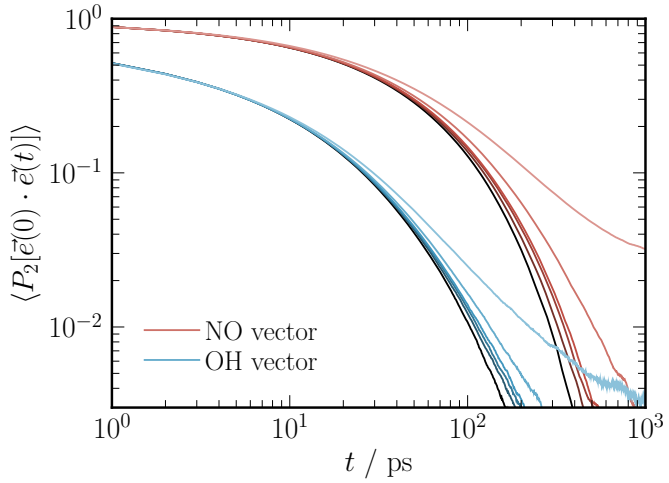

Figure S6: Reorientational correlation function $R_2(t) = \langle P_2\,[\vec{e}(0) \cdot \vec{e}(t)]\rangle$ for the O–H-bond vector and intramolecular N$\cdots$O vector. The correlation functions are only mildly perturbed by the introduction of position restraints with $k' = l \cdot k$ with $l = 0, 1, 1.5, 2, 4$, and 10. For $l = 10$ both correlation functions seem to approach a plateau value for long times t (in particular for the N$\cdots$O vector), indicating that isotropic reorientation is no longer possible.

S8 Long time Limiting Behaviour of the HB Population Correlation Function

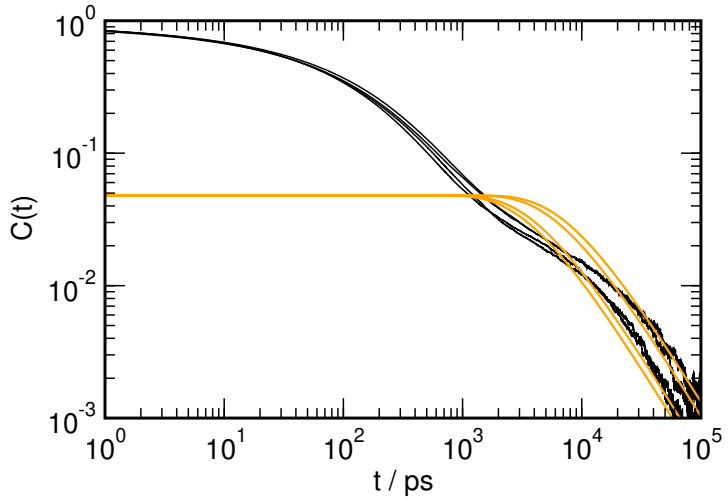

Figure S7: Solid black lines: HB population correlation function $C(t)$ for the (ca) HB of $[HOC_nPy][NTf_2]$ with $n = 2, 3, 4, 5$ at 300 K. Solid orange lines: Long time behaviour $C_{\text{long}}(t)$ according to Equation 14 in the manuscript using a parameter of $s = 1.2$.

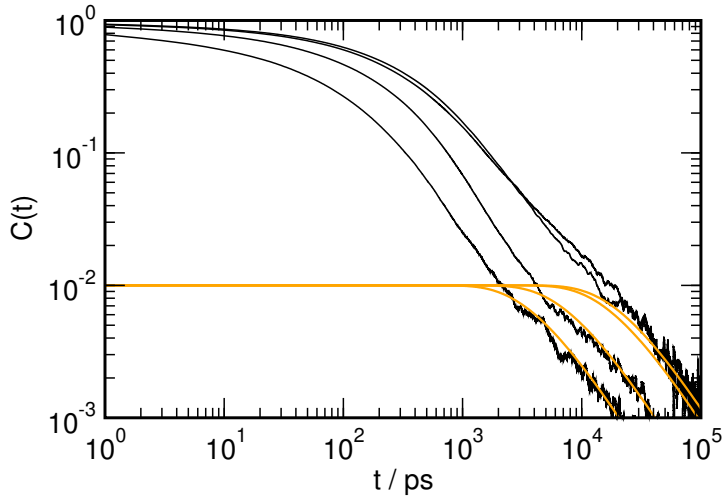

Figure S8: Solid black lines: HB population correlation function $C(t)$ for the (cc) HB of $[HOC_nPy][NTf_2]$ with $n = 2, 3, 4, 5$ at 300 K. Solid orange lines: Long time behaviour $C_{\text{long}}(t)$ according to Equation 14 in the manuscript.

S9 Reactive Flux Correlation Function Formalism

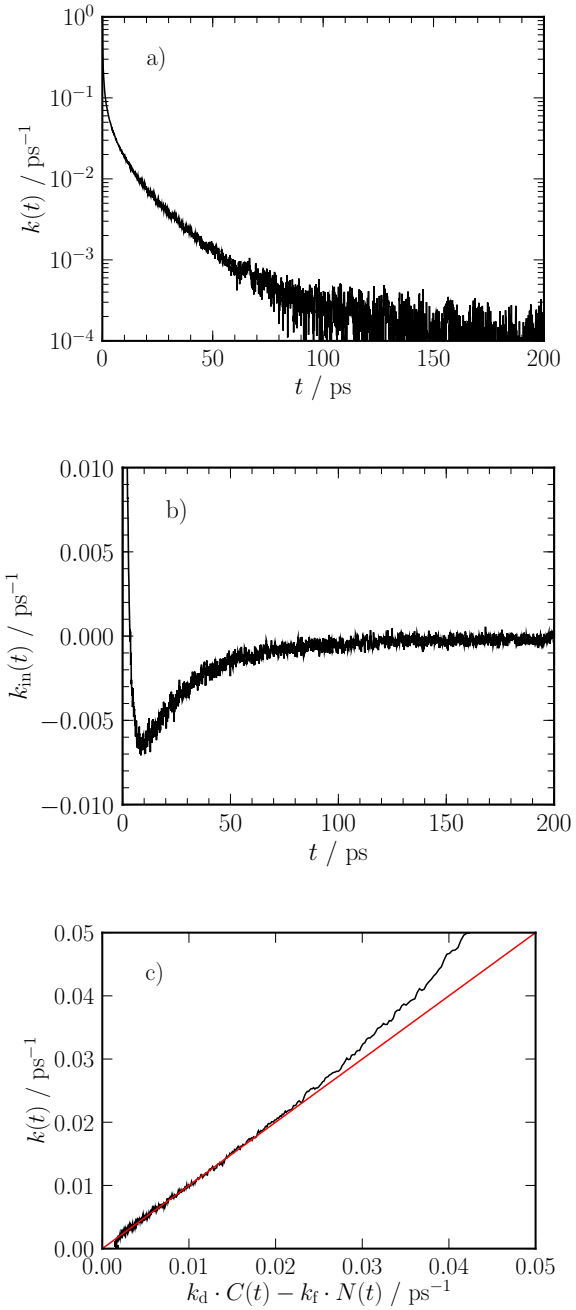

Figure S9: Kinetics of (ca) HB bond breaking for $[HOC_4Py][NTf_2]$ at 400 K: a) Semi-log plot of the reactive flux correlation function $k(t)$. b) Restricted rate function $k_{\mathrm{in}}(t)$. c) Correlation plot with $k_{\mathrm{d}}^{-1} = 7.2$ ps and $k_{\mathrm{f}}^{-1} = 9.9$ ps. The red solid line indicates the unity slope.

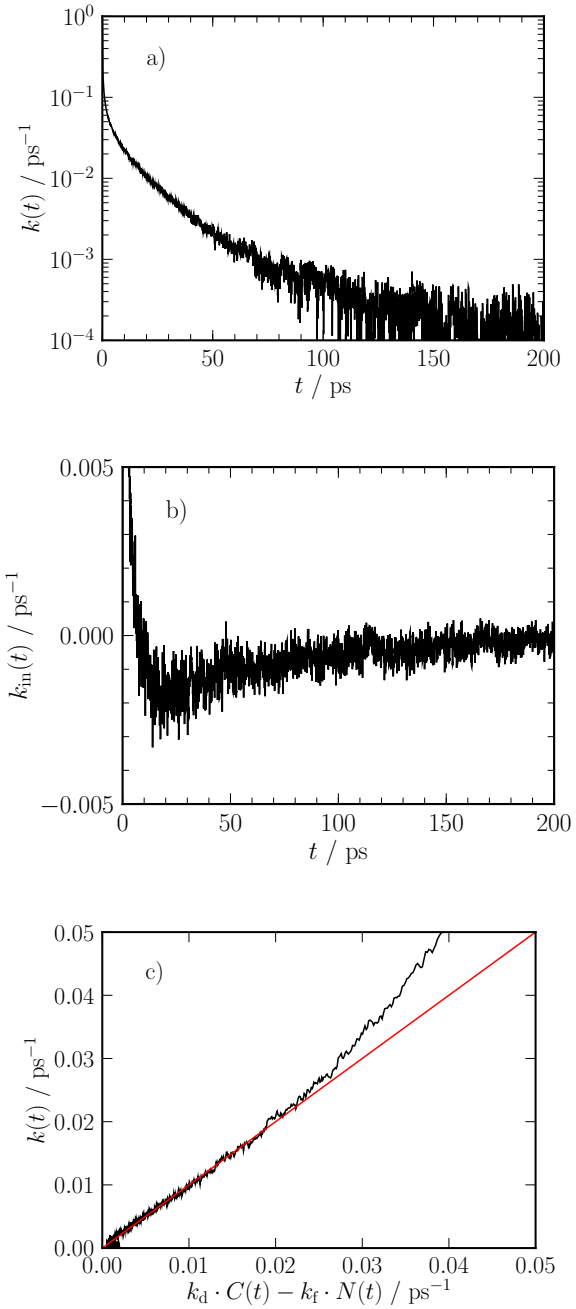

Figure S10: Kinetics of (cc) HB bond breaking for $[HOC_4Py][NTf_2]$ at 400 K: a) Semi-log plot of the reactive flux correlation function $k(t)$. b) Restricted rate function $k_{\mathrm{in}}(t)$. c) Correlation plot with $k_{\mathrm{d}}^{-1} = 13.0\,\mathrm{ps}$ and $k_{\mathrm{f}}^{-1} = 15.1\,\mathrm{ps}$. The red solid line indicates the unity slope.

Table S9: Exemplary analysis of the kinetics of HB breaking according to the approach of Luzar and Chandler: inverse rate of decay $k_{\mathrm{d}}^{-1} = \tau_{\mathrm{hb,d}}$, rate of reformation $k_{\mathrm{f}}^{-1} = \tau_{\mathrm{f}}$, and $\tau_{\mathrm{TST}} = k_{\mathrm{TST}}^{-1} = \lim_{t\to 0^+} k(t)^{-1}$

T / K	$\tau_{\mathrm{hb,d}} = k_{\mathrm{d}}^{-1}$ / ps	$\tau_{\mathrm{f}} = k_{\mathrm{f}}^{-1}$ / ps	τ_{TST} / ps
	$[HOC_2Py][NTf_2]$ (ca) HB		
300	134.9	246.9	1.47
320	57.4	97.6	1.32
340	33.0	56.8	1.19
360	18.6	30.5	1.07
380	12.3	20.1	0.97
400	8.8	14.4	0.88
	$[HOC_2Py][NTf_2]$ (cc) HB		
300	78.1	134.2	1.03
320	37.0	67.8	0.86
340	22.1	49.1	0.77
360	12.4	27.1	0.67
380	8.6	19.7	0.60
400	5.3	10.9	0.55
	$[HOC_4Py][NTf_2]$ (ca) HB		
300	142.5	187.1	1.50
320	66.3	97.0	1.34
340	26.5	34.7	1.17
360	17.3	24.2	1.05
380	10.4	14.1	0.93
400	7.2	9.9	0.84
	$[HOC_4Py][NTf_2]$ (cc) HB		
300	356.1	269.2	4.03
320	165.6	187.9	3.01
340	83.2	126.2	2.24
360	37.5	46.2	1.81
380	23.3	28.3	1.45
400	13.0	15.1	1.20

Table S10: Temperature dependence of $\tau_{\mathrm{hb,d}}$ and τ_{TST} following Arrhenius behaviour: $\tau_{\mathrm{x}}(T) = \tau_{\infty} \cdot \exp[E_{\mathrm{A}}/(RT)]$.

τ	τ_{∞} / 10^{-3} ps	E_{A} / kJ mol^{-1}
	$[HOC_2Py][NTf_2]$ (ca) HB	
$\tau_{\mathrm{hb,d}}$	2.30	27.1
τ_{TST}	191.88	5.1
	$[HOC_2Py][NTf_2]$ (cc) HB	
$\tau_{\mathrm{hb,d}}$	1.95	26.3
τ_{TST}	84.96	6.2
	$[HOC_4Py][NTf_2]$ (ca) HB	
$\tau_{\mathrm{hb,d}}$	0.75	30.2
τ_{TST}	147.59	5.8
	$[HOC_4Py][NTf_2]$ (cc) HB	
$\tau_{\mathrm{hb,d}}$	0.62	33.2
τ_{TST}	31.36	12.1

S10 FORTRAN Program Listing Random Walker

```
        program walker
C*****************************************************************
C
C       WALKER  Dietmar Paschek (C) 2021
C
C       Random walker describing a two domain model.
C
C       Compute the <h(0)*h(t)> = <h(t)>, since h(0)=1
C       contact-pair population correlation
C       function of a 3D-Random Walker sampled over many
C       trajectories starting at the origin.
C
C       Jump length unit: nm
C       Time length unit: ps
C       Random orientation after each step
C       Sampling over nsample trajectories
C
C*****************************************************************

        implicit none

        integer*4 nmax
        parameter (nmax=100000)

        integer*4 i, is, nsteps, nsample, itau, h(nmax)

        double precision deltat, deltar, deltas, dself, tau
        double precision astar, rstar, rs, r2s
        double precision xi, yi, zi, r2i, ri, dx, dy, dz
        double precision g, u, msd(nmax)

C.................................................................

        nsample=5000*1000
        deltat=1.0

C.......[HOC4Py][NTf2] 300 K (ca).................................

        dself=(0.74+0.68)*1e-11*1e6
        deltar=sqrt(dself*6.0)
        deltas=sqrt(3.3d0)*deltar
        tau=0.3**2/dself
        rs=1.05
        astar=0.97
        rstar=0.15
C.................................................................

        nsteps=nmax
        r2s=rs**2

        do i=1,nsteps
           h(i)=0
           msd(i)=0.0d0
        enddo
        do is=1,nsample
           xi=0.0
           yi=0.0
           zi=0.0
           u=0.0
           do while(u.eq.0.0)
              call random_number(u)
           enddo
           itau=int(-log(u)*tau)+1
           if (mod(is,1000).eq.0) then
```

```
            print*, is, itau
         endif
         do i=1,nsteps
            if (i.lt.itau) then
               call random_vector(dx,dy,dz,deltas)
               xi=xi+dx
               yi=yi+dy
               zi=zi+dz
               r2i=xi*xi+yi*yi+zi*zi
               if (r2i.gt.r2s) then
                  xi=xi-2.0*dx
                  yi=yi-2.0*dy
                  zi=zi-2.0*dz
                  r2i=xi*xi+yi*yi+zi*zi
               endif
            else
               call random_vector(dx,dy,dz,deltar)
               xi=xi+dx
               yi=yi+dy
               zi=zi+dz
               r2i=xi*xi+yi*yi+zi*zi
            endif
            ri=dsqrt(r2i)
            g=astar*exp(-ri/rstar)
            call random_number(u)
            if (u.le.g) then
               h(i)=h(i)+1
            endif
            msd(i)=msd(i)+r2i
         enddo
      enddo

      open (10,file="c_of_t.dat")
      open (20,file="msd_of_t.dat")
      do i=1,nsteps
         write(10,*)  dble(i)*deltat, dble(h(i))/dble(nsample)
         write(20,*)  dble(i)*deltat, msd(i)/dble(nsample)
      enddo
      close(10)
      close(20)

      end

C.....................................................................

      subroutine random_vector(dx,dy,dz,dr)
      implicit none
      double precision dx, dy, dz, dr, u1, u2
      double precision ran1,ran2,ransq,ranh
      ransq=2.0
      do while (ransq.gt.1.0)
         call random_number(u1)
         call random_number(u2)
         ran1=1.0-2.0*u1
         ran2=1.0-2.0*u2
         ransq=ran1**2+ran2**2
      enddo
      ranh=2.0*sqrt(1.0-ransq)
      dx=ran1*ranh*dr
      dy=ran2*ranh*dr
      dz=(1.0-2.0*ransq)*dr
      end
```

S11 C(t) for Random Walker on a Cubic lattice

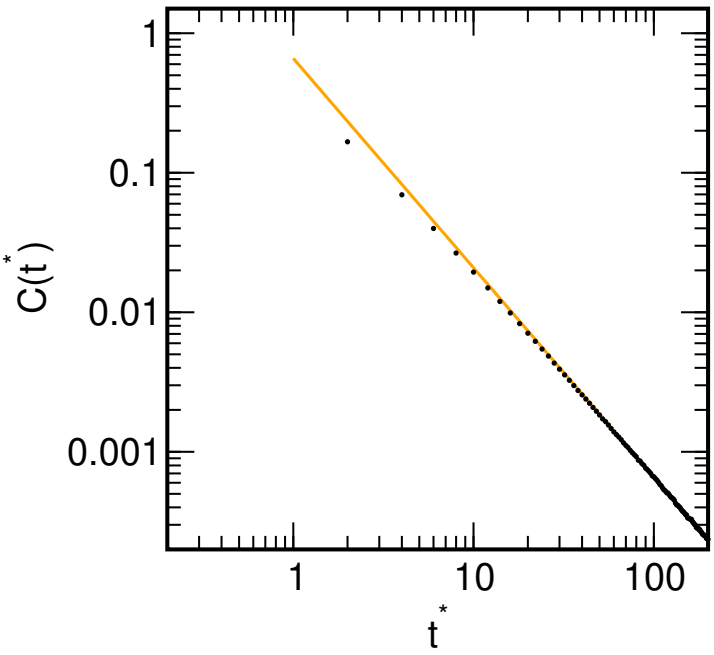

Figure S11: Black dots: $C(t)$ computed for a random walker with discrete jump-times on a cubic lattice. Next nearest neighbour distance d^* and time between jumps τ^* are unity. Hence the diffusion coefficient is $D^* = 1/6$ and the "acceptor density" $\rho^*_{\rm acc} = 1$. The solid orange line denotes $\lim_{t^*\to\infty} C(t^*) = (s\,\rho^*_{\rm acc}(4\pi D^* \cdot t^*)^{3/2})^{-1}$ with $s = 1/2$. Note that the walker can return to its starting point only at even times t^*.

S12 Performed MD Simulations: Layout and Technical Aspects

We have performed MD simulations of hydroxyl-functonalised ILs $[HOC_nPy][NTf_2]$ with n = 2,3,4,5. The simulations are covering the temperature range between 300 K and 400 K at a pressure of 1 bar. The *NPT* MD simulations of the $[HOC_nPy][NTf_2]$ ILs with $n = 2, 3, 4, 5$ were consisting of 512 ion pairs using periodic boundary conditions. A typical snapshot of a simulation box taken from a MD simulation of $[HOC_5Py][NTf_2]$ at 300 K is shown in Figure S12. MD simulations were performed using GROMACS 5.0.6.[5–9], while the most recent version of the MOSCITO suite of programs [10] was employed for topology file preparation. To assemble the system, the ions were first arranged on a *bcc* lattice and then equilibrated at 500 K and 1 bar for 2 ns. After another equilibration for 2 ns at the desired temperatures, production runs of 100 ns were carried out. The "NGOLP" force field describing the $[NTf_2]^-$ anion is discussed in Refs. [11, 12]. The molecular model for hydroxyl-functionalised pyridinium ions was derived from the OPLS force field for pyridine according to Jorgensen et al. [13], and is described in Ref. [14]. The integration time step for all simulations was 2 fs. As we used the *NPT* ensemble in our simulations, pressure and temperature of the simulated systems were controlled by means of the Nosé-Hoover thermostat [15, 16] and the Parrinello-Rahman barostat [17, 18] with coupling times $\tau_T = 1.0$ ps and $\tau_p = 2.0$ ps, respectively. The electrostatic interactions were treated by smooth particle mesh Ewald summation [19]. A real space cutoff of 1.2 nm was employed, and a mesh spacing of approximately 0.12 nm (4th order interpolation) was used to determine the reciprocal lattice contributions. The Ewald convergence parameter was set to a relative accuracy of the Ewald sum of 10^{-5}. All bond lengths were kept fixed during the simulation run and distance constraints were solved by means of the LINCS procedure [20]. Lennard-Jones cutoff corrections for energy and pressure [21] were applied.

To determine viscosities and hydrogen bond population correlation functions, autocorrelation functions over large time sets have to be computed. To evaluate time correlation functions for ultra large time sets with up to 20×10^6 entries efficiently, we applied the convolution theorem using fast Fourier transformations (FFT) [22, 23]. The computation of the properties from MD simulations were done using home-built software based on the MDANALYSIS [24, 25], NUMPY [26], and SCIPY [27] frameworks.

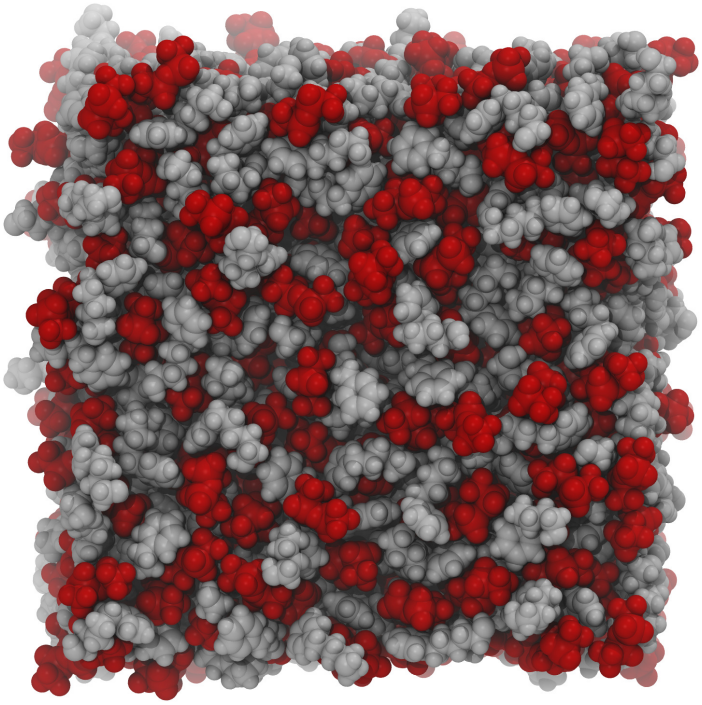

Figure S12: Snapshot of an entire MD box consisting of 512 ion pairs, taken from a the $[HOC_5Py][NTf_2]$ simulation at 300 K. $[HOC_5Py]^+$ cations are depicted in white, whereas $[NTf_2]^-$ anions are shown in red. The image was created using VMD [28].

S13 Force Field Validation

The snapshot of $[HOC_5Py][NTf_2]$ at 300 K depicted in Figure S12 highlights structural features of ionic liquids composed of roughly similar sized ions [29], such as the typical charge induced alternating order of anions and cations [30, 31]. The average cation/anion coordination numbers range between 7.4 and 7.5, as obtained from center-of-mass radial pair distribution functions (see SI).

Figure S13 shows a comparison between the mass density ρ in the simulation and the density of the respective IL obtained from measurements performed in our laboratory using an Anton Paar DMA 5000 M density meter. Although there is a consistent offset of about $50\,\mathrm{kg\,m^{-3}}$ for all studied ILs, the thermal expansion coefficients are in good agreement over the examined temperature range. Note that the relative density increase with increasing n is well in accordance with the experimental data. At the highest experimental temperature of 343.15 K, the relative deviation from the correspondingly interpolated simulation data lies between 3.9 % and 4.2 % for all ILs. Tabulated density data for both, MD simulation and experiments are provided in Tables S1 and S2 in the SI.

Figure S14 shows shear viscosities η calculated from our MD simulations using the Green-Kubo approach in combination with a comparison to experimental data obtained in our laboratory using a rolling-ball viscometer Lovis 2000 M/ME from Anton Paar. The viscosity data as a function of n and temperature show a satisfying agreement. Note the hierarchy of the viscosities as a function of n: while maintaining the strong Coulomb interactions between the ions, the added dispersion interactions with increasing n lead to a rising η with increasing chain length. In particular, however, we would like to point to the enhanced gap between viscosities observed between $n = 2, 3$ and $n = 4, 5$, which coincides with the enhancing lifetimes between (ca) hydrogen bonds (see discussion in hydrogen bond lifetime section in the paper). The temperature dependence of $\eta(T)$ is characterised by an increasing activation energy with decreasing temperature for both experimental and simulated viscosity data. This temperature dependence can be well described by a Vogel-Fulcher-Tammann (VFT) representation $\eta(T) = \eta_0 \cdot \exp[B/(T - T_0)]$ with a T_0 between 120 K and 150 K. (VFT fits are indicated as solid lines in Figure S14). Tabulated viscosity data for both, MD simulation and experiments are provided in Tables S3 and S4.

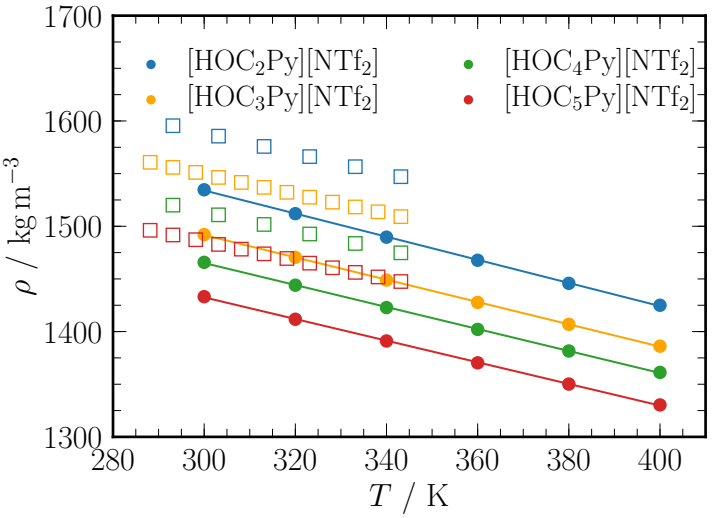

Figure S13: Density ρ of the ILs [HOC$_n$Py][NTf$_2$] ($n = 2, 3, 4, 5$) as a function of the temperature T. Circles: MD data. Squares: Experimental data obtained in our laboratory. Solid lines represent a linear fit to the MD data. The relative differences between simulated and experimental data at 343.15 K is less than 4.2 % for all studied ILs.

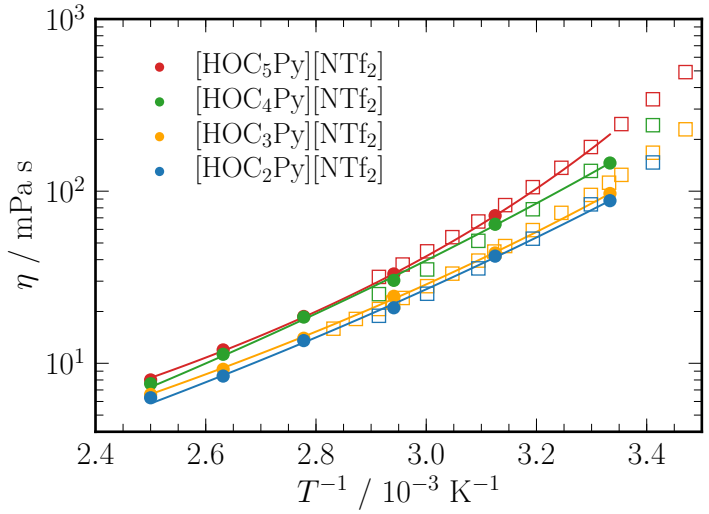

Figure S14: Viscosity η of the ILs [HOC$_n$Py][NTf$_2$] ($n = 2, 3, 4, 5$) as a function of the inverse temperature T^{-1}. There is a good agreement between experimental data measured in our laboratory (squares) and the viscosities acquired by our equilibrium MD simulations (circles). The lines represent a VFT-fit to the simulated data.

References

[1] T. Niemann, J. Neumann, P. Stange, R. Ludwig, S. Gartner, T. G. A. Young, D. Paschek, G. G. Warr, R. Atkin, *Angew. Chem. Int. Ed.* **2019**, *58*, 12887–12892.

[2] T. Niemann, D. H. Zaitsau, A. Strate, P. Stange, R. Ludwig, *Phys. Chem. Chem. Phys.* **2020**, *22*, 2763–2774.

[3] Y. Zhang, A. Otani, E. J. Maginn, *J. Chem. Theory Comput.* **2015**, *11*, 3537–3546.

[4] J. P. Hansen, I. R. McDonald, *Theory of Simple Liquids with Applications to Soft Matter*, 4th ed., Academic Press, **2013**.

[5] S. Páll, M. J. Abraham, C. Kutzner, B. Hess, E. Lindahl in Solving Software Challenges for Exascale, (Eds.: S. Markidis, E. Laure), Springer International Publishing, Cham, **2015**, pp. 3–27.

[6] S. Pronk, S. Páll, R. Schulz, P. Larsson, P. Bjelkmar, R. Apostolov, M. R. Shirts, J. C. Smith, P. M. Kasson, D. van der Spoel, B. Hess, E. Lindahl, *Bioinformatics* **2013**, *29*, 845–854.

[7] B. Hess, C. Kutzner, D. van der Spoel, E. Lindahl, *J. Chem. Theory Comput.* **2008**, *4*, 435–447.

[8] D. van der Spoel, E. Lindahl, B. Hess, G. Groenhof, A. E. Mark, H. J. C. Berendsen, *J. Comput. Chem.* **2005**, *26*, 1701–1718.

[9] H. J. C. Berendsen, D. van der Spoel, R. van Drunen, *Comput. Phys. Commun.* **1995**, *91*, 43–56.

[10] D. Paschek, A. Geiger, MOSCITO (Version 4.180), http://www.moscitomd.org, **2012**.

[11] J. Neumann, B. Golub, L.-M. Odebrecht, R. Ludwig, D. Paschek, *J. Chem. Phys.* **2018**, *148*, 193828.

[12] T. Köddermann, D. Paschek, R. Ludwig, *ChemPhysChem* **2007**, *8*, 2464–2470.

[13] W. L. Jorgensen, N. A. McDonald, *J. Mol. Struct.: THEOCHEM* **1998**, *424*, 145–155.

[14] J. Neumann, D. Paschek, A. Strate, R. Ludwig, *J. Phys. Chem. B* **2021**, *125*, 281–286.

[15] S.Nosé, *Mol. Phys.* **1984**, *52*, 255–268.

[16] W. G. Hoover, *Phys. Rev. A* **1985**, *31*, 1695–1697.

[17] M. Parrinello, A. Rahman, *J. Appl. Phys.* **1981**, *52*, 7182–7190.

[18] S. Nosé, M. L. Klein, *Mol. Phys.* **1983**, *50*, 1055–1076.

[19] U. Essmann, L. Petera, M. Berkowitz, T. Darden, H. Lee, L. Pedersen, *J. Chem. Phys.* **1995**, *103*, 8577–8593.

[20] B. Hess, H. Bekker, H. J. C. Berendsen, J. G. E. M. Fraaije, *J. Comp. Chem.* **1997**, *18*, 1463–1472.

[21] M. P. Allen, D. J. Tildesley, *Computer Simulation of Liquids*, Oxford University Press, Clarendon, Oxford, **1987**.

[22] T. S. Grigera, `arXiv:2002.01750v1` **2020**, `[cond-mat.stat-mech]`.

[23] W. H. Press, S. A. Teukolsky, W. T. Vetterling, P. Flannery, *Numerical Recipes in C: The Art of Scientific Computing*, 2nd ed., Cambridge University Press, Cambridge, USA, **1992**.

[24] N. Michaud-Agraval, E. J. Denning, T. B. Woolf, O. Beckstein, *J. Comput. Chem.* **2011**, *32*, 2319–2327.

[25] R. J. Gowers, M. Linke, J. Barnoud, T. J. E. Reddy, M. N. Melo, S. L. Seyler, J. Domański, D. L. Dotson, S. Buchoux, I. M. Kenney, O. Beckstein in Proceedings of the 15th Python in Science Conference, (Eds.: S. Benthall, S. Rostrup), Austin, TX, **2016**, pp. 98–105.

[26] T. Oliphant, NumPy: A guide to NumPy, USA: Trelgol Publishing, **2006**–.

[27] P. Virtanen, R. Gommers, T. E. Oliphant, M. Haberland, T. Reddy, D. Cournapeau, E. Burovski, P. Peterson, W. Weckesser, J. Bright, S. J. van der Walt, M. Brett, J. Wilson, K. J. Millman, N. Mayorov, A. R. J. Nelson, E. Jones, R. Kern, E. Larson, C. J. Carey, bibinitperiodI. Polat, Y. Feng, E. W. Moore, J. VanderPlas, D. Laxalde, J. Perktold, R. Cimrman, I. Henriksen, E. A. Quintero, C. R. Harris, A. M. Archibald, A. H. Ribeiro, F. Pedregosa, P. van Mulbregt, SciPy 1.0 Contributors, *Nature Methods* **2020**, *17*, 261–272.

[28] W. Humphrey, A. Dalke, K. Schulten, *Journal of Molecular Graphics* **1996**, *14*, 33–38.

[29] J. N. A. Canongia Lopes, A. A. Pádua, *J. Phys. Chem. B* **2006**, *110*, 3330–3335.

[30] D. Roy, N. Patel, S. Conte, M. Maroncelli, *J. Phys. Chem. B* **2010**, *114*, 8410–8424.

[31] E. Shelepova, D. Paschek, R. Ludwig, N. N. Medvedev, *J. Mol. Liq.* **2020**, *299*, 112121.

Declaration of Authorship

I hereby declare under oath that I have completed the work submitted here independently and have composed it without outside assistance. Furthermore, I have not used anything other than the resources and sources stated and where I have taken sections from these works in terms of content or text, I have identified this appropriately.

Jan Neumann
Rostock, June 14, 2021

Bibliography

[1] T. Köddermann, D. Paschek, R. Ludwig, *ChemPhysChem* **2007**, *8*, 2464.

[2] J. Neumann, B. Golub, L.-M. Odebrecht, R. Ludwig, D. Paschek, *J. Chem. Phys.* **2018**, *148*, 193828.

[3] J. Neumann, D. Paschek, A. Strate, R. Ludwig, *J. Phys. Chem. B* **2021**, *125*, 281.

[4] J. Neumann, R. Ludwig, D. Paschek, *J. Phys. Chem. B* **2021**, *125*, 5132.

[5] D. H. Zaitsau, J. Neumann, T. Niemann, A. Strate, D. Paschek, S. P. Verevkin, R. Ludwig, *Phys. Chem. Chem. Phys.* **2019**, *21*, 20308.

[6] T. Niemann, J. Neumann, P. Stange, S. Gärtner, T. G. Youngs, D. Paschek, G. G. Warr, R. Atkin, R. Ludwig, *Angew. Chem. Int. Ed.* **2019**, *58*, 12887.

[7] F. H. Stillinger, *Science* **1980**, *209*, 451.

[8] W. M. Latimer, W. H. Rodebush, *J. Am. Chem. Soc.* **1920**, *42*, 1419.

[9] G. A. Jeffrey, *An Introduction to Hydrogen Bonding*, *Vol. 12*, Oxford University Press New York, **1997**.

[10] G. R. Desiraju, T. Steiner, *The Weak Hydrogen Bond: In Structural Chemistry and Biology*, *Vol. 9*, International Union of Crystal, **2001**.

[11] L. Pauling, *The Nature of the Chemical Bond*, *Vol. 260*, Cornell University Press Ithaca, NY, **1960**.

[12] T. Steiner, *Angew. Chem. Int. Ed.* **2002**, *41*, 48.

[13] J. Bernstein, R. E. Davis, L. Shimoni, N.-L. Chang, *Angew. Chem. Int. Ed.* **1995**, *34*, 1555.

[14] M. Yoshizawa, W. Xu, C. A. Angell, *J. Am. Chem. Soc.* **2003**, *125*, 15411.

[15] P. A. Hunt, B. Kirchner, T. Welton, *Chem. Eur. J.* **2006**, *12*, 6762.

[16] P. A. Hunt, *J. Phys. Chem. B* **2007**, *111*, 4844.

[17] T. L. Greaves, C. J. Drummond, *Chem. Rev.* **2008**, *108*, 206.

[18] H. Weingärtner, *Angew. Chem. Int. Ed.* **2008**, *47*, 654.

[19] K. Fumino, A. Wulf, R. Ludwig, *Angew. Chem. Int. Ed.* **2009**, *48*, 3184.

[20] K. Fumino, A. Wulf, R. Ludwig, *Phys. Chem. Chem. Phys.* **2009**, *11*, 8790.

[21] C. Roth, T. Peppel, K. Fumino, M. Köckerling, R. Ludwig, *Angew. Chem. Int. Ed.* **2010**, *49*, 10221.

[22] R. Hayes, G. G. Warr, R. Atkin, *Chem. Rev.* **2015**, *115*, 6357.

[23] P. A. Hunt, C. R. Ashworth, R. P. Matthews, *Chem. Soc. Rev.* **2015**, *44*, 1257.

[24] P. Wasserscheid, T. Welton, *Ionic Liquids in Synthesis*, John Wiley & Sons, **2008**.

[25] T. Welton, *Chem. Rev.* **1999**, *99*, 2071.

[26] R. D. Rogers, K. R. Seddon, *Science* **2003**, *302*, 792.

[27] A. Lewandowski, A. Świderska-Mocek, *J. Power Sources* **2009**, *194*, 601.

[28] J. Claus, A. Jastram, E. Piktel, R. Bucki, P. A. Janmey, U. Kragl, *J. Appl. Polym. Sci.* **2021**, *138*, 50222.

[29] A. Knorr, K. Fumino, A.-M. Bonsa, R. Ludwig, *Phys. Chem. Chem. Phys.* **2015**, *17*, 30978.

[30] A. Knorr, R. Ludwig, *Sci. Rep.* **2015**, *5*, 1.

[31] A. Knorr, P. Stange, K. Fumino, F. Weinhold, R. Ludwig, *ChemPhysChem* **2016**, *17*, 458.

[32] A. Strate, T. Niemann, D. Michalik, R. Ludwig, *Angew. Chem. Int. Ed.* **2017**, *56*, 496.

[33] A. Strate, T. Niemann, R. Ludwig, *Phys. Chem. Chem. Phys.* **2017**, *19*, 18854.

[34] T. Niemann, A. Strate, R. Ludwig, H. J. Zeng, F. S. Menges, M. A. Johnson, *Angew. Chem. Int. Ed.* **2018**, *57*, 15364.

[35] F. S. Menges, H. J. Zeng, P. J. Kelleher, O. Gorlova, M. A. Johnson, T. Niemann, A. Strate, R. Ludwig, *J. Phys. Chem. Lett.* **2018**, *9*, 2979.

[36] T. Niemann, P. Stange, A. Strate, R. Ludwig, *ChemPhysChem* **2018**, *19*, 1691.

[37] T. Niemann, P. Stange, A. Strate, R. Ludwig, *Phys. Chem. Chem. Phys.* **2019**, *21*, 8215.

[38] T. Niemann, D. H. Zaitsau, A. Strate, P. Stange, R. Ludwig, *Phys. Chem. Chem. Phys.* **2020**, *22*, 2763.

[39] F. Stillinger, *Adv. Chem. Phys.* **1975**, *31*, 1.

[40] D. Rapaport, *Mol. Phys.* **1983**, *50*, 1151.

[41] F. Sciortino, S. Fornili, *J. Chem. Phys.* **1989**, *90*, 2786.

[42] D. A. Zichi, P. J. Rossky, *J. Chem. Phys.* **1986**, *84*, 2814.

[43] F. W. Starr, J. K. Nielsen, H. E. Stanley, *Physical Review E* **2000**, *62*, 579.

[44] D. Chandler, *J. Chem. Phys.* **1978**, *68*, 2959.

[45] I. Skarmoutsos, D. Dellis, R. P. Matthews, T. Welton, P. A. Hunt, *J. Phys. Chem. B* **2012**, *116*, 4921.

[46] I. Skarmoutsos, T. Welton, P. A. Hunt, *Phys. Chem. Chem. Phys.* **2014**, *16*, 3675.

[47] D. Paschek, B. Golub, R. Ludwig, *Phys. Chem. Chem. Phys.* **2015**, *17*, 8431.

[48] S. Gehrke, M. von Domaros, R. Clark, O. Hollóczki, M. Brehm, T. Welton, A. Luzar, B. Kirchner, *Faraday Discuss.* **2018**, *206*, 219.

[49] A. Strate, J. Neumann, V. Overbeck, A.-M. Bonsa, D. Michalik, D. Paschek, R. Ludwig, *J. Chem. Phys.* **2018**, *148*, 193843.

[50] S. Gehrke, B. Kirchner, *J. Chem. Eng. Data* **2019**, *65*, 1146.

[51] T. Köddermann, D. Reith, R. Ludwig, *ChemPhysChem* **2013**, *14*, 3368.

[52] K. Fujii, T. Fujimori, T. Takamuku, R. Kanzaki, Y. Umebayashi, S.-i. Ishiguro, *J. Phys. Chem. B* **2006**, *110*, 8179.

[53] D. Yalcin, I. D. Welsh, E. L. Matthewman, S. P. Jun, M. Mckeever-Willis, I. Gritcan, T. L. Greaves, C. C. Weber, *Phys. Chem. Chem. Phys.* **2020**, *22*, 11593.

[54] T. Klein, M. Piszko, M. Lang, J. Mehler, P. S. Schulz, M. H. Rausch, C. Giraudet, T. M. Koller, A. P. Fröba, *J. Chem. Eng. Data* **2020**, *65*, 4116.

[55] V. Overbeck, B. Golub, H. Schröder, A. Appelhagen, D. Paschek, K. Neymeyr, R. Ludwig, *J. Mol. Liq.* **2020**, *319*, 114207.

[56] A. E. Khudozhitkov, J. Neumann, T. Niemann, D. Zaitsau, P. Stange, D. Paschek, A. G. Stepanov, D. I. Kolokolov, R. Ludwig, *Angew. Chem. Int. Ed.* **2019**, *58*, 17863.

[57] A. Strate, J. Neumann, T. Niemann, P. Stange, A. E. Khudozhitkov, A. G. Stepanov, D. Paschek, D. I. Kolokolov, R. Ludwig, *Phys. Chem. Chem. Phys.* **2020**, *22*, 6861.

[58] T. Niemann, D. Zaitsau, A. Strate, A. Villinger, R. Ludwig, *Sci. Rep.* **2018**, *8*, 1.

[59] V. Kempter, B. Kirchner, *J. Mol. Struct.* **2010**, *972*, 22.

[60] T. Köddermann, C. Wertz, A. Heintz, R. Ludwig, *Angew. Chem. Int. Ed.* **2006**, *45*, 3697.

[61] T. Köddermann, C. Wertz, A. Heintz, R. Ludwig, *ChemPhysChem* **2006**, *7*, 1944.

[62] W. L. Jorgensen, D. S. Maxwell, J. Tirado-Rives, *J. Am. Chem. Soc.* **1996**, *118*, 11225.

[63] W. L. Jorgensen, N. A. McDonald, *J. Mol. Struct.: THEOCHEM* **1998**, *424*, 145.

[64] D. H. Zaitsau, V. N. Emel'yanenko, P. Stange, C. Schick, S. P. Verevkin, R. Ludwig, *Angew. Chem. Int. Ed.* **2016**, *55*, 11682.

[65] Y. Zhang, A. Otani, E. J. Maginn, *J. Chem. Theory Comput.* **2015**, *11*, 3537.

[66] J. S. Wilkes, *J. Mol. Catal. A: Chem.* **2004**, *214*, 11.

[67] O. Okoturo, T. VanderNoot, *J. Electroanal. Chem.* **2004**, *568*, 167.

[68] T. Yan, C. J. Burnham, M. G. Del Pópolo, G. A. Voth, *J. Phys. Chem. B* **2004**, *108*, 11877.

[69] C. Rey-Castro, L. F. Vega, *J. Phys. Chem. B* **2006**, *110*, 14426.

[70] A. Bagno, F. D'Amico, G. Saielli, *J. Mol. Liq.* **2007**, *131-132*, 17.

[71] O. Borodin, *J. Phys. Chem. B* **2009**, *113*, 11463.

[72] D. Bedrov, O. Borodin, Z. Li, G. D. Smith, *J. Phys. Chem. B* **2010**, *114*, 4984.

[73] C. Schröder, O. Steinhauser, *J. Chem. Phys.* **2010**, *133*, 154511.

[74] C. Schröder, *Phys. Chem. Chem. Phys.* **2012**, *14*, 3089.

[75] F. Dommert, K. Wendler, R. Berger, L. Delle Site, C. Holm, *ChemPhysChem* **2012**, *13*, 1625.

[76] M. H. Ghatee, A. R. Zolghadr, F. Moosavi, Y. Ansari, *J. Chem. Phys.* **2012**, *136*, 124706.

[77] M. Lísal, Z. Chval, J. Storch, P. Izák, *J. Mol. Liq.* **2014**, *189*, 85.

[78] M. Schmollngruber, V. Lesch, C. Schröder, A. Heuer, O. Steinhauser, *Phys. Chem. Chem. Phys.* **2015**, *17*, 14297.

[79] V. Lesch, H. Montes-Campos, T. Méndez-Morales, L. J. Gallego, A. Heuer, C. Schröder, L. M. Varela, *J. Chem. Phys.* **2016**, *145*, 204507.

[80] R. Ishizuka, N. Matubayasi, *J. Chem. Theory Comput.* **2016**, *12*, 804.

[81] D. Bedrov, J.-P. Piquemal, O. Borodin, A. D. MacKerell, B. Roux, C. Schröder, *Chem. Rev.* **2019**, *119*, 7940.

[82] K. Goloviznina, J. N. Canongia Lopes, M. Costa Gomes, A. A. H. Pádua, *J. Chem. Theory Comput.* **2019**, *15*, 5858.

[83] A. D. McNaught, A. Wilkinson, *Compendium of Chemical Terminology*, *Vol. 1669*, Blackwell Science Oxford, **1997**.

[84] S. von Bülow, J. T. Bullerjahn, G. Hummer, *J. Chem. Phys.* **2020**, *153*, 021101.

[85] N. Bloembergen, E. M. Purcell, R. V. Pound, *Phys. Rev.* **1948**, *73*, 679.

[86] P. Muller, *Pure Appl. Chem.* **1994**, *66*, 1077.

[87] G. R. Desiraju, *Angew. Chem. Int. Ed.* **2011**, *50*, 52.

[88] E. Arunan, G. R. Desiraju, R. A. Klein, J. Sadlej, S. Scheiner, I. Alkorta, D. C. Clary, R. H. Crabtree, J. J. Dannenberg, P. Hobza, H. G. Kjaergaard, A. C. Legon, B. Mennucci, D. J. Nesbitt, *Pure Appl. Chem.* **2011**, *83*, 1637.

[89] R. Kumar, J. R. Schmidt, J. L. Skinner, *J. Chem. Phys.* **2007**, *126*, 204107.

[90] A. K. Soper, *Phys. Rev. B* **2005**, *72*, 104204.

[91] A. K. Soper, *Empirical Potential Structure Refinement: A Users's Guide*, Rutherford Appleton Laboratory, Didcot, **2017**.

[92] S. Grimme, J. Antony, S. Ehrlich, H. Krieg, *J. Chem. Phys.* **2010**, *132*, 154104.

[93] S. Ehrlich, J. Moellmann, W. Reckien, T. Bredow, S. Grimme, *ChemPhysChem* **2011**, *12*, 3414.

[94] L. B. Skinner, C. Huang, D. Schlesinger, L. G. M. Pettersson, A. Nilsson, C. J. Benmore, *J. Chem. Phys.* **2013**, *138*, 074506.

[95] U. Bergmann, A. Di Cicco, P. Wernet, E. Principi, P. Glatzel, A. Nilsson, *J. Chem. Phys.* **2007**, *127*, 174504.

[96] A. H. Narten, A. Habenschuss, *J. Chem. Phys.* **1984**, *80*, 3387.

[97] C. H. Bennett in *Algorithms for Chemical Computations*, Chapter 4, p. 63.

[98] O. Markovitch, N. Agmon, *J. Chem. Phys.* **2008**, *129*, 084505.

[99] J. Busch, J. Neumann, D. Paschek, *J. Chem. Phys.* **2021**, *154*, 214501.

[100] D. Laage, J. T. Hynes, *Science* **2006**, *311*, 832.

[101] D. Laage, J. T. Hynes, *J. Phys. Chem. B* **2008**, *112*, 14230.

[102] A. A. Vartia, K. R. Mitchell-Koch, G. Stirnemann, D. Laage, W. H. Thompson, *J. Phys. Chem. B* **2011**, *115*, 12173.

[103] A. Luzar, D. Chandler, *Phys. Rev. Lett.* **1996**, *76*, 928.

[104] A. Luzar, D. Chandler, *Nature* **1996**, *379*, 55.

[105] A. Luzar, *J. Chem. Phys.* **2000**, *113*, 10663.